

Architecture, spatial metabolism and stress response of bacterial biofilms

Dissertation

kumulativ

zur Erlangung des Grades eines

Doktor der Naturwissenschaften

(Dr. rer. nat.)

des Fachbereichs Biologie der Philipps-Universität Marburg

vorgelegt von

Francisco Javier Díaz Pascual

aus Punta Arenas, Chile

Marburg, 2020

Originaldokument gespeichert auf dem Publikationsserver der
Philipps-Universität Marburg
<http://archiv.ub.uni-marburg.de>



Dieses Werk bzw. Inhalt steht unter einer
Creative Commons
Namensnennung
Keine kommerzielle Nutzung
Weitergabe unter gleichen Bedingungen
3.0 Deutschland Lizenz.

Die vollständige Lizenz finden Sie unter:
<http://creativecommons.org/licenses/by-nc-sa/3.0/de/>

Die vorliegende Arbeit wurde in der Zeit von Oktober 2015 bis Oktober 2020 unter der Betreuung von Herrn Prof. Dr. Knut Drescher am Max-Planck-Institut für terrestrische Mikrobiologie in Marburg angefertigt.

Vom Fachbereich Biologie der Philipps-Universität Marburg (Hochschulkennziffer 1180) als Dissertation angenommen am 05.01.2021

Erstgutachter: Prof. Dr. Knut Drescher

Zweitgutachter: Prof. Dr. Victor Sourjik

Tag der Disputation: 29.01.2021

Erklärung

Ich versichere, dass ich meine Dissertation mit dem Titel:

Architecture, spatial metabolism and stress response of bacterial biofilms

selbstständig ohne unerlaubte Hilfe angefertigt und mich dabei keiner anderen als der von mir ausdrücklich bezeichneten Quellen und Hilfsmittel bedient habe.

Diese Dissertation wurde in der jetzigen oder einer ähnlichen Form noch bei keiner anderen Hochschule eingereicht und hat noch keinen sonstigen Prüfungszwecken gedient.

Marburg, den 26.10.2020

Francisco Javier Díaz Pascual

Parts of this dissertation have been published or are in preparation for publication:

1. **Díaz-Pascual F.**, Lempp M., Noshok K., Jeckel H., Hansen M.F., Neuhaus K., Hartmann R., Link H., Drescher K. Spatiotemporal multi-omic analysis of *Escherichia coli* biofilm colonies reveals a novel cross-feeding of alanine. *In preparation*.

My contribution to this work included performing and designing all experiments (except for RNA work and mass spectrometry measurements), performing all data analysis (except developing the software for image analysis), creating all new strains, and writing the current version of the manuscript.

2. **Díaz-Pascual F.**, Hartmann R., Lempp M., Vidakovic L., Song B., Jeckel H., Thormann K., Yildiz F., Dunkel J., Link H., Nadell C., Drescher K. Breakdown of *Vibrio cholerae* biofilm architecture induced by antibiotics disrupts community barrier function. *Nature Microbiology* 4, 2136–2145 (2019).

My contribution to this work included designing, performing and analyzing all experiments (except for the *in silico* simulations and the mass spectrometry measurements), figure creating and contributing in the writing of the manuscript.

3. Hartmann R., Singh P., Pearce P., Mok R., Song B., **Díaz-Pascual F.**, Dunkel J., Drescher K. Emergence of three-dimensional order and structure in growing biofilms. *Nature Physics* 5, 251–256 (2019).

My contribution to this work included establishing a tunable and inducible plasmid-based system to control *rbmA* expression in *Vibrio cholerae* biofilms that was used for cell-cell attraction calibration, aiding with testing of the segmentation software used, and providing ideas for software improvement.

4. Beuter B., Gomes-Filho J., Randau L., **Díaz-Pascual F.**, Drescher K., Link H. Selective Enrichment of Slow-Growing Bacteria in a Metabolism-Wide CRISPRi Library with a TIMER Protein. *ACS Synthetic Biology* 7, 2775–2782 (2018).

My contribution included the construction of a single plasmid system containing the dCas9 enzyme and sgRNA systems used for CRISPRi, designing and testing multiple promoters and sgRNA constructs to ensure minimal leakage and tunable expression. This system was used as backbone for the CRISPRi library used in the study. I contributed to write the corresponding part of the manuscript.

The stated contributions of Francisco Javier Díaz Pascual to the publications or manuscripts in preparation, which are part of this dissertation, are herewith endorsed by:

Francisco Javier Díaz Pascual

Prof. Dr. Knut Drescher

Publications not included in this dissertation:

1. Yordanov S., Neuhaus K., Hartmann R., **Díaz-Pascual F.**, Vidakovic L., Singh P.K., Drescher K. Single objective high resolution light sheet fluorescence microscopy for standard sample geometries. *In preparation*.
2. Hartmann R., Jeckel H., Jelli E., Singh P.K., Vaidya S., Bayer M., Rode D., Vidakovic L., **Díaz-Pascual F.**, Fong J., Dragoš A., Lamprecht O., Thöming J., Netter N., Häussler S., Nadell C.D., Sourjik V., Kovács Á., Yildiz F.H., Drescher K. Quantitative image analysis of microbial communities with BiofilmQ. *Nature Microbiology* 6, 151–156 (2021)

Summary	15
Zusammenfassung	17
Chapter I: Introduction	19
Model organisms for the study of biofilms.....	22
Methods to investigate spatiotemporal processes in biofilms.....	23
Biofilm formation.....	24
Biofilm matrix.....	25
Biofilms are physiologically heterogeneous with cross-feeding potential.....	26
Slow-growing cells and stress response in biofilms.....	28
Dissertation outline	30
References	31
Chapter II: Emergence of three-dimensional order and structure in growing biofilms	35
Abstract.....	37
Main Text	38
Methods.....	47
References	52
Supplementary information	54
Chapter III: Spatiotemporal multi-omic analysis of <i>Escherichia coli</i> biofilm colonies reveals a novel cross-feeding of alanine	95
Abstract.....	97
Introduction	98
Results.....	99
Methods.....	110
References	116
Supplementary information	118
Chapter IV: Selective enrichment of slow-growing bacteria in a metabolism-wide CRISPRi library with a TIMER protein	129
Abstract.....	131
Introduction	132
Results and Discussion	133
Methods.....	141
References	144
Supplementary Information	146
Chapter V: Breakdown of <i>Vibrio cholerae</i> biofilm architecture induced by antibiotics disrupts community barrier function	157
Abstract.....	159
Main text.....	160
Methods.....	171
References	180
Supplementary information	182
Chapter VI: Discussion	201
On the future of biofilm research.....	208
References	210

Summary

Bacteria commonly live in communities, embedded in a self-produced matrix, termed as biofilms. Bacterial biofilms are involved in many processes in natural, clinical and industrial settings. They, for example, influence environmental biochemical cycles, increase the persistence and resistance to antibiotics in the context of infection, and are commonly associated with the damage of food and pipelines in industry. The study of biofilms, particularly the process of formation, cellular metabolism of biofilm-dwelling bacteria, and their collective stress response, is instrumental for the development of new methods to combat biofilms, as well as for understanding bacterial physiology in natural environments. This dissertation addresses and contributes to answering some of the open questions in the field of biofilm research: how are biofilms formed and what determines their architecture? How do biofilm heterogeneity and biofilm metabolism interplay? How do different microbial subpopulations interact within a single-species biofilm? How do biofilms respond to stress at the single-cell and multicellular levels, and what are the consequences of such responses?

In chapter 2, we showed that mechanical cell-cell interactions determine biofilm architecture in surface-attached *Vibrio cholerae* biofilms. Using single-cell segmentation of microscopy images and *in silico* simulations we defined an interaction potential that predicts the overall biofilm architecture.

To study biofilm heterogeneity and metabolic interactions between subpopulations within bacterial biofilms, we searched for novel metabolic amino acid cross-feeding in isogenic *Escherichia coli* biofilm colonies. In chapter 3, using metabolomics, global and spatial transcriptomics, and confocal fluorescence imaging, we found new evidence suggesting alanine cross-feeding between different regions of the biofilm. This cross-feeding interaction had important consequences for colony growth and morphology, and for bacterial survival within the biofilm.

Biofilms are hypothesized to have an enrichment of slow-growing cells caused by environmental heterogeneity. Due to a lack of techniques for monitoring spatial metabolism this idea has however not been validated *in vivo*. We developed a new method to study slow-growing cells. In chapter 4, as a proof of concept, slow growing cells were enriched from a CRISPRi library by sorting them according to a fluorescent growth rate reporter. This technique could be applied to study slow growing cells within bacterial biofilms.

In chapter 5, we focused on how biofilms respond to antibiotic stress. Using *V. cholerae* biofilms, we found that bacteria respond at the single-cell level and at the multicellular level when exposed to translational inhibitors. Specifically, the cell volume and cell-cell spacing increased upon protein synthesis inhibition. These architectural changes had important consequences for the ecology

of biofilms, in particular antibiotic-treated biofilms were prone to invasion by other bacterial cells and bacteriophages.

In conclusion, this dissertation contributes to answer important questions in the field of biofilm research. It improves our understanding of bacterial biofilms, and could facilitate the development of new strategies to combat biofilms in clinical and industrial settings. Furthermore, this work highlights the importance of applying techniques with single-cell resolutions to study biofilms.

Zusammenfassung

Bakterien schließen sich für gewöhnlich, eingebettet in einer selbst produzierten Matrix, in Gemeinschaften zusammen. Diese sogenannten Biofilme sind in vielen natürlichen, klinischen und industriellen Prozesse involviert. So beeinflussen sie beispielsweise biochemische Umweltzyklen, erhöhen bei Infektionen die Resistenz gegen Antibiotika und sind gemeinhin verbunden mit Ertragsverlusten in der Nahrungsmittelherstellung und industriellen Produktionen. Die Forschung an Biofilmen ist fundamental für die Entwicklung neuer Strategien zur Bekämpfung von Biofilmen, aber auch für das Verständnis der bakteriellen Physiologie in natürlichen Umgebungen. Eine große Rolle spielen hier insbesondere der Prozess der Biofilmformierung, der zelluläre Metabolismus und die kollektive Antwort auf Stressoren. Diese Dissertation gibt Antworten auf offene Fragen in der Biofilmforschung. Wie formen sich Biofilme und welche Faktoren bestimmen deren Architektur? Wie spielen Biofilmheterogenität und Metabolismus zusammen? Wie interagieren verschiedene mikrobielle Subpopulationen innerhalb eines isogenen Biofilms? Wie reagieren Biofilme auf dem einzel- und multizellulären Level auf Stress und was folgt aus der Reaktion?

In Kapitel 2 zeigen wir, dass mechanische Zell-Zell Interaktionen die Architektur von oberflächenverbundenen *Vibrio cholerae* Biofilmen bestimmt. Mittels Einzelzellsegmentierung von Mikroskopie Bildern und *in silico* Simulationen, konnten wir ein Interaktionspotential definieren, welches die Biofilmarchitektur vorhersagen kann.

Um Biofilmheterogenität und metabolische Interaktionen zu identifizieren, suchten wir nach unbeschriebenen Aminosäure cross-feeding Verhalten zwischen Subpopulationen, innerhalb eines isogenen *Escherichia coli* Biofilms. In Kapitel 3 beschreiben wir, gestützt durch Metabolom-Analysen, globalen und räumlichen Transkriptom-Analysen und Konfokalmikroskopie, ein Alanin-cross-feeding zwischen den Zellen verschiedener Biofilmregionen. Diese Interaktion hat wichtige Konsequenzen für die Form, sowie das Wachstum der Kolonie und für das Überleben der Bakterien innerhalb des Biofilms.

Es wird angenommen, dass Aufgrund der heterogenen Bedingungen innerhalb des Biofilms, langsam wachsende Zellen akkumulieren. Dies konnte jedoch bisher, wegen der fehlenden Technik Metabolismus räumlich nachzuverfolgen, *in vivo* nicht bewiesen werden. Dadurch motiviert, haben wir eine neue Methode entwickelt, um diese Zellen zu untersuchen. In Kapitel 4 haben wir als konzeptionellen Beweis, langsam wachsende Zellen mittels Fluss-Sortierers und einem fluoreszierenden Wachstumsraten-Reporter angereichert. Diese Technik kann dazu genutzt werden, langsam wachsende Zellen innerhalb von Biofilmen zu untersuchen.

Kapitel 5 befasst sich damit, wie Biofilme auf Stress durch Antibiotika reagieren. In *V. cholerae* Biofilmen haben wir herausgefunden, dass Bakterien auf dem einzel- und multizellulären Level auf Translationsinhibitoren reagieren. Als Folge, hat sich insbesondere das Zellvolumen und der Abstand zwischen den einzelnen Zellen erhöht. Diese architektonischen Veränderungen haben wichtige Folgen für die Ökologie der Biofilme, so sind sie anfälliger für die Invasion durch andere Bakterien oder Bakteriophagen.

Diese Dissertation trägt dazu bei, wichtige Fragen der Biofilmforschung zu beantworten und das Verständnis von Biofilmen zu verbessern. Dies kann dazu beitragen, neue Strategien für den Kampf gegen Biofilme in klinischen und industriellen Bereichen zu entwickeln. Außerdem unterstreicht diese Arbeit die Wichtigkeit der Verwendung von Techniken mit Einzellauflösung für die Forschung an Biofilmen.

Chapter I: Introduction

Bacteria are the most successful group considering their vast habitat distribution and extensive metabolic capacities¹. These prokaryotes are found from the Antarctic to the Equator, from deep-sea hydrothermal vents to the atmosphere² and in space³.

Despite bacteria being ubiquitous, humankind was unable to study their morphology, physiology and significance until powerful enough microscopes were invented in the 17th century⁴. Antonie Philips van Leeuwenhoek was the first to observe microorganisms in the 1670s. One of his samples from a dental plaque provided an insight that bacteria reside in communities. However, this observation was neglected during the following centuries, during which research was conducted in batch systems with bacteria exposed to a uniform environment. Today, it is widely accepted that bacteria mostly live in communities termed biofilms¹. Formally, biofilms are defined as 'aggregates of microorganisms in which cells are frequently embedded in a self-produced matrix of extracellular polymeric substances (EPS) that are adherent to each other and/or a surface'⁵. The study of biofilms is pivotal to understand the complex bacterial processes and interactions that occur in environmental and clinical settings.

Biofilms play an important role for many geochemical cycles in different environments⁶. They can be both useful and problematical for many industrial processes such as the production of biofuels, food production and waste water treatment⁷⁻⁹. They colonize most multicellular organisms where they can be a determining factor between a healthy and a sick individual¹⁰. In particular, their composition can influence the onset of diseases such as cancer, diabetes, infections, obesity and inflammatory bowel disease^{11,12}. Furthermore, it is estimated that approximately 60% of all chronic wound infections involve bacterial biofilms¹³. Biofilm-forming pathogens are notoriously hard to eradicate, partly because they can be up to 1,000 times more resistant to antibiotics¹⁴⁻¹⁶. These recalcitrant biofilms can grow on indwelling devices such as catheters or implants from where they are difficult to remove, thus causing persistent infections^{15,17}. They are often tolerant to mechanical stress, chemical stress (antibiotics and disinfectants), and biological stress (immune cells, predation and bacteriophages)¹⁸⁻²⁰. Amongst these, the increased antibiotic tolerance of biofilms is of paramount importance for human health. This is because tolerant cells can work as a stepping stone leading to resistance²¹. Moreover, the ever-rising levels of antibiotic resistance has been suggested as the greatest threat for human health in the near future²².

An important aspect of biofilms is their complex spatial structure and social interactions. When living in biofilms, bacteria are spatially structured in close proximity, which enable them to interact and communicate in ways that are not possible for planktonic or distantly located cells. Cells can interact by physical connections²³, mechanical interactions²⁴, electrical activity²⁵, and by producing, secreting and sensing chemical signals such as quorum sensing molecules²⁶. The sum of these interactions

determines the emergent properties within biofilms, i.e. phenotypes observable at the biofilm level that are more than the sum of single-cell phenotypes. Some of the emergent properties that biofilms can present are: biofilm architecture, metabolic cross-feeding²⁷ and increased tolerance to stresses²⁸. Biofilm development and properties vary immensely between bacterial species and hence, different model organisms and imaging techniques are required to study different features of interest.

Model organisms for the study of biofilms

The process of biofilm formation and the resultant architecture varies not only between different bacteria, but also between different strains of a single bacterial species. Our current understanding of bacterial biofilms largely originates from commonly studied bacterial species such as *Escherichia coli*, *Pseudomonas aeruginosa*, *Vibrio cholerae*, *Staphylococcus* sp. and *Bacillus subtilis*. These bacterial species were chosen for their ecological and medical relevance. In this dissertation, we have used more than one of these model systems to explore biofilm-related behaviours.

Escherichia coli was first discovered by Theodor Escherich in 1885. It is a Gram-negative rod-shaped bacterium commonly found in the lower intestine of warm-blooded organisms, such as mammals. Generally, it is considered a commensal bacterium, but some serotypes can cause infections. To study biofilms-related behaviours, it is commonly grown on agar as colonies or in microfluidic systems^{18,29}. The presence of rich information regarding functional annotation of genes, along with their role in various regulatory and metabolic pathways, makes *E. coli* a particularly useful model to study complex behaviours such as those that emerge in biofilm-dwelling cells. Making use of the previously known information about individually annotated genetic pathways of *E. coli*, we utilized this model organism to study its metabolism in batch cultures and cross-feeding interactions within biofilms (work described in chapters 3 and 4).

Vibrio cholerae was first isolated in 1854 by Filippo Pacini. It is a Gram-negative, comma-shaped bacterium and is the causative agent of cholera³⁰. Its natural environment is brackish or saltwater. From these environments it can be ingested by humans causing acute infections. Biofilm growth is important for survival in the human host as well as in its aquatic environment³¹. This was highlighted by the fact that filtrating particular larger than 20 μm from drinking water drastically decreased the probability of getting a cholera infection³². Moreover, *V. cholerae* cells with genetic modifications that influence biofilm architecture have been shown to have diminished fitness when grown on chitin³³. In order to understand the effect of *V. cholerae* on human physiology, it is of paramount relevance to study *V. cholerae* biofilms. This research is commonly performed using well established methods that mimic

conditions found in natural environments, such as microfluidic devices. Therefore, to study the organization of cells in biofilms and how cells in a biofilm respond to global stress, *V. cholerae* was used as model organism in chapter 2 and chapter 5.

Methods to investigate spatiotemporal processes in biofilms

As mentioned previously, in contrast to liquid cultures biofilms are phenotypically and genotypically heterogeneous. This means that many questions cannot be investigated using bulk or average measurements. Instead, biofilms need to be studied with techniques with high spatial resolution. Techniques that can be used for biofilm research in this manner include: Raman spectroscopy, mass spectrometry imaging (MSI), atomic force microscopy (AFM), confocal fluorescence imaging, and omics techniques combined with fluorescence-activated cell sorting (FACS). Raman spectroscopy and MSI have the capability to generate spatially-resolved measurements of a delimited number of metabolites across the various regions in a biofilm sample^{34,35}. AFM is used for the measurement of mechanical properties on biofilms, including adhesion and matrix properties³⁶. However, these techniques are limited in the type of information they can provide and they are technically complex.

In contrast, fluorescence microscopy-based approaches have been the gold-standard to analyse biofilms due to their widespread use and comprehensive applications. Fluorescence microscopy enables the use of light with specific wavelengths to excite particular molecules. Upon absorbing energy, these molecules can release light with a longer wavelength than the excitation wavelength, which can be collected with a detector. Fluorescence microscopy can be used for the analysis of transcriptional and translational reporters in samples with a spatiotemporal resolution. These approaches can also be applied to determine the overall biofilm architecture³⁷. In common epifluorescence microscopes, all *xy*-planes of a sample are illuminated at the same time, and light from multiple planes is collected simultaneously. Therefore, this type of microscope has relatively low *z*-resolution and cannot resolve images in three-dimensions, which is advantageous for biofilms research³⁸.

Three-dimension resolution can be acquired by confocal microscopy. Using a pinhole, confocal microscopes block light from all image planes with the exception of the focal plane. Thus, they collect different image slices that can be reconstructed into a 3D fluorescent image of a sample³⁸.

Imaging of biofilms with high spatial and temporal resolution generates volumes of data that can only be analysed using automated computer programs. Many software packages have been created and successfully applied to biofilm research. The most prominent of them is called COMSTAT, which

was published in the year 2000³⁹. Since then, there has been a revolution in imaging techniques, and the new major questions in the field have increasingly required single-cell resolution analysis methods lacking in previous software packages^{24,40,41}. To solve this issue, new pieces of software that incorporated state of the art algorithms for biofilms analysis have been developed⁴².

One of the main drawbacks of fluorescence microscopy is the relatively low number of reporters that can be used at the same time. This is limited by the laser wavelengths, fluorescent probes and emission filters used. For most microscopes, the upper-limited is 3-4 different reporters that can be simultaneously imaged. To analyse the transcriptional and translational levels of multiples genes in a high-throughput manner, techniques such as transcriptomics and proteomics have been developed. They enable to measure the levels of all transcripts and proteins simultaneously. These techniques are commonly used to measure average expression levels within a sample, which is not optimal to analyse heterogeneous samples. Recently, they have been combined with FACS to study the transcriptional levels of subpopulations in batch cultures⁴³. The application of these techniques to biofilms allows the detection of spatially regulated genes within biofilms.

Biofilm formation

Even though biofilm architecture, composition and size differ between species and strains, there are some general phenomena that are hallmarks of biofilm development. An important feature that is conserved across different bacterial species is that biofilms commonly grow on interphases of two different states of matter. They can form on liquid-air interphases, as it occurs in many water systems. The best studied model for this is *Bacillus subtilis* pellicles⁴⁴. In this type of biofilm, cells consume nutrients from the liquid and utilize molecular oxygen from the air. Biofilms can also grow on solid-air interphases such as animal or plant tissues, organic and inorganic surfaces, among many other places. This is modelled in laboratory settings commonly as aerobic biofilm colonies grown on agar²⁹. In this system, cells multiply whilst uptaking the nutritious media within the solid agar and consuming molecular oxygen from the air^{27,45}. Additionally, solid-liquid interphases support biofilm growth in almost any natural water system^{46,47}. A good example is the growth of many bacteria on organic particles undergoing sedimentation, which is called marine snow⁴⁸. In the laboratory this type of growth can be observed when growing biofilms in microfluidic devices, where the flow of liquid contains nutrients and molecular oxygen³³.

Regardless of their location and composition, biofilm growth requires cell-cell and cell-matrix interactions and occurs in sequential steps³¹ (Fig. 1.1). First, bacterial cells attach reversibly and then

irreversibly to a substrate using appendices such as flagella or pili³¹. Then, due to cell division they expand in two-dimensions across the substrate while secreting extrapolymeric substances (EPS). After reaching a certain size, the biofilm starts growing in height developing into a three-dimensional structure⁴⁰. This transition is mainly driven by mechanical interactions within the cells and between the cells and the EPS matrix²⁴. When the biofilm has reached a mature state, it can disperse as single cells or aggregates of cells by responding to different environmental and cellular cues²⁶. This process allows bacteria to colonize new environments restarting the biofilm growth cycle. It is however unclear which interactions predominantly drive the growth of a biofilm and the transitions between the different stages of biofilm formation.

In chapter 2 of this dissertation, we studied how *V. cholerae* bacterial cells interact to drive the growth dynamics and emergent properties observable in biofilms. Using experimental data and *in silico* simulated biofilms we were able to develop an interaction potential that is able to recapitulate and predict biofilm properties by using mechanical interactions.

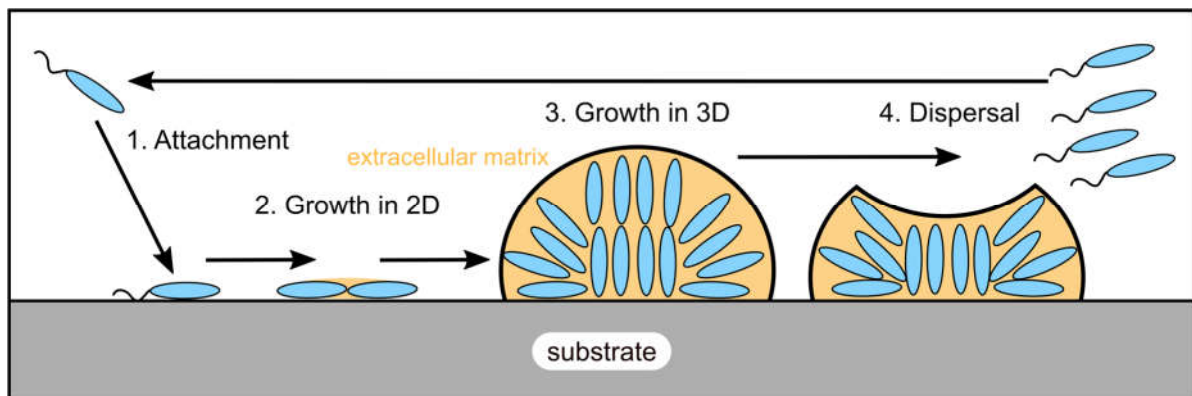


Figure 1.1. Stages of biofilm formation. Representation of the main steps of biofilm formation. First, bacterial cells (depicted in light blue) attach to a substrate (grey). Then they grow along the substrate while secreting EPS matrix (depicted in yellow). After reaching a certain size the biofilm starts to grow in height reaching a mature state. Due to cellular or environmental cues cells from the biofilm can disperse and colonize new environments restarting the cycle.

Biofilm matrix

The EPS matrix is a key factor that plays an important role through all stages of biofilm development^{49,50}. It serves as a scaffold that keeps cells together and adhered to surfaces. The matrix composition determines the type and strength of its specific interactions. It can be constituted of proteins, sugars, lipids and nucleic acids, with their exact compositions varying drastically between bacterial species.

The EPS matrix is one of the main reasons why biofilms are difficult to eradicate. By binding cells together, it provides structural stability to biofilms enabling them to tolerate mechanical stresses, such as shear⁵⁰. It can be a protective barrier for the cells, facilitating the evasion of predation by bacteriophages and immune cells^{18,51}. The EPS can also act as a diffusion barrier for large or charged molecules throughout the biofilm, including some antibiotics such as vancomycin and tobramycin⁵². The matrix can additionally capture molecules and act as a reservoir for nutrients. It can be used to support electron exchange between different regions of the biofilms⁵³. These features combined gives rise to spatial heterogeneity within biofilms, which ultimately also contributes to the resilient nature of biofilms.

Biofilms are physiologically heterogeneous with cross-feeding potential

As biofilms grow in size and the matrix composition changes, some molecules accumulate while others get consumed. This creates distinct local environments and high levels of phenotypic heterogeneity⁵⁴. One of the main reasons of this heterogeneity is the presence of solute gradients within biofilms^{53,54}. These gradients are created due to decreased molecule diffusion throughout biofilms in conjunction with bacterial metabolism^{45,53,55}. For some bacteria, around 10% of their genome can be composed of regulatory genes that respond to environmental changes such as in oxygen levels, pH, nutrients and other molecules⁵⁴. Therefore, cells exposed to different chemical concentrations are likely to perform different metabolic processes. These metabolically different bacteria can in turn modify their microenvironment creating stronger chemical gradients by processes such as fermentation and respiration^{27,45,56}. The most studied chemical gradient-derived heterogeneity in biofilms are the ones created by oxygen⁵⁴. Cells on the outside layers of a biofilm that are in contact with molecular oxygen actively consume it by respiration, creating an anaerobic environment in the biofilm core. The interplay between consumption and diffusion determine local molecular oxygen concentrations.

When a population of cells produce molecules that another group of cells utilize a metabolic cross-feeding is established⁵³. This interaction involves the transfer or sharing of metabolites, such as nitrogen-rich or carbon-rich nutrients, as well as redox molecules that participate in extracellular electron transport⁵³. Metabolite movement throughout the biofilms can be driven by diffusion, nanotubes or extracellular channels connecting different biofilm regions^{27,57–59}. Many examples of cross-feeding between genetically different organisms have been studied, such as mammalian organs and bacterial communities^{53,60–62}. Despite bacteria being able to secrete many metabolic by-products under specific metabolic states, there are very few cases in the literature where metabolic cross-

feeding has been described within isogenic bacterial populations. This is primarily due to the lack of techniques that permit reliable distinction between global and spatial metabolism, along with the absence of strong phenotypes when cross-feeding interactions are impeded⁶³.

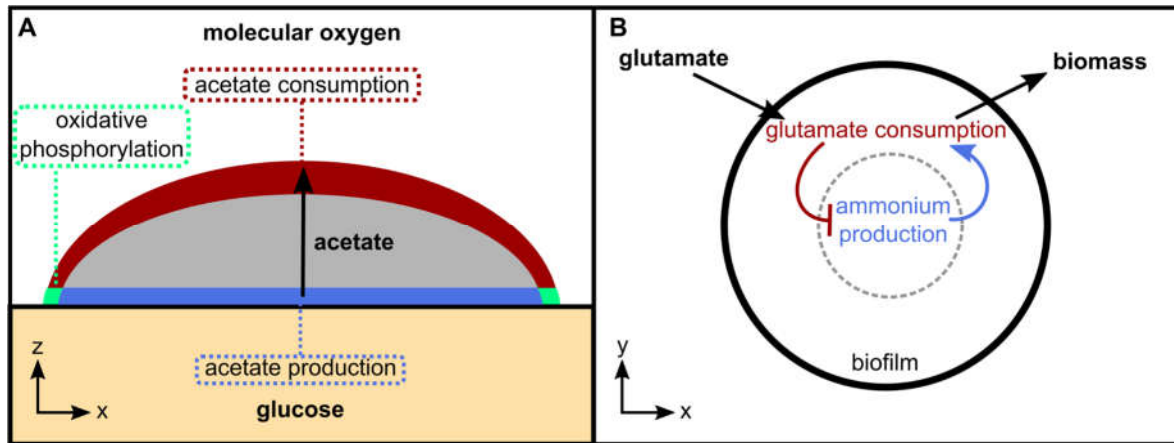


Figure 1.2. Examples of cross-feeding within isogenic bacterial biofilms. (A) Depiction of an *E. coli* biofilm colony grown aerobically on solid minimal medium with glucose as a carbon source. In this system, it has been suggested that anaerobic cells in presence of glucose (blue region) produce acetate that can diffuse throughout the colony^{27,64}. Cells in the aerobic area lacking glucose (red region) can consume acetate. Cells in green area have access to both glucose and oxygen and perform oxidative phosphorylation. This figure is adapted from Cole *et al*²⁷. **(B)** Model of ammonium cross-feeding within *B. subtilis* biofilms grown on glutamate as the sole nitrogen source. Interior and peripheral cells compete for glutamate. Cells on the periphery of the biofilm divide by consuming glutamate and ammonium, lowering the levels of glutamate in the interior. When ammonium levels decrease, growth in the periphery halts, allowing glutamate to diffuse to the core of the biofilm where ammonium can be produced from glutamate. Ammonium can rapidly diffuse out of the cells. When its levels increase above a certain threshold, growth is resumed in the periphery, creating an oscillatory system. This figure is adapted from Liu *et al.*⁶⁵

One of the few examples of metabolic cross-feeding described within a clonal bacterial population is the cross-feeding of acetate as a carbon source between different *E. coli* subpopulations (Fig. 1.2A)^{27,64}. This process, driven by chemical gradients within biofilms, occurs when *E. coli* colonies are grown on solid minimal medium with glucose as the sole carbon source. In this system, cells at the bottom boundary of the colony that are in contact with the agar uptake glucose (from the agar) and utilize molecular oxygen in the air (green area in Fig. 1.2). Meanwhile, the cells in the peripheral dome not in contact with the agar surface can utilize oxygen from the air but lack glucose (red area in Fig. 1.2). Oxygen consumption by cells in the periphery creates an oxygen gradient, resulting in the formation of an anaerobic environment in the interior region of the colony. Amongst these anaerobic cells, those in contact with glucose (blue area in Fig. 1.2) can produce acetate by fermentation. This acetate can diffuse through the colony to be utilized by cells that lack access to glucose but are in

presence of molecular oxygen (red area in Fig. 1.2). A computation analysis predicted that this cross-feeding gives a 4.5% fitness advantage after 36 hours of growth when compared to cells unable to perform acetate cross-feeding²⁷.

Another well-known example is the cross-feeding of ammonium as a nitrogen source in *Bacillus subtilis* biofilms^{25,65}. This has been described when flat biofilms are grown on minimal medium in microfluidic devices with glutamate as a nitrogen source (Fig. 1.2B). Interior and peripheral cells compete for glutamate. Cells take up ammonium to convert glutamate into glutamine, resulting in an increase in biofilm biomass. Since ammonium can freely diffuse across the membrane, its production is known as a “futile cycle”. Therefore, growth relies on ammonium production by cells in the inside of the biofilm. Thus, an oscillatory system arises, where cells on the periphery consume glutamate and ammonium until the ammonium concentration decreases below a certain threshold. When this occurs, growth on the periphery halts and glutamate diffuses into the biofilm core, allowing cells located there to utilize glutamate to produce ammonium. When the ammonium concentration increases, growth in the periphery resumes.

These examples clearly show that some phenotypes within clonal populations can only be understood by considering the metabolic interaction within two or more subpopulations created by different microenvironments. Studying these cross-feeding phenotypes is crucial to understand different processes such as biofilm growth, development and stress tolerance.

Even though cross-feeding interactions have important consequences for community fitness and resilience, all current studies that have either worked with metabolite average levels⁶⁶ or have only focused on a few usually predefined, hypothesis-based, metabolic pathways^{67,68}. Therefore, missing the possibility of discovering many new cross-feeding interactions within single-species biofilms. In the chapter 3 we explored the physiological heterogeneity within *E. coli* isogenic colonies in order to discover new cross-feeding interactions in a hypothesis-free manner. By using spatiotemporal transcriptomics and temporal metabolomics, we were able to find that *E. coli* colonies cross-feed alanine with important consequences for cell growth and viability, and colony morphology. This work contributes to the understanding of biofilm metabolism and heterogeneity, and could help to develop new methods to combat biofilms.

Slow-growing cells and stress response in biofilms

Biofilms heterogeneity is a key factor for bacterial survival to antibiotics for many reasons, such as modified microenvironments in some regions of the biofilm that decrease antibiotic efficacy,

physiological heterogeneity that makes cells insensitive to drugs, decreased diffusion of antimicrobial molecules into the biofilm, and the presence of antibiotic degrading enzymes⁶. Environmental and metabolic heterogeneity are key to understand biofilm tolerance to antibiotics, with both factors influencing each other. Bacteria alter their environment through metabolic processes by consuming substrates and secreting by-products. They can modify the local pH, redox conditions or oxygen concentration, thus decreasing the efficacy of antibiotics⁶. On the other hand, physiological heterogeneity often arises due to presence of chemical gradients. For example, cells located in biofilm layers in which nutrients cannot diffuse to can starve or enter a state of dormancy becoming non-growing or slow-growing⁶⁹. Since antibiotics commonly act by blocking cellular pathways such as transcription, replication, translation or cell wall biosynthesis, it was been shown that slow-growing cellular states confer high tolerance to antimicrobial compounds⁷⁰. Such observations has led to the suggestion that there is an enrichment of dormant cells located in the core of biofilms due to lack of nutrients⁶⁹. However, it has not been empirically validated due to the current technical limitation of imaging non-growing cells within communities, in particular the lack of reliable fluorescent reporters. In chapter 4 we focused on slow-growing cells. We developed a CRISPRi-based method to select and enrich for slow-growing cells using fluorescent growth rate reporter and flow cytometry that could be applied for biofilm research.

To develop new methods capable of treating and eradicating biofilms, it is not only important to answer why biofilms are highly resilient but as well how biofilms respond to stress. Biofilms can actively respond to stress as single cells, where the biofilm response corresponds to the sum of the response of each cell. Biofilms can also respond at the group level with synergistic community-intrinsic properties, where the collective response is not predictable from the response of each cell^{18,71–73}. Over the last decades there has been a great number of reports on how biofilms respond to many stresses from a global, average, point of view^{71,74,75}. However, this approach cannot distinguish between single-cell and multicellular responses due to the lack of single-cell resolution analysis methods. In chapter 5, we applied a newly developed single-cell analysis technique to address how *V. cholerae* biofilms respond to antibiotic stress. Using single-cell confocal microscopy and *in silico* simulations we found that biofilms respond as single cells, but also at the group level, with important consequences for the ecology and architecture of biofilms.

Dissertation outline

Biofilm research has progressed substantially in the past decades hand-in-hand with improvements in molecular biology, microscopy and image analysis capabilities. In particular, the development of genetic modification techniques, single-cell imaging, *in silico* image segmentations, and multi-omics techniques has contributed to answer many questions, but has raised many more. Some of the most imperative open questions on biofilms research are: how do biofilms form and what determines their architecture? How do biofilm heterogeneity and biofilms metabolism interplay? How do different microbial populations interact within a biofilm? How and where metabolic heterogeneity creates antibiotic tolerant subpopulations within biofilms? How do biofilms respond to stress at the single-cell and multicellular levels and what are the consequences of such responses? Answering these questions would help to develop new methods to combat biofilms and to better understand their role in natural environments and human health. This dissertation contributes to address each of these questions.

Chapter 2 shows that cell-cell and cell-matrix interactions are the main determinant of biofilms architecture until the point when biological and chemical heterogeneities become predominant. Furthermore, it describes an interaction potential that predicts the overall biofilm morphology, architecture and cellular order within *V. cholerae* biofilms.

In chapter 3 we show how metabolically-driven chemical heterogeneities create an alanine cross-feeding interaction within *E. coli* biofilms. This interaction driven by nutrient and oxygen gradients has large consequences for bacterial survival and colony growth dynamics in the aerobic region of the biofilms.

Chapter 4 we developed a new method to enrich slow-growing cells. This method could be applied to study the location and frequency of slow growing cells within biofilms. This would significantly help to develop new ways to combat antibiotic-resistant infections.

In chapter 5 is shown that *V. cholerae* biofilms respond to antibiotic stress at the single-cell and multicellular level. In particular, cells become larger in cell volume and the cell-cell spacing increases. These responses were driven by cellular metabolism and mechanical properties of the matrix, and have implications for the effects of antimicrobial therapy on the ecological succession of biofilm communities.

References

1. Flemming, H.-C. & Wuertz, S. Bacteria and archaea on Earth and their abundance in biofilms. *Nat. Rev. Microbiol.* **17**, 247–260 (2019).
2. Rothschild, L. J. & Mancinelli, R. L. Life in extreme environments. *Nature* **409**, 1092–1101 (2001).
3. Urbaniak, C. *et al.* Detection of antimicrobial resistance genes associated with the International Space Station environmental surfaces. *Sci. Rep.* **8**, 814 (2018).
4. Lane, N. The unseen world: reflections on Leeuwenhoek (1677) ‘Concerning little animals’. *Philos. Trans. R. Soc. Lond. B. Biol. Sci.* **370**, (2015).
5. Vert, M. *et al.* Terminology for biorelated polymers and applications (IUPAC Recommendations 2012). *Pure Appl. Chem.* **84**, 377–410 (2012).
6. Flemming, H.-C. *et al.* Biofilms: an emergent form of bacterial life. *Nat. Rev. Microbiol.* **14**, 563–575 (2016).
7. Halan, B., Buehler, K. & Schmid, A. Biofilms as living catalysts in continuous chemical syntheses. *Trends Biotechnol.* **30**, 453–465 (2012).
8. Ma, B. *et al.* Biological nitrogen removal from sewage via anammox: Recent advances. *Bioresour. Technol.* **200**, 981–990 (2016).
9. Van Houdt, R. & Michiels, C. W. Biofilm formation and the food industry, a focus on the bacterial outer surface. *J. Appl. Microbiol.* **109**, 1117–31 (2010).
10. de Vos, W. M. Microbial biofilms and the human intestinal microbiome. *npj Biofilms Microbiomes* **1**, 15005 (2015).
11. de Vos, W. M. & de Vos, E. A. Role of the intestinal microbiome in health and disease: from correlation to causation. *Nutr. Rev.* **70**, S45–S56 (2012).
12. Danneskiold-Samsøe, N. B. *et al.* Interplay between food and gut microbiota in health and disease. *Food Res. Int.* **115**, 23–31 (2019).
13. Højby, N. *et al.* ESCMID guideline for the diagnosis and treatment of biofilm infections 2014. *Clin. Microbiol. Infect.* **21 Suppl 1**, S1-25 (2015).
14. Nickel, J. C., Ruseska, I., Wright, J. B. & Costerton, J. W. Tobramycin resistance of *Pseudomonas aeruginosa* cells growing as a biofilm on urinary catheter material. *Antimicrob. Agents Chemother.* **27**, 619–24 (1985).
15. Hall, C. W. & Mah, T.-F. Molecular mechanisms of biofilm-based antibiotic resistance and tolerance in pathogenic bacteria. *FEMS Microbiol. Rev.* **41**, 276–301 (2017).
16. Stewart, P. S. & William Costerton, J. Antibiotic resistance of bacteria in biofilms. *Lancet* **358**, 135–138 (2001).
17. Costerton, J. W., Stewart, P. S. & Greenberg, E. P. Bacterial biofilms: a common cause of persistent infections. *Science* **284**, 1318–22 (1999).
18. Vidakovic, L., Singh, P. K., Hartmann, R., Nadell, C. D. & Drescher, K. Dynamic biofilm architecture confers individual and collective mechanisms of viral protection. *Nat. Microbiol.* **3**, 26–31 (2018).
19. Hanke, M. L. & Kielian, T. Deciphering mechanisms of staphylococcal biofilm evasion of host immunity. *Front. Cell. Infect. Microbiol.* **2**, 1–12 (2012).
20. Drescher, K., Shen, Y., Bassler, B. L. & Stone, H. a. Biofilm streamers cause catastrophic disruption of flow with consequences for environmental and medical systems. *Proc. Natl. Acad. Sci. U. S. A.* **110**, 4345–50 (2013).
21. Windels, E. M., Michiels, J. E., Van den Bergh, B., Fauvart, M. & Michiels, J. Antibiotics: Combatting Tolerance To Stop Resistance. *MBio* **10**, 1–7 (2019).
22. O’Neill, J. ed. Antimicrobial Resistance: Tackling a Crisis for the Health and Wealth of Nations. HM Government (2014).
23. Dubey, G. P. & Ben-Yehuda, S. Intercellular nanotubes mediate bacterial communication. *Cell* **144**, 590–600 (2011).
24. Beroz, F. *et al.* Verticalization of bacterial biofilms. *Nat. Phys.* **14**, 954–960 (2018).
25. Prindle, A. *et al.* Ion channels enable electrical communication in bacterial communities. *Nature* **527**, 59–63 (2015).
26. Singh, P. K. *et al.* *Vibrio cholerae* Combines Individual and Collective Sensing to Trigger Biofilm Dispersal. *Curr. Biol.* **27**, 3359–3366.e7 (2017).
27. Cole, J. A., Kohler, L., Hedhli, J. & Luthey-Schulten, Z. Spatially-resolved metabolic cooperativity within dense bacterial colonies. *BMC Syst. Biol.* **9**, 15 (2015).
28. Mah, T.-F. *et al.* A genetic basis for *Pseudomonas aeruginosa* biofilm antibiotic resistance. *Nature* **426**,

- 306–310 (2003).
29. Serra, D. O., Richter, A. M., Klauck, G., Mika, F. & Hengge, R. Microanatomy at cellular resolution and spatial order of physiological differentiation in a bacterial biofilm. *MBio* **4**, e00103-13 (2013).
 30. Ali, M., Nelson, A. R., Lopez, A. L. & Sack, D. A. Updated global burden of cholera in endemic countries. *PLoS Negl. Trop. Dis.* **9**, e0003832 (2015).
 31. Teschler, J. K. *et al.* Living in the matrix: assembly and control of *Vibrio cholerae* biofilms. *Nat. Rev. Microbiol.* **13**, 255–268 (2015).
 32. Colwell, R. R. *et al.* Reduction of cholera in Bangladeshi villages by simple filtration. *Proc. Natl. Acad. Sci. U. S. A.* **100**, 1051–1055 (2003).
 33. Drescher, K., Nadell, C. D., Stone, H. A., Wingreen, N. S. & Bassler, B. L. Solutions to the Public Goods Dilemma in Bacterial Biofilms. *Curr. Biol.* **24**, 50–55 (2014).
 34. Lanni, E. J. *et al.* MALDI-guided SIMS: Multiscale imaging of metabolites in bacterial biofilms. *Anal. Chem.* **86**, 9139–9145 (2014).
 35. Bodelón, G. *et al.* Detection and imaging of quorum sensing in *Pseudomonas aeruginosa* biofilm communities by surface-enhanced resonance Raman scattering. *Nat. Mater.* **15**, 1203–1211 (2016).
 36. Jonas, K. *et al.* Roles of curli, cellulose and BapA in *Salmonella* biofilm morphology studied by atomic force microscopy. *BMC Microbiol.* **7**, 70 (2007).
 37. Neu, T. R. & Lawrence, J. R. Innovative techniques, sensors, and approaches for imaging biofilms at different scales. *Trends Microbiol.* **23**, 233–42 (2015).
 38. Jonkman, J., Brown, C. M., Wright, G. D., Anderson, K. I. & North, A. J. Tutorial: guidance for quantitative confocal microscopy. *Nat. Protoc.* **15**, 1585–1611 (2020).
 39. Heydorn, A. *et al.* Quantification of biofilm structures by the novel computer program COMSTAT. *Microbiology* **146** (Pt 1, 2395–2407 (2000).
 40. Drescher, K. *et al.* Architectural transitions in *Vibrio cholerae* biofilms at single-cell resolution. *Proc. Natl. Acad. Sci.* **113**, E2066–E2072 (2016).
 41. Yan, J., Sharo, A. G., Stone, H. A., Wingreen, N. S. & Bassler, B. L. *Vibrio cholerae* biofilm growth program and architecture revealed by single-cell live imaging. *Proc. Natl. Acad. Sci.* **113**, 1–7 (2016).
 42. Hartmann, R. *et al.* BiofilmQ, a software tool for quantitative image analysis of microbial biofilm communities. *bioRxiv* 735423 (2019) doi:10.1101/735423.
 43. Rosenthal, A. Z. *et al.* Metabolic interactions between dynamic bacterial subpopulations. *Elife* **7**, 1–18 (2018).
 44. Vlamakis, H., Chai, Y., Beaugregard, P., Losick, R. & Kolter, R. Sticking together: building a biofilm the *Bacillus subtilis* way. *Nat. Rev. Microbiol.* **11**, 157–168 (2013).
 45. Warren, M. R. *et al.* Spatiotemporal establishment of dense bacterial colonies growing on hard agar. *Elife* **8**, 1–47 (2019).
 46. Battin, T. J., Besemer, K., Bengtsson, M. M., Romani, A. M. & Packmann, A. I. The ecology and biogeochemistry of stream biofilms. *Nat. Rev. Microbiol.* **14**, 251–63 (2016).
 47. Edwards, K. J., Wheat, C. G. & Sylvan, J. B. Under the sea: microbial life in volcanic oceanic crust. *Nat. Rev. Microbiol.* **9**, 703–712 (2011).
 48. Azam, F. & Malfatti, F. Microbial structuring of marine ecosystems. *Nat. Rev. Microbiol.* **5**, 782–91 (2007).
 49. Hobley, L., Harkins, C., MacPhee, C. E. & Stanley-Wall, N. R. Giving structure to the biofilm matrix: An overview of individual strategies and emerging common themes. *FEMS Microbiol. Rev.* **39**, 649–669 (2015).
 50. Dragoš, A. & Kovács, Á. T. The Peculiar Functions of the Bacterial Extracellular Matrix. *Trends Microbiol.* **25**, 257–266 (2017).
 51. Jesaitis, A. J. *et al.* Compromised host defense on *Pseudomonas aeruginosa* biofilms: characterization of neutrophil and biofilm interactions. *J. Immunol.* **171**, 4329–39 (2003).
 52. Stewart, P. S. Mechanisms of antibiotic resistance in bacterial biofilms. *Int. J. Med. Microbiol.* **292**, 107–113 (2002).
 53. Evans, C. R., Kempes, C. P., Price-Whelan, A. & Dietrich, L. E. P. Metabolic Heterogeneity and Cross-Feeding in Bacterial Multicellular Systems. *Trends Microbiol.* **2020**, 1–12 (2020).
 54. Stewart, P. S. & Franklin, M. J. Physiological heterogeneity in biofilms. *Nat. Rev. Microbiol.* **6**, 199–210 (2008).
 55. Stewart, P. S. *et al.* Reaction–diffusion theory explains hypoxia and heterogeneous growth within microbial biofilms associated with chronic infections. *npj Biofilms Microbiomes* **2**, 16012 (2016).
 56. Co, A. D., Van Vliet, S. & Ackermann, M. Emergent microscale gradients give rise to metabolic cross-

- feeding and antibiotic tolerance in clonal bacterial populations. *Philos. Trans. R. Soc. B Biol. Sci.* **374**, (2019).
57. Dubey, G. P. & Ben-Yehuda, S. Intercellular Nanotubes Mediate Bacterial Communication. *Cell* **144**, 590–600 (2011).
 58. Rooney, L. M., Amos, W. B., Hoskisson, P. A. & McConnell, G. Intra-colony channels in *E. coli* function as a nutrient uptake system. *ISME J.* (2020) doi:10.1038/s41396-020-0700-9.
 59. Pande, S. *et al.* Metabolic cross-feeding via intercellular nanotubes among bacteria. *Nat. Commun.* **6**, 6238 (2015).
 60. Smith, N. W., Shorten, P. R., Altermann, E., Roy, N. C. & McNabb, W. C. The Classification and Evolution of Bacterial Cross-Feeding. *Front. Ecol. Evol.* **7**, 1–15 (2019).
 61. De Beer, D., Schramm, A., Santegeeds, C. M. & Kuhl, M. A nitrite microsensor for profiling environmental biofilms. *Appl. Environ. Microbiol.* **63**, 973–7 (1997).
 62. Jang, C. *et al.* Metabolite Exchange between Mammalian Organs Quantified in Pigs. *Cell Metab.* **30**, 594–606.e3 (2019).
 63. San Roman, M. & Wagner, A. An enormous potential for niche construction through bacterial cross-feeding in a homogeneous environment. *PLOS Comput. Biol.* **14**, e1006340 (2018).
 64. Wolfsberg, E., Long, C. P. & Antoniewicz, M. R. Metabolism in dense microbial colonies: 13C metabolic flux analysis of *E. coli* grown on agar identifies two distinct cell populations with acetate cross-feeding. *Metab. Eng.* **49**, 242–247 (2018).
 65. Liu, J. *et al.* Metabolic co-dependence gives rise to collective oscillations within biofilms. *Nature* **523**, 550–554 (2015).
 66. Pisithkul, T. *et al.* Metabolic Remodeling during Biofilm Development of *Bacillus subtilis*. *MBio* **10**, 1–32 (2019).
 67. Qin, Y. *et al.* Heterogeneity in respiratory electron transfer and adaptive iron utilization in a bacterial biofilm. *Nat. Commun.* **10**, 3702 (2019).
 68. Şimşek, E. & Kim, M. The emergence of metabolic heterogeneity and diverse growth responses in isogenic bacterial cells. *ISME J.* **12**, 1199–1209 (2018).
 69. Yan, J. & Bassler, B. L. Surviving as a Community: Antibiotic Tolerance and Persistence in Bacterial Biofilms. *Cell Host Microbe* **26**, 15–21 (2019).
 70. Bakkeren, E., Diard, M. & Hardt, W.-D. Evolutionary causes and consequences of bacterial antibiotic persistence. *Nat. Rev. Microbiol.* **18**, 479–490 (2020).
 71. Hoffman, L. R. *et al.* Aminoglycoside antibiotics induce bacterial biofilm formation. *Nature* **436**, 1171–1175 (2005).
 72. Song, C. *et al.* Characterization of the interactions between tetracycline antibiotics and microbial extracellular polymeric substances with spectroscopic approaches. *Environ. Sci. Pollut. Res.* **21**, 1786–1795 (2014).
 73. Madsen, J. S., Sørensen, S. J. & Burmølle, M. Bacterial social interactions and the emergence of community-intrinsic properties. *Curr. Opin. Microbiol.* **42**, 104–109 (2018).
 74. Davison, W. M., Pitts, B. & Stewart, P. S. Spatial and temporal patterns of biocide action against *Staphylococcus epidermidis* biofilms. *Antimicrob. Agents Chemother.* **54**, 2920–7 (2010).
 75. Garcia, L. G. *et al.* Antibiotic activity against small-colony variants of *Staphylococcus aureus*: review of in vitro, animal and clinical data. *J. Antimicrob. Chemother.* **68**, 1455–64 (2013).

Chapter II: Emergence of three-dimensional order and structure in growing biofilms

Raimo Hartmann^{1,2}, Praveen K. Singh^{1,5}, Philip Pearce^{3,5}, Rachel Mok^{3,4,5}, Boya Song³,
Francisco Díaz- Pascual¹, Jörn Dunkel^{3*} and Knut Drescher^{1,2*}.

This chapter is written in manuscript style and was published in Nature Physics in November 2018. My contribution to this work included establishing a tunable and inducible plasmid-based system to control *rbmA* expression in *Vibrio cholerae* biofilms that was used for cell-cell attraction calibration, aiding with testing of the segmentation software used, and providing ideas for software improvement.

¹Max Planck Institute for Terrestrial Microbiology, Marburg, Germany.

²Department of Physics, Philipps-Universität Marburg, Marburg, Germany.

³Department of Mathematics, Massachusetts Institute of Technology, Cambridge, Massachusetts, USA

⁴Department of Mechanical Engineering,
Massachusetts Institute of Technology, Cambridge, Massachusetts, USA.

⁵These authors contributed equally: Praveen K. Singh, Philip Pearce, Rachel Mok.

*corresponding author.

Abstract

Surface-attached bacterial biofilms are self-replicating active liquid crystals and the dominant form of bacterial life on earth¹⁻⁴. In conventional liquid crystals and solid-state materials, the interaction potentials between the molecules that comprise the system determine the material properties. However, for growth-active biofilms it is unclear whether potential-based descriptions can account for the experimentally observed morphologies, and which potentials would be relevant. Here, we overcome previous limitations of single-cell imaging techniques^{5,6} to reconstruct and track all individual cells inside growing three-dimensional (3D) biofilms with up to 10,000 individuals. Based on these data, we identify, constrain, and provide a microscopic basis for an effective cell-cell interaction potential, which captures and predicts the growth dynamics, emergent architecture, and local liquid crystalline order of *Vibrio cholerae* biofilms. Furthermore, we show how external fluid flows control the microscopic structure and 3D morphology of biofilms. Our analysis implies that local cellular order and global biofilm architecture in these active bacterial communities can arise from mechanical cell-cell interactions, which cells can modulate by regulating the production of particular matrix components. These results establish an experimentally validated foundation for improved continuum theories of active matter and thereby contribute to solving the important problem of controlling biofilm growth.

Main Text

V. cholerae cells can swim through liquids as isolated individuals, but are more commonly attached to surfaces where they grow into clonal colonies termed biofilms, with reproducible spatial organization, global morphology, and cellular arrangements^{7,8}. Biofilm architectures often display striking local nematic order analogous to molecular ordering in abiotic liquid crystals, yet biofilms differ fundamentally in that they are active systems, driven by cell growth and metabolism¹⁻⁴. As these active nematic systems operate far from thermodynamic equilibrium⁹, there are no relevant fundamental conservation laws known that could be used to characterize the biofilm developmental dynamics. To achieve a detailed qualitative and quantitative understanding of such biologically-ubiquitous yet physically-exotic bacterial communities, we developed new experimental imaging and image analysis techniques for obtaining high spatiotemporal-resolution data of the biofilm developmental process up to 10^4 cells, representing mid-sized biofilm microcolonies that have already established the architectural state of macroscopic *V. cholerae* biofilms⁵. By using automated confocal microscopy, with an adaptive live-feedback between image acquisition, feature recognition, and microscope control, followed by a ground-truth-calibrated, novel 3D-image-segmentation technique (see Methods, Supplementary Information) we were able to observe complete 3D biofilm development at cellular resolution with minimal phototoxicity (Fig. 2.1a,b), and minimal segmentation error (Supplementary Information). The high temporal resolution ($\Delta t = 5\text{--}10$ min) allows for cell lineage reconstruction, measurements of local growth rates, and the identification of all cells in a field of view which are not related to the original biofilm founder cell (Fig. 2.1b,d).

When investigating whether the non-equilibrium dynamics of biofilm development and the emergence of local order can be captured quantitatively through effective cell-cell interaction potentials, it is important to account for the essential biophysical processes: cell growth, cell division, cell-surface interactions, and cell-cell interactions^{4,10-17}. Whereas growth and division are driven by nutrient availability and metabolism, cell-surface and cell-cell attraction are typically mediated by secreted or membrane-associated polysaccharides and proteins^{10,18}. For *V. cholerae* biofilms, the molecular basis for cell-cell interactions has been intensively investigated: cells are embedded in a self-secreted extracellular matrix, comprised of the *Vibrio* polysaccharide (VPS), extracellular DNA, and proteins¹⁹⁻²¹. The osmotic pressure resulting from a high concentration of matrix components in the intercellular space, as well as steric cell-cell interactions, are both expected to contribute to cell-cell repulsion. Cell-cell attraction is primarily mediated by the protein RbmA, which localizes throughout the biofilm (Fig. 2.1c)^{20,21}, links cells to each other²¹⁻²³, and whose expression levels are inversely related to cell-cell spacing (Fig. 2.2a). VPS also weakly binds cells together, yet elevated levels of VPS production

do not cause stronger cell-cell attraction or a decreased cell-cell spacing (Supplementary Figure 2.11). Based on these cell-cell interaction processes, we hypothesized that biofilm architectures are primarily determined by the relative strength of effective mechanical cell-cell attraction and repulsion forces.

To determine the impact of cell-cell attraction, we quantitatively compared the 3D biofilm architecture dynamics of a rugose wild type strain with straight cell shape (WT*) with that of a mutant strain ($\Delta rbmA$) with significantly weakened intercellular adhesion (see Methods). Biofilms grown in a low-shear environment approximately display hemispherical symmetry (Fig. 2.1d), which allows us to characterize the biofilm architectures (Fig. 2.1e) as a function of the distance to the biofilm centre in the basal plane, d_{centre} , using the cell number in the biofilm, N_{cells} , as a quantification of the developmental state. Our measurements reveal strong structural differences between the outer biofilm layer and its central part as well as several distinct architectural phases of the biofilm during growth (Fig. 2.1e,f). Interestingly, the cellular growth rate remains homogeneous in space during WT* biofilm development in our conditions and for our biofilm sizes (Fig. 2.1e, Supplementary Fig. 2.5), contrary to theories assuming steep nutrient gradients inside biofilms^{8,10}. The nematic order, cell-cell spacing, and cellular orientations with respect to the vertical (z) and radial (r) directions differ significantly between WT* and $\Delta rbmA$ mutants (Fig. 2.1e–f, see Supplementary Fig. 2.5–8), revealing the strong effect of cell-cell adhesion on biofilm architecture dynamics.

Based on the high-resolution spatiotemporal data of biofilm development of different bacterial strains, we investigated the hypothesis that the biofilm internal structure and external shape originate from mechanical interactions between cells. Focusing on a minimal model, we describe the effective mechanical interactions in terms of an effective potential that depends on the distance $r_{\alpha\beta}$ between neighbouring cells α and β , and their orientations \hat{n}_α and \hat{n}_β . We made the simplifying assumption that the potential is independent of the biofilm developmental state or nutrient levels. As shown below, this simplification suffices to capture the main features of the small to medium-sized biofilms studied here but is expected to become inaccurate at the later stages of biofilm development, when spatio-temporal heterogeneities become relevant. Given the molecular components of the cell-cell interaction and their qualitative effects on attraction and repulsion outlined above, we assume the potential

$$U = \epsilon_0 \epsilon_1 \left(e^{-\frac{\rho^2}{\lambda_r^2}} + \frac{v}{1 + e^{\left(\frac{\rho_a - \rho}{\lambda_a}\right)}} \right), \quad (1)$$

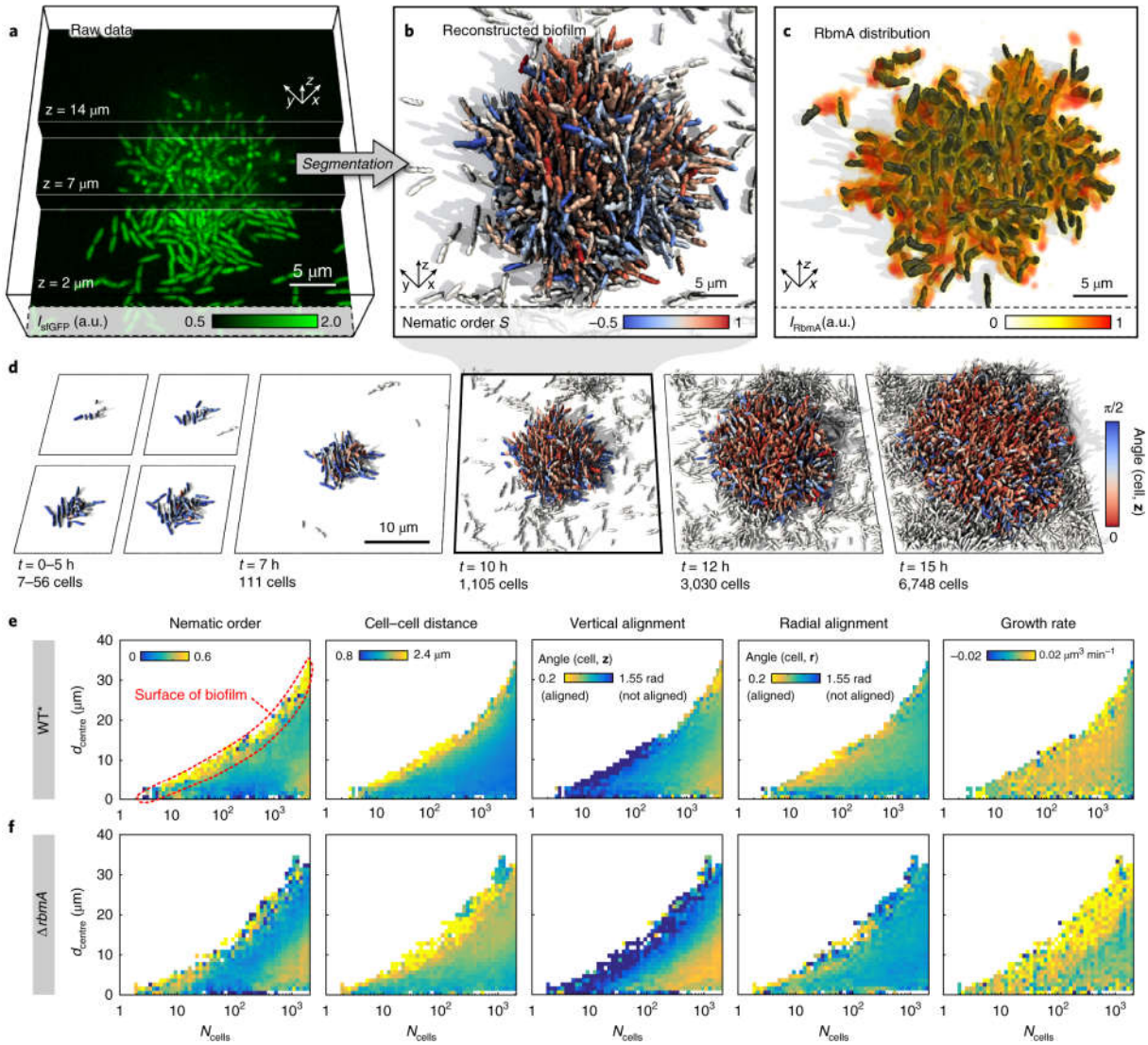


Figure 2.1. Dynamics of *V. cholerae* biofilm formation. **a**, Cells constitutively expressing a green fluorescent protein (sfGFP) were imaged with spinning disc confocal microscopy. Images at three different z -planes are highlighted. **b**, 3D reconstruction of the biofilm shown in panel **a**, where each cell is coloured according to the nematic order parameter $S = \langle 3/2(\hat{n}_i \cdot \hat{n}_j)^2 - 1/2 \rangle$ in its vicinity. High time resolution ($\Delta t = 5\text{--}10$ min) imaging allowed us to track cell lineages and discriminate cells (white) which are not direct descendants of the biofilm founder cell. **c**, The extracellular matrix protein RbmA mediates cell-cell adhesion and is distributed throughout the biofilm, as visualized by immunofluorescence. **d**, Time-resolved WT* biofilm growth series. Each cell is coloured according to the cellular alignment with the z -axis (for the $\Delta rbmA$ mutant see Supplementary Fig. 2.6). **e-f**, Heatmaps showing spatially resolved single-cell measurements of different biofilm structural properties inside WT* (**e**) and $\Delta rbmA$ (**f**) biofilms, which are used to characterize biofilm formation ($n > 3$ biofilms, standard deviations are shown in Supplementary Figs. 2.5 and 2.7 and the differences among both strains are highlighted in Supplementary Fig. 2.8), as a function of the distance to the biofilm centre (d_{centre}) and the number of cells inside the biofilm (N_{cells}).

where $\rho = r_{\alpha\beta}/\sigma$ is the shape-normalized cell-cell distance. The range parameter $\sigma(\hat{r}_{\alpha\beta}, \hat{n}_\alpha, \hat{n}_\beta)$ depends on the instantaneous cell lengths, the orientation of the cells relative to each other, and the

individual cell orientations, and it maps the potential onto non-identical ellipsoidal cells (see Supplementary Information, Eq. 20). The amplitude is set by the repulsion strength ϵ_0 and instantaneous cell lengths and cell orientations through the strength parameter $\epsilon_1(\hat{\mathbf{n}}_\alpha \cdot \hat{\mathbf{n}}_\beta)$ (Supplementary Information, Eq. 19). The first term of the interaction potential describes the combined effects of hard steric and osmotic repulsion with range λ_r (Fig. 2.2b). The second term corresponds to cell-cell attraction and adds an attractive well of relative depth ν , width λ_a , and position ρ_a (Fig. 2.2c). Each contribution and parameter in the potential U thus has a well-defined physical meaning (see schematic diagram in Supplementary Figure 2.15, Supplementary Table 2.3). We assume here that the interaction parameters are taken to be constant for a given bacterial strain, a simplification that could be relaxed in future models. With these simplifying assumptions, initial estimates of the potential parameters prior to systematic scans can be obtained from basic physical considerations (see Methods).

This potential was then implemented in a particle-based model of biofilm development, in which individual cells were modelled as growing and dividing ellipsoids without self-propulsion (see Supplementary Information) whose interactions are described by U . Bypassing previous limitations of individual-based biofilm models^{24,25}, all parameters of our model (cell aspect ratio, division time distribution; Supplementary Table 2.3) were determined from single-cell properties of experimental biofilms, and the dynamics were solved with a massively parallel computation approach using graphics processing units for evaluating all pair-wise interactions (Supplementary Information). To obtain the key potential parameters ϵ_0 , λ_r , ν , λ_a and ρ_a for *V. cholerae* biofilms, we assumed that the attractive term in U can be attributed primarily to RbmA levels, with the VPS acting as a Woods-Saxon background potential (Methods) akin to the mean-field potential in nucleon models. This assumption is motivated by the experimental findings that increased VPS levels do not increase the cell-cell attraction (Supplementary Figure 2.11), yet biofilms that lack RbmA display a small residual mechanical cohesion (Fig. 2.3e), indicating that VPS does contribute weakly to cell-cell binding. To first obtain the parameters ϵ_0 and λ_r , we fitted the repulsive part of the potential U by comparing experimental $\Delta rbmA$ biofilms, which lack the attractive potential term ($\nu = 0$), with simulated biofilms, using the mean squared difference (MSD) of a feature vector as a metric. The feature vector contains 14 different architectural properties and their temporal variation up to 300 cells (see Supplementary Fig. 2.14), allowing a comprehensive comparison of biofilm architecture and development between simulations and experiment at the same time. Note that even at small sizes, the *V. cholerae* biofilms used in this study produce RbmA and VPS (Supplementary Fig. 2.10). For $\Delta rbmA$ biofilms we found a broad minimum in the (ϵ_0, λ_r) -space as shown in the MSD heatmap (Supplementary Fig. 2.16), resulting in best-fit simulations that show high similarity to experiments (Supplementary Fig. 2.17). The effective

translational and rotational interaction forces acting on two neighbouring $\Delta rbmA$ cells for the best fit potential are illustrated in Fig. 2.2b for different cellular orientations. The interaction range for two aligned cells is very close to the experimentally observed average cell-cell spacing of the $\Delta rbmA$ mutant (dashed cell).

Because the attraction parameters (ν, λ_a, ρ_a) in the potential U depend on the concentration of RbmA, we genetically modified *V. cholerae* such that we can tune the production of RbmA (and therefore tune the strength of the attraction), by adding different concentrations of a compound that induces the *rbmA*-expression construct homogeneously inside the biofilm: arabinose (see Methods, Supplementary Fig. 2.13). Experimentally, we observed that increasing arabinose concentrations resulted in a decreased cell-cell spacing (Fig. 2.2a), consistent with the assumption that RbmA mediates cell-cell attraction. By fixing the repulsive component (ϵ_0, λ_r) based on the $\Delta rbmA$ biofilms, we then fitted the attractive potential component (ν, λ_a, ρ_a) for a range of different arabinose concentrations (Fig. 2.2c,d). The MSD isosurfaces in (ν, λ_a, ρ_a) -space and corresponding 3D renderings for simulated and experimental biofilms grown at 0.5% (w/v) of arabinose reveal tight fits (Supplementary Fig. 2.21-23), and the resulting best-fit interaction force displays an attractive region (red) at the average experimental cell-cell distance (Fig. 2.2c).

With the calibrated simulation, we then inferred an effective arabinose concentration for the WT* of $c = 0.68 \pm 0.19\%$ (w/v), by locating the WT* biofilm architecture in the (ν, λ_a, ρ_a) -space along the curve of different arabinose concentrations (Fig. 2.2d). Extracting an effective arabinose concentration and RbmA level for the WT* is based on the simplifying assumption that all cells in the biofilm express the same levels of the key matrix components, which represents a minimal model that is in quantitative agreement with the experimental data, as the best-fit (ν, λ_a, ρ_a) -values for the WT* are close to the effective (ν, λ_a, ρ_a) -values for WT* on the curve of different arabinose concentrations (Fig. 2.2d). The simulations based on the WT* parameters for biofilms up to 300 cells show good quantitative agreement with experiments (Fig. 2.2f). Remarkably, these simulations also show architectural properties that were not included in the feature vector used for MSD-minimization, such as local density variations and the occurrence of patches of highly aligned cells inside the biofilm (red cells in Fig. 2.2e, characterized by high local ordering), which are characteristic for biofilms with high concentrations of RbmA. Predictions of the architectural development for larger biofilms ($N_{\text{cells}} > 300$) show high quantitative and qualitative agreement with experimental data, for both the WT* (Fig. 2.2g,h) and $\Delta rbmA$ (Supplementary Fig. 2.24b) biofilms up to 10^3 cells. To achieve accurate simulation results for very large biofilms ($>10^3$ cells), spatiotemporal heterogeneity in gene expression, matrix composition, and growth rates likely have to be included in future simulations. Our combined

experimental and theoretical analysis therefore suggests that mechanical interactions between cells suffice to account for the internal cellular order and architecture up to mid-sized *V. cholerae* biofilms.

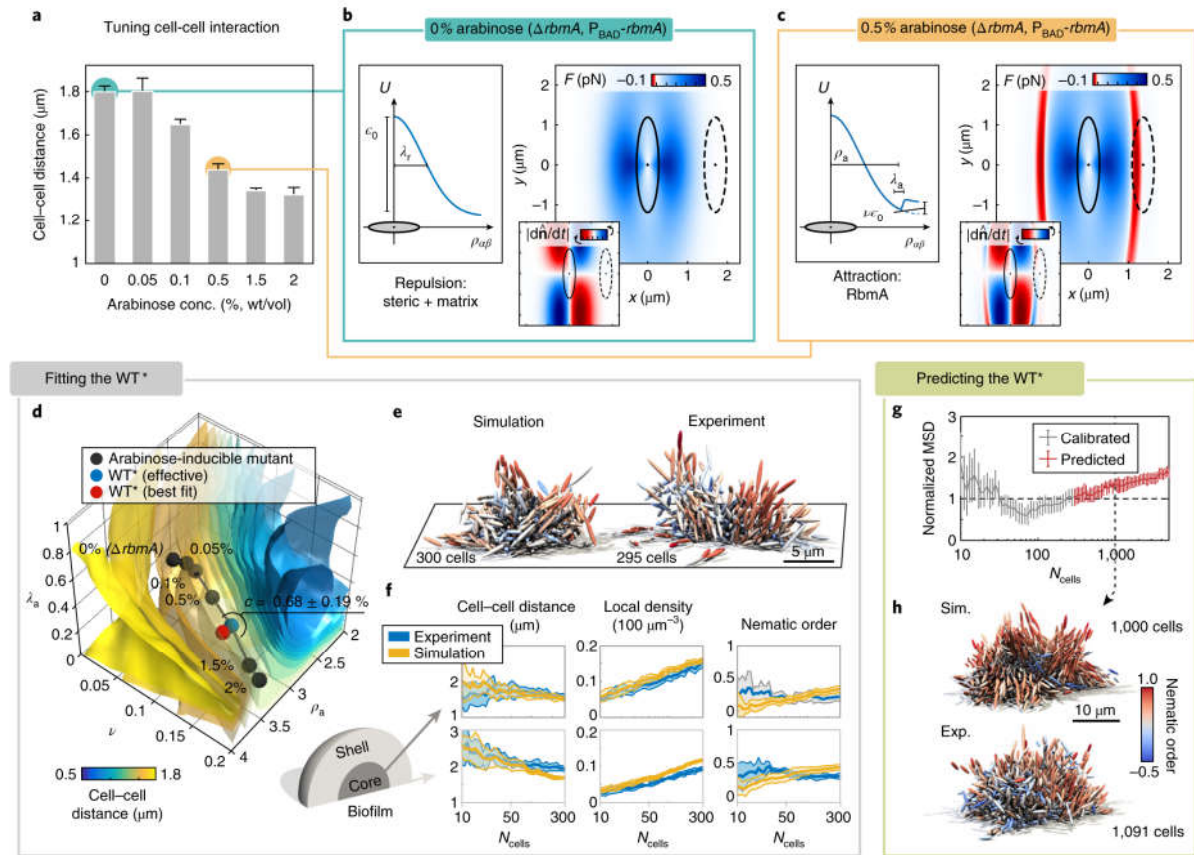


Figure 2.2. Biofilm architecture development is captured by an effective mechanical cell-cell interaction potential. **a**, Increased RbmA production (achieved by increasing arabinose concentration, see Methods) decreases the average cell-cell distance in biofilms. Without arabinose, no RbmA is produced and the biofilm architecture is identical to the $\Delta rbmA$ mutant ($n > 3$ biofilms). **b**, Cell-cell interaction inside $\Delta rbmA$ mutant biofilms lacking cell-cell adhesion, modelled by the repulsive interaction potential (left) and the resulting cell-cell interaction forces (right) for the best-fit potential and the most prominent cellular orientation (red: attractive, blue: repulsive). Inset: rotational interaction dynamics (red: clockwise rotation, blue: counter-clockwise rotation). For more details and additional orientations see Supplementary Figs. 2.18 and 2.19. The dashed cell is plotted at the average cell-cell distance obtained from the corresponding experiment in panel **a**. **c**, The cell-cell interaction potential (left) and force (right) resulting from the best-fit potential for biofilms with a particular level of cell-cell adhesion (0.5% arabinose). RbmA-mediated cell-cell adhesion gives rise to an attractive part (red), acting within the range of the experimentally determined average cell-cell distance (dashed cell). **d**, Best-fit simulation parameters for varying RbmA and arabinose concentrations (black dots) follow a line in (ν, λ_a, ρ_a) -parameter space and cross isosurfaces of average cell-cell distance (see colour bar, and compare with panel **a**; for more details about the fitting see Supplementary Fig. 2.23). The RbmA level of the WT* biofilms is inferred in terms of an effective arabinose concentration by locating the WT* along the line of different arabinose concentrations (blue point), which is very close to the best fit of the WT* (red point). **e**, Simulated (best fit) vs. experimental WT* biofilm. **f**, Comparison of biofilm architectural properties for the WT* experiment (blue) and the WT* simulation prediction (yellow). The architectural properties are spatially resolved for the core (left) and shell (right) of the biofilm (experiment: $n = 7$; simulation: $n = 10$). **g,h**, Simulation predictions of large ($N_{\text{cells}} = 1000$) WT* biofilms (based on the WT*-interaction potential calibrated with $N_{\text{cells}} < 300$) show quantitative (**g**) and qualitative (**h**) agreement with experiments (experiment: $n = 4$; simulation: $n = 10$). All error bars correspond to standard errors.

To determine how external fields can affect orientational order and morphology of 3D biofilms, we perturbed biofilm growth by applying external flow fields of varying strength, corresponding to shear rates of $\dot{\gamma} = 2\text{--}2000\text{ s}^{-1}$, typically encountered by bacteria in natural and man-made environments²⁶. At high shear rates ($> 600\text{ s}^{-1}$, corresponding to average flow speeds $>10\text{ mm/s}$ through the growth chamber), the WT* cells formed smaller, more compact biofilm colonies with droplet-like shapes, compared with low shear environments (Fig. 2.3a,b). To understand the mechanisms underlying these architectural changes, we investigated both local and global effects of increased shear on biofilms, and changes in matrix production. Exposure to higher shear resulted in a significantly decreased cell-cell spacing and lower growth rate in WT* biofilms (Fig. 2.3c), but the height-to-width aspect ratio was unaffected when comparing biofilms with similar N_{cells} (Fig. 2.3e) despite the increased levels of shear stress applied to the top (Fig. 2.3d). We therefore hypothesized that cells in WT* biofilms at higher shear secrete increased levels of RbmA, allowing increased cell-cell attraction forces to balance shear forces, but leading to a strong reduction in overall growth rate owing to the metabolic cost of increased RbmA production. Using a fluorescent transcriptional reporter for *rbmA* expression, we confirmed that high shear increases RbmA levels (Supplementary Fig. 2.12), indicating that cells actively modulate the mechanical cell-cell interactions via gene expression.

To explain the observed droplet-like shapes of biofilms grown at high shear rate, we investigated cellular alignment with flow and analysed biovolume flux inside the biofilm using the optical flow method (Fig. 2.3a,f, see Supplementary Information). We determined that cell alignment with flow increases with increasing shear rate (Fig. 2.3c,g) and an anisotropic “biomass shift” downstream occurs at $\dot{\gamma} > 60\text{ s}^{-1}$ (Fig. 2.3f), indicating that the observed biofilm shapes were caused by anisotropic expansion of cells aligned with the flow as a result of growth and viscoelastic deformation. Our above measurements regarding increased RbmA levels in WT* biofilms at high shear predict that if RbmA levels are in fact primarily responsible for cell-cell attraction, then most effects of shear on $\Delta\textit{rbmA}$ -mutant biofilms should be explained by shear-induced cell erosion. Indeed, these biofilms showed a reduction in upward growth with higher flow (Fig. 2.3e), indicating that shear forces are larger than cell-cell attraction forces. This was confirmed by simulations of shear-dependent erosion using a continuum model (see Supplementary Information), which captured the decreased volumetric growth of $\Delta\textit{rbmA}$ -mutant biofilms owing to cell erosion (Fig. 2.3h). Fluid flow therefore strongly affects biofilm architectural development through the effect of shear on growth rate, matrix composition, alignment with flow, biomass shift, and shear-induced erosion²⁷. These results demonstrate that mechanical interactions at the cellular scale remain important in sculpting biofilm architecture when an external field is applied.

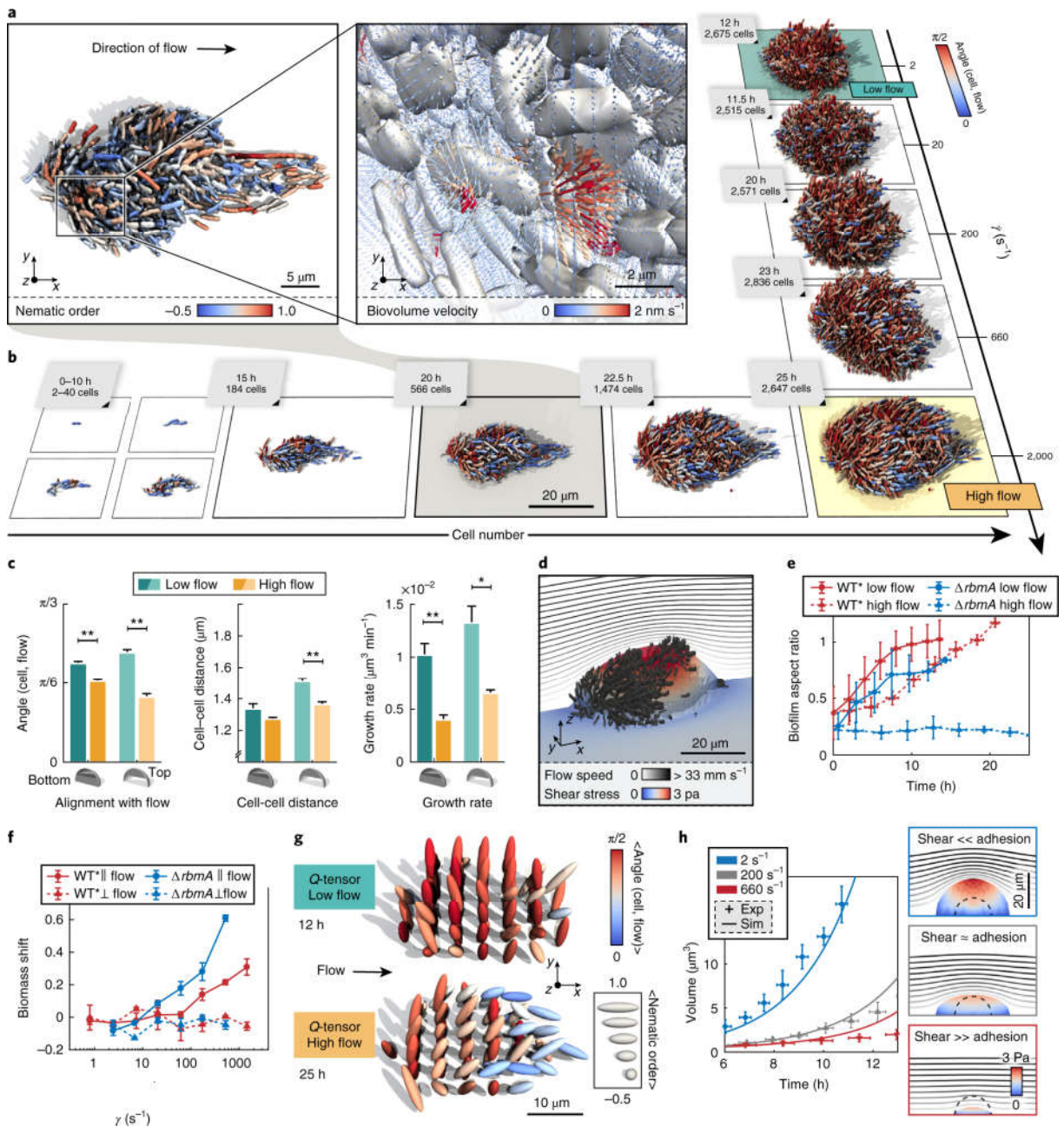


Figure 2.3. Biofilm architecture is shaped by external shear flow. **a**, WT* biofilms grown under strong shear ($\dot{\gamma} = 2000 \text{ s}^{-1}$) display droplet-like shapes. Inset: Biovolume flux field inside the biofilm (see Supplementary Information). **b**, WT* biofilms in high shear ($\dot{\gamma} = 2000 \text{ s}^{-1}$) display strong alignment with flow throughout growth, yet biofilms grown in flow with low shear ($\dot{\gamma} = 2\text{--}200 \text{ s}^{-1}$) do not show strong architectural modifications. **c**, Quantification of the effect of shear on biofilm architecture: measurements of cellular alignment with flow, cell-cell distance, and cell growth rate at the bottom and top of biofilms with sizes of $N_{\text{cells}} \sim 800$ cells show that WT* biofilms in high shear are smaller, more compact, and display stronger flow-alignment. Statistical significance: * is $p < 0.05$ and ** is $p < 0.01$ (t-test); error bars are standard error ($n = 4$ biofilms, error bars: standard errors). **d**, Simulated shear stress distribution for a WT* biofilm, demonstrating that the region of highest shear is at the top of the biofilm. The streamlines indicate the profile of the external flow. **e**, Biofilm aspect ratio (height/width) increases in time for WT* (red) biofilms, but decreases for $\Delta rbmA$ mutant biofilms (blue) in high flow owing to shear-induced erosion ($n = 4$, error bars: standard deviations). **f**, Biomass shift is defined as the fraction of the average total biomass flux through planes parallel (||) or perpendicular (\perp) to flow (see Supplementary Fig. 2.2 for details). Positive biomass shift along

the flow direction at higher shear rates indicates anisotropic biofilm expansion towards the downstream direction of the external flow. Zero biomass shift perpendicular to the flow indicates no directional bias ($n \geq 3$, error bars: standard errors). **g**, The tensorial nematic order parameter (Q-tensor, see Supplementary Information) and cellular alignment with the flow direction were measured at equally spaced points inside biofilms at low and high shear rates, indicating the regions in which cells are predominantly aligned with the flow and each other. **h**, Biofilm volumetric growth for $\Delta rbmA$ mutant biofilms is captured by a continuum model (see Supplementary Information) with varying ratios of shear-induced erosion and cell-cell adhesion (experiment: $n = 4$, error bars: standard deviations).

In conclusion, our combined experimental and theoretical analysis shows that the emergence of local nematic order in growing *V. cholerae* biofilms can be captured by an experimentally constrained minimal effective cell-cell interaction potential that translates molecular mechanisms into force parameters. Given the immense complexity of molecular interactions, metabolism, and signalling that occurs between the cells, the availability of an experimentally validated potential-based description of biofilm development presents a significant conceptual advance that can provide a microscopic basis for constructing predictive macroscopic continuum theories, by building on coarse-graining techniques recently developed for other classes of active matter^{9,28}. At the same time, a refined model will be needed to account for spatial heterogeneities and time-dependencies that likely become relevant at the later stages of biofilm development. Such progress is essential for identifying new strategies towards understanding, controlling and inhibiting biofilm growth under realistic physiological conditions, which remains one of the foremost challenges in biomedical^{18,29,30} and biophysical research^{5,10,31}.

Methods

Media and cloning approaches. All strains were grown in LB medium supplemented with appropriate antibiotics at 37°C for normal growth and during cloning. Biofilm experiments with *V. cholerae* were performed in M9 minimal medium, supplemented with 2 mM MgSO₄, 100 mM CaCl₂, MEM vitamins, 0.5% glucose, and 15 mM triethanolamine (pH 7.1). Standard molecular biology techniques were applied to construct plasmids and strains³². Restriction enzymes and DNA polymerase enzymes were purchased from New England Biolabs. Oligonucleotides were commercially synthesized by Eurofins. All *V. cholerae* strains used in this study are derivatives of the rugose variant of the wild type *V. cholerae* O1 biovar El Tor strain N16961 (termed strain KDV148). *V. cholerae* deletion mutations were engineered using the pKAS32 suicide vector harboured in *E. coli* S17-1 λpir³³. Complementation constructs were inserted at the lacZ site with the help of the suicide plasmid pKAS32. The plasmid pNUT542, containing the gene coding for the super-folder green fluorescent protein (*sfGFP*) expressed under the control of the *P_{tac}* promoter, was conjugated into all *V. cholerae* strains except for the complementation strain KDV1082²⁹. Plasmid clones were first constructed in the *E. coli* strain Top10 and then mated into *V. cholerae* with the help of an additional *E. coli* strain harbouring the conjugation plasmid pRK600. Arabinose was used as inducer to control the expression of *rbmA* from the arabinose-regulated promoter *P_{BAD}*. Details of the strains, plasmids, and oligonucleotides are listed in the Supplementary Information.

Strain Construction. The rugose variant of the *V. cholerae* N16961 (strain KDV148) displays strong surface attachment and biofilm formation as a consequence of high c-di-GMP production³⁴. *V. cholerae* cells are usually characterized by a slightly curved cell shape. To allow *V. cholerae* cells to be modelled by ellipsoids in theory and simulations, we generated a mutant with a straight cell shape (i.e. the common bacterial rod shape), by deleting the gene $\Delta crvA$ according to the method of Bartlett et al.³⁵. In detail, the 1 kb flanking regions of gene *crvA* (VCA1075) were amplified with the oligonucleotides kdo1182/kdo1183 and kdo1183/kdo1184, and the fused polymerase chain reaction (PCR) product was amplified using kdo1182/kdo1185. The final PCR product was ligated into plasmid pNUT144 (a derivative of pKAS32). The resulting plasmid pNUT961 was conjugated into strain KDV148, to generate the $\Delta crvA$ deletion mutant, following the selection protocol described earlier by Skorupski et al.³³. Finally, cells containing the correct mutation were screened by PCR. Plasmid pNUT542 was conjugated into KDV611 strain to construct strain KDV613 containing the $\Delta crvA$ deletion (referred to as WT*). The $\Delta rbmA$ deletion strain (KDV698) was constructed by conjugating plasmid pNUT336 into strain KDV611. The mutant screening was performed by PCR³⁶.

Tuning cell-cell interaction by inducing *rbmA* expression. To control the timing and rate of RbmA production, an inducible strain (KDV1082) was generated by conjugating plasmid pNUT1519 into the Δ *rbmA* strain KDV698. Plasmid pNUT1519 was created by cloning a P_{tac} -*sfgfp* construct into plasmid pNUT1268. Plasmid pNUT1268 is a derivative of plasmid pNUT542 in which P_{tac} -*sfgfp* was replaced with a construct of P_{BAD} -*rbmA*. P_{BAD} , an arabinose inducible promoter, and the *rbmA* gene were joined by PCR amplification with oligonucleotides kdo1435/kdo1436.

Visualization of secreted RbmA. To visualize RbmA during biofilm growth, the wild type copy of *rbmA* was exchanged by a FLAG-tagged *rbmA*¹⁶ (with the octapeptide DYKDDDDK) by mating the plasmid pNUT462 into the strain KDV148, resulting in *V. cholerae* strain KDV829. Successful FLAG-tagging of RbmA was confirmed by PCR and sequencing. The final strain KDV835 was generated by conjugating the fluorescence protein expression plasmid pNUT542 into strain KDV829. For RbmA visualization in flow chambers, biofilms were grown in M9 medium containing 1 μ g/mL of FLAG tag monoclonal antibody (L5) conjugated to AlexaFluor 555 (Thermo Scientific) and 1 mg/mL of filter-sterilized bovine serum albumin (BSA).

Measuring *rbmA* expression. To measure RbmA production during biofilm growth, the gene *mRuby3* was transcriptionally fused to *rbmA* on the chromosome, by introducing plasmid pNUT1401 into the strain KDV611. The transcriptional fusion of *rbmA*-*mRuby3* in the resulting strain (KDV1026) was confirmed by PCR and sequencing. The final strain KDV1027 was generated by mating the plasmid pNUT542 into strain KDV1026.

Flow chamber biofilm experiments. *V. cholerae* biofilms were grown in microfluidic flow chambers as described by Drescher *et al.*⁵ (chamber dimensions: [width, height, length] = [500, 100, 7000] μ m). Flow chambers were constructed from poly(dimethylsiloxane) (PDMS) bonded to glass coverslips using an oxygen plasma. The microfluidic design contained four independent channels on each coverslip. The manufacturing process of these microfluidic channels guarantees highly reproducible channel dimensions and surface properties. Each channel was inoculated with a culture of a particular *V. cholerae* strain. Cultures were grown overnight at 28° C in liquid LB medium under shaking conditions, back-diluted 1:200 in LB medium in the morning, and grown to OD₆₀₀ = 0.5 prior to channel inoculation. After inoculation of the channels, the cells were given 1 h to attach to the glass surface of the channel, before a flow of 100 μ L/min M9 medium was initiated for 45 s to wash away non-adherent cells and to remove LB growth medium from the channels. The flow rate was then set to a value between 0.1 and 100 μ L/min, corresponding to an average flow speed $\langle v \rangle$ between 0.03 and 33 mm/s and a shear rate $\dot{\gamma}$ between 2 and 2000 s⁻¹ (as indicated) until the end of the experiments. Flow rates were controlled using a high-precision syringe pump (Pico Plus, Harvard Apparatus).

Image acquisition. Single cells were reconstructed from confocal fluorescence image stacks acquired with a Yokogawa CSU confocal spinning disk unit mounted on a Nikon Ti-E inverted microscope, using an Olympus 100× silicone oil (refractive index = 1.406) objective with NA 1.35, a 488 nm and 552 nm laser (Coherent Sapphire), and an Andor iXon EMCCD camera. By using this specific objective, heavy distortions at axial positions $>10 \mu\text{m}$ into the biofilm (owing to refractive index mismatch of biofilms and standard immersion oil) are reduced. The physical resolution was 63.2 nm/pixel in the xy-plane and was set to 400 nm along axial direction. Images were acquired every 10 min at very low excitation light intensities with 90 ms exposure time, using the “EM-gain” of the Andor iXon EMCCD camera. A Nikon hardware autofocus was used to correct for focus drift. The hardware was controlled using $\mu\text{Manager}$ ³⁷. During acquisition a live feedback between image acquisition, image analysis, and microscope control was used to automatically detect the biofilm height to avoid imaging of empty space below and on top of the biofilm, to eliminate tracking of XY coordinates of non-biofilm forming cells, and to control temporal resolution (to reduce photobleaching and phototoxicity).

Image processing. Detailed descriptions of image processing, segmentation, segmentation validation, cell tracking, biomass shift, optical flow, 3D visualization, quantitative biofilm features that are measured, and the calculation of space-time heatmaps are provided in the Supplementary Information.

Individual cell particle-based model

Model description and implementation. The cells are modelled as interacting ellipsoids of half-length ℓ and half-width r , described by their centre position \mathbf{x} and orientation $\hat{\mathbf{n}}$. As cells operate at low Reynolds number ($Re \approx 10^{-4}$), we approximate the dynamics as over-damped, ignoring inertial effects. Cells can interact with the wall boundary and other cells through interaction potential functions, U_{bdy} and U (Eq. 1). Denoting the identity matrix by \mathbf{I} , the over-damped translational and orientational dynamics of a single cell are described by

$$\frac{d\mathbf{x}}{dt} = \boldsymbol{\Gamma}^{-1} \left[-\frac{\partial U_{bdy}}{\partial \mathbf{x}} - \frac{\partial V}{\partial \mathbf{x}} \right] \quad (2)$$

$$\frac{d\hat{\mathbf{n}}}{dt} = (\mathbf{I} - \hat{\mathbf{n}}\hat{\mathbf{n}}^T) \left[\boldsymbol{\Omega}^{-1} \left(-\frac{\partial U_{bdy}}{\partial \hat{\mathbf{n}}} - \frac{\partial V}{\partial \hat{\mathbf{n}}} \right) \right] \quad (3)$$

where $\boldsymbol{\Gamma}$ and $\boldsymbol{\Omega}$ are friction tensors and V is the total interaction potential with all other cells as described in the Supplementary Information. The steric interaction between a cell and the wall boundary is modelled with a repulsive interaction potential that is proportional to the overlap between a cell and the wall boundary. The instantaneous cell-length growth rate for a single cell is defined as

$$\frac{d\ell}{dt} = \frac{\ell}{\tau_g} \ln(2) \quad (4)$$

where ℓ is the half-length of the cell at time t and τ_g is the growth time constant. The cell width is constant throughout the simulation. For further details of the particle-based model, see the Supplementary Information.

Simulation implementation. A custom highly parallelized individual cell-based code employing graphics processing units (GPUs) was developed to perform the simulations. At each time step, we calculate cell-cell interactions using the all-pairs approach³⁸ such that all pair-wise interactions are evaluated. We use a standard explicit Euler scheme to numerically integrate the translational and orientational dynamics, Eq. (2) and (3), as described in the Supplementary Information.

Parameter estimation. Initial order-of-magnitude estimates for systematic scans of the parameters in the potential U were obtained from basic physical considerations (see also Supplementary Information), before systematic scans of the parameters were computed. The energy scale $\epsilon_0 \sim 0.05 - 5$ pN $\cdot\mu\text{m}$ of the cell-cell interactions was assumed to be within a few orders of magnitude of the energy scale of cell-flow interactions, which were calculated via Stokes drag on a typical cell near the edge of the biofilm at low flow rate (0.1 $\mu\text{L}/\text{min}$). The repulsive length scale $\lambda_r \sim 1$ (corresponding to approximately 1 μm for typically aligned cells) was estimated via the average cell-cell distance in the core of biofilms, where cell-cell repulsion dominates. The attraction shift $\rho_a \sim 1$ was estimated via the average cell-cell distance at the edge of biofilms, where attraction dominates. The attraction width $\lambda_a \sim 0.1$ was determined by considering the standard deviation of experimental cell-cell distances at the edge of biofilms.

Background potential. Cell-cell adhesion mediated by the VPS matrix component was modeled by a mean-field background Woods-Saxon potential³⁹, and was assumed to provide the weak cell-cell binding that prevents the disintegration of biofilms owing to fluid shear acting on ΔrbmA mutant biofilms (which lack the major cell-cell attraction, mediated by RbmA). The mean-field VPS-mediated binding strength was estimated to be approximately equal to the Stokes drag felt by a cell at the edge of the biofilm at low flow rate (0.1 $\mu\text{L}/\text{min}$), because significant numbers of cells in the ΔrbmA background were sheared off at higher flow rate (100 $\mu\text{L}/\text{min}$). However, WT* biofilms were found to be robust to this increased fluid shear, suggesting that the increased expression of *rbmA* at higher flow rate (Supplementary Information) increases the RbmA-mediated cell-cell attraction strength by approximately two orders of magnitude above the value predicted at low flow rate. In simulations

performed at zero shear, the VPS contribution to cell-cell attraction can be neglected as the Woods-Saxon potential is approximately constant in the bulk.

Comparing simulations with experimental data. The dynamic biofilm architecture was summarized in a feature vector representing key phenotypic and structural properties temporally. The similarity between a vector characterizing a simulation and a real biofilm was assessed in terms of the mean square distance (MSD) between them. For details, see the Supplementary Information.

Continuum model. The mathematical continuum model of growing biofilms in shear flow is described in the Supplementary Information.

References

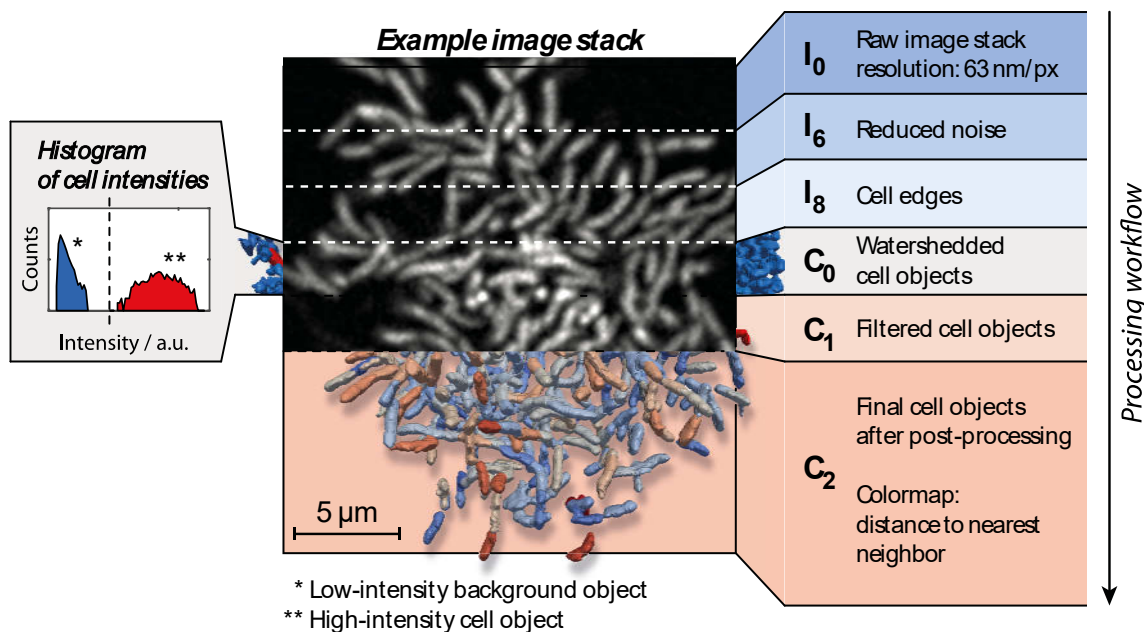
1. Zhou, S., Sokolov, A., Lavrentovich, O. D. & Aranson, I. S. Living liquid crystals. *Proc. Natl. Acad. Sci. U.S.A.* **111**, 1265–1270 (2014).
2. Hagan, M. F. & Baskaran, A. Emergent self-organization in active materials. *Curr. Opin. Cell Biol.* **38**, 74–80 (2016).
3. Doostmohammadi, A., Adamer, M. F., Thampi, S. P. & Yeomans, J. M. Stabilization of active matter by flow-vortex lattices and defect ordering. *Nat. Commun.* **7**, 1–9 (2016).
4. Volfson, D., Cookson, S., Hasty, J. & Tsimring, L. S. Biomechanical ordering of dense cell populations. *Proc. Natl. Acad. Sci. U.S.A.* **105**, 15346–15351 (2008).
5. Drescher, K. *et al.* Architectural transitions in *Vibrio cholerae* biofilms at single-cell resolution. *Proc. Natl. Acad. Sci. U.S.A.* **113**, E2066–E2072 (2016).
6. Yan, J., Sharo, A. G., Stone, H. A., Wingreen, N. S. & Bassler, B. L. *Vibrio cholerae* biofilm growth program and architecture revealed by single-cell live imaging. *Proc. Natl. Acad. Sci. U.S.A.* **113**, E5337–E5343 (2016).
7. Kragh, K. N. *et al.* Role of multicellular aggregates in biofilm formation. *MBio* **7**, 1–11 (2016).
8. Flemming, H.-C. *et al.* Biofilms: an emergent form of bacterial life. *Nat. Rev. Microbiol.* **14**, 563–575 (2016).
9. Marchetti, M. C. *et al.* Hydrodynamics of soft active matter. *Rev. Mod. Phys.* **85**, 1143–1189 (2013).
10. Persat, A. *et al.* The mechanical world of bacteria. *Cell* **161**, 988–997 (2015).
11. Liu, J. *et al.* Coupling between distant biofilms and emergence of nutrient time-sharing. *Science* **356**, 638–642 (2017).
12. Rodesney, C. A. *et al.* Mechanosensing of shear by *Pseudomonas aeruginosa* leads to increased levels of the cyclic-di-GMP signal initiating biofilm development. *Proc. Natl. Acad. Sci. U.S.A.* **114**, 5906–5911 (2017).
13. Grant, M. A. A., Waclaw, B., Allen, R. J. & Cicuta, P. The role of mechanical forces in the planar-to-bulk transition in growing *Escherichia coli* microcolonies. *J. R. Soc. Interface* **11**, 20140400 (2014).
14. You, Z., Pearce, D. J. G., Sengupta, A. & Giomi, L. Geometry and Mechanics of Microdomains in Growing Bacterial Colonies. *Phys. Rev. X* **8**, 031065 (2018).
15. Delarue, M. *et al.* Self-driven jamming in growing microbial populations. *Nat. Phys.* **12**, 762–766 (2016).
16. Seminara, A. *et al.* Osmotic spreading of *Bacillus subtilis* biofilms driven by an extracellular matrix. *Proc. Natl. Acad. Sci. U.S.A.* **109**, 1116–1121 (2012).
17. Trejo, M. *et al.* Elasticity and wrinkled morphology of *Bacillus subtilis* pellicles. *Proc. Natl. Acad. Sci. U.S.A.* **110**, 2011–2016 (2013).
18. Maier, B. & Wong, G. C. L. How bacteria use type IV pili machinery on surfaces. *Trends Microbiol.* **23**, 775–788 (2015).
19. Teschler, J. K. *et al.* Living in the matrix: assembly and control of *Vibrio cholerae* biofilms. *Nat. Rev. Microbiol.* **13**, 255–268 (2015).
20. Berk, V. *et al.* Molecular architecture and assembly principles of *Vibrio cholerae* biofilms. *Science* **337**, 236–239 (2012).
21. Fong, J. C. *et al.* Structural dynamics of RbmA governs plasticity of *Vibrio cholerae* biofilms. *Elife* **6**, e26163 (2017).
22. Maestre-Reyna, M., Wu, W.-J. & Wang, A. H.-J. Structural Insights into RbmA, a Biofilm Scaffolding Protein of *V. cholerae*. *PLoS One* **8**, e82458 (2013).
23. Fong, J. C. N., Karplus, K., Schoolnik, G. K. & Yildiz, F. H. Identification and characterization of RbmA, a novel protein required for the development of rugose colony morphology and biofilm structure in *Vibrio cholerae*. *J. Bacteriol.* **188**, 1049–1059 (2006).
24. Hellweger, F. L., Clegg, R. J., Clark, J. R., Plugge, C. M. & Kreft, J. U. Advancing microbial sciences by individual-based modelling. *Nat. Rev. Microbiol.* **14**, 461–471 (2016).
25. Lardon, L. A. *et al.* iDynoMiCS: next-generation individual-based modelling of biofilms. *Environ. Microbiol.* **13**, 2416–2434 (2011).
26. Marcos, Fu, H. C., Powers, T. R. & Stocker, R. Bacterial rheotaxis. *Proc. Natl. Acad. Sci. U.S.A.* **109**,

- 4780–4785 (2012).
27. Mitchell, W. H. & Spagnolie, S. E. A generalized traction integral equation for Stokes flow, with applications to near-wall particle mobility and viscous erosion. *J. Comput. Phys.* **333**, 462–482 (2017).
 28. Cates, M. E. & Tjhung, E. Theories of binary fluid mixtures: From phase-separation kinetics to active emulsions. *J. Fluid Mech.* **836**, P1.1–68 (2018).
 29. Singh, P. K. *et al.* *Vibrio cholerae* combines individual and collective sensing to trigger biofilm dispersal. *Curr. Biol.* **27**, 3359–3366.e7 (2017).
 30. Vidakovic, L., Singh, P. K., Hartmann, R., Nadell, C. D. & Drescher, K. Dynamic biofilm architecture confers individual and collective mechanisms of viral protection. *Nat. Microbiol.* **3**, 26–31 (2017).
 31. Smith, W. P. J. *et al.* Cell morphology drives spatial patterning in microbial communities. *Proc. Natl. Acad. Sci. U.S.A.* **114**, E280–E286 (2017).
 32. Sambrook, J., Fritsch, E. F. & Maniatis, T. *Molecular cloning: a laboratory manual*. (Cold Spring Harbor Laboratory Press, 1989).
 33. Skorupski, K. & Taylor, R. K. Positive selection vectors for allelic exchange. *Gene* **169**, 47–52 (1996).
 34. Beyhan, S. & Yildiz, F. H. Smooth to rugose phase variation in *Vibrio cholerae* can be mediated by a single nucleotide change that targets c-di-GMP signalling pathway. *Mol. Microbiol.* **63**, 995–1007 (2007).
 35. Bartlett, T. M. *et al.* A periplasmic polymer curves *Vibrio cholerae* and promotes pathogenesis. *Cell* **168**, 172–185.e15 (2017).
 36. Nadell, C. D., Drescher, K., Wingreen, N. S. & Bassler, B. L. Extracellular matrix structure governs invasion resistance in bacterial biofilms. *ISME J.* **9**, 1700–1709 (2015).
 37. Edelstein, A. D. *et al.* Advanced methods of microscope control using µManager software. *J. Biol. Methods* **1**, 1–10.e10 (2014).
 38. Nyland, L., Harris, M. & Prins, J. Fast n-body simulation with CUDA. *Simulation* **3**, 677–696 (2007).
 39. Woods, R. D. & Saxon, D. S. Diffuse surface optical model for nucleon-nuclei scattering. *Phys. Rev.* **95**, 577–578 (1954).

Supplementary information

Data Analysis

Image processing. Image processing was carried out using MatLab (MathWorks). In the following sections, raw data 3D image stacks are referred to as $I_0(t)$ and are matrices of dimension x , y , and z , which were acquired at a time point t (see Supplementary Fig. 2.2). Any intermediate processing result is labelled with consecutive indices $I_i(t)$. Prior to segmentation, subsequent image stacks were aligned along x , y , and z by image registration ($= I_1$). Floating cells which were not associated with a biofilm were removed by median filtering along z ($= I_2$). Image stacks that have been registered and for which floating cells have been removed, were then up-sampled along the z -dimension to obtain equal voxel side lengths ($= I_3$). Subsequently, noise was removed by filtering as follows. The eigenvalues of each xz - and each yz -plane were obtained by singular value decompositions and the lowest thirds of the calculated values were set to zero to reduce high frequency noise ($= I_4$). In addition, a 3D-convolution with an averaging kernel was performed ($= I_5$). Afterwards, the out-of-focus fluorescence was suppressed by slice-wise Top-hat filtering of the image stacks ($= I_6$, see Supplementary Fig. 2.2).



Supplementary Figure 2.1. Image processing pipeline. Biofilms on spinning disc confocal fluorescence image stacks are processed as illustrated, to obtain 3D models of biofilms based on individual cells.

Cell detection. Image stacks, $I_6(t)$, were further processed to identify individual cells. First, the gamma value was adjusted to $\gamma = 3$ to enhance the range between signal and background ($= I_7$). Second, a 3D-edge detection was performed by convolving the data with a 3D Laplacian-of-Gaussian (LoG) kernel of $0.82 \mu\text{m}$ cube length (corresponding to 13 px) ($= I_8$). In the obtained matrices $I_8(t)$, zero values represent those locations where the cell's fluorescence intensity values drop approximately by 50% in comparison to its local intensity maxima. These zero crossings were determined to obtain closed surfaces representing the cellular outlines ($= I_9$). To distinguish between the "inside" ($=$ cell) and "outside" ($=$ background) of such a closed surface, a 3D-Gaussian filter kernel was applied to I_6 with the same spatial dimension as the LoG kernel used for the edge detection. The local maxima of the resulting image stack were identified ($= I_{10}$) and used as seeds to "flood-fill" the cell interior in I_9 , yielding the binary image I_{11} containing all cell clusters. Cell de-clumping was performed by 3D-watershedding. The intensity landscape used for watershedding was obtained by enhancing the local maxima (I_{10}) inside I_6 by a factor of 10, followed by 3D-Gaussian smoothing and masking with I_{11} ($= I_{12}$). After watershedding, I_{12} was 3D-median filtered and binary cell objects ($= C_0$) were obtained and processed further, as described in the next sections.

Cell object processing. For the cell objects C_0 the average underlying intensities in stack I_7 were determined and assigned to each cell. As the edge-detection-based segmentation will also yield objects, which are background, a filtering step is required. Because the average intensities of such background objects (calculated based on I_7) are typically orders of magnitude lower than those of actual cells, the cell objects C_0 were filtered based on these intensity measurements in stack I_7 ($= C_1$). After neglecting background objects, segmentation results were corrected based on C_1 . Over-segmentation was corrected by merging very small cells below a certain volume threshold with neighbouring cells of largest contact area. Clumped cells in multicellular structures (characterized by large volume and low convexity) were dissected by fitting a Gaussian mixture distribution model (GMM) with N components (or number of underlying cells) to the corresponding voxel coordinate cloud. N was determined by counting the number of skeleton branches above a typical length threshold. The additional cells obtained after GMM clustering were checked for size. Very small objects were merged again with the neighbouring cell of largest contact area; the remaining de-clumped cells were used to replace the original multicellular structure. In addition, cells touching the image edges were removed. The cellular orientations and cell dimensions (length, height and width) were obtained by analysing the principal components (found by principal component analysis, PCA) of each cell volume (in other words: by fitting an ellipsoid into each cell). For additionally calculated cell features see the section on "Biofilm features". Final cell objects are referred to as C_2 (see Supplementary Fig. 2.2).

Cell tracking. To determine the single-cell growth rate, the resulting cells were tracked over successive time points. For time point t_i , the parent of each cell was determined by comparison with time point t_{i-1} , and finding the corresponding cell for which volume overlap was maximized and deviations in cell orientation were minimized. All cells that were not related to the biofilm founder cells were excluded from further analysis (at low flow rates a layer of non-related cells is usually formed after longer imaging, cf. white cells in Fig. 2.1b,d and Supplementary Fig. 2.3), resulting in the analysis of purely clonal biofilms. The accuracy of the segmentation was investigated by segmenting synthetic microscopy image stacks as described in the section on “Validation of biofilm segmentation”.

Biofilm features

Name	Parameter	Unit	Description
Axial cell position	$height$	μm	Z-coordinate of each cell centroid.
Cell alignment with direction of flow	$angle(n_{cell}, flow)$	rad	Angle between each cell's major axis (see cell size and orientation) and the direction of the flow.
Radial alignment	$angle(n_{cell}, r)$	rad	Angle between each cell's major axis (see cell orientation) and the radial vector r pointing from the centre of mass pinned down to the bottom of the biofilm ($z = 0 \mu\text{m}$) to the corresponding cell.
Vertical alignment	$angle(n_{cell}, z)$	rad	Angle between each cell's major axis (see cell orientation) and z .
Cell volume	v	μm^3	Cell volume as obtained by the segmentation.
Cell size	l, h, w	μm	Cell dimensions (length, height and width), as determined by principal component analysis (PCA) of the segmented cell (equivalent to fitting an ellipsoid into the cell and deriving the three eigenvalues which correspond to the lengths of the main axes).
Cell orientation	$n_{cell} = (e_1, e_2, e_3)$	μm	Vector of the cell's major axis determined by PCA (eigenvector with largest eigenvalue).
Distance to centre of mass	d_{centre}	μm	Assuming radially symmetric biofilm growth in spherical coordinates (which is a good estimate for the low flow regime) each cell can be described spatially by its distance to the centre of mass projected onto the $z = 0 \mu\text{m}$ plane.
Distance to nearest neighbour	$d_{nearest\ neighbour}$	μm	Euclidian centroid-to-centroid distance to the nearest cell.

Distance to surface	$d_{surface}$	μm	Shortest distance of a particular cell to the outer surface of the biofilm.
Local cell density	ρ_{local}	μm^{-3}	Number of cells in a vicinity defined as a sphere of radius $3 \mu\text{m}$ around a cell, normalized by the volume of the vicinity.
Local order (nematic order)	S		Nematic order parameter $S = \langle 3/2(n_i \cdot n_j)^2 - 1/2 \rangle$ in a vicinity defined as a sphere of radius $3 \mu\text{m}$ around a cell. n_i and n_j refer to the orientation vectors of cells i and j , respectively ¹ .
Single cell growth rate	$growth\ rate$	$\mu\text{m}^3\text{s}^{-1}$	Single cell growth rate dv_i/dt of cell i (fixed by cell tracking) with volume v_i as determined by comparing the cell volume in frame N and $N+1$ at times t_N and t_{N+1} : $\Delta v_i/\Delta t_N = (v_{i,N+1} - v_{i,N}) / (t_{N+1} - t_N)$. Potential bias caused by over-/under-segmentation and/or cell dispersion/off-shearing was corrected by setting v_{N+1} to zero for cells with no children and setting v_N to zero for cells with no parents. Using this approach, the global biofilm volume $V(t)$, as determined by segmentation, matches $V(t) = \int \sum \Delta v_i dt$.

Supplementary Table 2.1. List of calculated single-cell features.

Name	Parameter	Unit	Description
Aspect ratio	Z/XY		Biofilm height divided by average biofilm base radius.
Biofilm base circularity	B_{circ}		Deviation of biofilm base cross section from a circle $B_{\text{circ}} = 1-Z/XY $.
Global cell density	ρ_{biofilm}	$\mu\text{m}^3\text{s}^{-1}$	Number of cells divided by the volume of the biofilm's convex hull.
Biofilm volume	V	μm^3	Sum of the volume of all individual cells

Supplementary Table 2.2. List of calculated global biofilm features.

Optical flow. Pre-processed image stacks (I_s , for details see section on “Image processing”) were down-sampled to 1/4 of the initial resolution. The optical flow (= biovolume velocity) vector field (u_x, u_y, u_z) of isolated growing biofilms was determined for each containing voxel using the Horn-Schunck method² implemented in MatLab by Mustafa *et al.*³. Afterwards, the optical flow was set to zero in the space that did not contain cells. To investigate the effect of the external flow rate on net biomass movement, in terms of moving biovolume, the total biovolume flow through defined planes was calculated (see Supplementary Fig. 2.2). For external flow of growth medium v_{liquid} pointing in the positive y -direction, the total biovolume flow I_{BV}^{\parallel} through the xz -plane for different y -coordinates, and the total biovolume flow I_{BV}^{\perp} through the yz -plane for different x -coordinates, respectively, was calculated by summation over the biovolume fluxes through the corresponding planes (Eq. (1) and Eq. (2), Supplementary Fig. 2.2).

The biovolume flow I_{BV} through xz -planes (with plane normal vectors \hat{n}_y) parallel to v_{liquid} for different values of y_i is:

$$I_{BV}^{\parallel}(y_i, t) = \sum_{x,z,y=y_i} \hat{n}_y \cdot (u_x(t), u_y(t), u_z(t)) \quad (1)$$

The biovolume flow I_{BV} through yz -planes (with plane normal vectors \hat{n}_x) perpendicular to v_{liquid} for different values of x_i is:

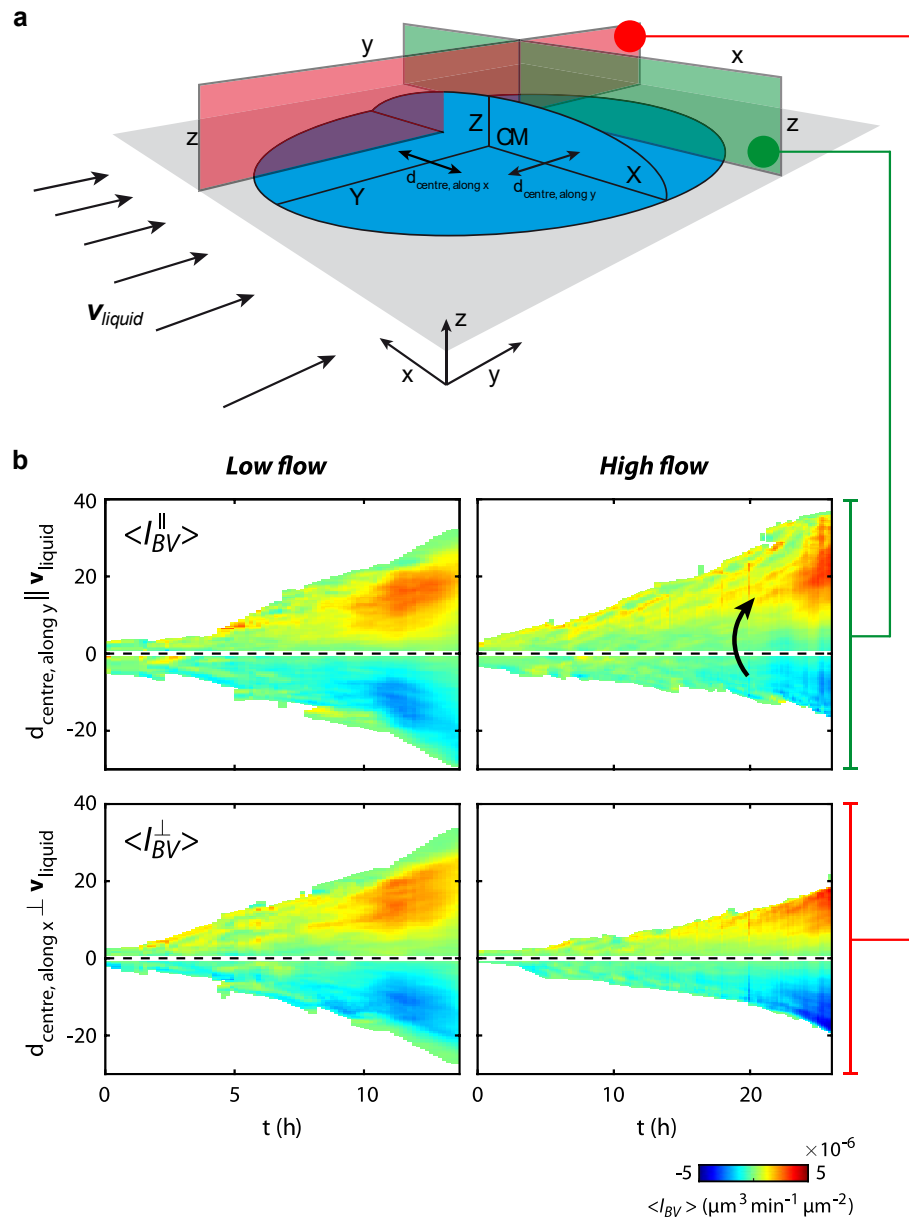
$$I_{BV}^{\perp}(x_i, t) = \sum_{x=x_i, z, y} \hat{\mathbf{n}}_x \cdot (u_x(t), u_y(t), u_z(t)) \quad (2)$$

To calculate the biomass shift (displayed in Fig. 2.3f of the main paper), the biovolume flow I_{BV} was summed up either along y or x-direction, was normalized by the sum of the absolute values, and the result was averaged over all time points:

$$biomass_shift^{\parallel} = \left\langle \frac{\sum_{y_i} I_{BV}^{\parallel}}{\sum_{y_i} |I_{BV}^{\parallel}|} \right\rangle \quad (3)$$

$$biomass_shift^{\perp} = \left\langle \frac{\sum_{x_i} I_{BV}^{\perp}}{\sum_{x_i} |I_{BV}^{\perp}|} \right\rangle \quad (4)$$

In Fig. 2.3f of the main paper, values are given as mean \pm standard deviation for $n = 3$ individual biofilms. For better visualization in Supplementary Fig. 2.2b, the averaged biovolume velocity through the xz- and yz-planes is shown, whereas for Fig. 2.3f the summed velocities were used.

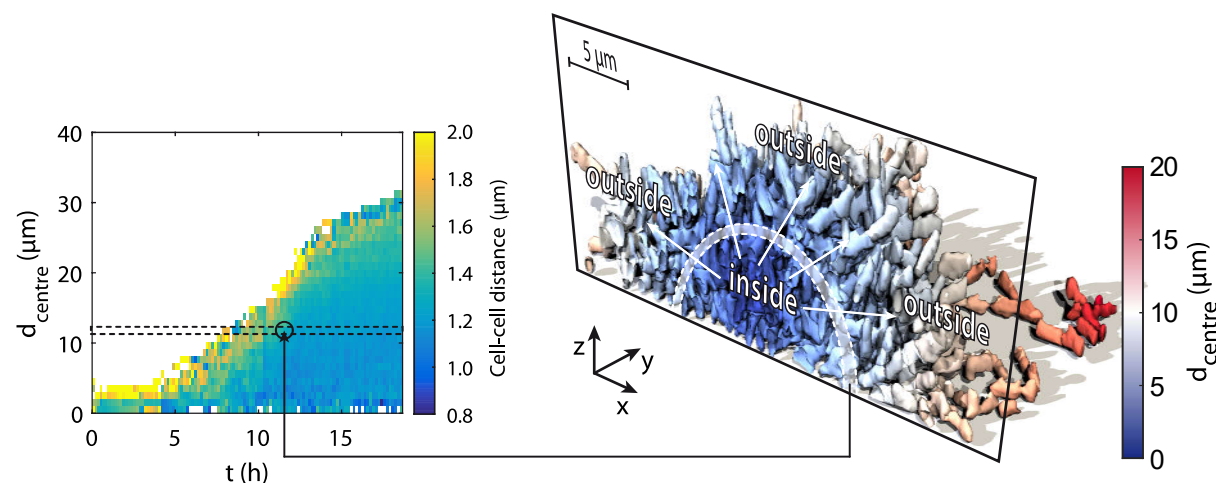


Supplementary Figure 2.2. Optical flow measurements of biomass movement inside a biofilm. **a**, The “optical flow” (= biovolume flow) of a growing biofilm (blue) through the green plane (perpendicular to the direction of flow v_{liquid} , indicated with black arrows) and through the red plane (parallel to the direction of v_{liquid}) was determined. **b**, In panel **a**, the positions of the red and green plane with respect to the centre of mass (CM) projected down to the bottom of the biofilm were varied (red plane: $d_{\text{centre, along } x}$; green plane: $d_{\text{centre, along } y}$). For each time point and value of d_{centre} the average biovolume flow through the corresponding plane is shown as coloured pixel in the heatmap. In the heatmap, red values indicate an average net flux in the positive x or y direction, whereas blue values indicate an average net flux in negative directions. The two heatmaps in the upper row show the biovolume flow with respect to the green plane perpendicular to the direction of the external flow v_{liquid} with distance $d_{\text{centre, along } y}$ to the centre. At high flow speed more biomass is moving in the direction of v_{liquid} than at low flow speed, as indicated by the black arrow, and the asymmetry along the $d_{\text{centre}} = 0$ axis. The two heatmaps in the bottom row show the flux through the red plane parallel to v_{liquid} (with distance $d_{\text{centre, along } x}$ to the centre). The two heatmaps in the bottom row show that irrespective of the flow speed, biofilms grow symmetrically in the direction perpendicular to the flow, as indicated by the symmetric heatmaps around the $d_{\text{centre}} = 0$ axis.

3D visualization. Segmented biofilms were exported using the mVTK library⁴ and rendered in ParaView 5.1.2 (Kitware) using OSPRay rendering with shadows.

Visualization of RbmA. FLAG-labelled RbmA was detected in an additional fluorescence channel. The fluorescence distribution was rendered as a semi-transparent cloud and overlaid with the reconstructed biofilm in ParaView (see Fig. 2.1c).

Space-time heatmaps of biofilm development. In Fig. 2.1, single cell parameters for the WT* and $\Delta rbmA$ mutant biofilms are visualized spatially and temporally resolved in heatmaps (standard deviations of the presented mean values are shown in Supplementary Fig. 2.3 and Supplementary Fig. 2.3, respectively). For these space-time heatmaps, the cells were binned with respect to a spatial descriptor (vertical height z , distance to surface d_{surface} , or distance to centre of mass d_{centre}) and the corresponding cell property values were averaged for this particular spatial descriptor across the biofilm at a particular time t , as shown schematically in Supplementary Fig. 2.2.



Supplementary Figure 2.3. Illustration showing how a single tile in the heatmap (left panel) was generated. In this heatmap, cell-cell distance (color-coded) is measured as a function of the distance to the centre of mass (CM) of the biofilm pinned down to the bottom (d_{centre}), shown on the y-axis of the heatmap. For each time point, all cells inside the biofilm are grouped according to their distance to the CM, as indicated by the white dashed lines in the 3D rendering, approximately corresponding to the black dashed lines in the heatmap. For all cells having a similar value of d_{centre} the cell-cell distances are averaged (right panel) and visualized as a coloured tile in the left panel.

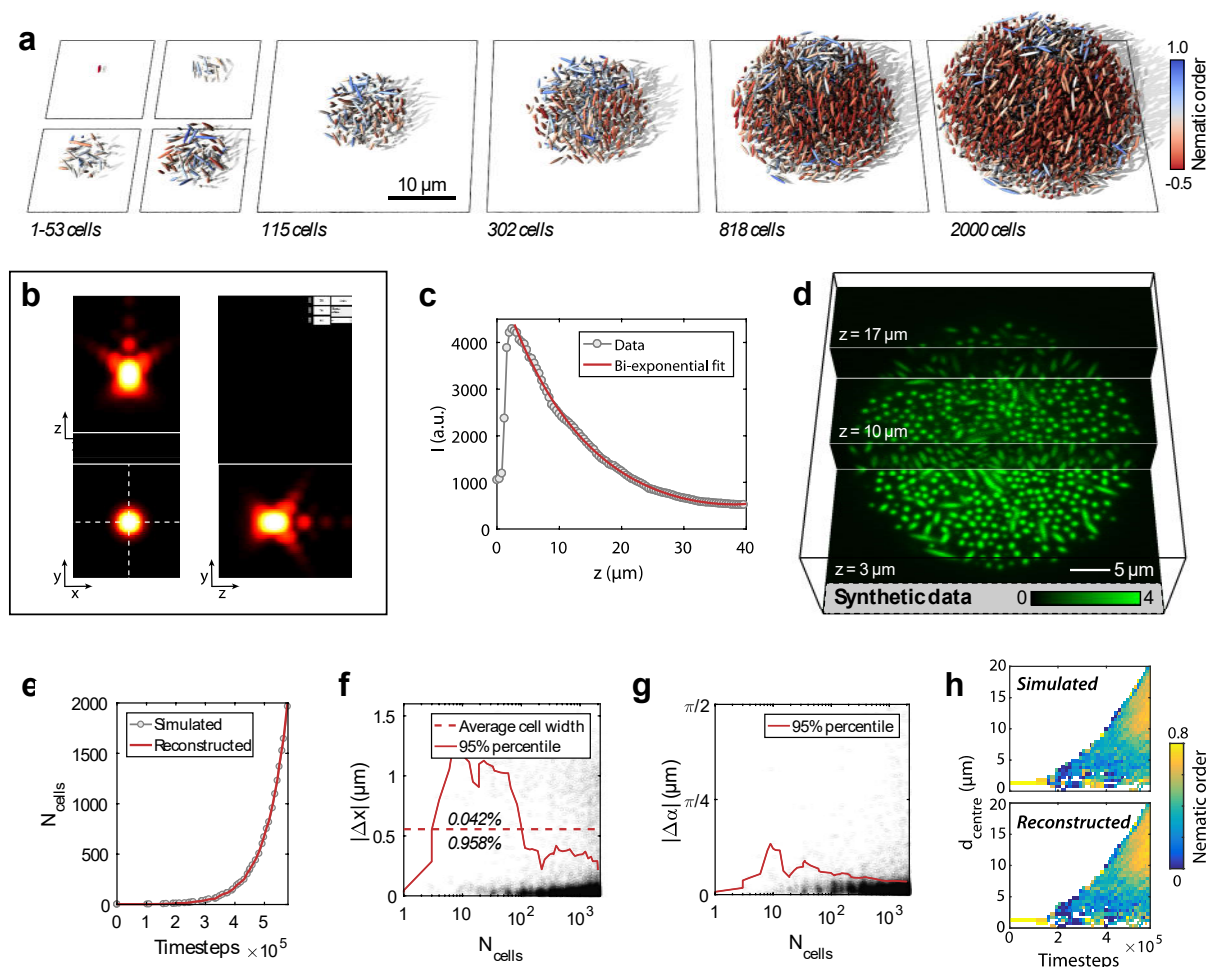
Liquid crystal (Q-tensor) representation of biofilms. To visualize the average cellular local order and alignment, an evenly spaced 3D-grid with 5 μm spacing was overlaid on the biofilm. For each grid node the uniaxial tensorial order parameter $Q_i = 1/2(3\mathbf{n}_i \otimes \mathbf{n}_i - \mathbb{I})$ was calculated⁵ for each cell i in a 2.5 μm vicinity, where \mathbf{n}_i denotes the cell orientation vector. Based on the individual cell tensors the average Q-tensor and its eigenvalues and eigenvectors were determined for each node. In Fig. 2.3g the

resulting values are represented as ellipsoids, where the largest eigenvalue and corresponding eigenvector are represented as the length and major axis orientation of each ellipsoid, respectively. The colour of each ellipsoid corresponds to the angle between the major axis vector \mathbf{n} of each ellipsoid and the direction of the flow.

Validation of biofilm segmentation. To benchmark the single-cell segmentation and tracking algorithms, the individual cell-based simulations (See section 0 of this document) were used to synthesize biofilm image stacks, which were convolved with the point spread function of the microscope we used and distorted by the addition of noise, to obtain data as similar as possible to the experimental data. In detail, a simulation up to $N = 2,000$ cells was performed using parameters which correspond to the $\Delta rbmA$ mutant (for biofilm renderings see Supplementary Fig. 2.2a, for a description of the simulation framework see the section on “Individual Cell-Based Simulations”).

The simulated biofilm data were converted into image stacks with a spatial resolution of 62.3 nm/pixel and a temporal resolution of approximately 10 min. The image stacks were blurred using a theoretical point spread function (PSF) corresponding to our microscopy setup (Supplementary Fig. 2.2b) (Huygens software, Scientific Volume Imaging) and down-sampled along z to match the axial resolution of the biofilm data (0.4 $\mu\text{m}/\text{pixel}$). Finally, the intensity levels were adjusted to the experimental data. To adjust the intensity levels, the average background intensity and the average cell intensity, depending on the axial imaging position z , were extracted from the experimental data. The average background intensity was independent of z ($I_{\text{background}} \approx 500$). To record the average cell intensity per plane, the corresponding intensity values were sorted and the highest 2000 values were averaged. The resulting curve $I_{\text{cell}}(z)$ was fitted with a bi-exponential function (Supplementary Fig. 2.2c), which was used to normalize the synthetic image stacks. Poisson-distributed noise was added to mimic noise due to photon detection inside the camera. The noise levels were estimated and generated using the algorithm proposed by Liu *et al.*⁶. The generated images (Supplementary Fig. 2.2d) were processed as described in the section on “Image processing”.

In Supplementary Fig. 2.2e-h the simulated dataset is compared with the reconstructed one in terms of cell number (Supplementary Fig. 2.2e), cell displacements (Supplementary Fig. 2.2f), differences in cellular orientation (Supplementary Fig. 2.2g), and internal order (Supplementary Fig. 2.2h). Based on this validation procedure, we determined that our image segmentation algorithms yielded accurate cell segmentation for > 95% of all cells.

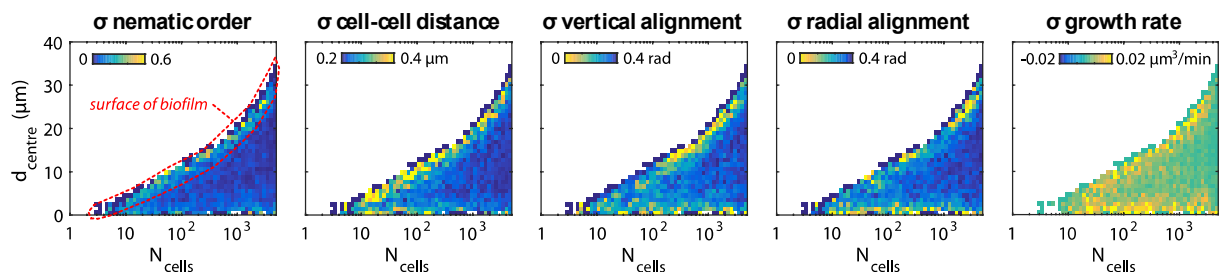


Supplementary Figure 2.4. Validation of the single-cell segmentation algorithms using synthetic images.

a, Time series of a rendered simulated biofilm, which was used to synthesize microscopic image stacks. **b**, Theoretical point spread function (PSF) of our experimental setup, used for convolution with the simulation data to obtain a more realistic dataset (see **d**). **c**, Experimentally determined typical average cell intensity curve $I_{\text{cell}}(z)$ versus the axial position z of the imaged plane. This intensity profile was used to introduce an intensity gradient along z in the synthetic image stacks (see **d**). **d**, Artificial image stacks obtained after convolution with the characteristic PSF (from **b**), intensity fading along z (from **c**), and distortion by typical Poisson-distributed detector noise. **e**, Simulated (grey) vs. reconstructed (red) cell numbers N_{cell} . **f**, Cell displacements Δx after reconstruction. The simulated and reconstructed data was overlaid. For each cell in the simulated dataset, the distance Δx to the closest cell in the corresponding reconstructed data was calculated. 95.8% of all reconstructed cells (for all time points) were closer than one cell width (dashed line) to the theoretical coordinates. Per time point, 95% of all cells deviated less than indicated by the solid red curve. **g**, Differences in cellular orientation (expressed as angle between the major axis of a cell in the simulated dataset and the major axis of the nearest cell in the reconstructed data $\Delta\alpha$). Per time point, 95% of all cells showed a difference in orientation smaller than indicated by the solid red curve. **h**, Spatially resolved distribution of the internal biofilm order of the simulated (top) and reconstructed (bottom) data.

Detailed Characterization of Biofilm Architecture

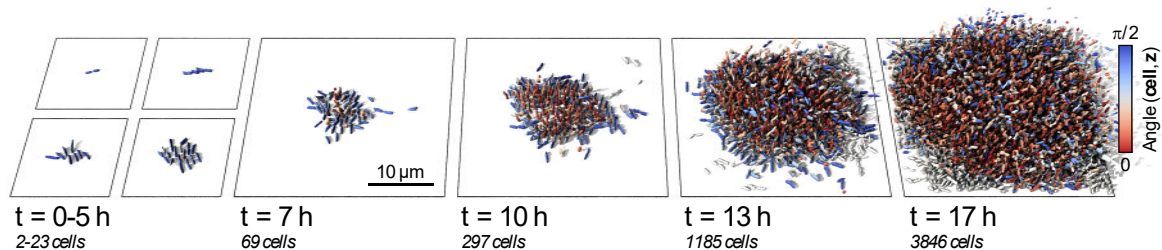
WT biofilm structure.* Following the growth dynamics of the WT* in an unperturbed low-flow environment, we found strong structural differences between the outer biofilm layer and the central part, and several distinct structural phases of the biofilm during growth (Fig. 2.1e). For each time point we characterized the biofilm spatially with respect to order, density, alignment, and growth to obtain a quantitative description of the WT* phenotype and standard deviations of the properties (Supplementary Fig. 2.3). Small biofilms of less than 50 cells were generally characterized by a relatively high order, and a low vertical alignment, indicating 2D growth. Then, a transition to three-dimensional growth occurred as indicated by an increasing vertical alignment. Generally, order and cell-cell spacing increased with distance from the biofilm centre for all biofilm sizes. The order at the centre of the biofilm decreased as the cell number increased up to biofilms with more than 1,000 cells, when the order in the centre increased again in agreement with previous structural analyses¹. This increase in order coincided with a local decrease in cell-cell spacing and a strong local increase in vertical cellular alignment. The radial alignment was higher at the outer parts of small- to medium-sized biofilms and decreased as the biofilms expanded. Surprisingly, the local growth rate, as measured by cell tracking, was constant in space and time, indicating that growth inside the observed biofilms was not limited by diffusion constraints of nutrients in our conditions.



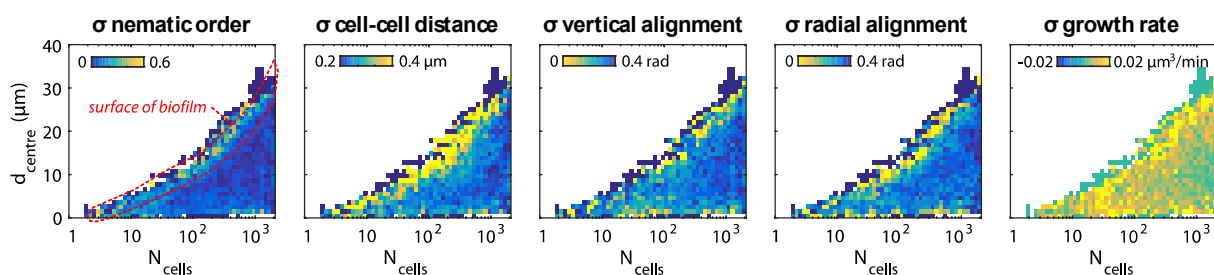
Supplementary Figure 2.5. Standard deviations of WT*-data shown in Fig. 2.1e for $n = 4$ (characterization of WT* biofilm architecture in an unperturbed low-flow environment).

$\Delta rbmA$ biofilm structure. We internally perturbed our model system by varying the strength of the attractive interaction. This was achieved by modifying the extracellular RbmA levels with an arabinose-inducible promotor (strain KDV1082, with genotype $\Delta rbmA$, $P_{BAD-rbmA}$). Biofilms lacking RbmA were more fragile and displayed an increased cell-cell spacing and increased order, in agreement with previous studies (Supplementary Fig. 2.3, Fig. 2.1f)^{1,7}. In comparison to the WT*, the order and vertical alignment inside the biofilm centre was higher, except in the bottom-most layer, where cells were on average oriented parallel to the surface (Fig. 2.1f). In summary, $\Delta rbmA$ mutant biofilms can be

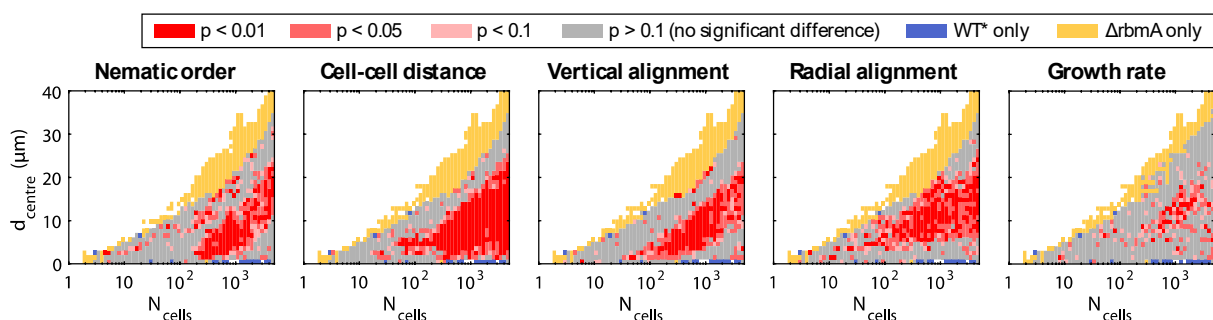
partitioned into three parts: the highly ordered core (i) is surrounded by a $\sim 5\mu\text{m}$ thick, disordered shell (ii), followed by the top outer layer (iii), which again has a slightly higher order. Cells inside the highly ordered core showed strong vertical alignment, whereas in the disordered shell and in the outer layer the vertical alignment was lost. The average cell-cell spacing was more than 30% higher than the WT*. Standard deviations of the properties in Fig. 2.1f are shown in Supplementary Fig. 2.3.



Supplementary Figure 2.6. Time-resolved biofilm growth series of the ΔrbmA -mutant in a low-flow environment. Each cell is coloured according to the cellular alignment with the z-axis pointing away from the substrate plane.

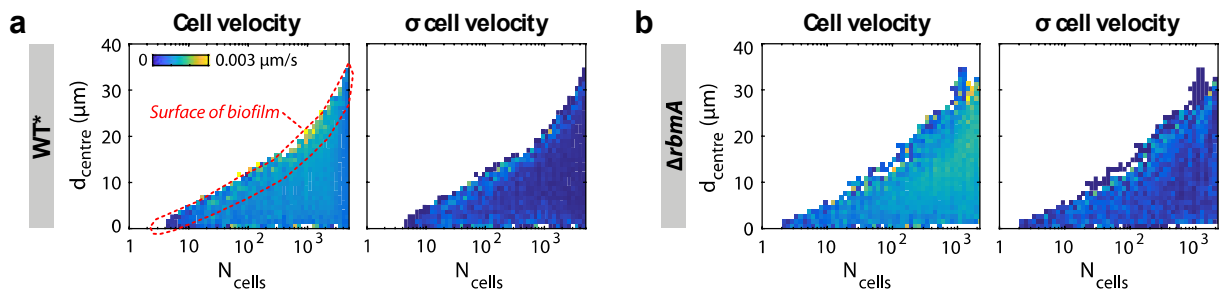


Supplementary Figure 2.7. Standard deviations of ΔrbmA -data shown in Fig. 2.1f for $n = 4$ (characterization of ΔrbmA -mutant biofilm architecture in a low-flow environment).



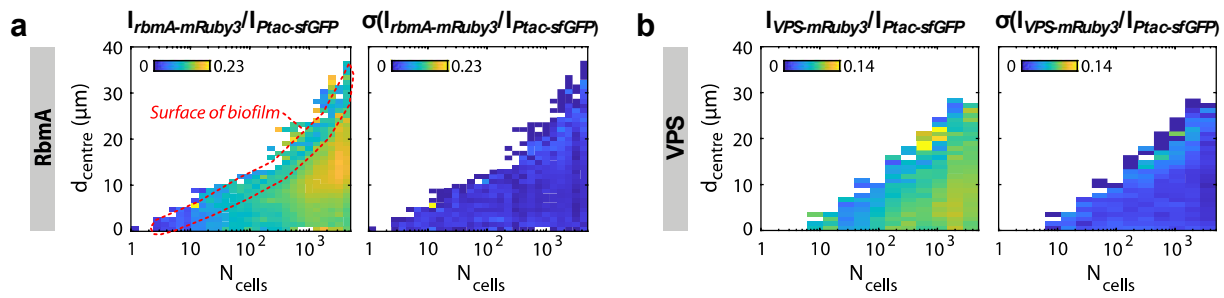
Supplementary Figure 2.8. Spatiotemporal differences between WT* and ΔrbmA biofilm architecture in a low-flow environment in relation to Fig. 2.1e,f. The data was compared using a two-tailed t-test, yielding p-values.

Cell motility inside biofilms. *V. cholerae* cells in rugose biofilms do not display flagellar or type IV pili mediated motility due to high levels of c-di-GMP^{8–10}, which represses expression of flagella and type IV pili. Twitching motility based on type IV pili has also never been observed for *V. cholerae*¹¹. As shown in Supplementary Fig. 2.3, the individual cell speed inside WT* and $\Delta rbmA$ biofilms is on the order of nm/s, i.e. much lower than flagella driven motility ($\sim 50 \mu\text{m/s}$)¹¹ or pilus-based motility ($\sim 1 \mu\text{m/s}$)¹², and increases slightly with increasing biofilm sizes. These data indicate that cell movement in *V. cholerae* biofilms is dominated by passive cell displacement due to biofilm expansion rather than active cell motility.



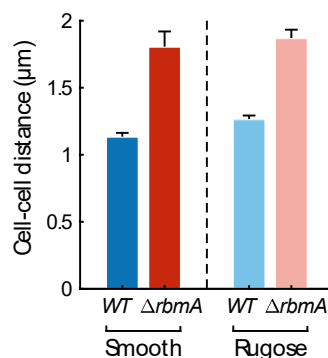
Supplementary Figure 2.9. Cell motility inside WT* and $\Delta rbmA$ biofilms in a low-flow environment. a, Average centroid velocity after linking cells in successive image stacks by cell tracking, and corresponding standard deviation for the WT* (n = 4). **b,** Corresponding data for the of $\Delta rbmA$ mutant (n = 4).

Spatiotemporal expression of rbmA and VPS in WT biofilms.* The *V. cholerae* rugose strain N16961, which was used during this study, is known to continuously produce extracellular matrix, including RbMA, even if the biofilms are small, due to this strain's intrinsically high c-di-GMP levels¹³. The expression of *rbmA* and VPS in an unperturbed low-flow environment were determined in the WT* (strain KDV1027 and KDV1218) using transcriptional fusions of *mRuby3* to the *rbmA* promoter or to the *vpsL* promoter, respectively. To measure *rbmA* and VPS expression in biofilms, the ratio of the background-subtracted *rbmA*-*mRuby3* fluorescence and VPS-*mRuby3* fluorescence, respectively, were divided by the background-subtracted signal of the constitutively expressed sfGFP, per cell (see Supplementary Fig. 2.2).



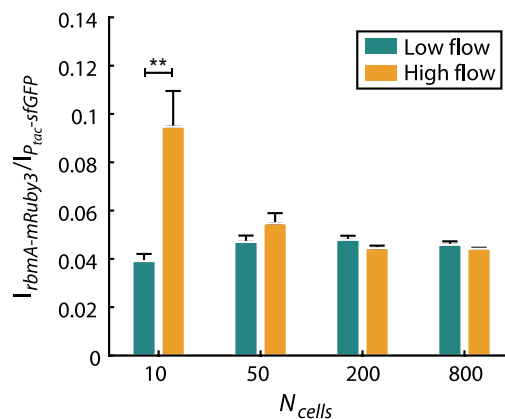
Supplementary Figure 2.10. Spatio-temporal expression of *rbmA* and VPS in the WT* strain in a low-flow environment. **a**, Expression of *rbmA* (left: mean values, right: standard deviation, $n = 3$ biofilms). In each cell the fluorescence of *rbmA-mRuby3* was normalized by the signal of the constitutive *Ptac*-promoter-driven sfGFP-fluorescence signal. **b**, Expression of VPS (left: mean values, right: standard deviation, $n = 6$ biofilms). In each cell the fluorescence of VPS-*mRuby3* was normalized by the signal of the constitutive *Ptac*-promoter-driven sfGFP fluorescence signal.

Effect of Vibrio polysaccharide (VPS) on cell-cell interaction. To test whether VPS can contribute to cell-cell attraction, we compared the average cell-cell spacing in biofilms of cells with normal VPS production (smooth colony phenotype, $\Delta rbmA$, KDV383) with a VPS overproduction strain (rugose colony phenotype, $\Delta rbmA$, KDV692). Transcriptome comparisons of smooth and rugose strains indicate strong induction of VPS production in the rugose strain¹⁰. Comparing the smooth WT and the smooth $\Delta rbmA$ mutant (or the rugose WT and the rugose $\Delta rbmA$ mutant), we observe an increase in cell-cell spacing due to lack of RbmA. Comparing the cell-cell spacing for the smooth $\Delta rbmA$ and rugose $\Delta rbmA$ (VPS overproduction) strains, we find a similar cell-cell spacing (Supplementary Fig. 2.2, red bars), indicating that increased VPS production does not mediate an increased cell-cell attraction. In addition, data for the smooth and Rugose WT (KDV103, and, KDV615, respectively) show that enhanced VPS production even slightly increases the cell-cell spacing (Supplementary Fig. 2.2, blue bars). Increased VPS production therefore does not increase cell-cell attraction.



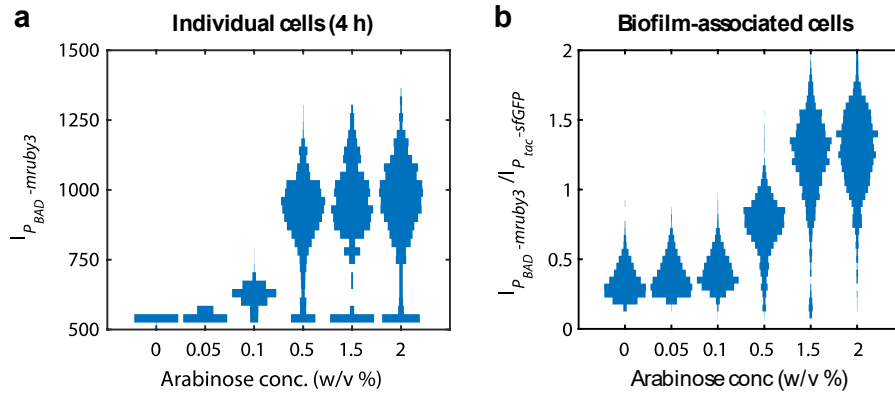
Supplementary Figure 2.11. Effect of VPS overproduction on cell spacing in a low-flow environment. The “cell-cell distance” measurement refers to the average cell centroid-centroid distance. Rugose variants produce more VPS compared with smooth strains¹⁰. Enhanced VPS production does not lead to a decreased cell-cell spacing, indicating that enhanced VPS production is not causing an increased cell-cell attraction.

*Expression of *rbmA* at low vs. high shear rates.* The expression of *rbmA* at low shear rate ($\dot{\gamma} = 2 \text{ s}^{-1}$) and high shear rate ($\dot{\gamma} = 2000 \text{ s}^{-1}$) was measured in the WT* strain (KDV1027) by calculating the ratio of the background-subtracted fluorescence of the *rbmA*-mRuby3 transcriptional reporter, divided by the background-subtracted signal of the constitutively expressed sfGFP, per cell (see Supplementary Fig. 2.2). Individual cell measurements were averaged per time point and biofilm. Cells in biofilms growing at high shear rates were found to express *rbmA* at higher levels than those in low shear rates, for small biofilms of 10-50 cells, when all cells experience an increased level of shear and there is little deflection of the flow by cells and matrix on the biofilm surface.



Supplementary Figure 2.12. Shear rate-dependent expression of *rbmA* for different biofilm sizes. In each cell the fluorescence intensity signal of the *rbmA*-mRuby3 transcriptional reporter was normalized by the signal of the constitutive *P_{tac}*-promoter-driven sfGFP fluorescence signal. Error bars correspond to the standard error ($n = 6$). Statistical significance: ** is $p < 0.01$ (Mann–Whitney–Wilcoxon test).

*Calibration of arabinose-induced expression of *rbmA*.* The expression of *rbmA* (and therefore cell-cell attraction strength) was controlled by the arabinose-inducible promoter *P_{BAD}* which was reported to be bi-stable for cells in liquid culture^{14,15}. However, for using this expression system for our purposes inside biofilms, a homogenous expression pattern is required. Therefore, we analyzed the expression pattern of *P_{BAD}*-*mRuby3* among individual cells (KDV1228) after 4 h of arabinose-induction (see Methods section in the main manuscript) in (a) shaken liquid cultures of individual cells, and (b) biofilm-associated cells (KDV1231) inside biofilms (300-500 cells) for different levels of arabinose (Supplementary Fig. 2.2). Bi-stable expression of *P_{BAD}* appears to be a characteristic behavior of individual cells in liquid culture, but not of biofilm-associated cells, as only few cells were found to be non-responsive to arabinose in biofilms (Supplementary Fig. 2.2).



Supplementary Figure 2.13. Stability of the expression of the arabinose-inducible promoter P_{BAD} . **a**, Bi-stable expression of P_{BAD} inside individual cells in shaken liquid culture, 4 h after inoculation. **b**, In contrast, a homogenous expression of P_{BAD} is observed for biofilm-associated cells. Data is shown as “violin plot” distributions.

Individual Cell-Based Simulations

Model description and implementation. The cells are modelled as interacting ellipsoids of half-length ℓ and half-width r , described by their position x and orientation \hat{n} . Owing to the fact that cells live at low Reynolds number ($Re \approx 10^{-4}$), we approximate the dynamics as over-damped, ignoring any inertial effects. Cells can interact with the wall boundary and other cells through interaction potential functions, U_{bdy} and V . Denoting the identity matrix by \mathbf{I} , the over-damped translational and orientation dynamics for a single cell are

$$\frac{dx}{dt} = \mathbf{\Gamma}^{-1} \left[-\frac{\partial U_{bdy}}{\partial x} - \frac{\partial V}{\partial x} \right] \quad (5)$$

$$\frac{d\hat{n}}{dt} = (\mathbf{I} - \hat{n}\hat{n}^T) \left[\mathbf{\Omega}^{-1} \left(-\frac{\partial U_{bdy}}{\partial \hat{n}} - \frac{\partial V}{\partial \hat{n}} \right) \right] \quad (6)$$

where $\mathbf{\Gamma}$ and $\mathbf{\Omega}$ are

$$\mathbf{\Gamma} = \gamma_m [\gamma_{\parallel} (\hat{n}\hat{n}^T) + \gamma_{\perp} (\mathbf{I} - \hat{n}\hat{n}^T)] \quad (7)$$

$$\mathbf{\Omega} = \omega_m \omega_R \mathbf{I} \quad (8)$$

Here, γ_m and ω_m are the typical translational and rotational drag coefficients for Stokes' drag in the extracellular matrix for a spheroid ($\gamma_m = 6\pi\mu_m r$, $\omega_m = 8\pi\mu_m r^3$). Surface adhesion of the cells is captured by increasing the magnitude of the friction tensor Γ by a factor of 30 if the cells are within $1.5 \cdot r$ of the surface. γ_{\parallel} , γ_{\perp} and ω_R are dimensionless geometric parameters characterizing the longitudinal and transverse friction parameters that depend only on the aspect ratio $a = \ell/r$ of the cell, as given by Han et al.¹⁶:

$$\gamma_{\parallel} = \frac{8/3}{\frac{2a}{1-a^2} + \frac{2a^2-1}{(a^2-1)^{3/2}} \ln\left(\frac{a+\sqrt{a^2-1}}{a-\sqrt{a^2-1}}\right)} \quad (9)$$

$$\gamma_{\perp} = \frac{8/3}{\frac{a}{a^2-1} + \frac{2a^2-3}{(a^2-1)^{3/2}} \ln(a+\sqrt{a^2-1})} \quad (10)$$

$$\omega_R = \frac{2}{3} \frac{a^4-1}{a \left(\frac{2a^2-1}{(a^2-1)^{3/2}} \ln(a+\sqrt{a^2-1}) - a \right)}, \quad (11)$$

$$\omega_m = 8\pi\mu_m r^3 a$$

An important property of our proposed orientation dynamics is that $\hat{\mathbf{n}} \cdot d\hat{\mathbf{n}}/dt = 0$, such that the unit length of $\hat{\mathbf{n}}$ is conserved.

The interaction between a cell and the wall boundary is modelled with a repulsive interaction potential, U_{bdy} , that is proportional to the overlap between a cell and the wall boundary. The wall boundary is represented as a plane. To determine this overlap, an overlap coordinate, z_o , is introduced such that $z_o < 0$ implies no contact with the boundary and $z_o > 0$ implies contact with the boundary. The overlap coordinate is defined as

$$z_o = \ell |\hat{\mathbf{n}} \cdot \hat{\mathbf{N}}| + r - \hat{\mathbf{N}} \cdot (\mathbf{x} - \mathbf{S}) \quad (12)$$

where $\hat{\mathbf{N}}$ is the unit normal of the plane and \mathbf{S} is a point on the plane. In the simulations, we set $\hat{\mathbf{N}} = [0, 0, 1]$ and $\mathbf{S} = [0, 0, 0]$ such that the wall is an xy plane located at the origin. Thus, repulsion from the wall can be represented by

$$U_{bdy} = \begin{cases} 0 & \text{if } z_o < 0 \\ \epsilon_{bdy} \exp\left(\frac{z_o}{\sigma_{bdy}}\right) & \text{if } z_o > 0 \end{cases} \quad (13)$$

ϵ_{bdy} captures the magnitude of the cell-boundary interaction, and σ_{bdy} is a scale factor of order of the half-width of the cell.

V is the total potential of a single cell α for all the N pairwise cell-cell interactions between cell α and cell β ($V = \sum_{\beta=1, \beta \neq \alpha}^N U$). The interaction between cell α and cell β is governed by the cell-cell interaction potential introduced in the section ‘‘Cell-cell interaction potential’’.

The instantaneous cell length growth rate for a single cell is

$$\frac{d\ell}{dt} = \frac{\ell}{\tau_g} \ln(2) \quad (14)$$

where ℓ is the half-length of the cell at time t and τ_g is the growth time constant (obtained by experimental measurements). The cell width is constant throughout the simulation. Following the Adder model described by Taheri-Araghi et al.¹⁷, the length added between birth and division (ℓ_{add}) is constant for each cell. Thus, the cells divide when they grow an additional ℓ_{add} from their birth length. At division, a random number M is drawn from a normal distribution with mean 0.5 and standard deviation $\sigma_{birth\ size}$. Suppose ℓ_p is the length of the cell before division, then the birth lengths of the daughter cells are $M\ell_p$ and $(1 - M)\ell_p$ such that the length of the parent cell is conserved. The new orientations of the daughter cells are drawn from a von Mises-Fisher distribution, with mean direction corresponding to the direction of the parent cell and concentration parameter κ .

If we use r , $\tau_t = \frac{\gamma_m r^2}{\epsilon_0}$, and ϵ_0 as characteristic length, time, and energy scales, we can recast Eq. (5), (6) and (14) in dimensionless form

$$\frac{d\mathbf{x}^*}{dt^*} = \left[\frac{1}{\gamma_{\parallel}} (\hat{\mathbf{n}}\hat{\mathbf{n}}^T) + \frac{1}{\gamma_{\perp}} (\mathbf{I} - \hat{\mathbf{n}}\hat{\mathbf{n}}^T) \right] \left[-\frac{\partial U_{bdy}^*}{\partial \mathbf{x}^*} - \frac{\partial V^*}{\partial \mathbf{x}^*} \right] \quad (15)$$

$$\frac{d\hat{\mathbf{n}}}{dt^*} = (\mathbf{I} - \hat{\mathbf{n}}\hat{\mathbf{n}}^T) \left[\frac{3}{4a\omega_R} \left(-\frac{\partial U_{bdy}^*}{\partial \hat{\mathbf{n}}} - \frac{\partial V^*}{\partial \hat{\mathbf{n}}} \right) \right] \quad (16)$$

$$\frac{d\ell^*}{dt^*} = \frac{\tau_t}{\tau_g} \ell^* \ln(2) \quad (17)$$

where superscript * indicates a dimensionless quantity and use has been made of the following definitions and ratios $\mathbf{x}^* = \mathbf{x}/r$, $\ell^* = \ell/r$, $t^* = t/\tau_t$, $V^* = V/\epsilon_0$ and $U_{bdy}^* = U_{bdy}/\epsilon_0$. Note that τ_t can be interpreted as the translational relaxation time, i.e. a time scale of how long it takes for a bacterium to reach an equilibrium configuration from the cell-cell interaction potential. If $z_o^* > 0$, the dimensionless boundary potential is $U_{bdy}^* = U_{bdy}/\epsilon_0 = \epsilon_r \exp(z_o^*/\sigma_{bdy}^*)$ where $\epsilon_r = \epsilon_{bdy}/\epsilon_0$, $z_o^* = z_o/r$, and $\sigma_{bdy}^* = \sigma_{bdy}/r$.

A custom, highly parallelized individual cell-based code employing graphics processing units (GPUs) was developed to perform the simulations. At each time step, we calculate cell-cell interactions using the all-pairs approach¹⁸ such that all pair-wise interactions are evaluated. We use a standard explicit Euler scheme to numerically integrate the dimensionless translational and orientational dynamics, Eq. (15) and (16) and growth law Eq. (17).

The key simulation parameters used for the simulations are shown in Supplementary Table 2.3.

Parameter	Value	Unit	Description
r	0.2775	μm	Average half-width of the bacteria from experimental measurements.
τ_g	6130	s	Growth time constant (average cell division time of biofilm-associated cells obtained from experiments).
μ_m	1	Pa·s	Estimate of the dynamic viscosity of EPS matrix at room temperature ¹⁹ .
γ_m	5.23	$\text{pN}\cdot\text{s}\cdot\mu\text{m}^{-1}$	Typical drag coefficient for Stokes' drag in EPS matrix ($\gamma_m = 6\pi\mu_m r$).
ϵ_r	10		Ratio comparing the strength of the bacteria-boundary interaction to the strength of the bacteria-bacteria interaction $\epsilon_r = \epsilon_{bdy}/\epsilon_0$.
σ_{bdy}^*	1		Non-dimensional boundary potential length scale parameter.
τ_t	8.05	s	Translational time scale due to repulsion in matrix (typical time needed for daughter cells in matrix to reach their equilibrium configurations due to repulsion after cell division).
l_{add}^*	3.65		Non-dimensional length added to bacteria after division.
$\sigma_{birth\ size}^*$	0.07		Non-dimensional standard deviation of the normal distribution for the daughter bacteria birth size.
κ	100		Concentration parameter for the von Mises-Fisher distribution for the daughter bacteria division orientation.
ϵ_0	$5\cdot 10^{-20}$	J	Strength of the repulsive part of the cell-cell potential.
λ_r	1.65		Width of the repulsive part of the cell-cell potential (corresponds to $1.16\ \mu\text{m}$ for typically aligned cells at $\sigma = 0.7\ \mu\text{m}$).
ν	0.13 (WT*)		Strength of the attractive part of the cell-cell potential (corresponds to $0.65\cdot 10^{-20}$ J).

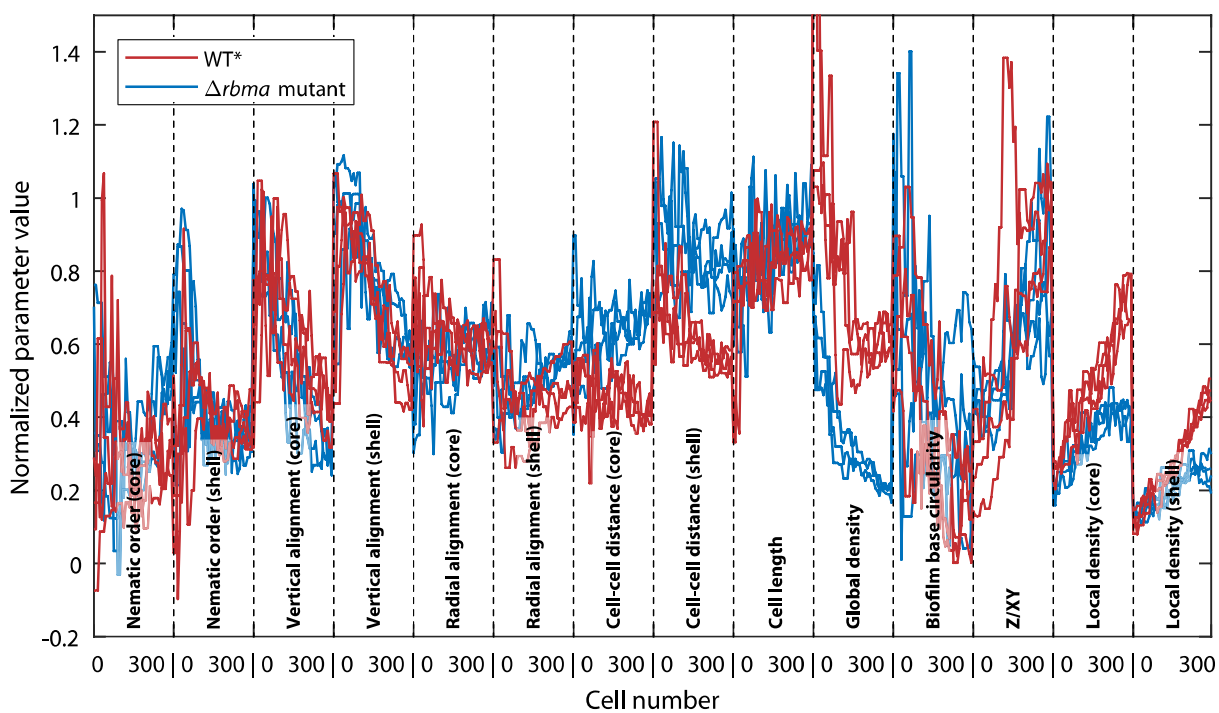
λ_a	0.16 (WT*)		Well-width of the attractive part of the cell-cell potential (corresponds to 0.11 μm for typically aligned cells at $\sigma = 0.7 \mu\text{m}$).
ρ_a	2.93 (WT*)		Position of the attractive part of the cell-cell potential (corresponds to 2.0 μm for typically aligned cells at $\sigma = 0.7 \mu\text{m}$).

Supplementary Table 2.3. Simulation parameters. All parameters are measured directly from experimental biofilms, except for the potential parameters ν , λ_a , ρ_a , ϵ_0 , λ_r , which were determined by fitting as described in the main text.

Comparing simulations with experimental data. For the purpose of comparing simulated and experimental biofilms, a set of parameters was chosen to represent the phenotype and architecture as fully and accurately as possible. These parameters include averaged single cell parameters, i.e. local order, vertical alignment, radial alignment, cell-cell distance, local density, cell length, and the following global biofilm parameters: global density, biofilm aspect ratio, and biofilm base circularity (see section on “Biofilm features”). The single cell parameters were determined for the biofilm core ($d_{\text{centre}} < \max(d_{\text{centre}})/2$) and the biofilm shell ($\max(d_{\text{centre}})/2 < d_{\text{centre}} < \max(d_{\text{centre}})$). The time-evolution of these parameters was compared for biofilms of cell numbers ranging from 10 to 300. To account for logarithmic growth, biofilms were sampled at 40 intermediate logarithmically spaced cell numbers yielding a characteristic biofilm feature vector shown in Supplementary Fig. 2.2. In addition, each parameter was normalized to a typical range as indicated in Supplementary Table 2.4. These feature vectors therefore capture biofilm architectural properties (via the different architectural parameters), as well as the temporal biofilm development (via the measurement of these parameters at different cell numbers). The similarity between a vector characterizing a simulation and an experimental biofilm was assessed in terms of the mean square distance (MSD) between the two feature vectors. The different parameters were weighted differently to account for their relative importance in representing biofilm phenotypes, as summarized in Supplementary Table 2.4.

Parameter	Normalization range [min max]	Weight
local order	0 – 0.8	10
vertical alignment	0.2 – 1.37	10
radial alignment	0.2 – 1.37	3
cell-cell distance	0.8 – 2	20
local density	0 – 0.2	10
cell length	1 – 3	1
global density	0 – 0.15	5
biofilm aspect ratio	0 – 0.8	1
biofilm base circularity	0 – 0.8	1

Supplementary Table 2.4 . Biofilm parameters and corresponding normalization ranges and weights.

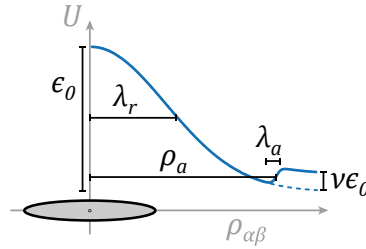


Supplementary Figure 2.14. Characteristic biofilm feature vector for several biofilms of the WT* (red) and the ΔrbmA-mutant (blue). The parameters correspond to the ones listed in Supplementary Table 2.4.

Cell-cell interaction potential. In our model, cells are subject to forces by neighbouring cells due to purely mechanical effects, including steric repulsion and the repulsion mediated by the effective osmotic pressure in the intercellular space, as well as the interaction with secreted matrix components (such as RbmA). While steric interactions and the osmotic pressure in the intercellular space are expected to result in net repulsive forces, RbmA is thought to directly link the cells together, thereby causing net cell-cell attraction^{20,21}, which we quantitatively confirmed (Fig. 2.2a). To account for these effects we suggest the cell-cell interaction potential between two particular cells, cell α and cell β , described by equation (18).

$$U = \epsilon_0 \cdot \epsilon_1 \left(e^{-\frac{\rho^2}{\lambda_r^2}} + \frac{v}{1 + e^{\left(\frac{\rho_a - \rho}{\lambda_a}\right)}} \right) \quad (18)$$

The first term in the interaction potential corresponds to cell-cell repulsion, and the second term corresponds to cell-cell attraction. The vector $\mathbf{r}_{\alpha\beta} = r_{\alpha\beta} \hat{\mathbf{r}}_{\alpha\beta}$ joins the cell centres and is directed from cell α to cell β , ϵ_0 describes the energy of the cell-cell interaction, ϵ_1 is a strength parameter accounting for the cell orientation configuration, $\rho = r_{\alpha\beta}/\sigma$ is the cell-cell distance normalized by the overlap shape-factor σ , λ_r is the repulsion width, v is the attraction strength, ρ_a is the attraction shift and λ_a is the attraction width, as summarized in Supplementary Table 2.3 and Supplementary Fig. 2.2.



Supplementary Figure 2.15. Effects of the cell-cell interaction potential parameters. ϵ_0 : Strength of repulsion due to combined effects of steric and matrix repulsion. λ_r : Range of repulsion in cell diameters. v : Relative strength of RbmA-mediated attraction. λ_a : Effective attractive range of RbmA in cell diameters. ρ_a : Effective distance of the attractive potential well.

The above strength and range parameters lead to different length scales of the cell-cell interaction forces depending on the orientation of the cells (see Fig. 2.2b,c, Supplementary Fig. 2.2, and Supplementary Fig. 2.2, respectively). The generalized forms of the strength and range parameters for non-identical ellipsoids are given by Cleaver et al.²² and are reproduced below for convenience

$$\epsilon_1 = \left[1 - \chi^2 (\hat{\mathbf{n}}_\alpha \cdot \hat{\mathbf{n}}_\beta)^2 \right]^{-1/2} \quad (19)$$

$$\sigma = \sigma_0 \left[1 - \chi \left(\frac{\xi(\hat{\mathbf{n}}_\alpha \cdot \hat{\mathbf{r}}_{\alpha\beta})^2 + \xi^{-1}(\hat{\mathbf{n}}_\beta \cdot \hat{\mathbf{r}}_{\alpha\beta})^2 - 2\chi(\hat{\mathbf{n}}_\alpha \cdot \hat{\mathbf{r}}_{\alpha\beta})(\hat{\mathbf{n}}_\beta \cdot \hat{\mathbf{r}}_{\alpha\beta})(\hat{\mathbf{n}}_\alpha \cdot \hat{\mathbf{n}}_\beta)}{1 - \chi^2(\hat{\mathbf{n}}_\alpha \cdot \hat{\mathbf{n}}_\beta)^2} \right) \right]^{-1/2} \quad (20)$$

where

$$\sigma_0 = \sqrt{r_\alpha^2 + r_\beta^2}, \quad (21)$$

$$\chi = \left[\frac{(\ell_\alpha^2 - r_\alpha^2)(\ell_\beta^2 - r_\beta^2)}{(\ell_\alpha^2 + r_\alpha^2)(\ell_\beta^2 + r_\beta^2)} \right]^{1/2}, \quad (22)$$

and

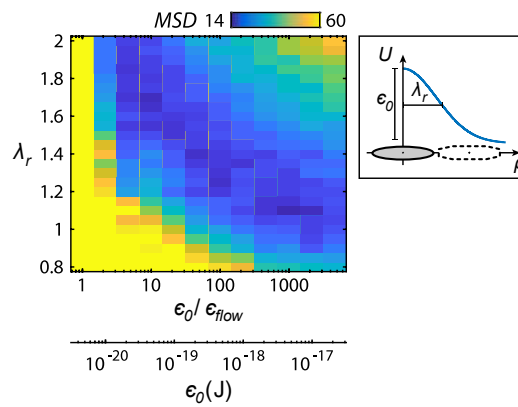
$$\xi = \left[\frac{(\ell_\alpha^2 - r_\alpha^2)(\ell_\beta^2 + r_\alpha^2)}{(\ell_\beta^2 - r_\beta^2)(\ell_\alpha^2 + r_\beta^2)} \right]^{1/2}. \quad (23)$$

For two ellipsoids α and β , $\hat{\mathbf{n}}_\alpha$, $\hat{\mathbf{n}}_\beta$ are their axial unit vectors, ℓ_α , ℓ_β are their half lengths, and r_α , r_β are their half widths.

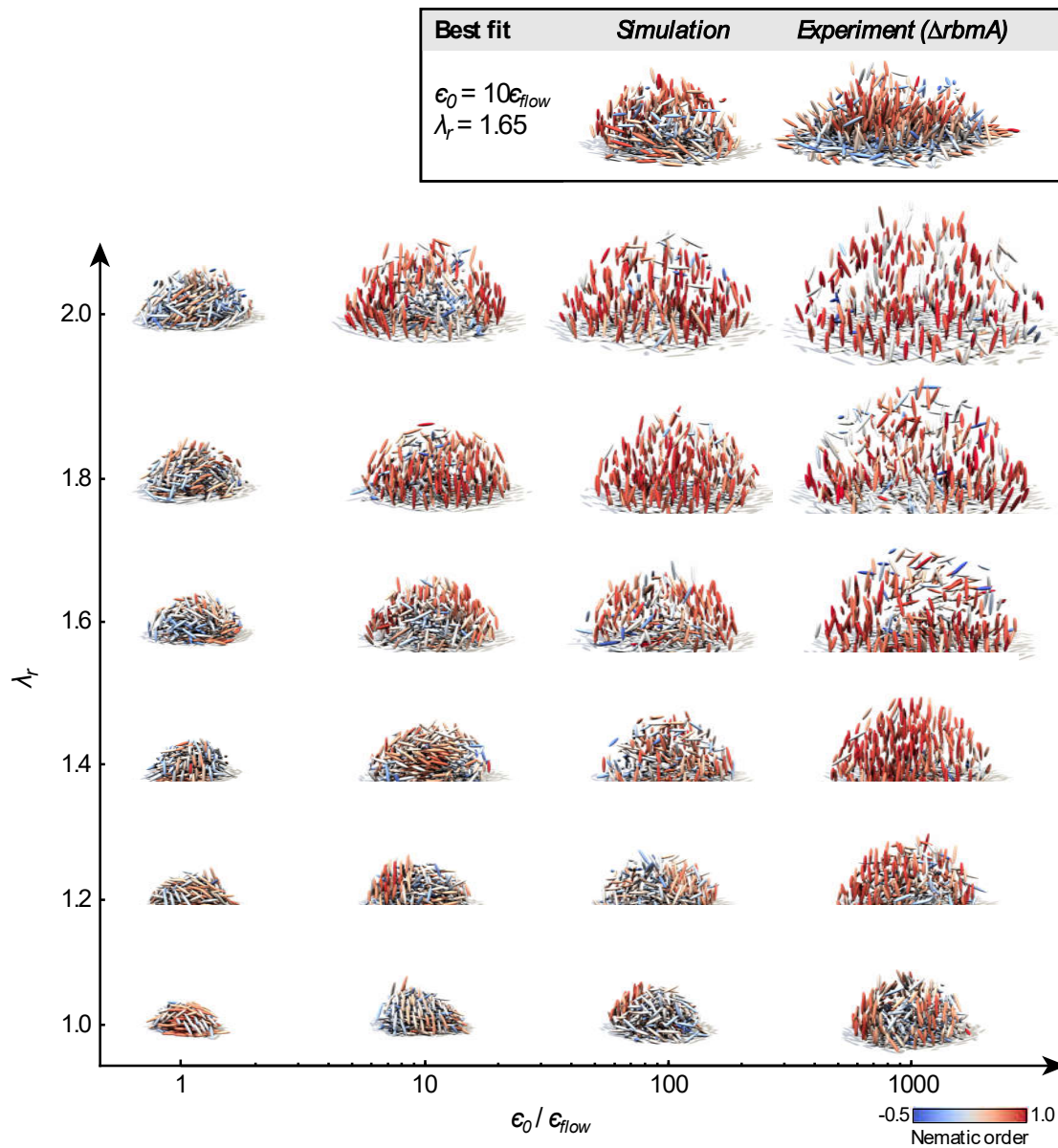
Influence of cell-cell repulsion on biofilm architecture

Biofilms grown from $\Delta rbmA$ cells, which lack RbmA proteins, were simulated by setting the strength of the attractive part of the cell-cell potential to zero ($v = 0$), as cell-cell attraction is primarily due to the levels of RbmA. Before computing systematic parameter scans for obtaining the repulsion-parameters ϵ_0 and λ_r of the interaction potential U , we estimated the parameters using the physical considerations: The energy scale of the cell-cell interactions was estimated to be within several orders of magnitude of the energy scale of interactions between the cells and the flow. Therefore, we simulated biofilms for values of ϵ_0 ranging from $10^0 \cdot \epsilon_{\text{flow}}$ to $10^4 \cdot \epsilon_{\text{flow}}$, where the cell-flow interaction energy $\epsilon_{\text{flow}} = 0.005 \text{ pN} \cdot \mu\text{m}$ was calculated by considering Stokes flow (with flow rate $0.1 \mu\text{L}/\text{min}$ in a channel with the dimensions used in the experiment) past a sphere with the typical cell volume of $0.4 \mu\text{m}^3$, being locating $2.4 \mu\text{m}$ above a no-slip boundary (as is typical for cells in the outer shells of biofilms). A typical cell-cell distance in the core of biofilms, where cell-cell repulsion dominates, is around $1 \mu\text{m}$, which corresponds to $\lambda_r = 1.4$ (for a typical overlap shape-factor of $\sigma = 0.7 \mu\text{m}$, which is

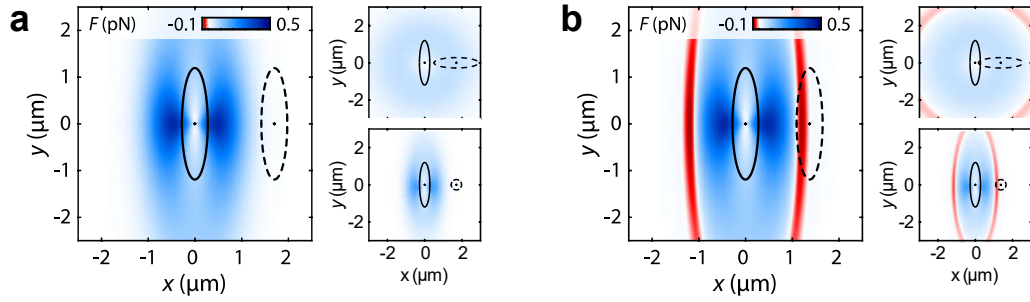
the value it would take for a sphere with the typical mean cell volume of $0.4 \mu\text{m}^3$). Therefore, we used values of λ_r from 0.8 to 2. The resulting MSD values upon a systematic variation of the cell-cell interaction energy ϵ_0 and repulsion width λ_r are visualized in Supplementary Fig. 2.2. Corresponding biofilm architecture phenotypes are shown in Supplementary Fig. 2.2. The identified parameters for the best fit between simulations and the experimentally observed $\Delta rbmA$ -phenotype are $\epsilon_0 = 10 \cdot \epsilon_{\text{flow}}$ ($5 \cdot 10^{-20}$ J) and $\lambda_r = 1.65$. The resulting translational and rotational forces are visualized in Fig. 2.2b, Supplementary Fig. 2.2a, and Supplementary Fig. 2.2a, respectively.



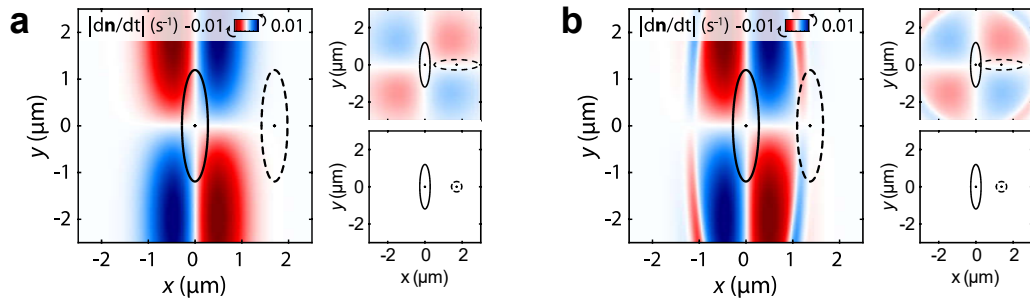
Supplementary Figure 2.16. Parameter screen to test the influence of cell-cell repulsion on biofilm architecture phenotype. Mean MSD values between feature vectors of $\Delta rbmA$ mutant biofilm simulations and experiments (see section on “Comparing simulations with experimental data”) upon variation of cell-cell interaction strength ϵ_0 and repulsion range λ_r . Inset: effect of parameter variation on the cell-cell interaction potential.



Supplementary Figure 2.17. Resulting simulated biofilms for different levels of cell-cell repulsion. The figure shows a subset of biofilm renderings corresponding to a range of different values for ϵ_0 and λ_r (cf. Fig. 2.2b and Supplementary Fig. 2.2). The colour of each cell corresponds to the nematic order.



Supplementary Figure 2.18. Translational cell-cell interaction forces. **a**, Translational forces for $\epsilon_0 = 10 \cdot \epsilon_{\text{flow}}$ ($5 \cdot 10^{-20}$ J), $\lambda_r = 1.65$, and $v = 0$ (corresponding to the $\Delta rbmA$ -mutant, cf. Fig. 2.2b) for different orientations. **b**, Translational forces for $\epsilon_0 = 10 \cdot \epsilon_{\text{flow}}$ ($5 \cdot 10^{-20}$ J), $\lambda_r = 1.65$, $v = 0.127$, $\lambda_a = 0.164$, and $\rho_a = 2.93$ (corresponding to an arabinose concentration of 0.5%, cf. Fig. 2.2c) for different orientations.



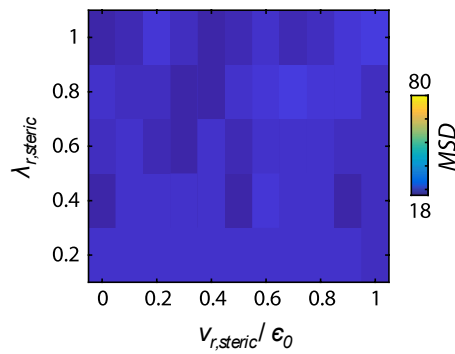
Supplementary Figure 2.19. Rotational cell-cell interaction dynamics. $|dn/dt| = |(I - \hat{n}_\beta \hat{n}_\beta)(-\Omega^{-1} \partial U / \partial \hat{n}_\beta)|$ acting on two neighbouring cells. **a**, Rotational dynamics for $\epsilon_0 = 10 \cdot \epsilon_{\text{flow}}$ ($5 \cdot 10^{-20}$ J), $\lambda_r = 1.65$, and $v = 0$ (corresponding to the $\Delta rbmA$ -mutant, cf. Fig. 2.2b) for different orientations. **b**, Rotational dynamics for $\epsilon_0 = 10 \cdot \epsilon_{\text{flow}}$ ($5 \cdot 10^{-20}$ J), $\lambda_r = 1.65$, $v = 0.127$, $\lambda_a = 0.164$, and $\rho_a = 2.93$ (corresponding to an arabinose concentration of 0.5%, cf. Fig. 2.2c) for different orientations. A positive speed (indicated in red) results in a clockwise rotation.

Influence of steric and osmotic pressure-mediated cell-cell repulsion on biofilm phenotype

The joint effects of steric cell-cell repulsion and osmotic pressure-mediated cell-cell repulsion were modelled with a relatively soft Gaussian function, cf. Eq. (18). To test if this model is appropriate, we performed the following analysis: To check the effect of both contributions to cell-cell repulsion separately, we embedded a second, short-ranged and very strongly repulsive part, representing steric repulsion, into the existing potential by adding another Gaussian function peaked at $p = 0$ characterized by v_{steric} and $\lambda_{r,\text{steric}} < \lambda_r$, see Eq. (24). Here, ϵ_0 and λ_r are fixed to the optimal values obtained by comparison with the experimental values for the $\Delta rbmA$ -mutant.

$$U = \epsilon_0 \cdot \epsilon_1 \left(e^{-\frac{\rho^2}{\lambda_r^2}} + v_{steric} \cdot e^{-\frac{\rho^2}{\lambda_{r,steric}^2}} + \frac{v}{1 + e^{\left(\frac{\rho_a - \rho}{\lambda_a}\right)}} \right) \quad (24)$$

The exploration of the parameter space is shown in Supplementary Fig. 2.20. The additional term for hard-steric repulsion in Eq. (24) does not have any influence on the biofilm phenotype as the MSD values show no variance irrespective of interaction strength v_{steric} and range $\lambda_{r,steric}$. This justifies modelling the effects of hard steric and soft osmotic pressure-mediated repulsion in a combined manner, as cells are unlikely to interact exclusively via hard and very short-ranged steric repulsion (the matrix prevents them from getting close enough together).



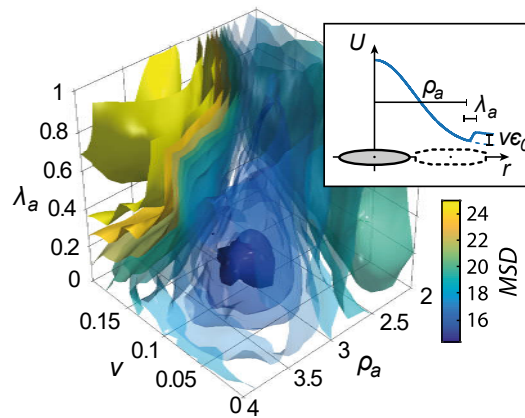
Supplementary Figure 2.20. Parameter screen to test the influence of hard steric cell-cell repulsion on biofilm phenotype. The figure shows MSD values upon variation of v_{steric} and $\lambda_{r,steric}$. Owing to its longer length scale, soft, osmotic pressure-mediated repulsion prevents cells from getting close enough to interact directly through hard steric repulsion.

Influence of RbmA-mediated cell-cell attraction on biofilm phenotype

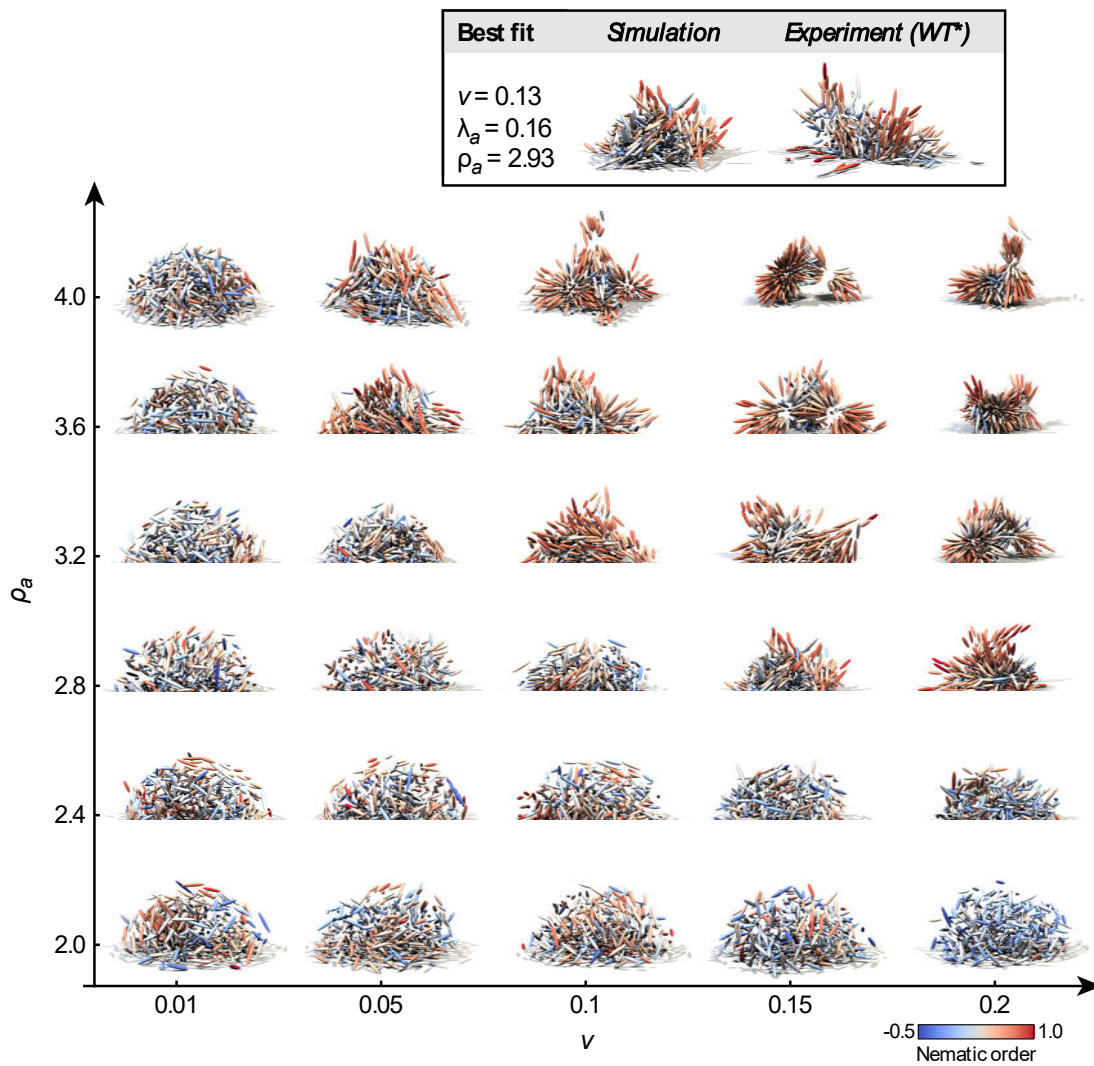
The attractive part in the cell-cell potential is thought to be governed by RbmA. Having fixed the cell-cell repulsion parameters ϵ_0 and λ_r for the $\Delta rbmA$ phenotype, the remaining parameters influencing cell-cell attraction (namely v , ρ_a , and λ_a) were determined by finding the best fits when comparing the simulations with biofilms of different RbmA concentrations (by varying the expression of the *rbmA* gene using the arabinose-inducible P_{BAD} promoter). Prior to systematic parameter scans with simulations, we estimated the parameters using the following considerations: The attraction shift ρ_a was estimated for each arabinose concentration by considering the typical cell-cell distance at the edge of biofilms, where attraction dominates. These estimates suggested using values of ρ_a between 2 and 4 (again using $\sigma = 0.7 \mu\text{m}$). The attraction width λ_a was estimated by considering the standard deviation of cell-cell

distances near the edge of biofilms, which was found to be approximately $0.3 \mu\text{m}$ for all biofilms; therefore, we expected λ_a to be around 0.4 (again using $\sigma = 0.7 \mu\text{m}$).

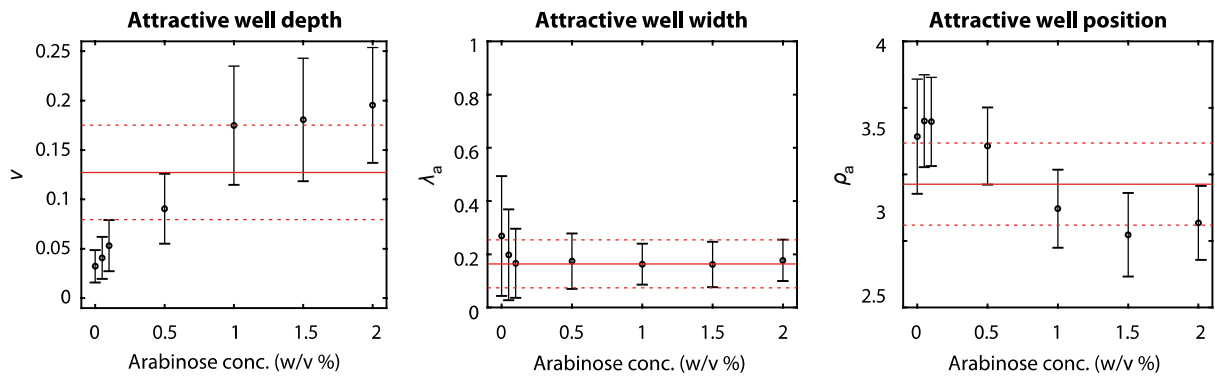
The resulting MSD values resulting from simulations conducted with a systematic variation of v , λ_a and ρ_a are shown in Supplementary Fig. 2.2. The resulting translational and rotational forces for selected conditions are visualized in Fig. 2.2c, Supplementary Fig. 2.2b, and Supplementary Fig. 2.2b, respectively. Corresponding biofilm phenotypes are shown in Supplementary Fig. 2.2. The 5% best matching simulations (5% lowest MSD values) for a given condition were chosen and the mean of the corresponding values for v , λ_a and ρ_a was defined as the best fit. In Supplementary Fig. 2.2 the obtained mean values \pm standard deviation are displayed. The best-fit parameters for the experimentally observed WT*-phenotype were $v = 0.13$, $\lambda_a = 0.16$ and $\rho_a = 2.93$.



Supplementary Figure 2.21. Parameter screen to test the influence of RbmA-mediated cell-cell attraction on biofilm phenotype. MSD values for feature vectors of biofilms with arabinose-inducible *rbmA* expression grown at 0.5% arabinose (w/v) and simulations (see section “Comparing simulations with experimental data) upon variation of cell-cell interaction strength v , and well width λ_a and well position ρ_a . Inset: effect of parameter variation on the cell-cell interaction potential.

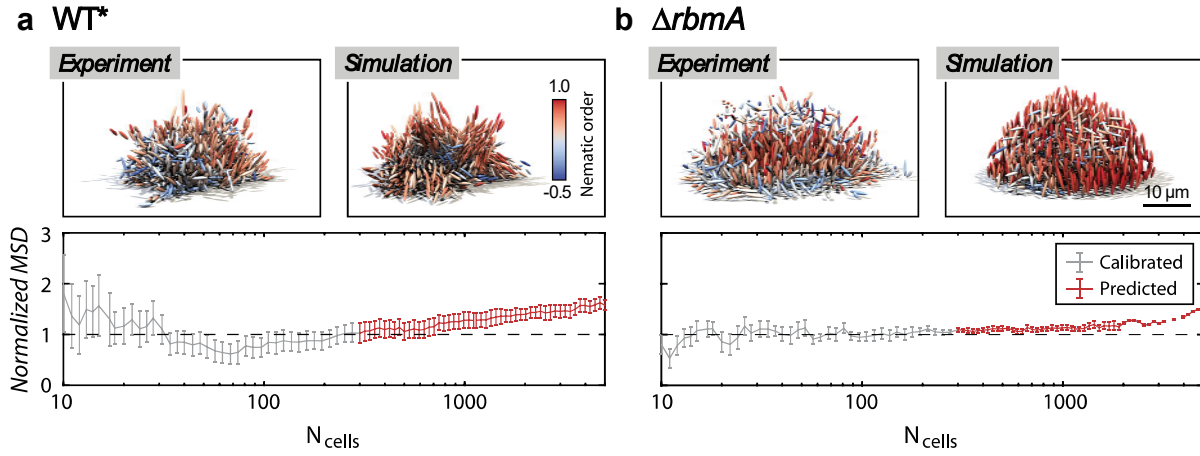


Supplementary Figure 2.22. Resulting simulated biofilms for different levels of RbmA-mediated cell-cell attraction. The figure shows biofilm renderings corresponding to selected values of v and ρ_a while keeping λ_a constant at $\lambda_a = 0.16$ (cf. Fig. 2.2e). Each cell is coloured according to the nematic order.



Supplementary Figure 2.23. Fitting of the attractive potential parameters. The graphs show the approximate position of the MSD minimum in $(v, \lambda_a$ and $\rho_a)$ -space of the 5% best-matching simulations at increasing arabinose concentrations, corresponding to increasing amounts of secreted RbmA. Each data point refers to the median position of the minimum and the error bars indicate the lower and upper quartile. The position of the WT* is shown in red (solid lines: median values, dashed lines: lower/upper quartiles).

Predicting the structure of larger biofilms. The cell-cell interaction potential was calibrated based on biofilms with up to 300 cells (section “Comparing simulations with experimental data”). To test the ability of the calibrated simulations to predict the structure of biofilms with more than 300 cells, a feature vector containing the same parameters as the ones used in section 0 was used. The MSD between the experimental and simulation feature vectors was calculated for biofilms sampled at 40 intermediate logarithmically spaced cell numbers from 10 to 300 and from 300 to 1000, separately for each chosen number of cells (in contrast to section 0 where a single MSD between temporal feature vectors was calculated), and was normalized by the average value of the MSD between 10 and 300 cells. For cell numbers between 300 and 1000, the MSD at each cell number was found to be close to the average value of the MSD between 10 and 300 cells for WT* and $\Delta rbmA$ biofilms, and strong qualitative agreement was observed between simulated and experimental biofilms with up to 1000 cells (Supplementary Fig. 2.2). These results indicate the remarkable ability of the potential-based simulations calibrated on biofilm development up to 300 cells to predict the development of larger biofilms.



Supplementary Figure 2.24. Predicting phenotypes of larger biofilms. **a**, Rendered WT* experimental (left) and simulated biofilm (right) for approximately 1000 cells. Bottom: normalized MSD of feature vectors for experimental ($n = 7$) and simulated biofilms ($n = 3$). These data are also shown in Fig. 2.2g,h. **b**, Rendered $\Delta rbmA$ experimental (left) and simulated biofilm (right) for approximately 1000 cells. Bottom: normalized MSD of feature vectors for experimental ($n = 4$) and simulated biofilms ($n = 3$). Error bars were calculated by Gaussian error propagation of the standard deviations of the individual measurements.

Continuum Model

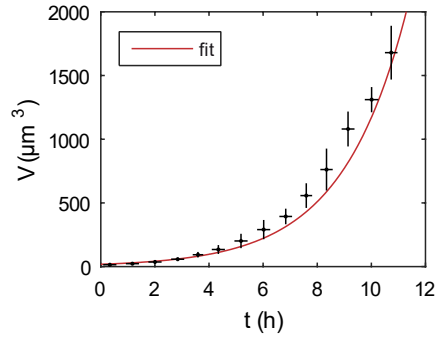
Mathematical model of a growing biofilm in shear flow. For this model, we assume that the biofilm colony is located in the centre of a rectangular channel. Fluid flows through the channel in the x -direction with a prescribed flow rate. Flow is modelled by the Stokes equations

$$\nabla \cdot \mathbf{u} = 0, \quad \mu \nabla^2 \mathbf{u} = \nabla p \quad (25)$$

with a no-slip condition ($\mathbf{u} = \mathbf{0}$) applied on the channel walls and on the surface of the biofilm. The biofilm surface $z = S(x, y, t)$ grows or shrinks in the direction of its outer unit normal \mathbf{n} , with velocity

$$\begin{aligned} \mathbf{U} &= \alpha(\mathbf{x}, t) \mathbf{n} - \beta |(\mathbb{I} - \mathbf{nn}) \boldsymbol{\sigma} \cdot \mathbf{n}| \mathbf{n} \\ &= \alpha(\mathbf{x}, t) \mathbf{n} - \beta \boldsymbol{\tau} \mathbf{n} \end{aligned} \quad (26)$$

where the first term on the right hand side represents movement owing to cell growth and division, and the second term represents erosion proportional to the shear stress $\boldsymbol{\tau}$ imposed on the surface by the fluid; here $\boldsymbol{\sigma}$ is the stress tensor of the fluid. For a hemispherical biofilm growing uniformly in the radial direction at a rate r_0 , with a base centred at the origin, $\alpha(\mathbf{x}, t) = r_0 r$, where $r = |\mathbf{x}|$. This leads to exponential volumetric growth in time, $V(t) = V_0 \exp(3r_0 t)$, where V_0 is the volume of the biofilm at $t = 0$. The growth rate r_0 is found by fitting an exponential curve to experimental data of volume versus time for a $\Delta rbmA$ -mutant in a channel with an average flow velocity of $\langle v \rangle = 0.03$ mm/min (Supplementary Fig. 2.2).



Supplementary Figure 2.25. Volume of $\Delta rbmA$ -mutant (black) growing at a very low flow speed ($\langle v \rangle = 0.03$ mm/min). Exponential fit (red).

Numerical method. The surface of the biofilm is represented by the zero level set of a level set function ϕ , which satisfies the Hamilton-Jacobi equation²³

$$\phi_t + a(x, t)|\nabla\phi| = 0. \quad (27)$$

Here $a = |\mathbf{U}|$ is the normal speed of the surface.

Equation (27) is solved using the Level Set Toolbox²⁴ in Matlab, which approximates the time derivative with an explicit total variation diminishing Runge-Kutta integration scheme. The spatial grid is uniform in each direction, with a smaller step size in the z -direction. A symmetry condition ($\nabla\phi \cdot \mathbf{n} = 0$) is applied along the xz -plane through the centre of the biofilm. At all other boundaries, ghost nodes are added and filled with data linearly extrapolated from the computational boundary²⁴.

At each timestep, the steady Stokes equations (25) are solved using the finite-element package deal.II²⁵, with the surface height $z = S(x, y, t)$ used as input to denote the grid points at which the no-slip condition should be applied. The finite-element mesh is locally refined in all directions around the biofilm surface. A uniform velocity value is imposed at the inflow boundary, and the flow is allowed to develop in an entrance region. A symmetry condition ($\mathbf{u} \cdot \mathbf{n} = 0$) is applied on the xz -plane through the centre of the biofilm. The stress tensor σ at the biofilm surface is output for use in equation (26) at the next timestep. The value of σ is interpolated to the level set spatial grid. The total drag force in the direction of the flow on a hemisphere is checked to agree with the value calculated by Pozrikidis *et al.*²⁶.

The shear stress applied to real biofilms is calculated by incorporating experimental data from wild-type biofilms into the continuum model. The convex hull of the set of cell centroids at a specific time point is extracted, after some outlying cells and cells not descended from the biofilm population have been removed. The surface is smoothed by binarizing the volumes inside and outside the convex hull, then applying a Gaussian filter. The flow and the biofilm surface are assumed to be symmetric

about the mid-plane of the biofilm, as before (i.e. flow is only simulated on one half of the experimental domain, chosen arbitrarily).

Strain	Genotype/Relevant features	Reference
<i>E. coli</i>		
S17-1 λ pir	$\Delta lacU169$ ($\Phi lacZ\Delta M15$), <i>recA1</i> , <i>endA1</i> , <i>hsdR17</i> , <i>thi-1</i> , <i>gyrA96</i> , <i>relA1</i> , λ pir	De Lorenzo <i>et al.</i> ²⁷
TOP10	<i>mcrAD</i> (<i>mrr</i> - <i>hsdRMS</i> - <i>mcrBC</i>) $\Phi 80lacZ\Delta M15\Delta lacX74deoRrecA1$ <i>araD139\Delta</i> (<i>ara-leu</i>)7697 <i>galU galK rpsL endA1 nupG</i>	Invitrogen
<i>V. cholerae</i>		
KDV101	wild type strain N16961 (O1 El Tor, Sm ^R)	Meibom <i>et al.</i> ²⁸
KDV103	N16961 <i>lacZ:P_{tac}-mKOKappa</i>	Drescher ¹
KDV115	N16961 <i>vpvC^{W240R} lacZ:P_{tac}-mKOKappa</i>	Drescher ¹
KDV148	N16961 <i>vpvC^{W240R}</i> (matrix hyperproducer phenotype)	Drescher ¹
KDV383	N16961 $\Delta rbmA$, <i>lacZ:P_{tac}-mKOKappa</i>	Drescher lab
KDV611	N16961 <i>vpvC^{W240R}</i> , $\Delta crvA$	This work
KDV613	N16961 <i>vpvC^{W240R}</i> , $\Delta crvA$ contains plasmid pNUT542	This work
KDV692	N16961 <i>vpvC^{W240R}</i> , $\Delta rbmA$ contains plasmid pNUT542	This work
KDV698	N16961 <i>vpvC^{W240R}</i> , $\Delta crvA$, $\Delta rbmA$	This work
KDV815	N16961 <i>vpvC^{W240R}</i> , $\Delta rbmA$, $\Delta crvA$ contains plasmid pNUT542	This work
KDV829	N16961 <i>vpvC^{W240R}</i> , <i>rbmA::3xFLAG</i>	This work
KDV835	N16961 <i>vpvC^{W240R}</i> , <i>rbmA::3xFLAG</i> contains plasmid pNUT542	This work
KDV1026	N16961 <i>vpvC^{W240R}</i> , $\Delta crvA$, <i>rbmA:mRuby3</i>	This work
KDV1027	N16961 <i>vpvC^{W240R}</i> , $\Delta crvA$, <i>rbmA:mRuby3</i> and plasmid pNUT542	This work
KDV1082	N16961 <i>vpvC^{W240R}</i> , $\Delta rbmA$, $\Delta crvA$ contains plasmid pNUT1519	This work
KDV1218	N16961 <i>vpvC^{W240R}</i> , $\Delta crvA$ contains plasmid pNUT844	This work
KDV1228	N16961 <i>vpvC^{W240R}</i> , $\Delta crvA$ contains plasmid pNUT1734	This Work
KDV1231	N16961 <i>vpvC^{W240R} lacZ:P_{tac}-mKOKappa</i> and plasmid pNUT1734	This Work

Supplementary Table 2.5. Bacterial strains used in this study.

Plasmids	Origin, Marker	Comments	References
pNUT015	pR6K, Amp ^R	pKAS32	Skorupski <i>et al.</i> ²⁹
pNUT144	pR6K, Amp ^R , Kan ^R	pKAS32 with Kan ^R	Drescher <i>et al.</i> ³⁰
pNUT336	pR6K, Amp ^R	pKAS32 Δ <i>rbmA</i> (<i>vc0928</i>)	Nadell <i>et al.</i> ³¹
pNUT462	pR6K, Amp ^R	pNUT144 <i>rbmA</i> ::3xFLAG (translational fusion)	Drescher lab stock
pNUT542	pSC101*, Gent ^R	P_{tac} - <i>sfgfp</i>	Singh <i>et al.</i> ³²
pNUT844	p15a, Gent ^R	P_{tac} - <i>sfgfp</i> , P_{vpsL} - <i>mRuby2</i>	Drescher lab stock
pNUT961	pR6K, Amp ^R , Kan ^R	pNUT144 Δ <i>crvA</i> (<i>vca1075</i>)	This work
pNUT1268	pSC101*, Gent ^R	pNUT542 with P_{BAD} - <i>rbmA</i> to replace P_{tac} - <i>sfgfp</i>	This work
pNUT1401	pR6K, Amp ^R , Kan ^R	pNUT144 <i>rbmA</i> : <i>mRuby3</i> (transcriptional fusion)	This work
pNUT1519	pSC101*, Gent ^R	pNUT1268 with P_{tac} - <i>sfgfp</i>	This work
pNUT1734	pSC101*, Gent ^R	pNUT1268 with <i>sfgfp</i> to replace <i>rbmA</i>	This work

Supplementary Table 2.6. Plasmids used in this study.

Chapter II: Emergence of three-dimensional order and structure in growing biofilms

Name	Sequence	Function
KDO1182	GGGTCTAGAGCTCGATATAGCGATCCACCACTTC	Plasmid pNUT961 construction
KDO1183	GAGTTTTACCCACACCGTCCCTGCAACATATTTATGTTTAGCC	Plasmid pNUT961 construction
KDO1184	GGGACGGTGTGGGTAAAACCTCAGACCAAACAAAG	Plasmid pNUT961 construction
KDO1185	TTTGCGGCCGCCGCATGCCGTCATAGAAACCAG	Plasmid pNUT961 construction
KDO1433	TTTAAAGTTAGACAACGCAATATATCCTAGTTATAAAAAATTTAACGC CA	Plasmid pNUT1268 construction
KDO1434	CTAGGATATATTGCGTTGTCTAACTTTAAAGGATCTATCATGAACAAA	Plasmid pNUT1268 construction
KDO1435	TTATTTTTTTACCACTGTCATTGACTGTTC	Plasmid pNUT1268 construction
KDO1436	ATGCATAAATAACAAAACTGCTAAACGTT	Plasmid pNUT1268 construction
KDO1667	TTGCGGCCGCGTTACAAGAACCCGGAAGAATGTG	Plasmid pNUT1401 construction
KDO1716	CCTAGTGGCTTATTTTTTTACCACTGTCATTGACTGTTC	Plasmid pNUT1401 construction
KDO1717	CAGTGGTAAAAAATAAGCCACTAGGAGGTGGTTGATGGTG	Plasmid pNUT1401 construction
KDO1718	GAAGTGTATAAATAAATTTACCTAGTCACTTAGTCGTATGTATAAAAA ACCGC	Plasmid pNUT1401 construction
KDO1719	CTAAGTGACTAGGTAAATTTATTTATACAGTTCATCCATACCACCACCC AG	Plasmid pNUT1401 construction
KDO1720	GGTTGCTAGCGTCTACCTTGGCAGCACTAAAGGTACC	Plasmid pNUT1401 construction
KDO389	GCTTGCTCAATCAATCACCGGATCC	Plasmid pNUT1519 construction
KDO578	TTCACACCTCCTGTACGCGCGGC	Plasmid pNUT1519 construction
KDO2162	ATAACTAGGATATATTGCGATGAGCAAAGGTGAAGAACTGTTTAC	Plasmid pNUT1734 construction
KDO2163	GCTCATCGCAATATATCCTAGTTATAAAAAATTTAACGCCAG	Plasmid pNUT1734 construction
KDO2164	GAGCTCTACAAGTAAATGCATAAATAACAAAACTGCTAAACGTTATT C	Plasmid pNUT1734 construction

KDO2165	GTTATTTATGCATTTACTTGTAGAGCTCGTCCATGCCGTGAG	Plasmid pNUT1734 construction
---------	--	----------------------------------

Supplementary Table 2.7. DNA oligonucleotides used in this study. Sequences are given in the 5'→3' direction.

References for supplementary information

1. Drescher, K. *et al.* Architectural transitions in *Vibrio cholerae* biofilms at single-cell resolution. *Proc. Natl. Acad. Sci. U.S.A.* **113**, E2066–E2072 (2016).
2. Horn, B. K. P. & Schunck, B. G. Determining optical flow. *Artif. Intell.* **17**, 185–203 (1981).
3. M. A. Mustafa. Horn-Schunck optical flow method for 3-D images. (2014). Available at: <https://de.mathworks.com/matlabcentral/fileexchange/37053-horn-schunck-optical-flow-method-for-3-d-images>. (Accessed: 2nd November 2017)
4. Flandin, G. mVTK: a MATLAB VTK library. (2017). Available at: <http://www.artefact.tk/software/matlab/mvtk/>. (Accessed: 2nd November 2017)
5. Sonnet, A. M. & Virga, E. G. Dynamics of dissipative ordered fluids. *Phys. Rev. E* **64**, 031705 (2001).
6. Liu, X., Tanaka, M. & Okutomi, M. Single-image noise level estimation for blind denoising. *IEEE Trans. Image Process.* **22**, 5226–5237 (2013).
7. Yan, J., Sharo, A. G., Stone, H. A., Wingreen, N. S. & Bassler, B. L. *Vibrio cholerae* biofilm growth program and architecture revealed by single-cell live imaging. *Proc. Natl. Acad. Sci. U.S.A.* **113**, E5337–E5343 (2016).
8. Beyhan, S., Tischler, A. D., Camilli, A. & Yildiz, F. H. Transcriptome and phenotypic responses of *Vibrio cholerae* to increased cyclic di-GMP level. *J. Bacteriol.* **188**, 3600–3613 (2006).
9. Watnick, P. I., Lauriano, C. M., Klose, K. E., Croal, L. & Kolter, R. The absence of a flagellum leads to altered colony morphology, biofilm development and virulence in *Vibrio cholerae* O139. *Mol. Microbiol.* **39**, 223–235 (2001).
10. Yildiz, F. H., Liu, X. S., Heydorn, A. & Schoolnik, G. K. Molecular analysis of rugosity in a *Vibrio cholerae* O1 El Tor phase variant. *Mol. Microbiol.* **53**, 497–515 (2004).
11. Utada, A. S. *et al.* *Vibrio cholerae* use pili and flagella synergistically to effect motility switching and conditional surface attachment. *Nat. Commun.* **5**, 4913 (2014).
12. Conrad, J. C. Physics of bacterial near-surface motility using flagella and type IV pili: Implications for biofilm formation. *Res. Microbiol.* **163**, 619–629 (2012).
13. Beyhan, S. & Yildiz, F. H. Smooth to rugose phase variation in *Vibrio cholerae* can be mediated by a single nucleotide change that targets c-di-GMP signalling pathway. *Mol. Microbiol.* **63**, 995–1007 (2007).
14. Fritz, G. *et al.* Single cell kinetics of phenotypic switching in the arabinose utilization system of *E. coli*. *PLoS One* **9**, e89532 (2014).
15. Megerle, J. A., Fritz, G., Gerland, U., Jung, K. & Rädler, J. O. Timing and dynamics of single cell gene expression in the arabinose utilization system. *Biophys. J.* **95**, 2103–2115 (2008).
16. Han, Y., Alsayed, A., Nobili, M. & Yodh, A. G. Quasi-two-dimensional diffusion of single ellipsoids: Aspect ratio and confinement effects. *Phys. Rev. E* **80**, 011403 (2009).
17. Taheri-Araghi, S. *et al.* Cell-size control and homeostasis in bacteria. *Curr. Biol.* **25**, 385–391 (2015).
18. Nyland, L., Harris, M. & Prins, J. Fast n-body simulation with CUDA. *Simulation* **3**, 677–696 (2007).
19. Pavlovsky, L., Younger, J. G. & Solomon, M. J. In situ rheology of *Staphylococcus epidermidis* bacterial biofilms. *Soft Matter* **9**, 122–131 (2013).
20. Fong, J. C. *et al.* Structural dynamics of RbmA governs plasticity of *Vibrio cholerae* biofilms. *Elife* **6**, e26163 (2017).
21. Persat, A. *et al.* The mechanical world of bacteria. *Cell* **161**, 988–997 (2015).
22. Cleaver, D. J., Care, C. M., Allen, M. P. & Neal, M. P. Extension and generalization of the Gay-Berne potential. *Phys. Rev. E* **54**, 559–567 (1996).
23. Osher, S., Fedkiw, R. & Piechor, K. Level set methods and dynamic implicit surfaces. *Appl. Mech. Rev.* **57**, B15 (2004).
24. Mitchell, I. M. The flexible, extensible and efficient toolbox of level set methods. *J. Sci. Comput.* **35**, 300–329 (2008).
25. Arndt, D. *et al.* The deal.II library, version 8.5. *J. Numer. Math.* **25**, 137–145 (2017).
26. Pozrikidis, C. Shear flow over a protuberance on a plane wall. *J. Eng. Math.* **31**, 29–42 (1997).
27. De Lorenzo, V. & Timmis, K. N. Analysis and construction of stable phenotypes in gram-negative bacteria with Tn5- and Tn10-derived minitransposons. *Methods Enzymol.* **235**, 386–405 (1994).

28. Meibom, K. L. *et al.* The *Vibrio cholerae* chitin utilization program. *Proc. Natl. Acad. Sci. U.S.A.* **101**, 2524–9 (2004).
29. Skorupski, K. & Taylor, R. K. Positive selection vectors for allelic exchange. *Gene* **169**, 47–52 (1996).
30. Drescher, K., Nadell, C. D., Stone, H. A., Wingreen, N. S. & Bassler, B. L. Solutions to the public goods dilemma in bacterial biofilms. *Curr. Biol.* **24**, 50–55 (2014).
31. Nadell, C. D., Drescher, K., Wingreen, N. S. & Bassler, B. L. Extracellular matrix structure governs invasion resistance in bacterial biofilms. *ISME J.* **9**, 1700–1709 (2015).
32. Singh, P. K. *et al.* *Vibrio cholerae* combines individual and collective sensing to trigger biofilm dispersal. *Curr. Biol.* **27**, 3359–3366.e7 (2017).

Chapter III: Spatiotemporal multi-omic analysis of *Escherichia coli* biofilm colonies reveals a novel cross-feeding of alanine

Francisco Díaz-Pascual¹, Martin Lempp¹, Kazuki Noshō¹, Hannah Jeckel^{1,2}, Mads Frederik Hansen¹, Konstantin Neuhaus^{1,2}, Raimo Hartmann¹, Hannes Link^{1,3}, and Knut Drescher^{1,2,3}.

This chapter is written in manuscript style and is an ongoing project. My contribution to this work included performing and designing all experiments (except for RNA work and mass spectrometry measurements), performing all data analysis (except developing the software for image analysis), creating all new strains, and writing the current version of the manuscript.

¹Max Planck Institute for Terrestrial Microbiology, Marburg, Germany.

²Synmikro Center for Synthetic Microbiology, Philipps-Universität Marburg, Marburg, Germany.

³Department of Physics, Philipps-Universität Marburg, Marburg, Germany.

Abstract

Bacteria often live in dense communities termed biofilms. As biofilms develop, metabolites are consumed and produced by the bacterial metabolism, creating chemical heterogeneity. Consequently, the distinct local environments create subpopulations where cell metabolism differentiates. These subpopulations can interact by metabolic cross-feeding, with important consequences for community fitness and growth dynamics. Despite the high importance of these interactions, very few have been described within single-species communities. Here, we discovered a novel alanine cross-feeding by analysing the spatiotemporal changes in transcripts and amino acids of *Escherichia coli* biofilm colonies. We found that the alanine exporter *alaE* and the alanine degradation operon *dadAX* were upregulated during colony development. Specifically, alanine is secreted from anaerobically growing cells with access to nutrients, increasing the extracellular concentration of alanine. Cells in the aerobic region of the colony, where glucose and ammonium are deficient, subsequently convert alanine into pyruvate and ammonium in a *dadAX* dependent manner. Comparative studies of knockout mutants demonstrated that this alanine cross-feeding interaction is pivotal for colony development in terms of cellular viability, colony morphology and growth dynamics.

Introduction

A large number of bacterial genes are involved in adaptation towards changing environmental conditions¹. Coherently, the metabolic profile of a cell strongly depends on its local environment. Traditionally, the association between metabolism and environment has been studied in homogeneous batch cultures. However, bacteria primarily live in spatially structured multicellular communities embedded in an extracellular matrix, known as biofilms². In biofilms, bacteria often encounter chemical gradients created by decreased solute diffusion and bacterial metabolism^{1,3,4}. Thus, biofilm-associated cells can be divided into distinct physiological and metabolic subpopulations based on their spatial location^{5,6}.

When two or more subpopulations coexist, some metabolites produced by one of the subpopulations can reach another population and can be used by it, in a process termed metabolic cross-feeding^{4,7,8}. Many metabolic interactions have been found between genetically different microorganisms^{8–13} and isogenic bacteria grown in liquid cultures^{14,15}. In contrast, the study of cross-feeding within single-species biofilms has remained challenging due to a lack of visible or highly specific phenotypes. Hence, only a handful of studies have been conducted on metabolic cross-feeding within single-species biofilms^{16–19}. These studies have found that, under certain conditions, *Bacillus subtilis* colonies can differentially produce and consume ammonium¹⁸, *Escherichia coli* colonies can cross-feed acetate^{16,17}, and *Pseudomonas aeruginosa* biofilms share lactate as a carbon source¹⁹. To the best of our knowledge, all studies have either worked with metabolite average levels²⁰ or focused on a few, usually predefined and hypothesis-based metabolic pathways^{21,22}. Thus, a range of metabolic interactions that potentially have important consequences for community fitness and resilience might have been overlooked^{7,23–25}.

Amino acids are essential for bacterial metabolism and can potentially be cross-fed between bacteria²⁶. They are frequently transported across the cell membrane and many amino acid exporters have been described^{27–29}, yet the role of these transporters in bacterial physiology remains largely unknown. We hypothesized that amino acid exporters could create an accumulation of extracellular amino acids that could lead to metabolic cross-feeding interactions in dense communities. To study this, we chose *E. coli* as model organism, since the current knowledge on amino acid metabolism and amino acids exporters is extensive compared to other species.

To identify unprecedented amino acid cross-feeding interactions within *E. coli* biofilm colonies, we used a combination of temporal and spatial omics, i.e. transcriptomics and metabolomics. This approach enabled us to get new insights on how metabolism changes globally during colony

development, and spatially between different regions of the colony biofilm. We found a differential secretion and consumption of alanine within *E. coli* biofilm colonies, driven by the alanine exporter *alaE* and the alanine degradation operon *dadAX*. Secretion of alanine mainly occurs in the anaerobic region of the colony. The secreted alanine is then consumed in the aerobic region of the colony, where glucose and ammonium are deficient, with important consequences for their local cellular viability, growth, and colony morphology. This novel approach of combining temporal and spatial transcriptomics and metabolomics to bacterial colonies helps to better understand these communities and eventually to identify new strategies to combat biofilms.

Results

To study *E. coli* colony metabolism and find potential amino acid cross-feeding interactions, we first analysed colony growth on solid M9 minimal medium for up to 72 h. In this medium glucose and ammonium are the sole carbon and nitrogen sources. To enable quick transfer of the colonies for downstream analysis, they were grown on top of membrane filters. Initially, we identified heterogeneous colony development due to swimming of the wild type *E. coli* (Supplementary Fig. 3.1). Thus, to obtain reproducible colony sizes, a flagella deficient strain ($\Delta fliC$) -termed parental strain- was used for all following experiments. We observed that colonies displayed two growth phases: they grew exponentially in volume, height and diameter for up to 24 h, before switching to linear growth (Fig. 3.1a and Fig. 3.1b). As shown by other groups, this change of colony growth dynamics suggests a change in metabolism due to nutrient penetration and consumption³⁰. To study the global changes during growth, we first performed whole colony transcriptomics (Fig. 3.1c and Supplementary Fig. 3.2a). The transcriptomic profile reflected the transition between growth phases, i.e. a clear change at the transcript level was observable after 24 h. At 72 h, 239 genes of 4,231 detected genes were differentially expressed in comparison to 12 h (fold changes >4 or <-4, and FDR p -value >0.05). As the colonies grew, they consume oxygen and less cells had access to molecular oxygen. Therefore, to validate the data, we mined the transcriptomic data for well-known oxygen regulated pathways. As expected, pathways like mixed acid fermentation³¹ and TCA cycle were differentially regulated (Supplementary Fig. 3.3a and Supplementary Fig. 3.3c).

Chapter III: Spatiotemporal multi-omic analysis of *Escherichia coli* biofilm colonies reveals a novel cross-feeding of alanine

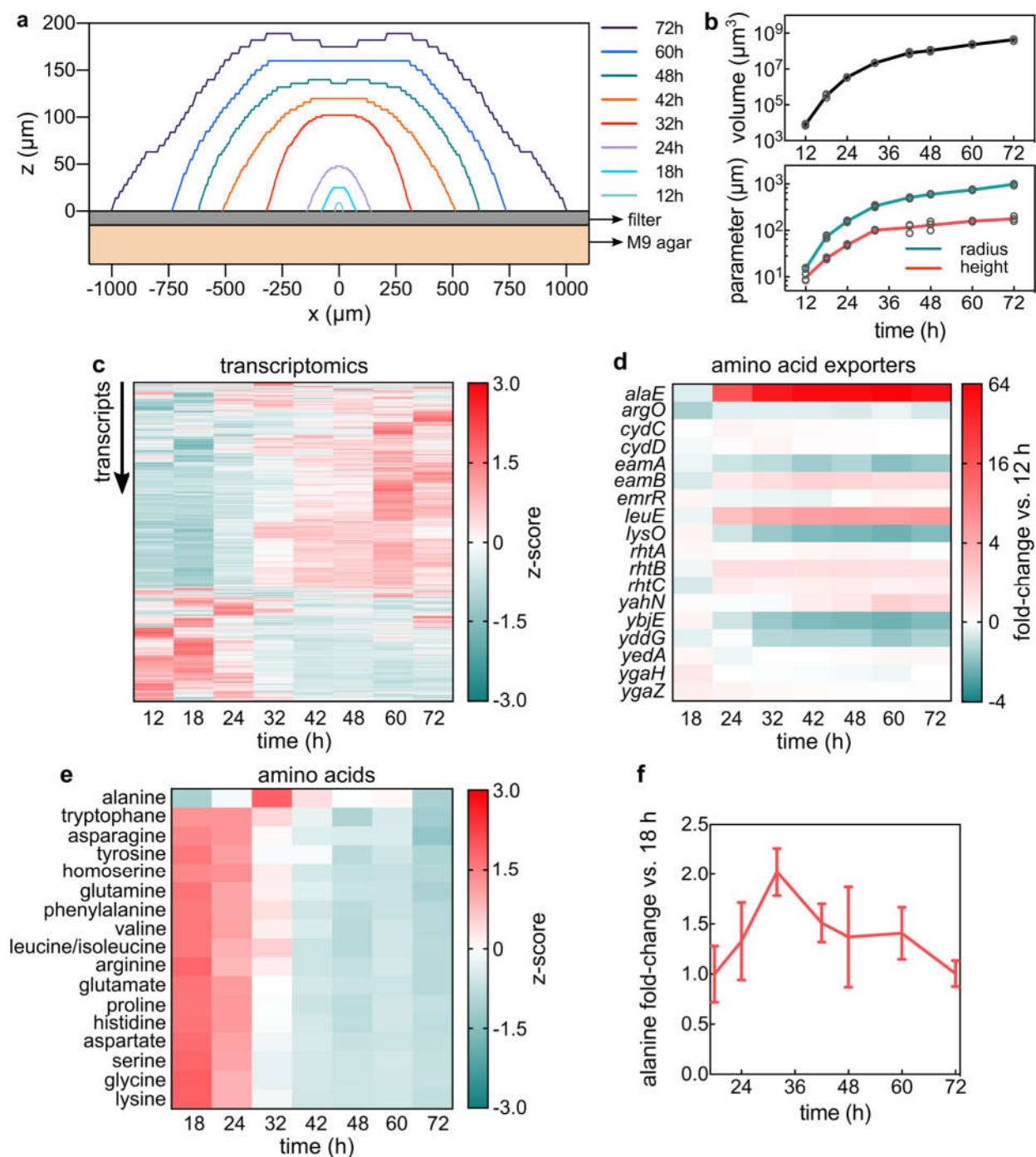


Figure 3.1. *E. coli* biofilm colonies growth, transcriptomic and amino acid dynamics. (a) xz cross-sectional profile of *E. coli* biofilm colonies grown on solid agar at different time points. Each line corresponds to a representative colony. (b) Volume (top panel), radius and height (bottom panel) of colonies as a function of time. Data are mean \pm standard deviation (s.d.), $n = 3$. (c) Dynamics of expression profile of 4,231 genes over time, $n = 3$. (d) Average expression fold-changes of known amino acid exporters during colony growth in comparison to 12 h colonies, $n = 3$. (e) Amino acid dynamics during colony growth, $n = 3$. (f) Fold-change in alanine levels in comparison to 18 h. Data are mean \pm standard deviation (s.d.), $n = 3$.

Any metabolite cross-feeding requires that cells secrete these metabolites. Therefore, to find new amino acid cross-feeding interactions, we focused on the expression dynamics of all known amino acid exporters. We found that the expression of the alanine exporter *alaE*³² was up-regulated 50-fold, when comparing colonies of 72 h to colonies of 12 h (Fig. 3.1d). None of the other amino acid exporters were strongly up-regulated during colony growth. Interestingly, we found that the level of alanine had a different pattern from the rest of amino acids, i.e. was the only that did not decrease over time (Fig. 3.1e-f, Supplementary Fig. 3.2b and Supplementary Fig. 3.4). Thus, we decided to further analyse the metabolism of alanine within *E. coli* colonies.

Alanine transport and degradation are spatially regulated within biofilm colonies.

A potential alanine cross-feeding requires an alanine-secreting population and an alanine-consuming population spatially separated. In order to identify if such subpopulations were present, we acquired spatial transcriptomic data by utilizing the dependency of GFP-derived proteins on molecular oxygen to mature their chromophores³³. Using a strain that constitutively expresses the fluorescent protein mRuby2, we observed at 72 h only the outer aerobic shell of the colonies was fluorescent. In particular, only the cells up to 30 μm from the colony surface were fluorescent (Fig. 3.2a-b). Consistent with the idea that this fluorescence was driven by an oxygen gradient, the fluorescent fraction of the colony decreased during growth (insert in Fig. 3.2b). To eliminate the possibility that the observed fluorescence profile was due to imaging artefacts, such as insufficient laser penetration, we disrupted 72 h colonies and imaged single-cells. As anticipated, we observed that only some cells presented fluorescence (Supplementary Fig. 3.5a). Furthermore, since the oxygen gradient is mainly created by oxygen consumption¹, it should disappear when metabolic processes that consume it are hindered. As expected, when moving a colony to a plate lacking glucose, molecular oxygen penetrated throughout the colony. This allowed mRuby2 proteins located in the former anaerobic region, to become fluorescent allowing the imaging of the whole colony (Supplementary Fig. 3.5b-c). By using fluorescence-activated cell sorting (FACS) we separated the aerobic (fluorescent) and anaerobic (not fluorescent) populations and subject them to RNA-seq (Fig. 3.2c and Supplementary Fig. 3.6). As control, we first analysed known pathways regulated by oxygen concentration. We found differential expression of genes involved in the TCA cycle and mixed acid fermentation verifying that spatial transcriptomics could be reliably applied (Supplementary Fig. 3.3b and Supplementary Fig. 3.3d).

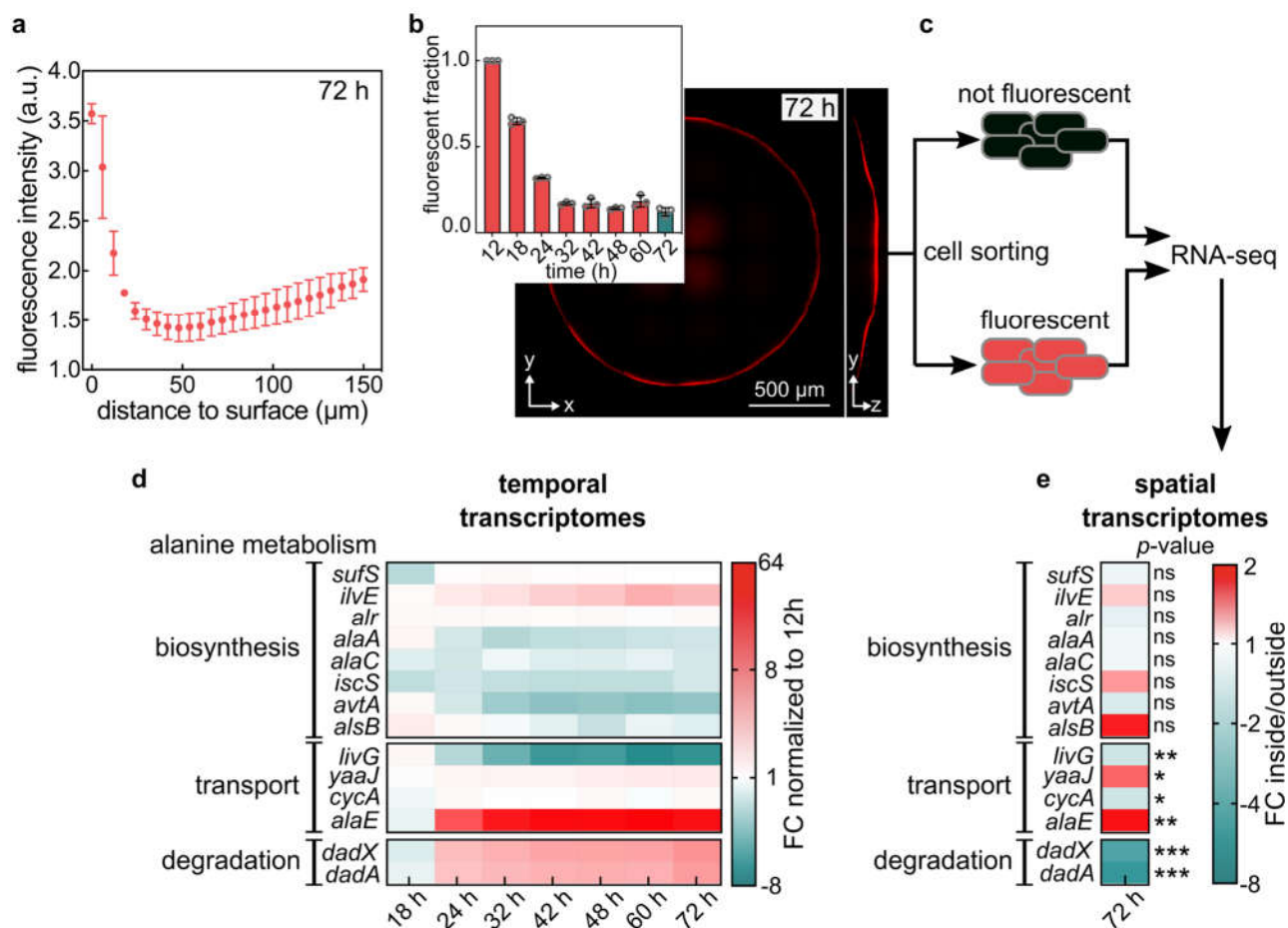


Figure 3.2. Alanine transport and degradation are spatially regulated within colonies. (a) Fluorescence intensity of 72 h colonies in function of the distance to the surface of the colony. Data are mean \pm s.d., $n = 3$. (b) Fluorescent image of a representative 72 h colony. Insert: Fluorescent fraction of colonies at different time points. Data are mean \pm s.d., $n = 3$. (c) Scheme of the sorting procedure. Cells from a 72 h colony were sorted according to their fluorescence and subjected to RNA-seq. (d) Heat maps showing the fold-changes in expression levels of alanine related genes over time in comparison to the 12 h timepoint in whole colony measurements. Data are means, $n = 3$. (e) Spatial fold-changes between the inside (not fluorescent) and outside (fluorescent) regions of 72 h colonies. Data are means, $n = 4$. Non-significant data are labeled as ns. p -values correspond to FDR p -values. * $p < 0.05$, ** $p < 0.01$, *** $p < 0.001$.

When analysing alanine metabolism, we observed changes in the spatial expression of genes involved in alanine transport and degradation, but not biosynthesis (Fig. 3.2d-e). In particular, the expression of the alanine exporter *alaE* was up-regulated 1.9-fold in the non-fluorescent region. Noticeably, alanine degradation into pyruvate was also spatially regulated. Two pathways for converting alanine to pyruvate are known. These are the reversible conversion by enzymes involved in the alanine biosynthetic pathways, and the irreversible conversion mediated by the *dadAX* operon. The latter encodes a racemase (*dadX*) and a dehydrogenase (*dadA*)³⁴. At 72h, the expression of the *dadAX* operon was down-regulated (-5-fold for *dadA* and -6-fold for *dadX*) in the non-fluorescent region in comparison to the fluorescent region. In contrast, *dadAX* expression was up-regulated in the average

temporal measurements (6-fold for *dadA* and 5-fold for *dadX*) when comparing 72 h colonies to 12 h colonies. These results suggest: I) from a global point of view, colonies up-regulate alanine export and degradation during colony development, and II) the anaerobic region of the colony preferentially secretes alanine and the aerobic region of the biofilm converts alanine into pyruvate.

Alanine export and consumption influence bacterial survival in the aerobic region of the colony

To determine which genes are involved in the spatial regulation of alanine metabolism, we created single and multiple gene deletions of all known alanine transport and degradation genes. None of them had effects on the growth rate of liquid cultures, or were detrimental for colony height or radius after 72 h of growth (Supplementary Fig. 3.7). Using Sytox Green, a fluorescent nucleic acid stain that can only penetrate dead cells with disrupted membranes, we measured the percentage of dead biomass in the aerobic region of the colony in function of height (Fig. 3.3a and Supplementary Fig. 3.8). We observed that all colonies presented low percentages of cell death in the bottom of the colony that is closest to the solid medium, and increased cell death in the very top of the colony that is furthest from the medium. Interestingly, the region in between, i.e. at around 50% of the maximum colony height, had increased cell death when cells carried the double *alaE-dadAX* deletion. These colonies have a diminished capability to export alanine and to convert alanine into pyruvate and ammonium.

Alanine is exported via AlaE in the anaerobic region of the colony

The increased cell death in the $\Delta alaE\Delta dadAX$ mutants could be caused by a hindered alanine cross-feeding. However, for this to be true, alanine has to be secreted. Thus, we analysed the level of extracellular alanine and detected this amino acid in all mutant colonies (Fig. 3.3b). Interestingly and coherent with the research of Katsube *et al.*³⁵, the presence of extracellular alanine in the $\Delta alaE$ and $\Delta alaE\Delta dadAX$ mutants suggests that other exporter mechanisms that can partly compensate for the function of AlaE exist.

To test where in the colony alanine is secreted, we mimicked the growth conditions of different colony regions. In particular, we measured alanine in the supernatants of liquid cultures grown in presence or absence of the main nutrients found in the solid medium: glucose and ammonium, and molecular oxygen. We were only able to detect abundant alanine in the supernatant of exponentially growing cultures in the presence of glucose and ammonium under anaerobic conditions (Fig. 3.3c). This environment corresponds to the anaerobic base of the colony, where cells are in contact with the glucose- and ammonium-rich agar, and suggest that alanine is secreted in that region.

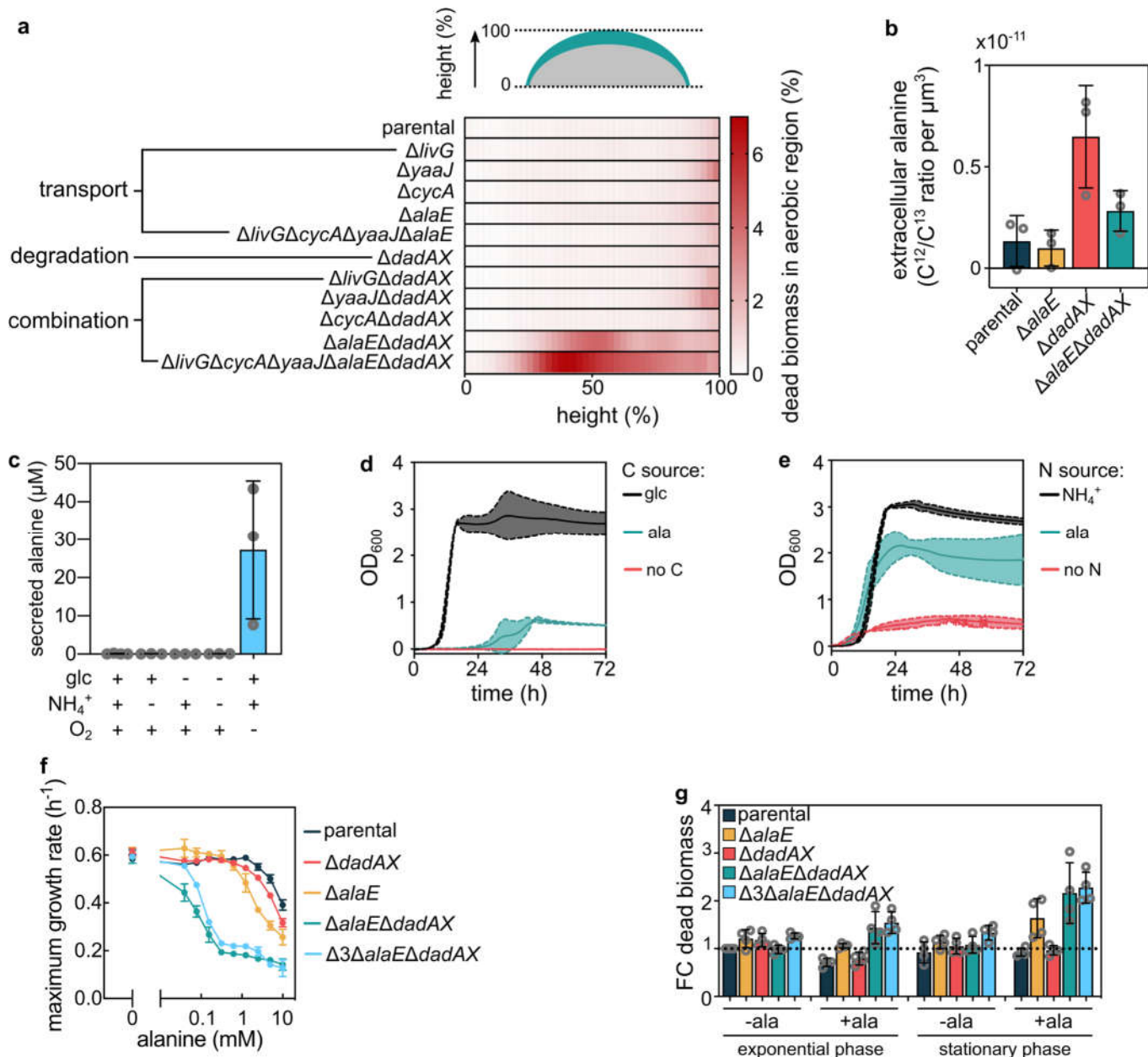


Figure 3.3. The anaerobic region of the colony secretes alanine that influences cell survival of the aerobic region. (a) Fraction of dead biomass in function of the normalized colony height. Only the aerobic region of the colony was used for this measurement (depicted as green in the colony diagram). Data shown corresponds to means, $n = 3$. Errors are shown in Supplementary Fig. 3.8. (b) Colony extracellular alanine levels. Data are mean \pm s.d., $n = 3$. (c) Alanine concentration in the supernatant of liquid cultures grown in presence or absence of glucose (glc), ammonium (NH_4^+) and molecular oxygen (O_2). (d) Growth curves using minimal medium with ammonium as nitrogen source and different carbon (C) sources: glucose (5 g/L), alanine (10 mM) or no carbon source. (e) Growth curves using minimal medium with glucose as a carbon source and different nitrogen (N) sources: ammonium (22.6 mM), alanine (5 mM) or no nitrogen source. For d and e continuous middle lines correspond to the mean and the dotted lines to the standard deviations, $n = 3$. (f) Maximum liquid culture growth rate in function of the concentration of exogenically added alanine. $\Delta 3$ corresponds to $\Delta livG\Delta cycA\Delta yaaJ$. Data are mean \pm s.d., $n = 3$. (g) Dead biomass, measured as Sytox Green fluorescence normalized by the optical density at 600 nm (OD_{600}), in presence or absence of alanine. The timepoints chosen in correspond to when cultures reached half of maximum OD_{600} for exponential phase or when they reached their maximum OD_{600} for stationary phase. The values were normalized by the parental

strain during exponential phase without alanine. When used, alanine had a final concentration of 5 mM. Data are mean \pm s.d., $n = 4$.

Alanine modulates growth in a concentration-dependent manner

In order to investigate whether extracellular alanine can function as the single glucose or nitrogen source, we replaced either glucose or ammonium for alanine in liquid cultures (Fig. 3.3d-e). We found that secreted alanine can act as a carbon and nitrogen source, thus indicating potential cross-feeding between bacteria.

A previous study has found that excess levels of intracellular alanine can inhibit growth²⁸. Therefore, we hypothesized that mutants carrying the *alaE-dadAX* double deletion might have a reduced cell growth rate, due to accumulation of intracellular alanine. In line with this, we observed that mutants with the *alaE* deletion grown aerobically in liquid cultures were more sensitive to exogenously added alanine than parental strain (Fig. 3.3f). Noteworthy, we observed a strikingly high sensitivity against alanine for the *alaE-dadAX* double mutants. This is because high levels of intracellular alanine can be toxic, and these mutants accumulate alanine intracellularly due to their reduced capability to degrade or export alanine²⁸. This result was not due to nonspecific effects of alanine (such as osmolarity changes), as no significant differences between the mutants and the parental strain were observed when serine was added instead of alanine (Supplementary Fig. 3.9). Thus, extracellular alanine can modulate bacterial growth, and depending on the genotype and the alanine concentration it can promote or inhibit growth.

Alanine concentration and metabolism influences cellular viability

Since colonies can accumulate alanine in their extracellular space and their growth rate can be inhibited by alanine, it is rational to hypothesize that toxic levels of alanine are the cause of the decreased viability of the *alaE-dadAX* double deletion mutants (Fig 3.3a). Thus, we tested if alanine-dependent modulation of bacterial growth affected cell viability. First, we exposed cells of the parental strain (with or without ammonium and glucose) to 5 mM of alanine, and we monitored viability using Sytox Green staining. We measured cell death levels at the timepoint where growing cultures reached half of their maximum OD₆₀₀, or after 24 h of starvation for non-growing cultures. We found that there was a strong increase in cell death when cultures could not grow (due to lack of glucose, ammonium and alanine) in comparison to growing cultures (Supplementary Fig. 3.10). This observation was independent of whether glucose and ammonium were the carbon and nitrogen sources or if alanine provided these atoms. This indicates that alanine can support cell survival by acting as a nitrogen and carbon source.

Afterwards we tested if alanine can influence cell survival of the $\Delta alaE\Delta dadAX$ mutant strains, and if so under which conditions. In particular, we analysed the effect of alanine during growth (exponential phase) or after nutrients have been depleted (stationary phase) in liquid cultures. The actively growing cultures resembled the aerobic periphery of the colony that is in contact with oxygen, glucose and ammonium, while the stationary phase cultures resemble the aerobic region above, which is nutrient depleted if no cross-feeding is present. Interestingly, we found that alanine causes death in the stationary phase cultures of mutants that carry an *alaE* deletion (Fig. 3.3g). This effect was increased when the strains additionally carried a deletion of *dadAX*. These results show that an elevated intracellular alanine concentration can cause cell death in aerobic cultures that have depleted other nutrients. This explains that alanine can inhibit growth and cause increased cell death in nutrient deprived $\Delta alaE\Delta dadAX$ mutant colonies. The reason why we did not observe increased cell death in colonies of the single $\Delta alaE$ mutant is most likely because these colonies can convert alanine into pyruvate and ammonium, and have low levels of extracellular alanine.

Alanine cross-feeding has important consequences for colony shape, growth and survival

The data shown suggests that alanine, secreted in the anaerobic region of the colony, can reach the aerobic region and either: I) Function as a carbon and nitrogen source and support bacterial growth or II) Inhibit growth and ultimately decrease cell viability if cells are unable to reduce their intracellular alanine levels. Therefore, we propose an unprecedented alanine cross-feeding interaction, created by the sum of glucose, ammonium and oxygen gradients generated by bacterial metabolism (Fig. 3.4a). As a colony grows, chemical gradients are created. Cells at the bottom periphery of the colony (depicted as red in Fig. 3.4a) have access to molecular oxygen, glucose and ammonium, and perform oxidative phosphorylation. Cells in the bottom of the colony (depicted as yellow in Fig. 3.4a) are anaerobic and they have access to glucose and ammonium from the medium. These cells ferment glucose and secrete alanine via *AlaE* and at least one other unknown mechanism. Secreted alanine diffuses through the colony and can eventually be converted into biomass by aerobic nutrient-deficient cells (depicted as green in Fig. 3.4a). If alanine levels are not reduced, it inhibits growth and increases cell death in this region. Alanine does not reach the upper-most region of the colony (dark green in Fig. 3.4a) because it is consumed by the lower aerobic biofilm layers.

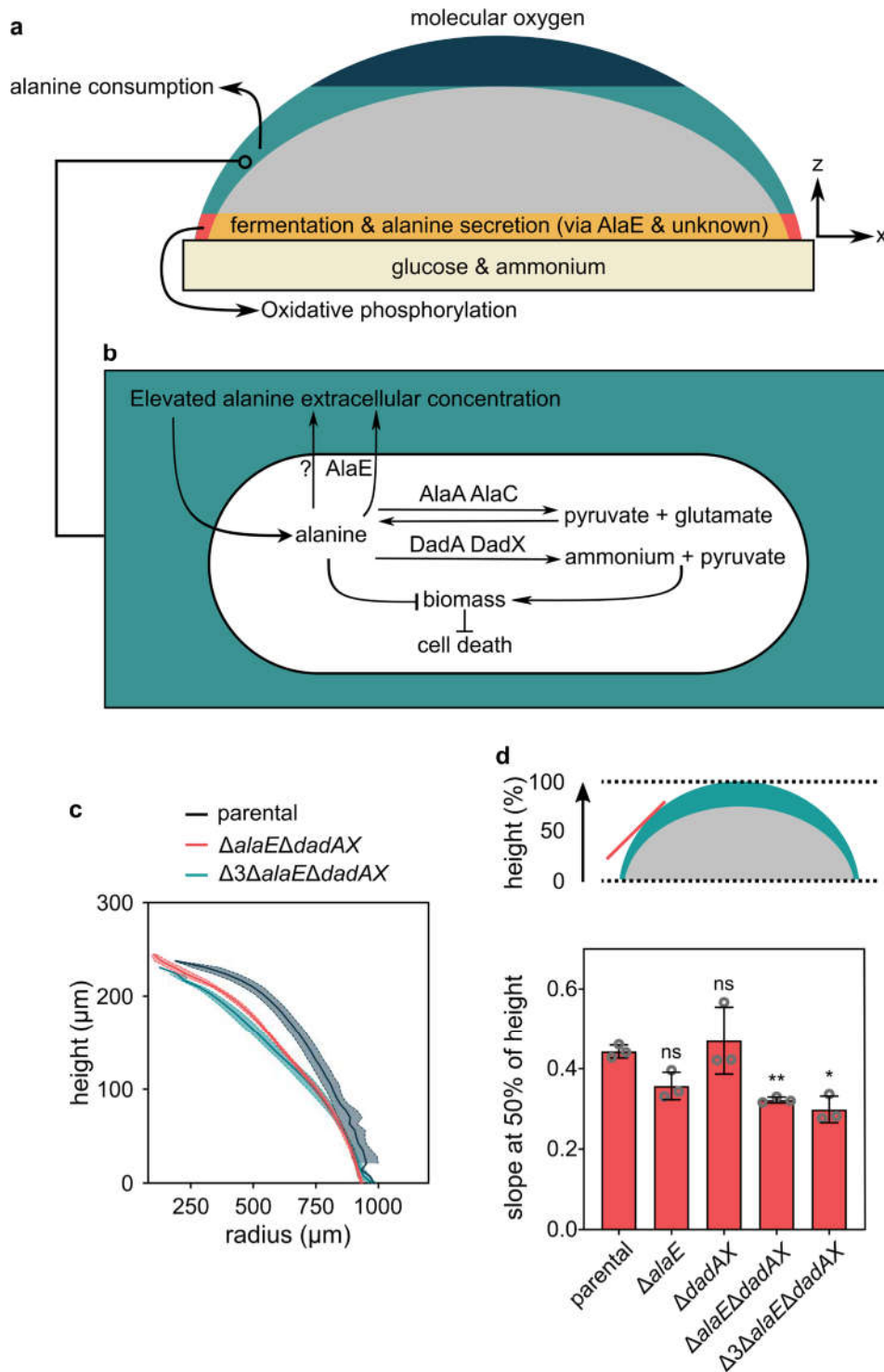


Figure 3.4. Model of alanine cross-feeding. (a) xz-cross-sectional diagram of *E. coli* biofilm colonies. Glucose and ammonium are provided in the solid agar media. Cells in the bottom layers of the biofilms have access to glucose and ammonium. Only cells in the outer periphery shell of the biofilm have access to oxygen. Cells in the red area can consume ammonium, glucose and oxygen to perform oxidative phosphorylation. Cells in bottom anaerobic region (depicted as yellow) have access to glucose and ammonium, but not oxygen. They ferment glucose and secrete alanine. The secreted alanine can be consumed by the aerobic cells above this layer (depicted as green). They convert alanine into pyruvate and ammonium, that can be used for growth and to maintain cell viability. (b) Depiction of alanine metabolism in green region. Cells are exposed to high

levels of extracellular alanine. If this high level of alanine is not reduced by enzymatic reactions or export, it can inhibit growth and decrease cell viability. Cells in this region export alanine and convert it to pyruvate and ammonium, which can be used for biomass. (c) Colony radius in function of the height. Central lines correspond to the mean and the shaded area to the s.d., $n = 3$ (d) Absolute value of the slope of curves in c when height is equal to half of the maximum height. Data are mean \pm s.d., $n = 3$. Statistical significances are calculated in comparison to the parental strain using a one-way ANOVA with Dunnett's multiple comparisons test. * p -value < 0.05 , ** p -value < 0.01 . Non-significant differences are labelled as ns. $\Delta 3$ corresponds to $\Delta livG\Delta cycA\Delta yaaJ$.

If this model is correct, mutants with *alaE-dadAX* deletions should have decreased growth in the aerobic nutrient-deficient region in comparison to the parental strain. This should be particularly detectable in the aerobic region at approximately 50% of the colony height, where we found that cell death had its maximum. When colony dimensions were measured, we observed that these mutants had a decreased colony curvature in comparison to the parental strain (Fig. 3.4c and Fig. 3.4d), even though they had similar maximum diameter and height (Supplementary Fig. 3.7). This supports the hypothesis that alanine is in fact converted into pyruvate and ammonium in this biofilm region. When this occurs, it can be used for growth. However, if its levels are not decreased, it inhibits local growth.

Discussion

While the number of bacteria within a colony is low, cells are exposed to a homogeneous environment. During this period, all cells have sufficient nutrients to grow at a constant rate and the colony grows exponentially. At approximately 24 hours of growth, certain colony regions cannot access enough nutrients to grow because they are consumed by cells in closer proximity to the medium. When this occurs, the growth rate of the colony decays eventually becomes linear. This was shown in this study, and it is congruent to what was extensively modelled and described by many other groups, including a pioneer study by S. J. Pirt in 1967³⁶ and recently by Warren *et al.*³⁰ These models show that on coarse average, colony growth dynamics can be predicted just by considering a growing layer in the bottom of the colony, while all remaining cells are practically dormant. However, these models were unable to predict local growth rates, cell viability, metabolic activities and cross-feeding interactions.

The study of metabolite cross-feeding is pivotal to understand the biofilm growth style⁴. However, only a handful have been described for single-species biofilms. Here we showed evidence for a novel alanine cross-feeding interaction that is driven by chemical gradients created by bacterial metabolism during colony development. Cells on the surface of the colony consume oxygen and create an anaerobic environment for the colony core. Bacteria growing anaerobically in the bottom of the

colony secrete alanine into the extracellular space. This extracellular alanine can inhibit growth and cause cell death, if its levels remain elevated. Thus, cells in the aerobic region that cannot access to glucose and ammonium, convert alanine into ammonium and pyruvate, which in turn can be used for biomass. Interestingly, Warren *et al.* predicted triangular colonies by only considering growth in the layer in contact with the solid medium³⁰. This, however, does not correspond to the experimental colonies that deviate from this shape. As shown here, the existence of this alanine-driven growth far from the medium can explain the rounder colony shape observed experimentally.

The proposed alanine cross-feeding relies on the alanine exporter AlaE to secrete alanine. Several amino acid exporters exist, and it has been shown that they have important roles when bacteria are challenged with elevated levels of amino acids or amino acid analogues^{27,28,37}. However, their functions under natural growing conditions have remained unknown. Moreover, it has been unclear under which conditions could bacteria secrete amino acids. To the best of our knowledge, this study is the first to describe the role and importance of an amino acid exporter during bacterial growth. We showed that under anaerobic conditions cells can use the exporter AlaE to accumulate alanine in the extracellular space, which can be taken up by other cells. This exemplifies the importance to expand the research on this group of transporters in the context of bacterial communities.

The study of biofilm cross-feeding interactions can enable the comparison of tissue-like structures, such as biofilms, to eukaryotic systems. In particular, certain *B. subtilis* biofilms that can propagate an action potential have been compared to neurons in a nervous system³⁸. Remarkably, the here described alanine cross-feeding within *E. coli* colonies resembles the Cahill cycle (also called glucose-alanine cycle), that occurs between the muscle and liver of mammals³⁹. In this cycle, when muscles degrade amino acids for energy, alanine and α -ketoglutarate are produced from *L*-glutamate and pyruvate. Alanine is then transported to the liver, where its ammonia enters the urea cycle and the remaining pyruvate is converted into glucose. This represents an example on how bacterial systems via different evolutionary lineages, and for different reasons, can develop mechanisms that are found in multicellular organisms.

Methods

Media and strains. All *E. coli* strains used in this study are derivatives of the *E. coli* K-12 AR3110 strain⁴⁰. All strains carried a constitutively expressed fluorescent protein under the control of the tac promoter (P_{tac}) lacking the *lac* operator inserted in the chromosome at the *attB* site. To generate chromosomal deletions, the lambda red system was used to replace the target region with an antibiotic cassette flanked by FRT sites. Then, the Flp-FRT recombination system was utilized to remove the antibiotic cassette. All the strains, plasmids and oligonucleotides used are listed in Supplementary Table 3.1, Supplementary Table 3.2, Supplementary Table 3.3 respectively.

Cultures were grown in LB-Miller medium (10 g l⁻¹ NaCl, 10 g l⁻¹ tryptone, 5 g l⁻¹ yeast extract) or M9 minimal medium supplemented with 5 g l⁻¹ D-glucose. The M9 medium consisted of: 42.3 mM Na₂HPO₄ (Carl Roth, P030.2), 22 mM KH₂PO₄ (Carl Roth 3904.1), 11.3 mM (NH₄)₂SO₄ (Carl Roth 3746.2), 8.56 mM NaCl (Carl Roth, HN00.2), 0.1 mM CaCl₂ (Sigma-Aldrich, C5670), 1 mM MgSO₄, (Sigma-Aldrich, M2643), 60 μM FeCl₃ (Sigma-Aldrich, 31332), 2.8 μM thiamine-HCl (Sigma-Aldrich T4625), 6.3 μM ZnSO₄ (Sigma-Aldrich Z0251), 7 μM CuCl₂ (Sigma-Aldrich 307483), 7.1 μM MnSO₄ (Sigma-Aldrich M8179), 7.6 μM CoCl₂ (Carl Roth 7095.1). M9 agar plates were made using 8 mL of M9 supplemented with 5 g l⁻¹ D-glucose (hereafter called M9 medium for simplicity) with 1.5 % w/v agar-agar into 35x10 mm petri dishes (Sarstedt, 82.1135.500).

Colony biofilm growth. Cultures were inoculated from frozen glycerol stocks kept at -80°C into LB-Miller medium with kanamycin (50 μg mL⁻¹) and grown for 5 h at 37°C with shaking at 220 rpm. At this point, 1 μL of the culture were inoculated into 5 mL of M9 medium (without antibiotics), placed into a 100 mL Erlenmeyer flask and grown at 37°C with shaking at 220 rpm. The cultures were always kept in exponential phase by back-dilutions. Aliquots from these cultures were taken at different time points and their optical density at 600 nm (OD₆₀₀) were adjusted to have a determined number of colony forming units (CFU), which depended on the biomass needed. These bacterial suspensions were filtered using a 0.45 μm pore size polyvinylidene fluoride membrane filter of diameter 5 mm, unless stated otherwise. The filters carrying the cells were placed on top of M9 agar plates and incubated at 37°C for up to 72 h.

Microscopy. All imaging was performed using a Yokogawa spinning-disc confocal unit mounted on a Nikon Ti-E inverted microscope. A 40x air extra-long working distance (ELWD) objective (numerical aperture (NA) 0.60, Nikon) was used for all imaging, except for mutant screening (Supplementary Fig. 3.7) where a 4x air objective (NA 0.13, Nikon) was used, and single-cell imaging (Supplementary Fig. 3.5a) where a 100x oil objective (NA 0.4, Nikon) was used. All imaging was done

using an incubator kept at 37 °C. To avoid imaging through the filter, colonies were imaged facing down and the Petri dish lid was removed. To avoid loss of humidity, the stage was sealed with foil. To avoid condensation on the objective it was kept warm using a heating ring at 37 °C.

Colony detection and biovolume measurements with adaptive microscopy. When the colony growth of the wild type *E. coli* strain AR3110 was analysed, cells swimming on the filters and in between the colonies were observed. These cells caused heterogeneous colony growth and shape (Supplementary Fig. 3.1). To avoid this, all subsequently experiments were performed using a flagella-deficient ($\Delta fliC$) strain, termed as parental strain. This strain did not present swimming bacteria, and the colonies were homogenous in growth rate and shape (Fig. 3.1b and Supplementary Fig. 3.1).

For biomass determination, colonies were grown as explained above with the addition of 0.2 μm dark red fluorescent beads (Invitrogen, F8807) to the bacterial suspension prior to filtering. Using adaptive microscopy these beads were used to find and focus the correct focal plane for imaging. At 12 h, 18 h, 24 h, 32 h, 42 h, 48 h, 60 h and 72 h of colony growth, plates containing the filters were imaged. The complete membrane filter was imaged using a custom-made MATLAB (version 2019b, Mathworks) script and the number of colonies were determined. Subsequently, several randomly selected colonies were imaged in 3D and the biovolume was calculated. To obtain the biovolume, the outline of the colony was identified by thresholding the image gradient in each z-slice. The convex area of this binary image was then used as a measure for the biomass present in this plane such that summation over all slices followed by multiplication with the appropriate μm^3 volume per voxel yielded the overall biovolume.

Liquid growth assays. Cultures were inoculated from -80 °C frozen stocks into LB-Miller media and grown for 5 hours at 37 °C with shaking at 220 rpm. Each culture was back-diluted 5,000-fold into 5 mL of M9 medium placed into a 100 mL Erlenmeyer flask, and grown at 37 °C with shaking at 220 rpm. At an OD_{600} of 0.3 they were washed 2 times in M9 lacking glucose and ammonium and resuspended in the same volume of the corresponding media. These bacterial solutions were diluted ten times and placed in a 96-well plate (Sarstedt, 82.1581.001). They were grown at 37 °C with shaking in using a microtiter plate reader (Epoch2, Biotek). Data was analysed using MATLAB (version 2019b, Mathworks)

Measurement of extracellular alanine in liquid culture supernatants. Cultures were inoculated from frozen -80 °C stocks into LB-Miller media with kanamycin (50 $\mu\text{g mL}^{-1}$) and grown for 5 hours at 37 °C with shaking at 220 rpm. The cultures were back-diluted 5,000-fold into 5 mL of M9 medium placed into a 100 mL Erlenmeyer flask and grown at 37 °C with shaking at 220 rpm. They were kept in exponential phase by back-dilutions. At an OD_{600} of 0.3 the cultures were centrifuged at 14,000 g for 2

min. For aerobic growth conditions, the pellets were suspended in M9 supplemented with glucose and the OD₆₀₀ was adjusted to 0.1. For aerobic starvation conditions, the pellets were suspended in same volume of M9 lacking ammonium but supplemented with glucose, M9 lacking glucose but supplemented with ammonium, or M9 without glucose or ammonium. They were grown in Erlenmeyer flasks at 37 °C with shaking at 220 rpm as previously. For anaerobic conditions, the pellets were suspended in the corresponding medium and placed in a closed 15 mL conical centrifuge tube filled to the top. The tubes were placed horizontally and incubated at 37 °C with shaking at 100 rpm. For starving conditions, the samples were taken after 2 h of incubation. For aerobic and anaerobic growing conditions, samples were taken during exponential growing phase. Samples were taken and analysed using metabolomics as described below.

Sample preparation for metabolomics. To measure metabolites in colonies over time, filters with grown colonies were transferred into 150 µL 40:40:20 (v/v) acetonitrile/methanol/water at -20°C for metabolite extraction. A crystal bead was used to disrupt the colonies while vortexing.

To measure extracellular metabolites from colonies, the filters with colonies were resuspended in 1 mL PBS at 37°C. The suspension was vacuum-filtered using a 0.45 µm pore size filter (HVLPO2500, Merck Millipore) and of the 100 µL flow-through were mixed with 400 µL 50:50 (v/v) acetonitrile/methanol at -20°C.

To measure extracellular metabolites from liquid cultures, 1 mL of grown cultures were filtered on a 0.45 µm pore size filter (HVLPO2500, Merck Millipore). 100 µL flow through were mixed with 400 µL 50:50 (v/v) acetonitrile/methanol at -20°C.

All extracts were centrifuged for 15 minutes at 11,000 g at -9 °C and stored at -80 °C.

Mass spectrometry measurements. For metabolomics, centrifuged extracts were mixed with ¹³C-labeled internal standards. Chromatographic separation was performed on an Agilent 1290 Infinity II LC System (Agilent Technologies) equipped with an Acquity UPLC BEH Amide column (2.1 x 30 mm, particle size 1.8 µm, Waters) for acidic conditions and an iHilic-Fusion (P) HPLC column (2.1 x 50 mm, particle size 5 µm, Hilicon) for basic conditions. The following binary gradients with a flow rate of 400 µl min⁻¹ were applied. Acidic condition: 0-1.3 min isocratic 10% A (water with 0.1% v/v formic acid, 10 mM ammonium formate), 90% B (acetonitrile with 0.1% v/v formic acid,), 1.3-1.5 min linear from 90% to 40% B; 1.5-1.7 min linear from 40% to 90% B, 1.7-2 min isocratic 90% B. Basic condition: 0-1.3 min isocratic 10% A (water with formic acid 0.2% (v/v), 10 mM ammonium carbonate),

90% B (acetonitrile); 1.3-1.5 min linear from 90% to 40% B; 1.5-1.7 min linear from 40% to 90% B, 1.7-2 min isocratic 90% B. The injection volume was 3.0 μ l (full loop injection).

Ions were detected using an Agilent 6495 triple quadrupole mass spectrometer (Agilent Technologies) equipped with an Agilent Jet Stream electrospray ion source in positive and negative ion mode. The source gas temperature was set to 200 °C, with 14 L min⁻¹ drying gas and a nebulizer pressure of 24 psi. Sheath gas temperature was set to 300 °C and the flow to 11 L min⁻¹. Electrospray nozzle and capillary voltages were set to 500 and 2500 V, respectively. Metabolites were identified by multiple reaction monitoring (MRM). MRM parameters were optimized and validated with authentic standards⁴¹. Metabolites were measured in ¹²C- and ¹³C isoforms, and the data was analysed with a published Matlab code⁴¹.

Data analysis for metabolomics. For colony average measurements the mass spectrometry measurements were normalized by the total biovolume measured with confocal imaging. For liquid culture experiments, the mass spectrometry measurements were normalized by OD₆₀₀. For colony extracellular measurements (Fig 3.3b), the mass spectrometry measurements were normalized by colony number and average colony volume.

To create heatmaps of the metabolomic dynamics the software Genesis was used⁴².

Transcriptomics. Colonies were grown as previously described. At 12 h, 18 h, 24 h, 32 h, 42 h, 48 h, 60 h and 72 h of growth, filters with the colonies were immediately frozen using liquid nitrogen and stored at -80 °C. Afterwards, samples were thawed at room temperature. A crystal bead and 600 μ l of cell lysis buffer were added. Lysis buffer consisted of TE (10 mM Tris, adjusted to pH 8.0 with HCl, 1 mM EDTA) and 1 mg/mL of chicken egg lysozyme (Sigma, L6876). The colonies were disrupted by vortexing and the cell suspension was moved to a new tube. Then, total RNA was extracted using a previously described hot SDS/phenol method⁴³ with some modifications as follows. Cells were lysed at 65°C for 2 min in the presence of 1% (w/v) SDS, and the lysate was incubated with 750 μ l of Roti-Aqua-Phenol (Carl Roth, A980) at 65 °C for 8 min, followed by the addition of 750 μ l chloroform (Sigma, C2432) to the aqueous phase and centrifugation using a phase lock gel tube (VWR, 733-2478). RNA was purified by ethanol precipitation and dissolved in 60 μ l of RNase-free water. Samples were then treated with TURBO DNase (Thermo Fisher, AM2238) and rRNA depletion was performed using Ribo-Zero rRNA Removal Kit (Bacteria) (Illumina, MRZB12424). Library preparation was carried out using NEBNext Ultra II Directional RNA Library Prep with Sample Purification Beads (NEB, E7765S). Sequencing was carried out at Max Planck-Genome-centre Cologne (Germany) using an Illumina HiSeq3000 with 150 bp single reads. All transcriptomic analysis was performed using the software CLC Genomics Workbench 11.0

(<https://digitalinsights.qiagen.com>). The *E. coli* K-12 W3310 genome⁴⁴, parental strain of *E. coli* AR3110⁴⁰, was used as reference for annotation. For heatmap creation, clustering of transcripts was performed using the software Genesis⁴².

Spatial transcriptomics. Filters carrying 72 h colonies were put into a 2 mL tube. Cells were suspended in 1 mL of phosphate-buffered saline (PBS; 8 g l⁻¹ NaCl, 0.2 g l⁻¹ KCl, 1.44 g l⁻¹ Na₂HPO₄, 0.24 g l⁻¹ KH₂PO₄, pH 7.4) by vortexing and pipetting, and fixed with 4 % formaldehyde (Sigma, F8775) for 10 min at room temperature. Formaldehyde fixation did not affect the transcriptomic profile or the fluorescence intensity (Supplementary Fig. 3.11). Then, cells were washed three times with PBS and the cell suspension was filtered with a 5 µm pore size filter (Sartorius, 17594) to remove aggregates. Cells were sorted according to fluorescence using a FACS machine (BD FACSAria Fusion). Approximately 10e6 cells were collected in 10 mL of PBS. To concentrate the samples, they were vacuum-filtered using a 0.45 µm membrane filter (Millipore, HVLP02500). The filters containing the cells were suspended in 400 µL of the lysis buffer (same components as above). The suspension was frozen in liquid nitrogen and preserved at -80 °C.

Total RNA was extracted using the same hot SDS/phenol method with the following optimization to minimize the steps and loss of RNA; after treatment with phenol, both aqueous and organic phase were directly transferred to a phase lock gel tube (VWR, 733-2478) without centrifugation. Chloroform was added and centrifuged at 15,000 rpm for 15 min at 12°C. After centrifugation, RNA in the aqueous phase was purified and collected in 10 µL of RNase-free water using Agencourt RNAClean XP (Beckman Coulter, A63987) according to the manufacturer's recommendations. Samples were then treated with TURBO DNase (Thermo Fisher, AM2238) and rRNA depletion was performed using Ribo-Zero rRNA Removal Kit (Bacteria) (Illumina, MRZB12424). Library preparation was carried out using NEBNext Ultra II Directional RNA Library Prep with Sample Purification Beads (NEB, E7765S). Sequencing was carried out at Max Planck-Genome-Centre (Cologne, Germany) using an Illumina HiSeq3000 with 150 bp single reads.

Measurements of biomass death. To measure the amount of dead biomass within colonies, the colonies were grown as before with the exception that Sytox Green (ThermoFisher, S7020) with a final concentration of 2.5 µM was added to the M9 agar plates. After 72 h the colonies were imaged and analysed. Fluorescent areas in both the live and dead channels were identified via thresholding. The fraction of dead biomass was calculated as the ratio between fluorescent volume present in both the live and dead channel, divided by all fluorescent volume present in the live channel. To measure the

dead biomass in the aerobic region of the colony, only cells at 30 μm or closer to the surface of the colony were considered.

To measure the amount of dead biomass in liquid cultures, exponentially growing cultures were incubated in a 96-well plate with the corresponding media and in presence of Sytox Green (2.5 μM) at 37°C. The OD₆₀₀ and Sytox Green fluorescence were measured using a microtiter plater reader (Spark 10M, Tecan). The dead biomass was calculated as the Sytox Green fluorescence normalized by the OD₆₀₀.

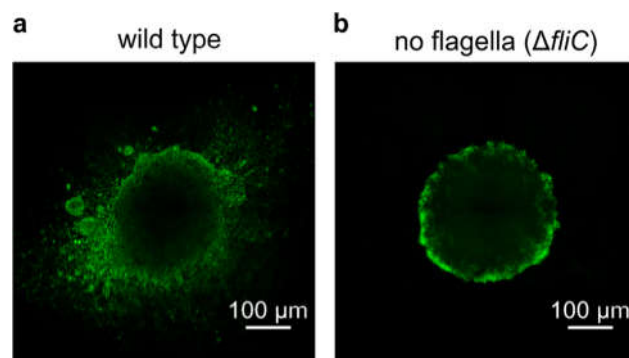
Statistical analysis. All statistical analysis was carried out using GraphPad version 8 for Mac (GraphPad Software, San Diego, California USA, www.graphpad.com). Prism 8 for Mac, except for the statistical analysis for transcriptomic data that was performed using the software CLC Genomics Workbench 11.0 (<https://digitalinsights.qiagen.com>).

References

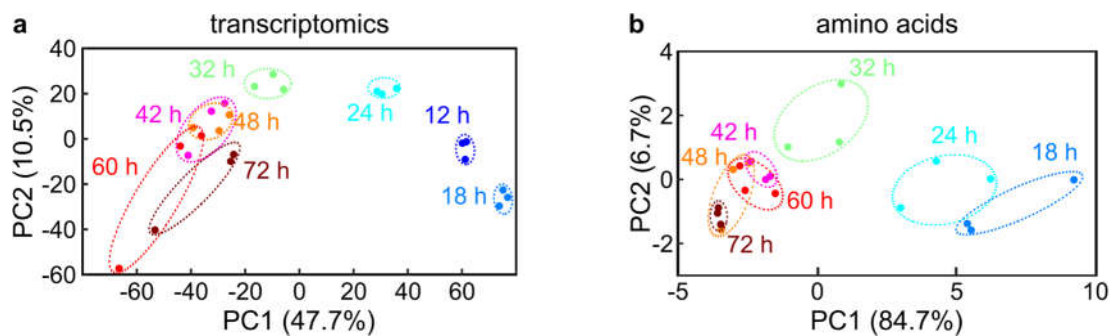
1. Stewart, P. S. & Franklin, M. J. Physiological heterogeneity in biofilms. *Nat. Rev. Microbiol.* **6**, 199–210 (2008).
2. Flemming, H.-C. & Wuertz, S. Bacteria and archaea on Earth and their abundance in biofilms. *Nat. Rev. Microbiol.* **17**, 247–260 (2019).
3. Ackermann, M. A functional perspective on phenotypic heterogeneity in microorganisms. *Nat. Rev. Microbiol.* **13**, 497–508 (2015).
4. Evans, C. R., Kempes, C. P., Price-Whelan, A. & Dietrich, L. E. P. Metabolic Heterogeneity and Cross-Feeding in Bacterial Multicellular Systems. *Trends Microbiol.* **2020**, 1–12 (2020).
5. van Vliet, S. *et al.* Spatially Correlated Gene Expression in Bacterial Groups: The Role of Lineage History, Spatial Gradients, and Cell-Cell Interactions. *Cell Syst.* **6**, 496-507.e6 (2018).
6. Schreiber, F. & Ackermann, M. Environmental drivers of metabolic heterogeneity in clonal microbial populations. *Curr. Opin. Biotechnol.* **62**, 202–211 (2020).
7. San Roman, M. & Wagner, A. An enormous potential for niche construction through bacterial cross-feeding in a homogeneous environment. *PLOS Comput. Biol.* **14**, e1006340 (2018).
8. Smith, N. W., Shorten, P. R., Altermann, E., Roy, N. C. & McNabb, W. C. The Classification and Evolution of Bacterial Cross-Feeding. *Front. Ecol. Evol.* **7**, 1–15 (2019).
9. Yang, Y.-L., Xu, Y., Straight, P. & Dorrestein, P. C. Translating metabolic exchange with imaging mass spectrometry. *Nat. Chem. Biol.* **5**, 885–887 (2009).
10. Watrous, J. D. *et al.* Microbial metabolic exchange in 3D. *ISME J.* **7**, 770–780 (2013).
11. Moree, W. J. *et al.* Interkingdom metabolic transformations captured by microbial imaging mass spectrometry. *Proc. Natl. Acad. Sci.* **109**, 13811–13816 (2012).
12. Kim, D. *et al.* *Candida albicans* stimulates *Streptococcus mutans* microcolony development via cross-kingdom biofilm-derived metabolites. *Sci. Rep.* **7**, 41332 (2017).
13. Henson, M. A., Orazi, G., Phalak, P. & O’Toole, G. A. Metabolic Modeling of Cystic Fibrosis Airway Communities Predicts Mechanisms of Pathogen Dominance. *mSystems* **4**, 1–20 (2019).
14. Rosenthal, A. Z. *et al.* Metabolic interactions between dynamic bacterial subpopulations. *Elife* **7**, 1–18 (2018).
15. Nikolic, N. *et al.* Cell-to-cell variation and specialization in sugar metabolism in clonal bacterial populations. *PLoS Genet.* **13**, 1–24 (2017).
16. Wolfsberg, E., Long, C. P. & Antoniewicz, M. R. Metabolism in dense microbial colonies: ¹³C metabolic flux analysis of *E. coli* grown on agar identifies two distinct cell populations with acetate cross-feeding. *Metab. Eng.* **49**, 242–247 (2018).
17. Cole, J. A., Kohler, L., Hedhli, J. & Luthey-Schulten, Z. Spatially-resolved metabolic cooperativity within dense bacterial colonies. *BMC Syst. Biol.* **9**, 15 (2015).
18. Liu, J. *et al.* Metabolic co-dependence gives rise to collective oscillations within biofilms. *Nature* **523**, 550–554 (2015).
19. Lin, Y., Cornell, W. C., Jo, J., Price-Whelan, A. & Dietrich, L. E. P. The *Pseudomonas aeruginosa* Complement of Lactate Dehydrogenases Enables Use of D- and L-Lactate and Metabolic Cross-Feeding. *MBio* **9**, 1–12 (2018).
20. Pisithkul, T. *et al.* Metabolic Remodeling during Biofilm Development of *Bacillus subtilis*. *MBio* **10**, 1–32 (2019).
21. Qin, Y. *et al.* Heterogeneity in respiratory electron transfer and adaptive iron utilization in a bacterial biofilm. *Nat. Commun.* **10**, 3702 (2019).
22. Şimşek, E. & Kim, M. The emergence of metabolic heterogeneity and diverse growth responses in isogenic bacterial cells. *ISME J.* **12**, 1199–1209 (2018).
23. Co, A. D., Van Vliet, S. & Ackermann, M. Emergent microscale gradients give rise to metabolic cross-feeding and antibiotic tolerance in clonal bacterial populations. *Philos. Trans. R. Soc. B Biol. Sci.* **374**, (2019).
24. Williamson, K. S. *et al.* Heterogeneity in *Pseudomonas aeruginosa* biofilms includes expression of ribosome hibernation factors in the antibiotic-tolerant subpopulation and hypoxia-induced stress

- response in the metabolically active population. *J. Bacteriol.* **194**, 2062–2073 (2012).
25. Schiessl, K. T. *et al.* Phenazine production promotes antibiotic tolerance and metabolic heterogeneity in *Pseudomonas aeruginosa* biofilms. *Nat. Commun.* **10**, 762 (2019).
 26. Pande, S. *et al.* Privatization of cooperative benefits stabilizes mutualistic cross-feeding interactions in spatially structured environments. *ISME J.* **10**, 1413–1423 (2016).
 27. Tsuchiya, H. *et al.* Structural basis for amino acid export by DMT superfamily transporter YddG. *Nature* **534**, 417–20 (2016).
 28. Katsube, S., Ando, T. & Yoneyama, H. L-Alanine Exporter, AlaE, of *Escherichia coli* Functions as a Safety Valve to Enhance Survival under Feast Conditions. *Int. J. Mol. Sci.* **20**, 4942 (2019).
 29. Franke, I., Resch, A., Dassler, T., Maier, T. & Bock, A. YfiK from *Escherichia coli* Promotes Export of O-Acetyserine and Cysteine. *J. Bacteriol.* **185**, 1161–1166 (2003).
 30. Warren, M. R. *et al.* Spatiotemporal establishment of dense bacterial colonies growing on hard agar. *Elife* **8**, 1–47 (2019).
 31. Baisa, G., Stabo, N. J. & Welch, R. A. Characterization of *Escherichia coli* D-cycloserine transport and resistant mutants. *J. Bacteriol.* **195**, 1389–99 (2013).
 32. Hori, H. *et al.* Inducible L-alanine exporter encoded by the novel gene *ygaW* (*alaE*) in *Escherichia coli*. *Appl. Environ. Microbiol.* **77**, 4027–34 (2011).
 33. Tsien, R. Y. The green fluorescent protein. *Annu. Rev. Biochem.* **67**, 509–44 (1998).
 34. Lobočka, M., Hennig, J., Wild, J. & Kłopotowski, T. Organization and expression of the *Escherichia coli* K-12 *dad* operon encoding the smaller subunit of D-amino acid dehydrogenase and the catabolic alanine racemase. *J. Bacteriol.* **176**, 1500–10 (1994).
 35. Katsube, S., Sato, K., Ando, T., Isogai, E. & Yoneyama, H. Secretion of d-alanine by *Escherichia coli*. *Microbiology* **162**, 1243–1252 (2016).
 36. Pirt, S. J. A kinetic study of the mode of growth of surface colonies of bacteria and fungi. *J. Gen. Microbiol.* **47**, 181–97 (1967).
 37. Nandineni, M. R. & Gowrishankar, J. Evidence for an Arginine Exporter Encoded by *yggA* (*argO*) That Is Regulated by the LysR-Type Transcriptional Regulator ArgP in *Escherichia coli*. *J. Bacteriol.* **186**, 3539–3546 (2004).
 38. Prindle, A. *et al.* Ion channels enable electrical communication in bacterial communities. *Nature* **527**, 59–63 (2015).
 39. Felig, P. The glucose-alanine cycle. *Metabolism.* **22**, 179–207 (1973).
 40. Serra, D. O., Richter, A. M. & Hengge, R. Cellulose as an Architectural Element in Spatially Structured *Escherichia coli* Biofilms. *J. Bacteriol.* **195**, 5540–5554 (2013).
 41. Guder, J. C., Schramm, T., Sander, T. & Link, H. Time-Optimized Isotope Ratio LC–MS/MS for High-Throughput Quantification of Primary Metabolites. *Anal. Chem.* **89**, 1624–1631 (2017).
 42. Sturn, A., Quackenbush, J. & Trajanoski, Z. Genesis: cluster analysis of microarray data. *Bioinformatics* **18**, 207–8 (2002).
 43. Jahn, C. E., Charkowski, A. O. & Willis, D. K. Evaluation of isolation methods and RNA integrity for bacterial RNA quantitation. *J. Microbiol. Methods* **75**, 318–24 (2008).
 44. Hayashi, K. *et al.* Highly accurate genome sequences of *Escherichia coli* K-12 strains MG1655 and W3110. *Mol. Syst. Biol.* **2**, (2006).
 45. Vidakovic, L., Singh, P. K., Hartmann, R., Nadell, C. D. & Drescher, K. Dynamic biofilm architecture confers individual and collective mechanisms of viral protection. *Nat. Microbiol.* **3**, 26–31 (2018).
 46. Datsenko, K. A. & Wanner, B. L. One-step inactivation of chromosomal genes in *Escherichia coli* K-12 using PCR products. *Proc. Natl. Acad. Sci. U. S. A.* **97**, 6640–5 (2000).
 47. Cherepanov, P. P. & Wackernagel, W. Gene disruption in *Escherichia coli*: TcR and KmR cassettes with the option of Flp-catalyzed excision of the antibiotic-resistance determinant. *Gene* **158**, 9–14 (1995).

Supplementary information

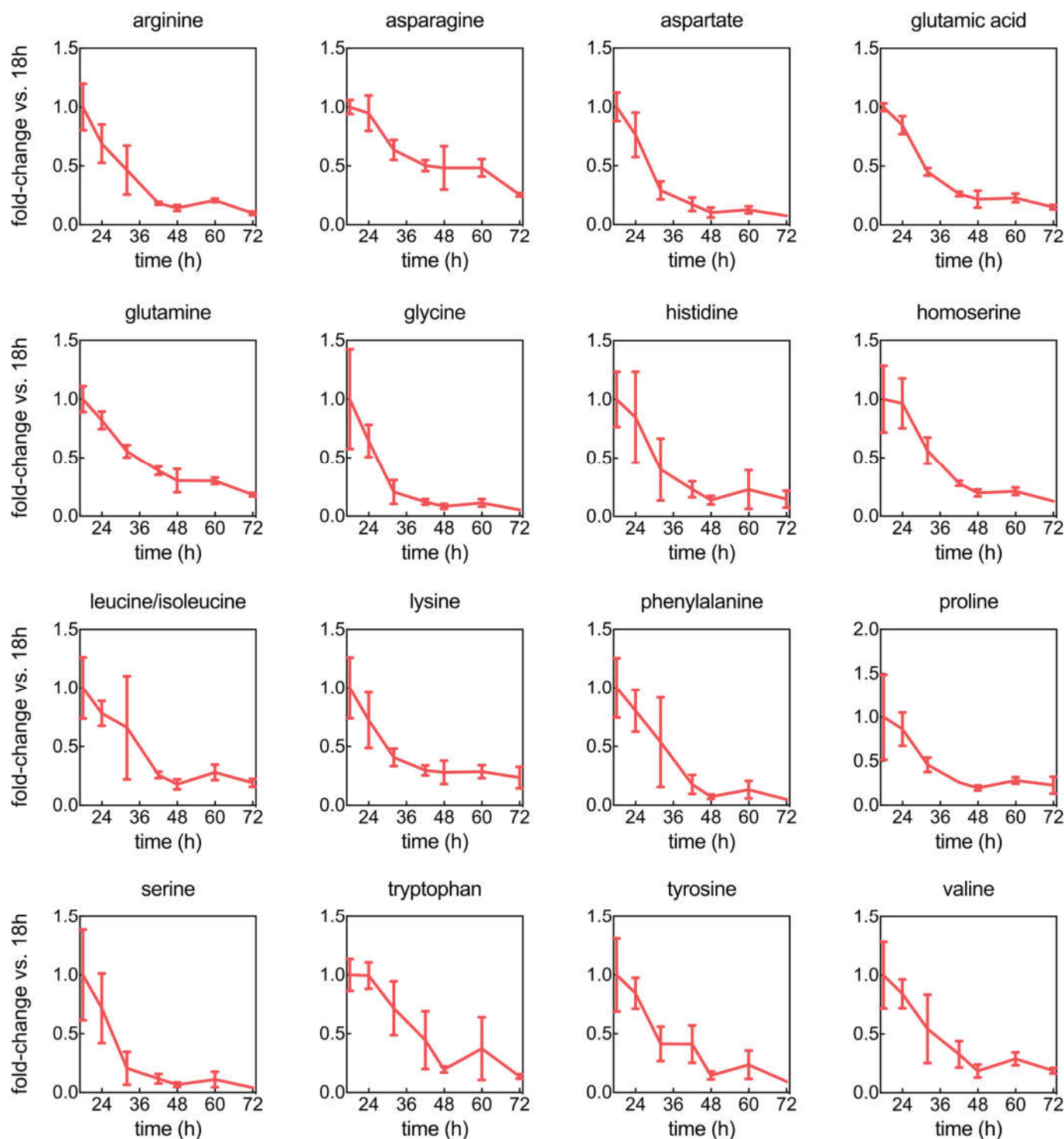


Supplementary Figure 3.1. In contrast to wild-type colonies, flagella-deficient ($\Delta fliC$) colonies are homogeneous in size and shape. Snapshots of xy -planes of colonies made by the wild type strain (a) or a strain lacking the flagellar gene *fliC* (b) grown for 24 h.

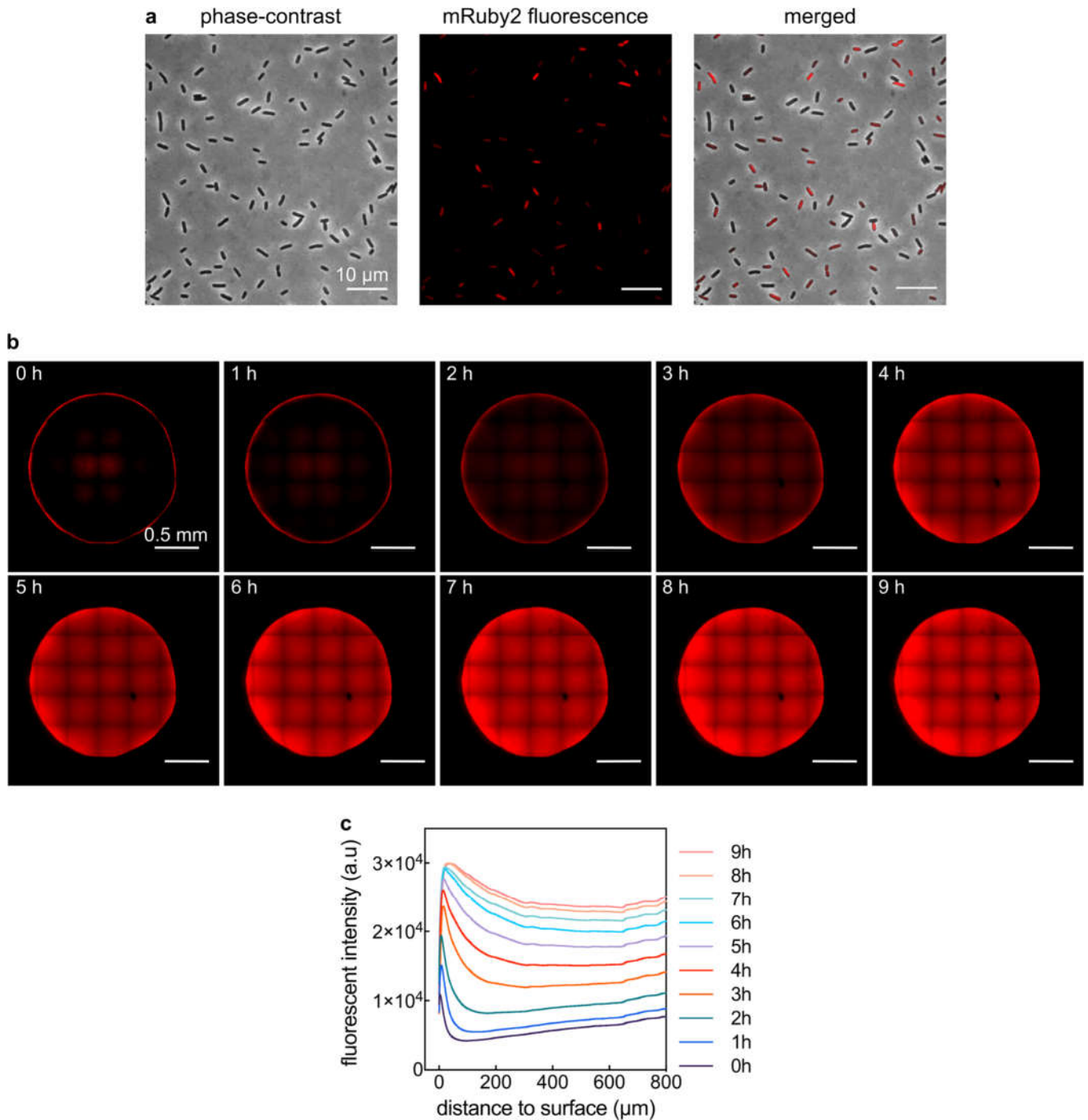


Supplementary Figure 3.2. Principal component analysis of transcriptomic and metabolomic data. (a) Principal component analysis (PCA) of transcriptomic data presented in Fig. 3.1c. (b) Principal component analysis (PCA) of amino acid data presented in Fig. 3.1e. Each circle represents a different independent replicate.

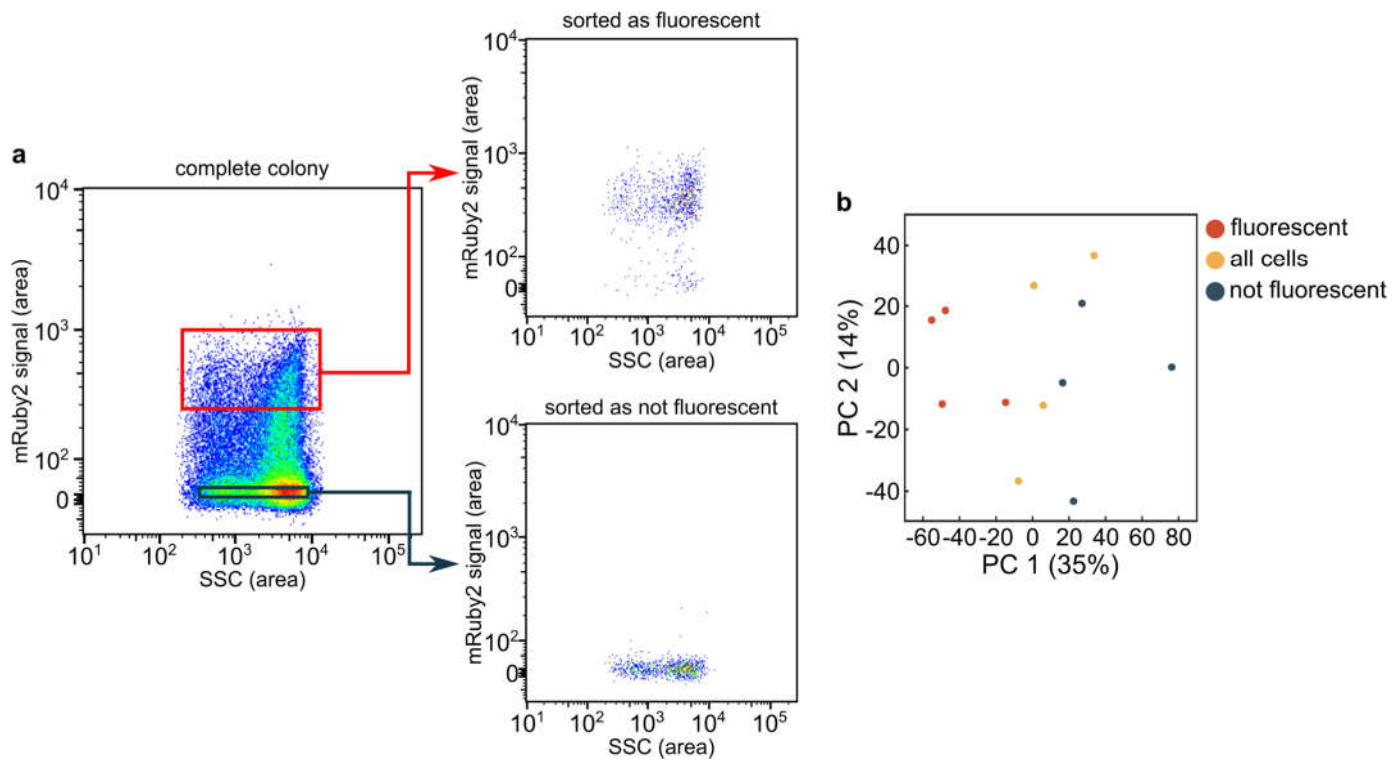
Chapter III: Spatiotemporal multi-omic analysis of *Escherichia coli* biofilm colonies reveals a novel cross-feeding of alanine



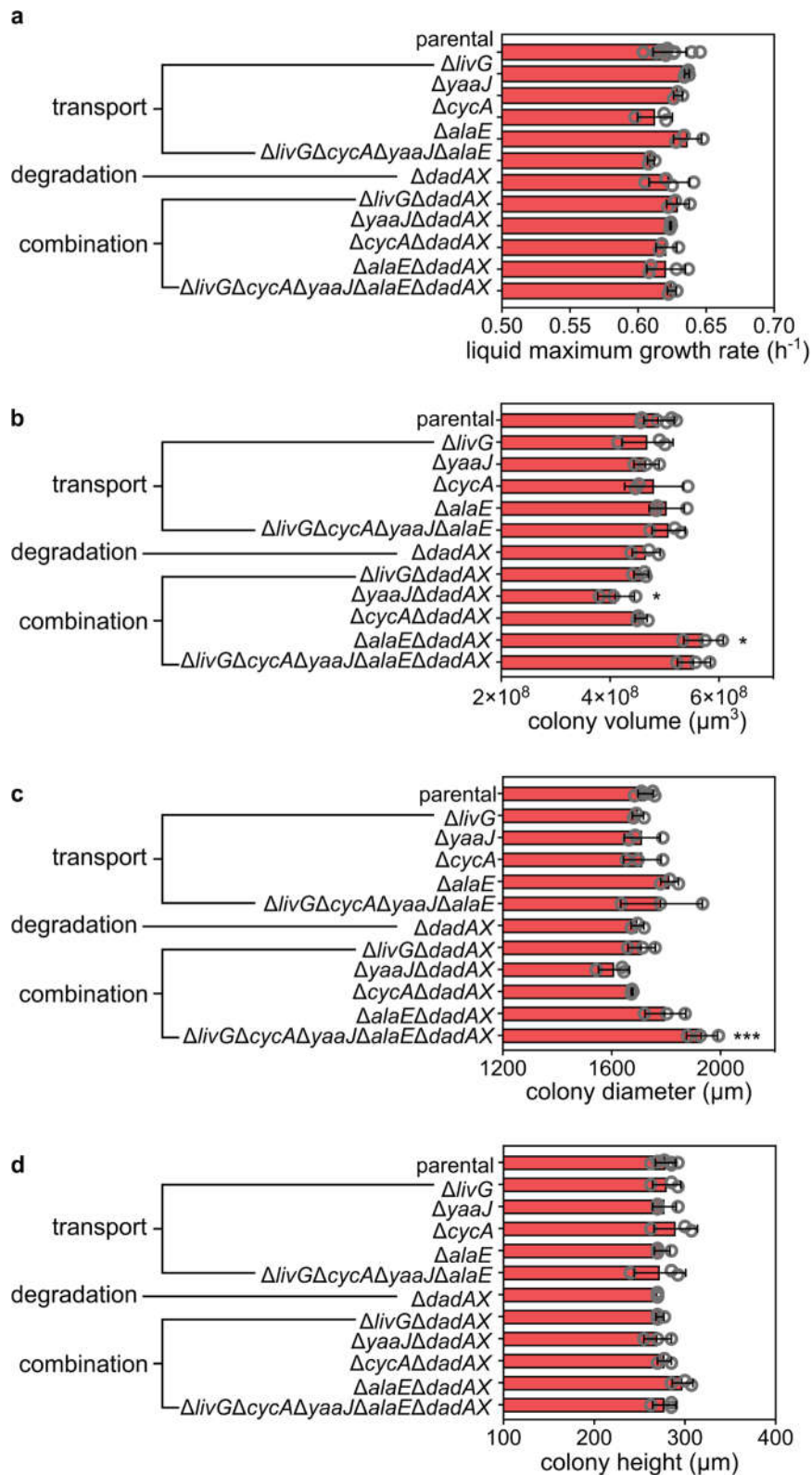
Supplementary Figure 3.4. Amino acid levels during colony growth. Fold-changes of amino acids levels in function of time during colony development in comparison to 18 h colonies. Data are mean \pm s.d., $n = 3$.



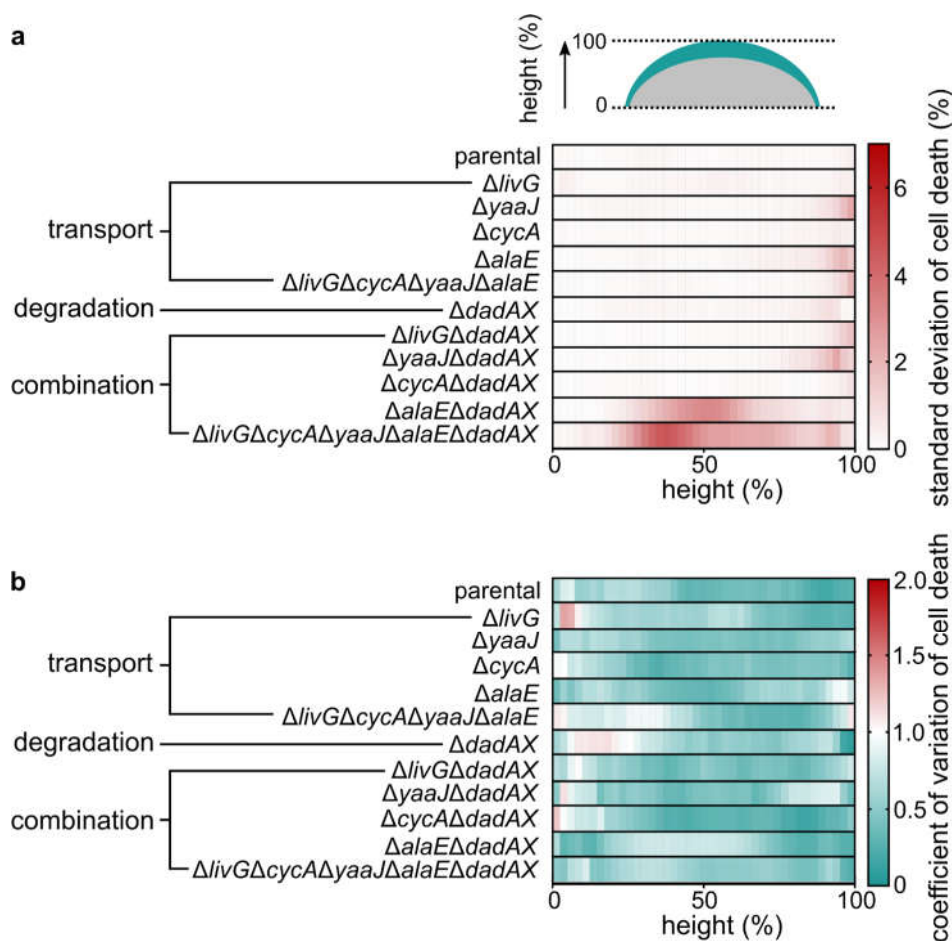
Supplementary Figure 3.5. Fluorescent gradients observed in colonies are not due to imaging artefacts. (a) Snapshot of cells coming from a 72 h colony resuspended in PBS. (b) Snapshots of a *xy*-plane of 72 h colony 60 μm above the substrate. At 0 h the colony was moved to a solid agar plate with the same medium, but lacking glucose. Cells stop consuming molecular oxygen allowing it to penetrate into the colony. (c) Quantification of **b**. Fluorescent intensity in function of distance to colony surface.



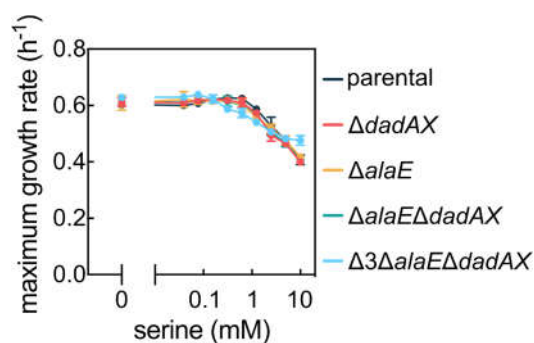
Supplementary Figure 3.6. Sorting of cells according to their fluorescence. (a) Representative sorting of a 72 h colony according to mRuby2 fluorescence using FACS. (b) Principal component analysis RNA-seq of 72 h colonies sorted according to fluorescence. Each data point corresponds to an independent replicate.



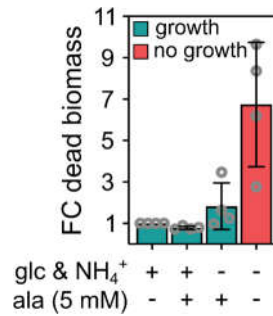
Supplementary Figure 3.7. Growth rate and colony size for alanine mutants. (a) Maximum growth rate in batch cultures. Colony volume (b), diameter (c) and height (d) at 72 h of growth. Data are mean \pm s.d., each data point is shown as a grey circle. Statistical significances are calculated in comparison to the parental strain using a one-way ANOVA with Bonferroni's correction for multiple comparisons. If no significance is shown it means data was not significantly different from the parental strain. * p -value $<$ 0.05, ** p -value $<$ 0.01.



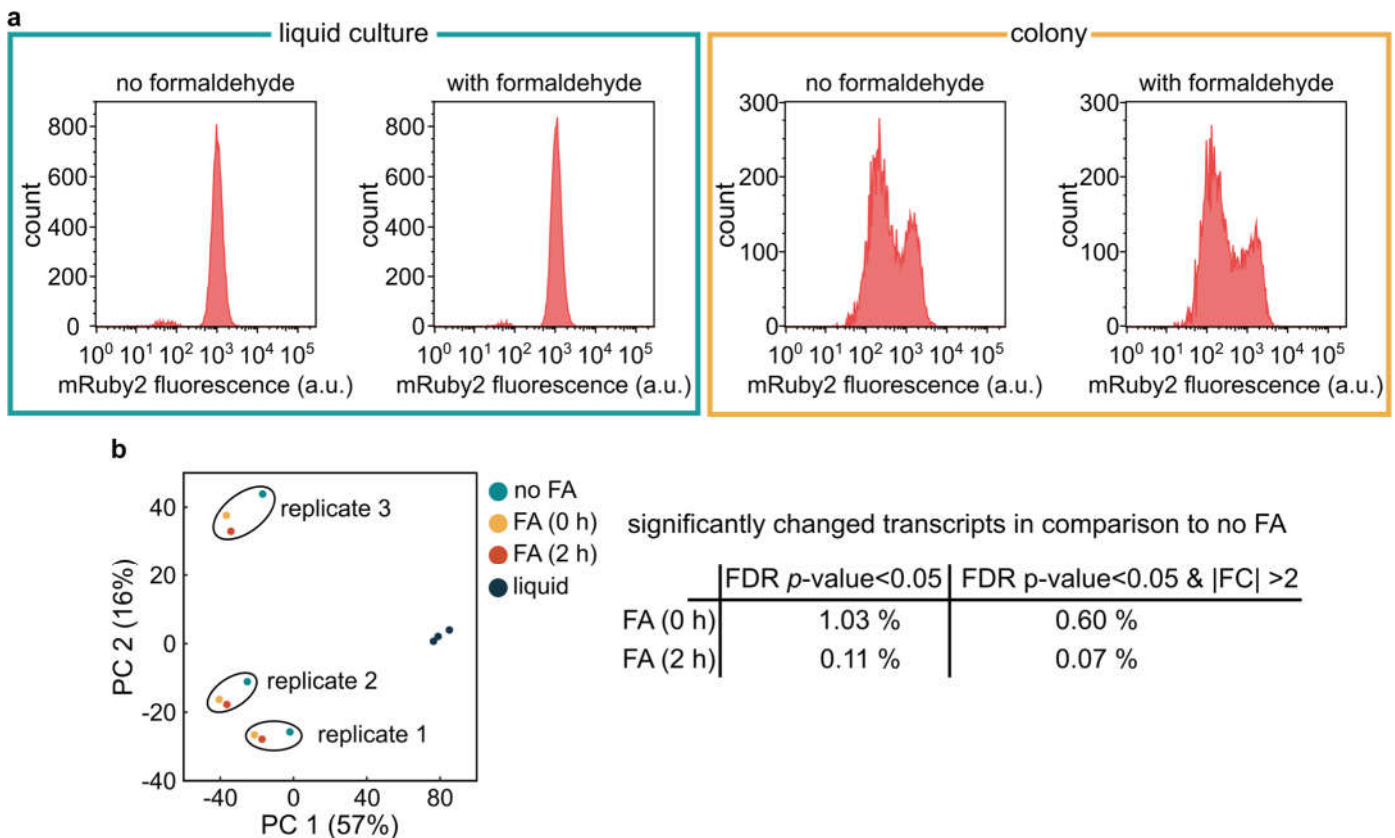
Supplementary Figure 3.8 Standard deviation and coefficient of variation for colony spatial cell death. Heatmaps with the standard deviations (a) and coefficient of variation (b) for the data shown in Fig. 3.3a.



Supplementary Figure 3.9. Effects of alanine on maximum growth rate are specific to alanine. Maximum liquid culture growth rate in function of the concentration of exogenically added serine. $\Delta 3$ corresponds to $\Delta livG \Delta cycA \Delta yaaJ$. Data are mean \pm s.d., $n=3$.



Supplementary Figure 3.10. Dead biomass, measured as Sytox Green fluorescence normalized by the optical density at 600 nm (OD₆₀₀). The timepoints chosen corresponded to when the cultures reached half the maximum OD₆₀₀ for (cultures that presented growth, depicted in green) or after 24 hours of incubation (for cultures that did not present growth; shown in red). Values were normalized by the culture growing on glc and NH₄⁺ lacking alanine (first column). When used, alanine had a final concentration of 5 mM. Data are mean ± s.d., *n* = 4.



Supplementary Figure 3.11. Formaldehyde fixation does not affect fluorescence or transcriptome. (a) Fluorescence of *E. coli* constitutively expressing mRuby2 with or without 2 hours of formaldehyde (FA) fixation. On the left *E. coli* was grown on a batch culture, and on the right as a colony. (b) Principal component analysis of the transcriptomic profile of 72 h fixed with FA for 0 h, 2 h or without fixation. As control cells from a batch culture were also analysed. Each data dot corresponds to an independent replicate. On the right, as a table, are the number of differentially expressed genes in comparison to the not fixated condition. As threshold either a FDR *p*-value < 0.05, or a FDR *p*-value < 0.05 and an absolute fold-change (FC) > 2 were used

Supplementary Table 3.1: Bacterial strains used in this study

Strain	Genotype/ Relevant features	Reference
KDE261	<i>E. coli</i> strain carrying plasmid pCP20	Drescher lab stock
KDE262	<i>E. coli</i> strain carrying plasmid pKD46	Drescher lab stock
KDE264	<i>E. coli</i> strain carrying plasmid pKD3	Drescher lab stock
KDE265	<i>E. coli</i> strain carrying plasmid pKD4	Drescher lab stock
KDE474	<i>E. coli</i> AR3110 WT	Serra <i>et al.</i> ⁴⁰
KDE2338	<i>E. coli</i> strain carrying plasmid pNUT2338	Drescher lab stock
KDE679	AR3110, P _{tac} - <i>mRuby2-mRuby2</i> and Kan ^R inserted at <i>attB</i> site (P _{tac} without operator).	Drescher lab stock ⁴⁵
KDE722	KDE679 with $\Delta fliC::scar$	Drescher lab stock ⁴⁵
KDE1899	AR3110, $\Delta fliC::scar$	This study
KDE2007	KDE679 with $\Delta fliC::scar$, $\Delta alaE::scar$	This study
KDE2009	KDE679 with $\Delta fliC::scar$, $\Delta dadAX::scar$	This study
KDE2086	KDE679 with $\Delta fliC::scar$, $\Delta alaE::scar$, $\Delta dadAX::scar$	This study
KDE2183	KDE679 with $\Delta fliC::scar$, $\Delta cycA::scar$	This study
KDE2185	KDE679 with $\Delta fliC::scar$, $\Delta livG::scar$	This study
KDE2438	KDE679 with $\Delta fliC::scar$, $\Delta yaaJ::scar$	This study
KDE2533	KDE679 with $\Delta fliC::scar$, $\Delta cycA::scar$, $\Delta livG::scar$, $\Delta alaE::scar$, $\Delta yaaJ::scar$	This study
KDE2564	KDE679 with $\Delta fliC::scar$, $\Delta cycA::scar$, $\Delta dadAX::scar$	This study
KDE2607	KDE679 with $\Delta fliC::scar$, $\Delta yaaJ::scar$, $\Delta dadAX::scar$	This study
KDE2638	KDE679 with $\Delta fliC::scar$, $\Delta cycA::scar$, $\Delta livG::scar$, $\Delta alaE::scar$, $\Delta yaaJ::scar$, $\Delta dadAX::scar$	This study

Abbreviations: Kan = kanamycin. Superscript "R" = resistance. "-" = fusion. "::" = insertion.

Scar corresponds to 5'-GAAGTTCCTATACTTTCTAGAGAATAGGAACTTC-3'

Supplementary Table 3.2: Plasmids used in this study

Plasmid	Genotype/ Relevant features	Reference
pKD3	Temperature sensitive replication, chloramphenicol acetyl transferase cassette flanked <i>by frt</i> , Amp ^R	Datsenko & Wanner ⁴⁶
pKD4	Temperature sensitive replication, Tn5 neomycin phosphotransferase cassette flanked <i>by frt</i> , Amp ^R	Datsenko & Wanner ⁴⁶
pKD46	Temperature sensitive replication, arabinose-inducible lambda recombinase genes. Amp ^R	Datsenko & Wanner ⁴⁶
pCP20	Temperature sensitive replication, Flp recombinase gene, Chl ^R , Amp ^R	Cherepanov & Wackernagel ⁴⁷
pNUT2338	Rep101, Kan ^R , P _{tac} - <i>mRuby2-mRuby2</i>	This study

Abbreviations: Kan = kanamycin, Amp = ampicillin, Chl = chloramphenicol. Superscript "R" = resistance.

"-" = fusion.

Supplementary Table 3.3: DNA oligonucleotides used in this study

Name	Sequence (5' to 3' direction)	Description
KDO834	ACAAC TTTTGTCTTTTACCTTCCCGTTTCGCTCAAGTTAGTATTT GACAATTAATCATCGGCTCGTATAATG	Insertions at the <i>attB</i> site
KDO894	TGGCTGTTTTGAAAAAATTCTAAAGGTTGTTTTACGACGTGTA GGCTGGAGCTGCTTC	<i>fliC</i> deletion
KDO895	AATCAGTTACAACGATTAACCCTGCAGCAGAGACAGAACCTGC ATATGAATATCCTCCTTAG	<i>fliC</i> deletion
KDO1662	TCCGGGCTATGAAATAGAAAAATGAATCCGTTGAAGCCTGCTTTT CATGGGAATTAGCCATGGTCC	Insertions at the <i>attB</i> site
KDO2562	CATCTCCATTAACATCCCATTACGCTTTTATTAAGGAGCATTAGCG TGTAGGCTGGAGCTGCTTC	<i>alaE</i> deletion
KDO2563	GCCAGTTAAAGACGCGACTGGCGATGCCAGTCGCGAAAAGAAGA GATGGGAATTAGCCATGGTCC	<i>alaE</i> deletion
KDO2566	TTAGATTATTCTTTTACTGTATCTACCGTTATCGGAGTGGCTG TGTAGGCTGGAGCTGCTTC	<i>dadAX</i> deletion
KDO2567	TTTTTGCACCCAGAAGACGTTGCCTCCGATCCGGCTTACAACAAG ATGGGAATTAGCCATGGTCC	<i>dadAX</i> deletion
KDO2845	CGTAGAGCCTGAACAACACAGACAGGTACAGGAAGAAAAAAC GTGTAGGCTGGAGCTGCTTC	<i>cycA</i> deletion
KDO2846	CTAAAAGCTGGATGGCATTGCGCCATCCAGCATGATAATGCGGG GTCCATATGAATATCCTCCTTAG	<i>cycA</i> deletion
KDO2841	ACTGAAGCTGAAAAACGGCGCAGCGAAAGGAGAGCAGGCATGA TTGTGTAGGCTGGAGCTGCTTC	<i>livG</i> deletion
KDO2842	GGCGTGACTTTGTCAAAGGACAACATGACTTTTTCCATCTTAGG TCCATATGAATATCCTCCTTAG	<i>livG</i> deletion
KDO3481	GTTTACACAGGAAAGTCATCGCGACCGCAATAAGAGGGATATG CGTGTAGGCTGGAGCTGCTTC	<i>yaaJ</i> deletion
KDO3482	GCCGACTTTAGCAAAAAATGAGAATGAGTTGATCGATAGTTGTG AATGGGAATTAGCCATGGTCCAT	<i>yaaJ</i> deletion
KDO3256	ACCTTTGCTAACCATCAACCACCTCCTTTAGTTTAATTAAGGTG	pNUT2338 construction
KDO3257	GTACCGCTAGCGGTGTAGGCTGGAGCTGCTTC	pNUT2338 construction

Chapter IV: Selective enrichment of slow-growing bacteria in a metabolism-wide CRISPRi library with a TIMER protein

Dominik Beuter¹, José Vicente Gomes-Filho¹, Lennart Randau¹, **Francisco Díaz-Pascual**¹, Knut Drescher^{1,2}, Hannes Link^{1*}

This chapter is written in manuscript style and was published in ACS Synthetic Biology in November 2018. My contribution included the construction of a single plasmid system containing the dCas9 enzyme and sgRNA systems used for CRISPRi, designing and testing multiple promoters and sgRNA constructs to ensure minimal leakage and tunable expression. This system was used as backbone for the CRISPRi library used in the study. I contributed to write the corresponding part of the manuscript.

¹ Max Planck Institute for Terrestrial Microbiology, Marburg, Germany.

² Department of Physics, Philipps-Universität Marburg, Marburg, Germany.

*corresponding author.

Abstract

Construction of pooled genetic variant libraries has become very fast and versatile. The current limitation of this technique is to select cells with a desired phenotype from very large libraries. Especially cells with poor fitness and slow growth are difficult to select because they are rapidly outcompeted by fitter cells. Here, we demonstrate selective and high-throughput enrichment of slow-growing strains using a fluorescent TIMER protein and flow cytometry. As a proof of principle, we created a metabolism-wide CRISPR interference library for *Escherichia coli* and enriched targets that interfere with amino acid metabolism. After enrichment of slow-growing cells, the CRISPRi library consisted almost entirely of targets that block amino acid biosynthesis. These results provide general guidelines for how to enrich slow-growing strains from a large pool of genetic variants, with applications in genetic screens, metabolic engineering, and synthetic biology.

Introduction

Cellular growth is an important physiological parameter of microbes and directly reflects the competitive fitness of cells. Growth is typically measured by the biomass increase of a microbial culture in shaking flasks or in plate readers¹, and more recently at the single cell level by microscopy². Although these methods in principle allow growth measurements of hundreds of strains in parallel, they are laborious and time consuming and not feasible for very large libraries of genetic variants. Creation of such libraries has become very fast and versatile due to recent developments of CRISPR-based genome editing^{3,4}, and interference methods⁵. For example, CRISPR interference (CRISPRi) allows transcriptional downregulation of almost any gene by expressing a catalytically inactive dCas9 and a single guide RNA (sgRNA) that specifies the target gene by a 20 nt base pairing region⁶. CRISPRi screens have been performed in a wide range of microbes, using either growth assays of individual arrayed strains⁷⁻⁹ or pooled competition assays^{10,11}. For pooled growth assays the strain library is cultured in a single pot and the library composition is measured at different time points by deep sequencing of variable genetic elements or barcodes.

A current limitation of pooled competition assays is that they only allow enrichment of fast-growing cells. Enrichment of slow-growing cells is currently not possible, although these cells may have interesting phenotypes and are therefore desirable to isolate for further experiments. For example, slow-growing strains with a high metabolic activity are relevant for overproduction of chemicals in two-stage bioprocesses^{12,13}. Moreover, isolating and analyzing strains with poor fitness can inform synthetic biology about genetic parts that are a burden for the host¹⁴.

A method to enrich slow-growing cells should preferably be based on flow cytometry, to achieve high-throughput and automated sorting. One such method has been developed for yeast¹⁵. It utilizes the property of a chitinase deletion strain that is unable to separate daughter cells from mother cells after cell division which leads to the formation of microcolonies in culture flasks. Sorting of these microcolonies according to their sizes using flow cytometry results in fractions that are enriched for cells with particular growth rates. However, this method is not applicable to bacterial cells and the chitinase deletion may cause secondary effects in the base strain. A similar method, applicable to *E. coli* cells, is based on encapsulating bacterial cells in gel beads, in which they form microcolonies¹⁶. While it was shown that these microcolony-containing beads could be sorted using flow cytometry, separation based on different growth rates has not been reported.

To overcome the lack of a reliable method to enrich slow-growing bacterial cells, we evaluated here a fluorescent TIMER protein¹⁷ for its potential to identify slow-growing strains from a pooled CRISPRi library. TIMER is a variant of the *Discosoma* red fluorescent protein (dsRed) that is green-fluorescent directly after protein synthesis, but matures with a time delay to a red-fluorescent form¹⁷. It has been shown that the ratio of green/red copies of TIMER indicates the growth rate of *Salmonella*, such that slow-growing cells appeared red, and faster-growing cells were greener¹⁸. So far, applications of TIMER focused on cell growth in tissues¹⁸ and biofilms¹⁹. We therefore first validated the relationship between TIMER and growth rates of *E. coli* batch cultures, and then used the TIMER protein to enrich slow-growing cells in a metabolism-wide CRISPRi library.

Results and Discussion

In order to utilize the TIMER protein in a large library of pooled genetic variants, we verified that the green/red fluorescence ratio reliably displays the growth rate across genetically different strains. As a starting point, we expressed TIMER in three *E. coli* strains (MG1655, NCM3722 and BW25113) using a low copy number and a high copy number plasmid. In glucose medium and glycerol medium the three *E. coli* strains had different growth rates, which correlated well with the green/red fluorescence ratios (Supplementary Fig. 4.1). The correlation was stronger when expressing TIMER from the high copy plasmid, when compared to the low copy plasmid. This effect is probably due to the low expression, which resulted in a higher variability of green/red ratios between single cells (Figure 4.1a). We therefore chose the high copy number plasmid for TIMER expression, although the burden of expressing TIMER reduced growth by 15-20 % in all three *E. coli* strains. The low copy number plasmid caused no detectable growth burden (Supplementary Fig. 4.1).

Next we examined the dynamics of TIMER in a batch culture of *E. coli* NCM3722 with glucose minimal medium. Cells were cultivated in microtiter plates to measure simultaneously optical density (OD) and the green/red fluorescence ratio (Figure 4.1b). To achieve different growth rates, we added trimethoprim in different, sublethal concentrations to the culture. Trimethoprim is an antibiotic which inhibits the enzyme dihydrofolate reductase in the folate biosynthetic pathway. The green/red ratio varied usually at the beginning of the cultivation and stabilized during mid-exponential phase when cells reached an OD of 0.5. At higher OD the green/red ratio increased, potentially due to changes in oxygen concentrations, which is known to affect maturation of TIMER¹⁷. As expected, the green/red ratios dropped upon entry to stationary phase, but full maturation into the red form required

Chapter IV: Selective enrichment of slow-growing bacteria in a metabolism-wide CRISPRi library with a TIMER protein

approximately 6 hours. Despite this highly dynamic behavior of TIMER during batch cultivations, the green/red ratio correlated with the growth rate. Especially during mid-exponential growth when cultures reached an OD of 0.5, the green/red ratio correlated linearly with the growth rate in 22 cultures with different trimethoprim levels (Pearson $R^2 = 0.99$, Figure 4.1c). At lower and higher ODs the correlation was less pronounced (Supplementary Fig. 4.2). These data show that TIMER indicates the growth rate of bacteria particularly well during the mid-exponential growth phase of a batch culture.

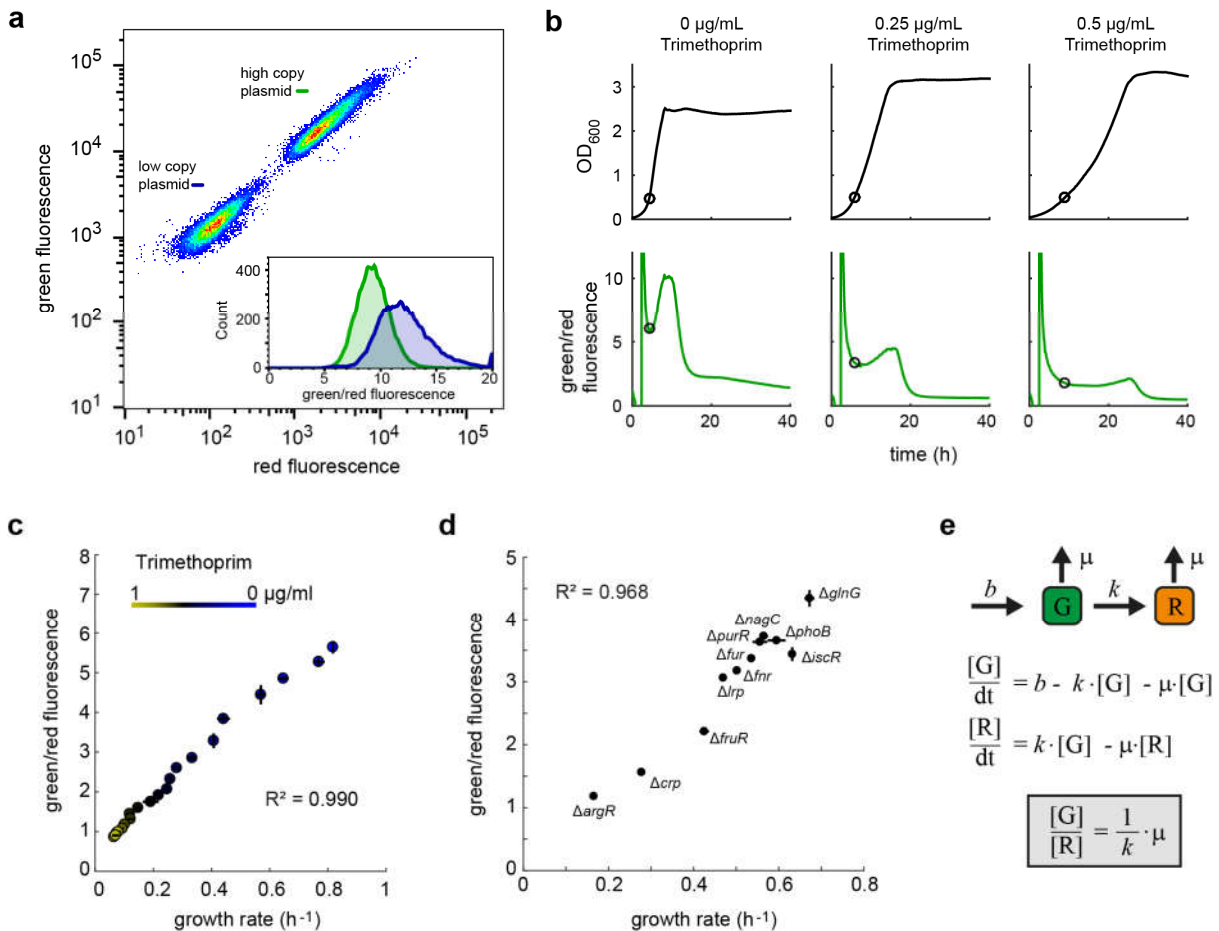


Figure 4.1. Relationship between growth rate and fluorescent TIMER protein in *E. coli*. (a) Green and red fluorescence signals of single *E. coli* NCM3722 cells expressing TIMER from a high and low copy number plasmid. The insert shows distribution of green/red ratios. (b) Optical density and green/red fluorescence of *E. coli* NCM3722 cultures with glucose minimal medium (left), and with trimethoprim added (middle and right). Lines are means of n=3 microtiter plate cultures, black dots indicate an optical density of 0.5 and TIMER fluorescence ratio at this time. (c) Green/red fluorescence ratio is plotted against the growth rate of *E. coli* NCM3722, at the time point when cells reached OD = 0.5. Shown are results for 22 cultures with different trimethoprim levels. The amount of trimethoprim in each culture is indicated by the color of each dot. Dots are means of n = 3 cultures and lines show standard deviations. (d) Green/red fluorescence ratio is plotted against the growth rate of *E. coli* BW25113 with deletion of genes encoding transcription factors. (e) A simplified model of TIMER. The expression rate of TIMER proteins is b , μ is the growth rate, and TIMER changes from red to green with first order kinetics and rate constant k . $[G]$ is the concentration of green TIMER protein, $[R]$ the concentration of red TIMER protein.

To test how genetic perturbations affect the TIMER-growth rate correlation, we expressed TIMER in 11 *E. coli* strains with deletions of genes encoding transcription factors. The transcription factors regulate the expression of 31 to 513 different genes²⁰, and their deletion resulted in growth rates between 0.2 and 0.6 h⁻¹. During mid-exponential growth, the green/red ratio correlated again well with the growth rates of all strains (Figure 4.1d). Moreover, the TIMER signal was reproducible between three independent cultures. Thus, we conclude that TIMER robustly reflects growth perturbations of *E. coli* enforced by deletion of transcription factors, as well as by enzyme inhibitors (trimethoprim).

Consistent with previous findings in chemostat cultures¹⁸, we found a linear relationship between the green/red ratio of TIMER and the growth rate. This relationship suggests that a simple mathematical model sufficiently explains the behavior of TIMER in *E. coli* cells (Figure 4.1e). The model includes the expression rate b of TIMER proteins, their dilution by the growth rate μ , and the rate constant k for TIMER maturation from green to red. Solving the steady state equation shows that the ratio between green and red TIMER protein is proportional to the growth rate, and inversely related to the maturation constant. The model also shows that TIMER is not affected by the expression rate b , which explains similar green/red ratios with the high and low copy number plasmid (Figure 4.1a).

Next we sought to apply TIMER for the selective enrichment of growth-deficient strains in a large genetic variant library. Based on the most recent genome-scale metabolic model of *E. coli*, *iML1515*²¹, we constructed a comprehensive CRISPRi library that targets each of the 1515 genes in the model, enabling dCas9 based downregulation of all metabolism-related genes (Figure 4.2a). For each gene, we designed 4 to 5 sgRNAs whose binding sites are equally distributed on the coding strand. Targeting different loci within a gene should result in different levels of downregulation by dCas9⁶. The resulting library included 7184 sgRNAs, which we cloned in a pooled approach using array-synthesized oligonucleotides on the CRISPRi plasmid (pNUT1527) which harbors both dCas9 and the sgRNA (Figure 4.2b and Methods). Expressing dCas9 together with a non-targeting control sgRNA caused no tangible growth burden in *E. coli* NCM3722 (Supplementary Fig. 4.3). Directly after plasmid assembly, the CRISPRi plasmids were transformed into *E. coli* NCM3722, which already carried the TIMER plasmid. Next generation sequencing (NGS) of sgRNAs showed that 7094 out of 7184 sgRNAs were present in the library and that they were normally distributed (Supplementary Fig. 4.4).

in these cells. Then we isolated the fraction with the lowest green/red fluorescence ratios by FACS (Figure 4.2c). As a reference, cells with high green/red ratio were sorted as well. While cells from the low green/red fraction were expected to have a growth defect, we expected cells from the high green/red fraction to grow either faster or similar than the non-targeting control strain. To test these expected growth phenotypes, we picked 47 (low green/red ratio) and 45 (high green/red ratio) isolates from each fraction and cultured them individually in a plate reader. All isolates from the high green/red fraction grew similar to the control strain, with growth rates $> 0.52 \text{ h}^{-1}$ and lag phases below 8.6 hours (Figure 4.2d). In contrast, 37 out of 47 strains from the fraction with low green/red ratio had a growth defect. Poor growth was either reflected by low growth rates $< 0.52 \text{ h}^{-1}$ and/or long lag phases above 8.6 hours (Figure 4.2d). A strong effect of CRISPRi on lag phases has been reported recently⁹, and is presumably caused by escape mutants or a compensatory response. Thus, strains with growth defects were enriched with TIMER, including both strains with reduced growth rates and long lag phases.

Because cells were isolated upon amino acid depletion, we expected that a major fraction of the growth-impaired strains have sgRNAs that target genes in amino acid biosynthesis. Indeed, sequencing sgRNAs of 28 strains with the strongest growth defect showed that 11 sgRNAs targeted genes, which encode enzymes in the *de novo* biosynthesis of amino acids (Figure 4.2d). Another 5 sgRNAs targeted genes involved in assimilatory sulfate reduction, a pathway needed for the *de novo* biosynthesis of cysteine. The remaining 12 strains were not directly linked to amino acid metabolism, although genes like the TCA cycle gene *sdh* are indirectly involved in the supply of amino acid precursors (e.g. oxaloacetate). To test if CRISPRi blocked the targeted amino acid pathways, we measured intracellular metabolites in the *aroC*, *argG* and *hisD* strain (Supplementary Fig. 4.5). In the *aroC* strain we observed a strong increase of shikimate-5-phosphate, which is upstream of *aroC* encoded chorismate synthase. Shikimate-5-phosphate was almost undetectable in the *hisD*, *argG* and the control strain. The same specific increase of reaction substrates (histidinol and citrulline) occurred in the *hisD* and *argG* strain, indicating that CRISPRi caused bottlenecks at the targeted reactions.

To obtain a global picture of the library composition after sorting by TIMER, we used next generation sequencing (NGS). For this purpose, we repeated the amino acid depletion experiment and sorted 100,000 cells to ensure sufficiently high coverage of the library (Supplementary Fig. 4.6). The experiment was performed twice to test if selective enrichment with TIMER is robust and reproducible. The composition of the library was measured by sequencing of sgRNA guides with NGS. Normalized reads per sgRNA guide sequence were used to calculate the abundance of each strain. The theoretical abundance of strains with targets in amino acid metabolism was 12 % (837 out of 7184 targets,

Chapter IV: Selective enrichment of slow-growing bacteria in a metabolism-wide CRISPRi library with a TIMER protein

Supplementary Table 4.2). In fact, before amino acid depletion the library contained 12 % sgRNAs targeting amino acid related genes, showing that culturing in presence of amino acids introduced no bias (Figure 4.3a). As expected on the basis of sequencing of individual strains in the previous enrichment, this fraction increased to about 50 % after TIMER enrichment (Figure 4.3a).

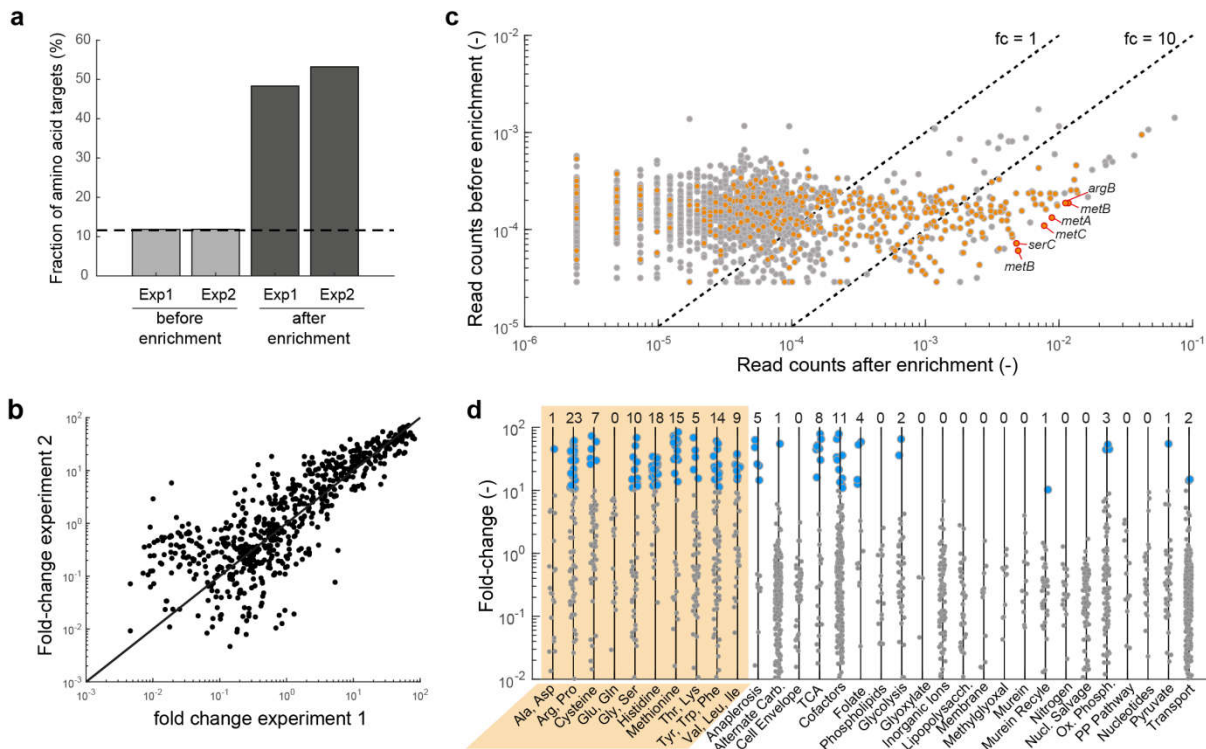


Figure 4.3. Enrichment of amino acid targets in the CRISPRi library. (a) Fraction of sgRNAs in the library that target genes in amino acid metabolism, before and after sorting. Shown are results of two independent experiments (Exp1 and Exp2). Sorting in both experiments is shown in Supplementary Fig. 4.4. The theoretical fraction of amino acid related targets is indicated by a dashed line (12%; 837 out of 7184 sgRNAs). (b) Fold-change of sequencing reads before and after TIMER enrichment in the two independent experiments (Exp1 and Exp2). Each dot represents a sgRNA detected in both experiments. (c) Normalized sequencing read counts for each sgRNA before and after sorting. sgRNAs targeting amino acid genes are shown as orange dots. Dashed lines show fold-changes of 1 and 10. Names of amino acid genes with highest enrichment are shown (fold change >60). (d) Fold change of reads before and after TIMER enrichment in experiment 1. sRNAs are sorted according to the metabolic category of the target gene. Metabolic categories are defined in *iML1515*. Blue dots are highly enriched targets (fold-change >10). Numbers above categories indicate the total amount of sgRNAs with fold-change >10 per category.

To quantify enrichment of single strains, we calculated the fold-change of their abundance before and after enrichment. The fold-change for single strains was remarkably consistent between the two independent experiments, demonstrating that enrichment by TIMER is robust and reproducible

(Figure 4.3b). In total 141 out of the 7184 strains in the library were more than 10-fold enriched in both experiments (Figure 4.3c). 61% of these highly enriched strains were again related to amino acid metabolism. The most highly enriched strains had targets in arginine and proline metabolism (28 strains), histidine metabolism (18 strains), and methionine metabolism (15 strains) (Figure 4.3d). In fact, sgRNAs targeting *metA*, *metB* and *metC* had the highest fold change in the whole library (fold change > 60, Figure 4.3c). This sensitivity of the methionine pathway is consistent with recent data, which shows that methionine biosynthesis operates at maximum capacity in *E. coli*²². Therefore, any disturbance of enzyme levels by transcriptional downregulation should immediately affect growth. Except glutamine and glutamate metabolism, all amino acid pathways had highly enriched targets (Figure 4.3d). The low enrichment of glutamate/glutamine targets reflects a certain robustness, which may be due to the central role of these pathways in ammonia assimilation and transamination reactions. Other highly enriched targets were almost exclusively related to central metabolism (Figure 4.3d). In particular, genes associated with anaplerotic reactions like PEP carboxylase were highly enriched because they supply amino acid precursors. For the same reason, genes of the TCA cycle were enriched, which provides precursors for aspartate and glutamate derived amino acids. Finally, we tested if off-target effects influenced our results¹¹. In total 635 sgRNAs had off-targets in amino acid metabolism, while on-targets were not related to amino acids (Supplementary Table 4..2). These off-targets were not enriched after TIMER selection (Supplementary Fig. 4.7), showing that off-target binding of dCas9 is not a source of false positives in the experiments. Taken together, almost all highly enriched targets were either directly or indirectly related to the *de novo* biosynthesis of amino acids. The spurious occurrence of other targets could be caused by inaccurate sorting or natural growth fluctuations, but they could also indicate more distal and so far unknown interactions with amino acid metabolism.

In conclusion, an efficient and robust enrichment of slow-growing strains from large genetic variant libraries can be achieved using the TIMER protein. A limitation of this technique is the slow response of TIMER upon growth perturbations and pronounced dynamics of the green/red ratio when growth is not balanced. While previous studies used chemostat cultivation to circumvent this problem¹⁸, we have shown here that TIMER can also be used in batch cultivations. We recommend enriching cells in mid-exponential phase as TIMER reflects the growth rate most reliably at this stage. It is also important to cultivate cells for several generations, to ensure that TIMER expression, maturation, and growth is balanced (Figure 4.1e). In our experimental set-up, a 6 hour growth period after perturbing growth by removal of amino acids was sufficient to achieve such conditions. However, it is important to note that the longer the growth period, the smaller the fraction of slow or non-

growing strains will become. Eventually there is a risk to completely lose the fraction of slow-growing cells. Nevertheless, we could successfully enrich a fraction that consisted of only 2 % of the total population (Figure 4.2c and Supplementary Fig. 4.4). Finally, it is possible that the growth burden of the TIMER protein (Supplementary Fig. 4.1) amplified the effect of amino acid starvation, and for future studies it is desirable to integrate TIMER in the genome and to optimize expression levels.

The strength of the presented approach lies in the high-throughput isolation of slow growing strains. Mere identification of slow growers can be more practically achieved using growth based competition experiments. However, accurate determination of growth rates of strains with negative fitness phenotypes is usually difficult in pooled growth screens due to the low abundance of these strains, and the accompanying higher variability in abundance due to experimental bottlenecks. The here-proposed TIMER method provides an alternative measure of growth performance that we have shown to correlate well with growth rates determined in plate reader experiments. Future studies should clarify which method provides better information about negative phenotypes. We anticipate that the ability to select thousands of strains with poor growth opens up new possibilities in metabolic engineering and synthetic biology. Examples are screening of dynamic valves that balance growth and overproduction^{23,24}, or selecting for slow growth during laboratory evolution²⁵.

Methods

Strains and plasmids. *E. coli* strains were MG1655 (DSMZ No. 18039), BW25113²⁶ and NCM3722²⁷. Single gene deletion mutants were obtained from the KEIO collection²⁶. TIMER was expressed from plasmids pSC101_TIMER¹⁸ and pBR322-C_TIMER. Plasmid pBR322-C_TIMER derived from pBR322_TIMER¹⁸ in which we replaced the ampicillin resistance cassette with a chloramphenicol resistance cassette. All strains, plasmids, and oligonucleotides are listed in Supplementary Table 4.1.

CRISPR interference. To construct the CRISPRi plasmid pNUT1527, the sgRNA and its constitutive promoter were amplified by PCR from pgRNA-strain (Addgene #44251). A second DNA fragment containing the dCas9 protein (derived from Addgene #44249) was also amplified by PCR. Both fragments were then joined together by overlap PCR. This new fragment was introduced into a low copy number plasmid with a pSC101 origin of replication (pNUT1270), by restriction cloning using the enzymes PacI and NotI (New England Biolabs, USA). Afterwards, the dCas9 promoter was replaced by the IPTG-inducible *Ptac* promoter and a copy of the *lacIQ1* repressor²⁸ was added into the plasmid by overlap PCR to assure a tight regulation of the *Ptac* promoter. sgRNA guide sequences were designed with Matlab by searching for 4 to 5 equally distributed NGG PAM sites on the coding strand of each gene in the *iML1515* model²¹, and selecting 20 nt regions adjacent to PAM sites. Off-targets were determined as genes that exhibit at least 9 nt perfect complementarity to sgRNA guide sequences and an adjacent PAM motif¹¹. The sgRNAs were synthesized as 150 nt oligonucleotides (Agilent Technologies), consisting of the 20 nt sgRNA guide sequences and 65 nt flanking regions homolog to the pNUT1527 backbone. Oligonucleotides were amplified by PCR with primers listed in Supplementary Table 4.1. To minimize bias in the library we used 15 cycles of amplification. The pNUT1527 backbone was linearized by PCR and amplified oligonucleotides were inserted by Gibson assembly. The Gibson assembly product was purified and subsequently transformed into electrocompetent *E. coli* NCM3722 carrying pBR322-C_TIMER. After plating on nine petri dishes with 15 cm diameter we obtained approximately 10^7 colonies. Colonies were washed from the plates and stored as glycerol stocks. The non-targeting control sgRNA guide sequence was GCGCCAGTTGTA AAAACAAA.

Media and cultivation. All cultivations were performed using M9 minimal medium with 5 g L^{-1} glucose. For amino acid supplementation, all 20 amino acids were added to the culture, each at 1 mM. Where appropriate, chloramphenicol (35 mg L^{-1}), kanamycin (50 mg L^{-1}) and gentamycin (15 mg L^{-1}) were added to the medium. The CRISPRi library was cultivated in the presence of $10 \text{ }\mu\text{M}$ IPTG to induce dCas9 expression. For growth in microtiter plates, cultures were grown in 96-well flat transparent microtiter

plates (Greiner Bio-One International). LB pre-cultures were inoculated from glycerol stocks and incubated at 37°C until all cultures reached stationary phase. From the LB pre-culture a second pre-culture in M9 minimal medium was inoculated with a dilution of 1:200 and incubated overnight. The M9 pre-culture was used to inoculate main cultures with 1:200 dilutions. To culture isolates from the CRISPRi library, M9 minimal medium with amino acids was inoculated from glycerol stocks. From this pre-culture the M9 glucose main culture was inoculated with 1:200 dilutions. Plates were incubated at 37°C and linear shaking in a Synergy H1 plate reader (BioTek Instruments Inc, USA). In 10 minute intervals optical density (OD) was measured at 600 nm, as well as green fluorescence (excitation: 490 nm, emission: 530 nm) and red fluorescence (excitation: 560 nm, emission: 592 nm). OD and fluorescence measurements were corrected for offsets and blanks, and growth rates were calculated as $\ln(\text{OD})/\text{dt}$ by linear regression over time windows of 1 hour. For enrichment experiments, the CRISPRi library was cultivated in 100 mL shaking flasks with 5 mL M9 medium supplemented with amino acids and 5 g L⁻¹ glucose. The culture was directly inoculated with 10 µL of the CRISPRi library glycerol stock. After 6 hours, when cells reached OD of 0.5, the culture was vacuum-filtered on a 0.45 µm pore size filter (HVLP02500, Merck Millipore). Cells on the filter were re-suspended in M9 glucose medium without amino acids using different dilutions of 1:10, 1:100 and 1:1000. After 6 hours incubation, the 1:100 culture reached mid-exponential phase and was used for cell sorting.

Metabolite Measurements. Cells were cultured in 12-well flat transparent microtiter plates as described above. When cells reached ODs between 0.9 and 1, 100 µL culture aliquots were vacuum-filtered on a 0.45 µm pore size filter (HVLP02500, Merck Millipore). Filters were immediately transferred into 40:40:20 (v-%) acetonitrile/methanol/water at -20°C for extraction. Extracts were centrifuged for 15 minutes at 13,000 rpm at -9 °C. Centrifuged extracts were analyzed by LC-MS/MS, with an Agilent 6495 triple quadrupole mass spectrometer (Agilent Technologies) as described previously²⁹.

Flow cytometry. Cells were diluted in fresh medium prior to analysis and sorting of fractions if needed. For fluorescence-activated cell analysis a BD LSRFortessa SORP flow-cytometer (BD Biosciences, NJ, USA) was used. Fluorescence-activated cell sorting was carried out on a BD FACS Aria Fusion (BD Biosciences, NJ, USA). 561-nm lasers, 502 long pass and 532/22 bandpass filters were used for the detection of the red fraction of TIMER. 488-nm lasers, 600 long pass and a 520/30 band pass filters were used for green fluorescent TIMER. To identify cells in the forward/side scatter plot, 488-nm lasers were used. 10,000 or 100,000 cells were sorted per sample according to the red/green fluorescence

ratio. BD FACSDiva software version 8.0 (BD Biosciences, NJ, USA) and FlowJo v10.4.1 (FlowJo LLC, Ashland, OR, USA) were used for analysis of the acquired data.

Next generation sequencing and data analysis. A two-step PCR approach was used to generate amplified target regions that are compatible with Illumina sequencing. In the first PCR step, a 300 bp fragment consisting of the sgRNA sequence and flanking regions on both sides were amplified with oligonucleotides containing sequences specific to the target region and universal Illumina adapter sequences for the second round of PCR reactions. For the first PCR, Q5 polymerase (New England Biolabs, USA) has been used and following settings been used: 98°C for 10 sec, 12 cycles of 98 °C for 10 sec, 65 °C for 30 sec and 72 °C for 15 sec; final extension at 72 °C for 5 min. As template, 150 ng purified library plasmids have been used in a 50 µl PCR reaction. The PCR reactions were cleaned up by gel extraction using a NucleoSpin Gel and PCR Clean-up Kit (Macherey-Nagel, Germany). In the second PCR step, different pairs of indexes (i5 and i7) were attributed to each amplicon. PCR was performed using Phusion High-Fidelity DNA Polymerase (New England Biolabs, USA) with the following conditions: 98 °C for 30 sec; 12 cycles of 98 °C for 10 sec, 55 °C for 30 sec and 72 °C for 20 sec; final extension at 72 °C for 5 min. The PCR products were cleaned up using AMPure XP beads (Beckman Coulter). After clean-up, 10 µL of each library was pooled. The concentration of the library pool was measured using the Qubit dsDNA BR Assay on a Qubit 2.0 Fluorometer. The pooled sequences were then diluted to a final concentration of 2 nM and loaded on a MiniSeq High Output Cartridge following the manufacturer's instructions. 50% PhiX sample was spiked in to ensure sufficient sequence diversity. Sequences were obtained from single-end reads and mapped to the 7184 sgRNAs in the library using a Matlab Script. Only sequences that mapped to sgRNA guide sequences in the reference library (Supplementary Table 4.2) were used to calculate read counts. Fold changes were calculated as: $(reads_{after} / reads_{after,total}) / (reads_{before} / reads_{before,total})$, where *before* and *after* indicates before/after enrichment, and *total* the total read counts. Sequences with less than 10 reads before enrichment were removed from further analysis.

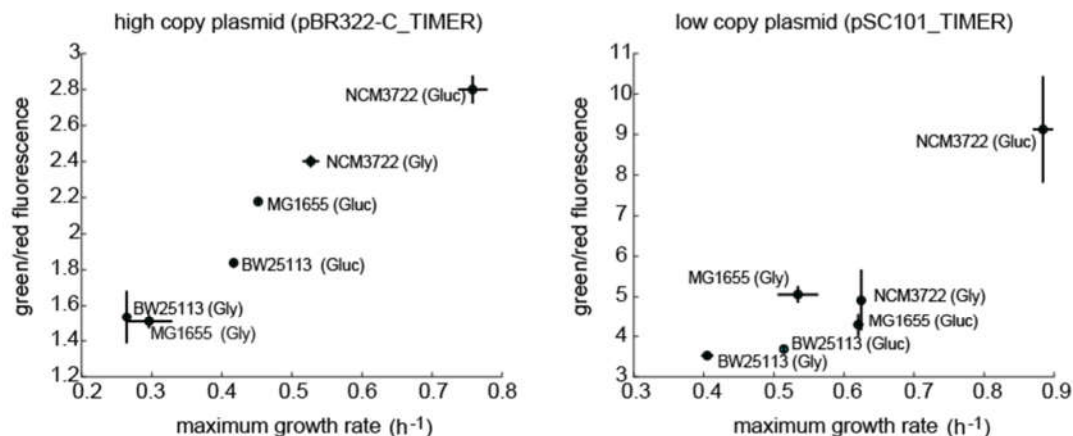
References

1. Brochado, A. R., Telzerow, A., Bobonis, J., Banzhaf, M., Mateus, A., Selkrig, J., Huth, E., Bassler, S., Beas, J. Z., Zietek, M., Ng, N., Foerster, S., Ezraty, B., Py, B., Barras, F., Savitski, M. M., Bork, P., Göttig, S., and Typas, A. (2018) Species-specific activity of antibacterial drug combinations. *Nature* **559**, 259–263.
2. Wang, P., Robert, L., Pelletier, J., Dang, W. L., Taddei, F., Wright, A., and Jun, S. (2010) Robust growth of *Escherichia coli*. *Curr. Biol. CB* **20**, 1099–1103.
3. Bao, Z., Hamedirad, M., Xue, P., Xiao, H., Tasan, I., Chao, R., Liang, J., and Zhao, H. (2018) Genome-scale engineering of *Saccharomyces cerevisiae* with single-nucleotide precision. *Nat. Biotechnol.* **36**, 505–508.
4. Roy, K. R., Smith, J. D., Vonesch, S. C., Lin, G., Tu, C. S., Lederer, A. R., Chu, A., Suresh, S., Nguyen, M., Horecka, J., Tripathi, A., Burnett, W. T., Morgan, M. A., Schulz, J., Orsley, K. M., Wei, W., Aiyar, R. S., Davis, R. W., Bankaitis, V. A., Haber, J. E., Salit, M. L., St Onge, R. P., and Steinmetz, L. M. (2018) Multiplexed precision genome editing with trackable genomic barcodes in yeast. *Nat. Biotechnol.* **36**, 512–520.
5. Dominguez, A. A., Lim, W. A., and Qi, L. S. (2016) Beyond editing: repurposing CRISPR–Cas9 for precision genome regulation and interrogation. *Nat. Rev. Mol. Cell Biol.* **17**, 5–15.
6. Qi, L. S., Larson, M. H., Gilbert, L. a., Doudna, J. a., Weissman, J. S., Arkin, A. P., and Lim, W. a. (2013) Repurposing CRISPR as an RNA-guided platform for sequence-specific control of gene expression. *Cell* **152**, 1173–1183.
7. Peters, J. M., Colavin, A., Shi, H., Czarny, T. L., Larson, M. H., Wong, S., Hawkins, J. S., Lu, C. H. S., Koo, B. M., Marta, E., Shiver, A. L., Whitehead, E. H., Weissman, J. S., Brown, E. D., Qi, L. S., Huang, K. C., and Gross, C. A. (2016) A comprehensive, CRISPR-based functional analysis of essential genes in bacteria. *Cell* **165**, 1493–1506.
8. Smith, J. D., Schlecht, U., Xu, W., Suresh, S., Horecka, J., Proctor, M. J., Aiyar, R. S., Bennett, R. A. O., Chu, A., Li, Y. F., Roy, K., Davis, R. W., Steinmetz, L. M., Hyman, R. W., Levy, S. F., and St. Onge, R. P. (2017) A method for high-throughput production of sequence-verified DNA libraries and strain collections. *Mol. Syst. Biol.* **13**, 913.
9. Liu, X., Gallay, C., Kjos, M., Domenech, A., Slager, J., Van Kessel, S. P., Knoop, K., Sorg, R. A., Zhang, J.-R., and Veening, J.-W. (2017) High-throughput CRISPRi phenotyping identifies new essential genes in *Streptococcus pneumoniae*. *Mol Syst Biol* **13**, 931.
10. Wang, T., Guan, C., Guo, J., Liu, B., Wu, Y., Xie, Z., Zhang, C., and Xing, X.-H. (2018) Pooled CRISPR interference screening enables genome-scale functional genomics study in bacteria with superior performance. *Nat. Commun.* **9**, 2475.
11. Cui, L., Vigouroux, A., Rousset, F., Varet, H., Khanna, V., and Bikard, D. (2018) A CRISPRi screen in *E. coli* reveals sequence-specific toxicity of dCas9. *Nat. Commun.* **9**, 1912.
12. McKinlay, J. B., Oda, Y., Rühl, M., Posto, A. L., Sauer, U., and Harwood, C. S. (2014) Non-growing *Rhodospseudomonas palustris* Increases the Hydrogen Gas Yield from Acetate by Shifting from the Glyoxylate Shunt to the Tricarboxylic Acid Cycle. *J. Biol. Chem.* **289**, 1960–1970.
13. Burg, J. M., Cooper, C. B., Ye, Z., Reed, B. R., Moreb, E. A., and Lynch, M. D. (2016) Large-scale bioprocess competitiveness: the potential of dynamic metabolic control in two-stage fermentations. *Curr. Opin. Chem. Eng.* **14**, 121–136.
14. Ceroni, F., Algar, R., Stan, G.-B., and Ellis, T. (2015) Quantifying cellular capacity identifies gene expression designs with reduced burden. *Nat. Methods* **12**, 415–418.
15. van Dijk, D., Dhar, R., Missarova, A. M., Espinar, L., Blevins, W. R., Lehner, B., and Carey, L. B. (2015) Slow-growing cells within isogenic populations have increased RNA polymerase error rates and DNA damage. *Nat. Commun.* **6**, 7972.
16. Duarte, J. M., Barbier, I., and Schaerli, Y. (2017) Bacterial Microcolonies in Gel Beads for High-Throughput Screening of Libraries in Synthetic Biology. *ACS Synth. Biol.* **6**, 1988-1995.
17. Tersikh, a, Fradkov, a, Ermakova, G., Zarskiy, a, Tan, P., Kajava, a V., Zhao, X., Lukyanov, S., Matz, M., Kim, S., Weissman, I., and Siebert, P. (2000) “Fluorescent timer”: protein that changes color with time. *Science* **290**, 1585–1588.

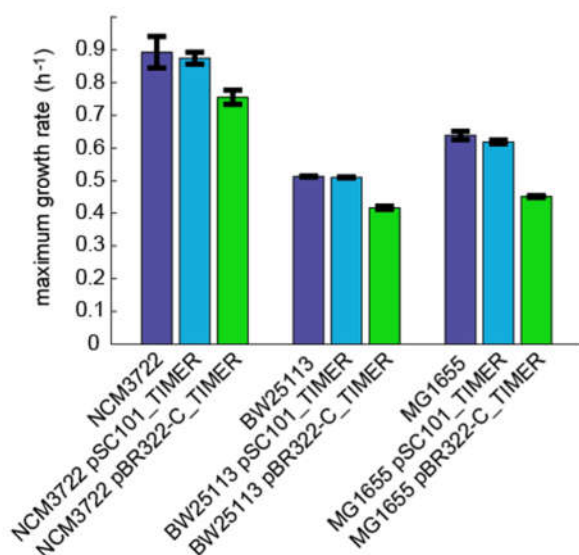
18. Claudi, B., Spröte, P., Chirkova, A., Personnic, N., Zankl, J., Schürmann, N., Schmidt, A., and Bumann, D. (2014) Phenotypic variation of *salmonella* in host tissues delays eradication by antimicrobial chemotherapy. *Cell* **158**, 722–733.
19. Besharova, O., Suchanek, V. M., Hartmann, R., Drescher, K., and Sourjik, V. (2016) Diversification of gene expression during formation of static submerged biofilms by *Escherichia coli*. *Front. Microbiol.* **7**, 1–17.
20. Gama-Castro, S., Salgado, H., Santos-Zavaleta, A., Ledezma-Tejeda, D., Muñoz-Rascado, L., García-Sotelo, J. S., Alquicira-Hernández, K., Martínez-Flores, I., Pannier, L., Castro-Mondragón, J. A., Medina-Rivera, A., Solano-Lira, H., Bonavides-Martínez, C., Pérez-Rueda, E., Alquicira-Hernández, S., Porrón-Sotelo, L., López-Fuentes, A., Hernández-Koutoucheva, A., Del Moral-Chávez, V., Rinaldi, F., and Collado-Vides, J. (2016) RegulonDB version 9.0: high-level integration of gene regulation, coexpression, motif clustering and beyond. *Nucleic Acids Res.* **44**, D133-43.
21. Monk, J. M., Lloyd, C. J., Brunk, E., Mih, N., Sastry, A., King, Z., Takeuchi, R., Nomura, W., Zhang, Z., Mori, H., Feist, A. M., and Palsson, B. O. (2017) iML1515, a knowledgebase that computes *Escherichia coli* traits. *Nat. Biotechnol.* **35**, 904–908.
22. Li, G.-W., Burkhardt, D., Gross, C., and Weissman, J. S. (2014) Quantifying absolute protein synthesis rates reveals principles underlying allocation of cellular resources. *Cell* **157**, 624–635.
23. Gupta, A., Reizman, I. M. B., Reisch, C. R., Prather, K. L. J. (2017) Dynamic regulation of metabolic flux in engineered bacteria using a pathway-independent quorum-sensing circuit. *Nat. Biotechnol.* **35**, 273-279.
24. Ceroni, F., Boo, A.; Furini, S., Gorochofski, T. E., Borkowski, O., Ladak, Y. N., Awan, A. R.; Gilbert, C., Stan, G.-B., Ellis, T. (2018) Burden-driven feedback control of gene expression. *Nat. Methods* **15**, 387-393.
25. Conrad, T. M., Lewis, N. E., Palsson, B. Ø. (2011) Microbial laboratory evolution in the era of genome-scale science. *Mol. Syst. Biol.* **7**, 509.
26. Baba, T., Ara, T., Hasegawa, M., Takai, Y., Okumura, Y., Baba, M., Datsenko, K. a, Tomita, M., Wanner, B. L., and Mori, H. (2006) Construction of *Escherichia coli* K-12 in-frame, single-gene knockout mutants: the Keio collection. *Mol. Syst. Biol.* **2**, 2006.0008.
27. Soupene, E., Heeswijk, W. C. van, Plumbridge, J., Stewart, V., Bertenthal, D., Lee, H., Prasad, G., Paliy, O., Charernnoppakul, P., and Kustu, S. (2003) Physiological Studies of *Escherichia coli* Strain MG1655: Growth Defects and Apparent Cross-Regulation of Gene Expression. *J. Bacteriol.* **185**, 5611–5626.
28. Glascock, C. B., and Weickert, M. J. (1998) Using chromosomal lacI^Q1 to control expression of genes on high-copy-number plasmids in *Escherichia coli*. *Gene* **223**, 221–231.
29. Guder, J. C., Schramm, T., Sander, T., and Link, H. (2017) Time-Optimized Isotope Ratio LC-MS/MS for High-Throughput Quantification of Primary Metabolites. *Anal. Chem.* **89**, 1624–1631.

Supplementary Information

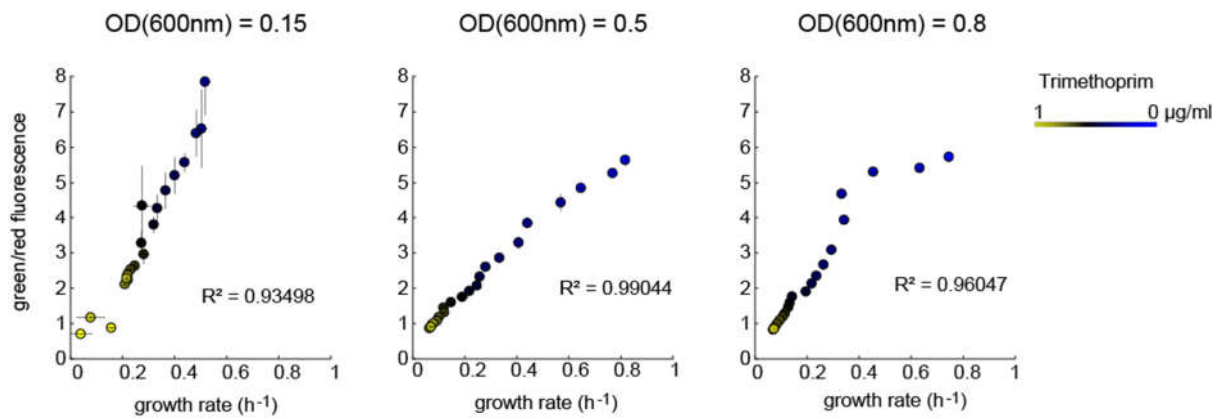
a



b

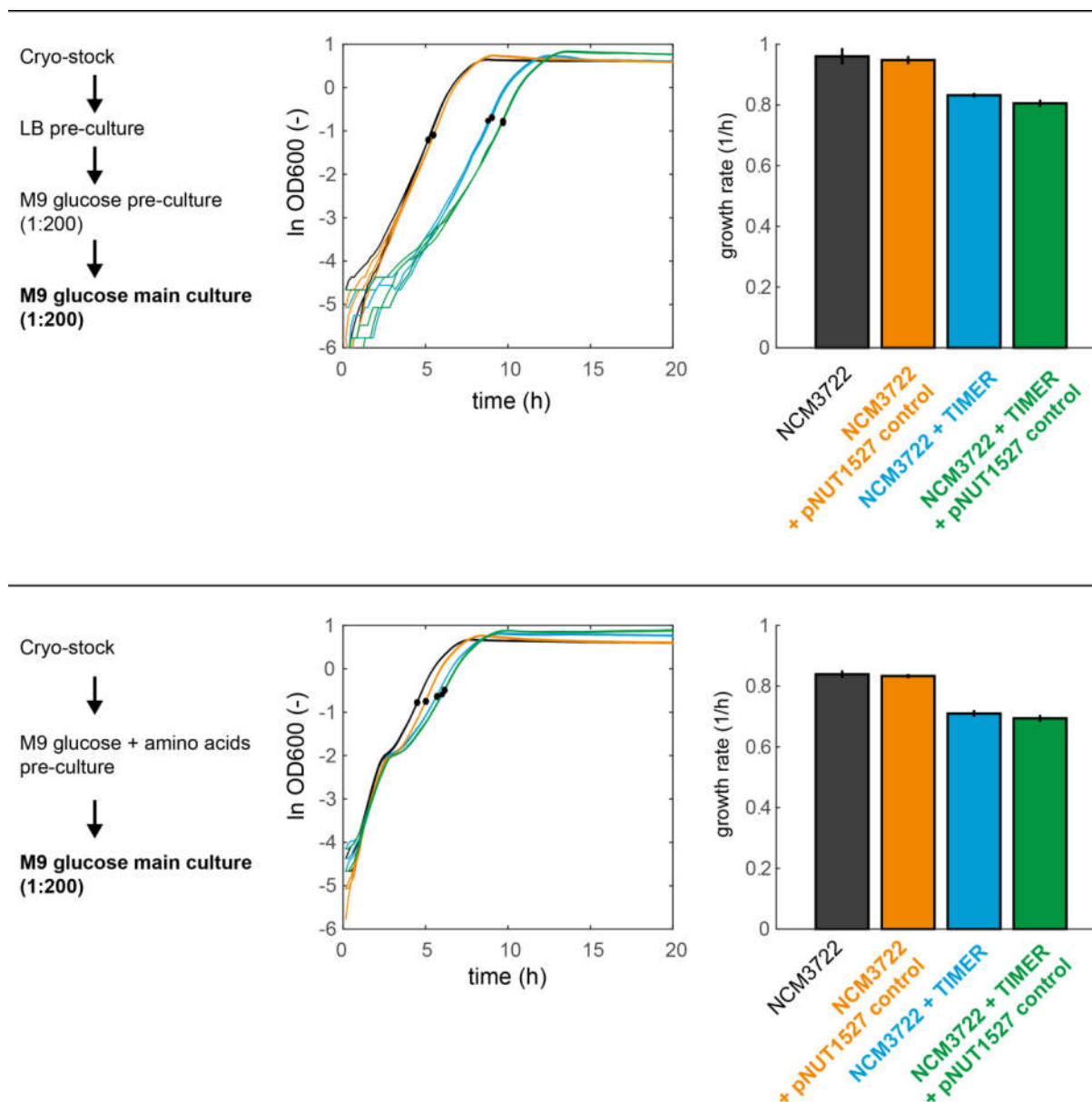


Supplementary Figure 4.1. TIMER expression from a high and low copy plasmid in three *E. coli* strains. (a) Correlation of growth and green/red fluorescence in three different *E. coli* strains growing on glucose or glycerol, expressing TIMER from a high copy number plasmid (left) and low copy number plasmid (right). Dots are means of $n=3$ microtiter plate cultures and lines show standard deviations. **(b)** Maximum growth rates of three different *E. coli* strains growing on M9 glucose minimal medium expressing TIMER from the low copy (pSC101) or high copy number plasmid (pBR322). Means and standard deviation of $n = 3$ cultures.

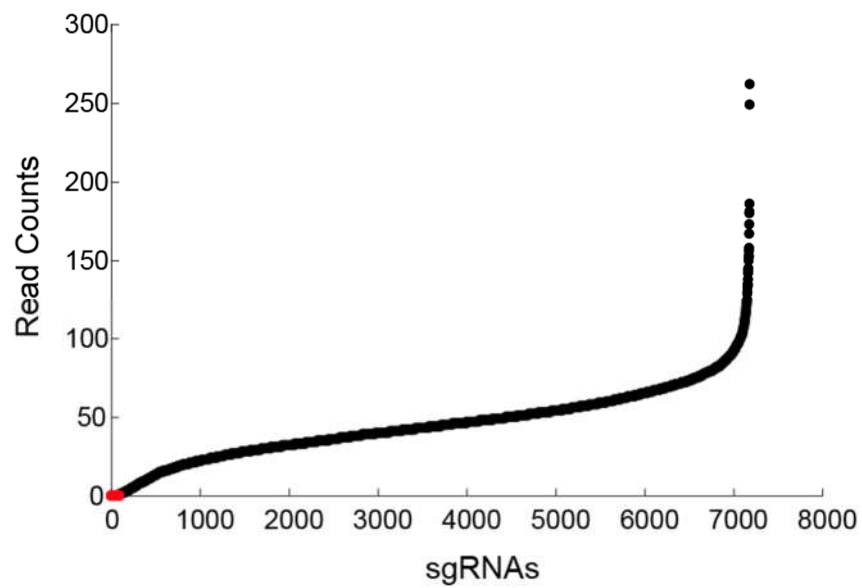


Supplementary Figure 4.2. Correlation of growth rates and green/red fluorescence at different optical densities. *E. coli* cultures were treated with different sublethal concentrations of trimethoprim to modulate the growth rates. The green/red fluorescence ratios were compared at different optical densities (OD), representing early exponential (OD = 0.15, left), mid-exponential (OD = 0.5, middle) and late exponential growth phase (OD = 0.8, right). R² is the Pearson correlation coefficient. Dots are means of *n* = 3 microtiter plate cultures and lines show standard deviations.

Chapter IV: Selective enrichment of slow-growing bacteria in a metabolism-wide CRISPRi library with a TIMER protein

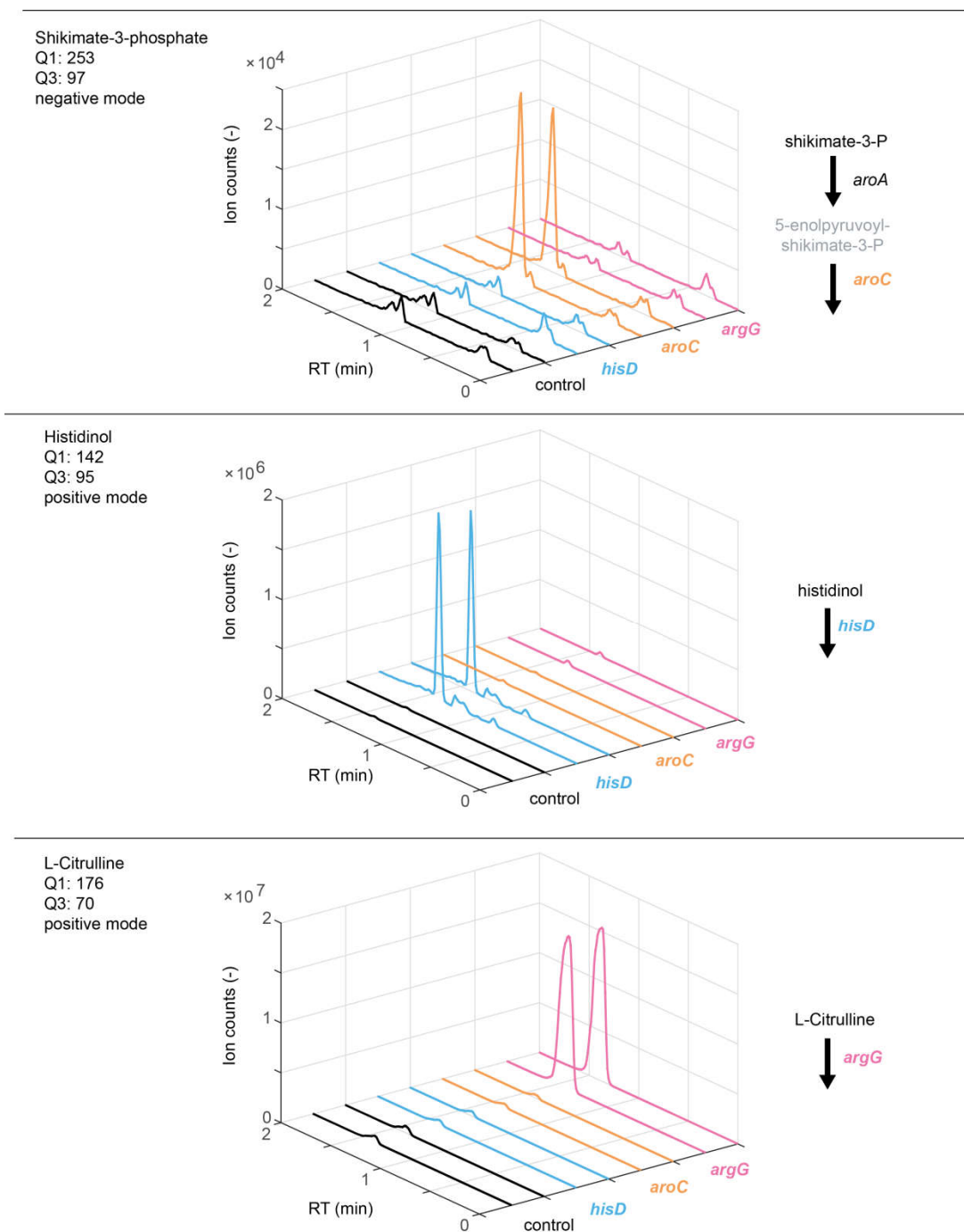


Supplementary Figure 4.3. Effect of pNUT1527 with a non-targeting control sgRNA on growth of *E. coli* NCM3722. Growth curves and maximum growth rates of four *E. coli* strains: i) NCM3722 (wild-type) ii) NCM3722 with the CRISPRi plasmid pNUT1527 with a non-targeting control sgRNA iii) NCM3722 expressing the TIMER plasmid pBR322-C_TIMER iv) NCM3722 expressing both TIMER and the non-targeting control plasmid (control strain). Shown are three independent cultures in 96 well plates. Black dots in growth curves indicate the time when cultures reached maximum growth. The upper panel are cultivation conditions used to characterize TIMER in Figure 4.1. The lower panel are cultivation conditions used to characterize isolates from the CRISPRi library in Figure 4.2. The cultivation protocol is indicated on the left (see also Methods).

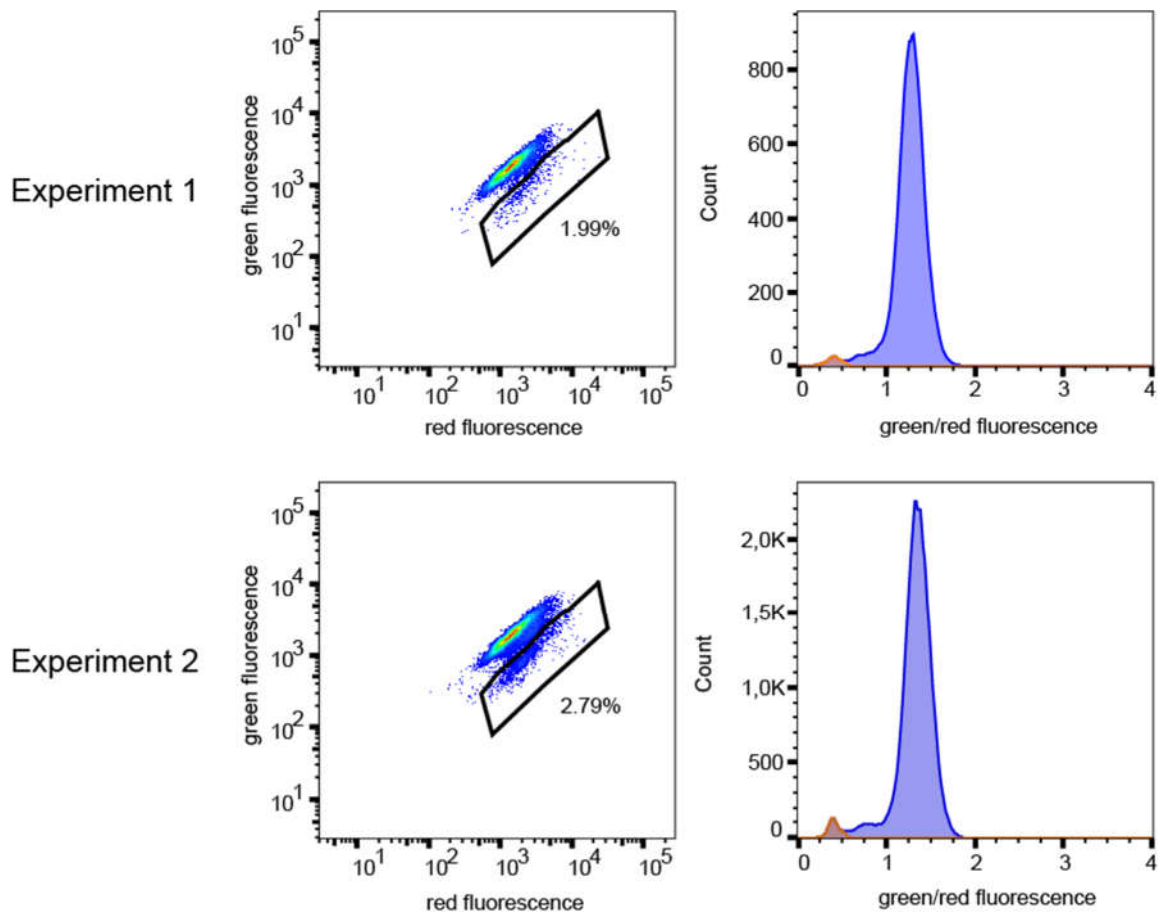


Supplementary Figure 4.4. Distribution of sgRNAs in the CRISPRi library after assembly. Read counts of sgRNAs after assembly of the CRISPRi library. 7094 of 7184 sgRNAs (98.7%) were present in the library (black dots), 90 sgRNAs (1.3%, red dots) were not detected.

Chapter IV: Selective enrichment of slow-growing bacteria in a metabolism-wide CRISPRi library with a TIMER protein

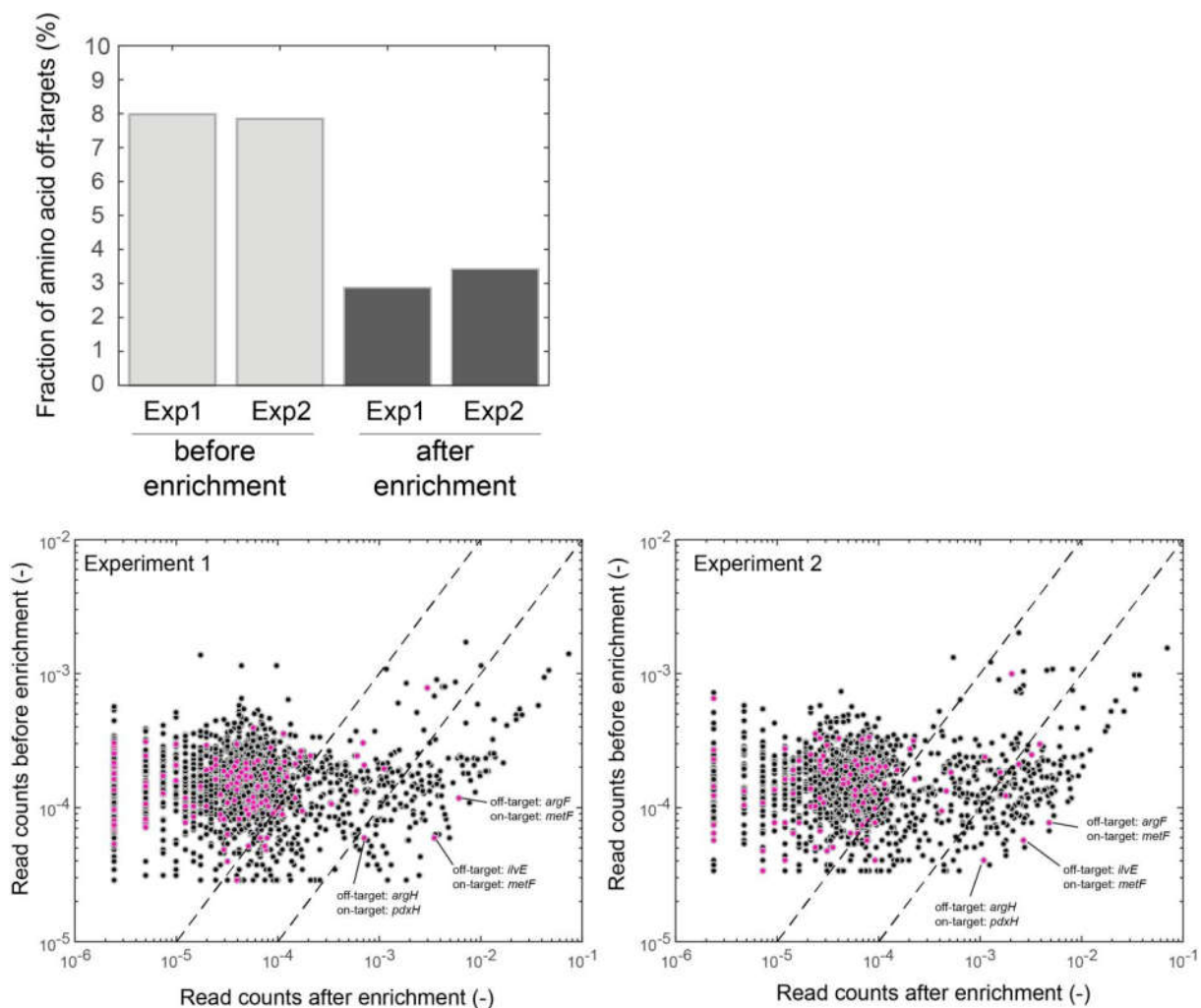


Supplementary Figure 4.5. LC-MS/MS analysis of amino acid intermediates in CRISPRi strains. Shikimate-5-phosphate, histidinol and citrulline in the CRISPRi strains targeting *argG*, *aroC* and *hisD*. The control is a strain with a non-targeting sgRNA. Shown are chromatograms of samples from two independent cultures. LC-MS/MS parameters are shown on the left. The targeted pathways are indicated on the right.



Supplementary Figure 4.6. Cell sorting for next generation sequencing of slow-growing cells in the CRISPRi library. 6 hours after removal of amino acids, 100,000 cells with the lowest green/red fluorescence ratio (gated area in the left plot, orange in the right plot) were sorted from two independent shake flasks (experiment 1 and experiment 2). The sorted cells were subsequently analyzed with next generation sequencing.

Chapter IV: Selective enrichment of slow-growing bacteria in a metabolism-wide CRISPRi library with a TIMER protein



Supplementary Figure 4.7. sgRNAs with off-targets in amino acid metabolism. Upper panel: Fraction of sgRNAs in the library with off-targets in amino acid metabolism (and no on-target in amino acid metabolism), before and after sorting. Shown are results of two independent experiments (Exp1 and Exp2). Lower panels: Normalized sequencing read counts for each sgRNA before and after sorting. sgRNAs with off-targets in amino acid metabolism are shown as purple dots. The three sgRNAs with highest enrichment in both experiments are indicated: *argF*, *argH* in arginine and *ilvE* in isoleucine biosynthesis. Their on-targets are *metF* (folate biosynthesis), and *pdxH* (pyridoxal-phosphate biosynthesis), which are important cofactors of amino acid biosynthesis.

Supplementary Table 4.1. Strains, Plasmids and Oligonucleotides used in this study.

Strain	Genotype	Reference/Origin
<i>E. coli</i> NCM3722	<i>E. coli</i> NCM3722	27
<i>E. coli</i> MG1655	F-, lambda-, rph-1	DSMZ No. 18039
<i>E. coli</i> BW25113	<i>lacI</i> ⁺ <i>rrnBT14</i> Δ <i>lacZ</i> WJ16 <i>hsdR514</i> Δ <i>araBADAH33</i> Δ <i>rhaBADLD78</i>	26
<i>E. coli</i> BW25113 Δ <i>argR</i>	<i>lacI</i> ⁺ <i>rrnBT14</i> Δ <i>lacZ</i> WJ16 <i>hsdR514</i> Δ <i>araBADAH33</i> Δ <i>rhaBADLD78</i> Δ <i>argR</i>	26
<i>E. coli</i> BW25113 Δ <i>crp</i>	<i>lacI</i> ⁺ <i>rrnBT14</i> Δ <i>lacZ</i> WJ16 <i>hsdR514</i> Δ <i>araBADAH33</i> Δ <i>rhaBADLD78</i> Δ <i>crp</i>	26
<i>E. coli</i> BW25113 Δ <i>fnr</i>	<i>lacI</i> ⁺ <i>rrnBT14</i> Δ <i>lacZ</i> WJ16 <i>hsdR514</i> Δ <i>araBADAH33</i> Δ <i>rhaBADLD78</i> Δ <i>fnr</i>	26
<i>E. coli</i> BW25113 Δ <i>fruR</i>	<i>lacI</i> ⁺ <i>rrnBT14</i> Δ <i>lacZ</i> WJ16 <i>hsdR514</i> Δ <i>araBADAH33</i> Δ <i>rhaBADLD78</i> Δ <i>fruR</i>	26
<i>E. coli</i> BW25113 Δ <i>fur</i>	<i>lacI</i> ⁺ <i>rrnBT14</i> Δ <i>lacZ</i> WJ16 <i>hsdR514</i> Δ <i>araBADAH33</i> Δ <i>rhaBADLD78</i> Δ <i>fur</i>	26
<i>E. coli</i> BW25113 Δ <i>glnG</i>	<i>lacI</i> ⁺ <i>rrnBT14</i> Δ <i>lacZ</i> WJ16 <i>hsdR514</i> Δ <i>araBADAH33</i> Δ <i>rhaBADLD78</i> Δ <i>glnG</i>	26
<i>E. coli</i> BW25113 Δ <i>iscR</i>	<i>lacI</i> ⁺ <i>rrnBT14</i> Δ <i>lacZ</i> WJ16 <i>hsdR514</i> Δ <i>araBADAH33</i> Δ <i>rhaBADLD78</i> Δ <i>iscR</i>	26
<i>E. coli</i> BW25113 Δ <i>lrp</i>	<i>lacI</i> ⁺ <i>rrnBT14</i> Δ <i>lacZ</i> WJ16 <i>hsdR514</i> Δ <i>araBADAH33</i> Δ <i>rhaBADLD78</i> Δ <i>lrp</i>	26
<i>E. coli</i> BW25113 Δ <i>nagC</i>	<i>lacI</i> ⁺ <i>rrnBT14</i> Δ <i>lacZ</i> WJ16 <i>hsdR514</i> Δ <i>araBADAH33</i> Δ <i>rhaBADLD78</i> Δ <i>nagC</i>	26
<i>E. coli</i> BW25113 Δ <i>phoB</i>	<i>lacI</i> ⁺ <i>rrnBT14</i> Δ <i>lacZ</i> WJ16 <i>hsdR514</i> Δ <i>araBADAH33</i> Δ <i>rhaBADLD78</i> Δ <i>phoB</i>	26
<i>E. coli</i> BW25113 Δ <i>purR</i>	<i>lacI</i> ⁺ <i>rrnBT14</i> Δ <i>lacZ</i> WJ16 <i>hsdR514</i> Δ <i>araBADAH33</i> Δ <i>rhaBADLD78</i> Δ <i>purR</i>	26
Plasmid	Genotype	Reference
pSC101_TIMER	Tet ^r , TIMER in pSC101	18
pBR322_TIMER	Amp ^r , TIMER in pBR322	18

Chapter IV: Selective enrichment of slow-growing bacteria in a metabolism-wide CRISPRi library with a TIMER protein

pBR322-C_TIMER	Cmp ^r , TIMER in pBR322	This study
pNUT1527	Gent ^r , Ptac-dCas9, pJ23119-sgRNA	This study

Chapter IV: Selective enrichment of slow-growing bacteria in a metabolism-wide CRISPRi library with a TIMER protein

Oligonucleotide	Sequence	Purpose
pBR_CMP_BB_F	GACGTCTAAGAAAAGTGCAGACCAAGTTTACT CATATATAC	Amplification of pBR322_TIMER for exchange of the resistance cassette
pBR_CMP_BB_R	TGGTGAGAATCCAAAATGTATTTAGAAAATAA ACAAAAGAG	Amplification of pBR322_TIMER for exchange of the resistance cassette
Cmp_pBR_fwd	CTAAATACATTTTGGATTCTCACCAATAAAAAAC G	Amplification of Cmp ^r for exchange of the resistance cassette in pBR322_TIMER
Cmp_pBR_rev	GGTCTGACAGTTTTCTTAGACGTCAGGTGGC	Amplification of Cmp ^r for exchange of the resistance cassette in pBR322_TIMER
kdo1742	TATAGCGGCCGCAATAGGCGTATCACGAGGC AGA	amplification of Addgene #44251
kdo1740	GAAAATGAGACGTCCAGTTCACCGACAAACAA CAG	amplification of Addgene #44251
kdo1741	TCGGTGAAGTGGACGTCTCATTTTCGCCAGATA TCGAC	amplification of Addgene #44249
kdo1739	GCGCTTAATTAAGCGAGTCAGTGAGCGAGG	amplification pNUT1270
kdo1737	GCGCTTAATTAACAGTAATGACCTCAGAACTCC ATCTGG	amplification pNUT1270
kdo1860	CCAGATATCGACCAAGCGAGCTCTCTAGACGCC A	amplification of lacIQ1
Kdo525	TTTAGACCTCCTTAGCTCCTGAATTCCTA	amplification of lacIQ1
OH_amp_fwd	TAAGGATGATTTCTGGAATTCTAAAG	Amplification of pooled oligonucleotides
OH_amp_rev	GTGCCACTTTTTCAAGTTGATAAC	Amplification of pooled oligonucleotides
EcF_forward	GTTTTAGAGCTAGAAATAGCAAGTTAAAATAAG GC	Amplification of pNUT1527 for Gibson Assembly with amplified pooled oligonucleotides
EcF_reverse	ACTAGTATTATACCTAGGACTGAGCTAGC	Amplification of pNUT1527 for Gibson Assembly with amplified pooled oligonucleotides
NGS_F2_adapter	TCGTCGGCAGCGTCAGATGTGTATAAGAGACA GCGCAATAGGCGTATCACGAGG	Amplification of a 300 bp fragment of pNUT1527 including the sgRNA
NGS_R2_adapter	GTCTCGTGGGCTCGGAGATGTGTATAAGAGAC AGCGACGG CGCTATTAGATCC	Amplification of a 300 bp fragment of pNUT1527 including the sgRNA
Custom_N701	CAAGCAGAAGACGGCATAACGAGATTGCCTTA GTCTCGTGGGCTCGG	17 oligo
Custom_N702	CAAGCAGAAGACGGCATAACGAGATCTAGTACG GTCTCGTGGGCTCGG	17 oligo

Chapter IV: Selective enrichment of slow-growing bacteria in a metabolism-wide CRISPRi library with a TIMER protein

Custom_N703	CAAGCAGAAGACGGCATAACGAGATTTCTGCCT GTCTCGTG GGCTCGG	17 oligo
Custom_N704	CAAGCAGAAGACGGCATAACGAGATGCTCAGGA GTCTCGTG GGCTCGG	17 oligo
Custom_N705	CAAGCAGAAGACGGCATAACGAGATAGGAGTCC GTCTCGTG GGCTCGG	17 oligo
Custom_N706	CAAGCAGAAGACGGCATAACGAGATCATGCCTA GTCTCGTG GGCTCGG	17 oligo
Custom_S502	AATGATACGGCGACCACCGAGATCTACACCTCT CTATTCGT CGGCAGCGTC	15 oligo
Custom_S503	AATGATACGGCGACCACCGAGATCTACACTATC CTCTTCGT CGGCAGCGTC	15 oligo

Chapter V: Breakdown of *Vibrio cholerae* biofilm architecture induced by antibiotics disrupts community barrier function

Francisco Díaz-Pascual¹, Raimo Hartmann¹, Martin Lempp¹, Lucia Vidakovic¹, Boya Song², Hannah Jeckel^{1,3}, Kai M. Thormann⁴, Fitnat H. Yildiz⁵, Jörn Dunkel², Hannes Link^{1,6}, Carey D. Nadell^{1,7} and Knut Drescher^{1,3,6*}

This chapter is written in manuscript style and was published in Nature Microbiology in October 2019. My contribution to this work included designing, performing and analyzing all experiments (except for the *in silico* simulation and the mass spectrometry measurements), figure creating and contributing in the writing of the manuscript.

¹Max Planck Institute for Terrestrial Microbiology, Marburg, Germany.

²Department of Mathematics, Massachusetts Institute of Technology, Cambridge, MA, USA.

³Department of Physics, Philipps-Universität Marburg, Marburg, Germany.

⁴Institut für Mikrobiologie und Molekularbiologie, Justus-Liebig-Universität Gießen, Gießen, Germany.

⁵Department of Microbiology and Environmental Toxicology, University of California, Santa Cruz, Santa Cruz, CA, USA.

⁶Synmikro Center for Synthetic Microbiology, Philipps-Universität Marburg, Marburg, Germany.

⁷Department of Biological Sciences, Dartmouth College, Hanover, USA

*corresponding author.

Abstract

Bacterial cells in nature are frequently exposed to changes in their chemical environment^{1,2}. The response mechanisms of isolated cells to such stimuli have been investigated in great detail. By contrast, little is known about the emergent multicellular responses to environmental changes, such as antibiotic exposure³⁻⁷, which may hold the key to understanding the structure and functions of the most common type of bacterial communities: biofilms. Here, by monitoring all individual cells in *Vibrio cholerae* biofilms during exposure to antibiotics that are commonly administered for cholera infections, we found that translational inhibitors cause strong effects on cell size and shape, as well as biofilm architectural properties. We identified that single-cell-level responses result from the metabolic consequences of inhibition of protein synthesis and that the community-level responses result from an interplay of matrix composition, matrix dissociation and mechanical interactions between cells. We further observed that the antibiotic-induced changes in biofilm architecture have substantial effects on biofilm population dynamics and community assembly by enabling invasion of biofilms by bacteriophages and intruder cells of different species. These mechanistic causes and ecological consequences of biofilm exposure to antibiotics are an important step towards understanding collective bacterial responses to environmental changes, with implications for the effects of antimicrobial therapy on the ecological succession of biofilm communities.

Main text

Exposure to antibiotics is an important stimulus for bacteria, and is likely to be ubiquitous inside patients receiving antibiotic therapy as well as in the broader environment, where biofilm formation and antibiotic-mediated microbial warfare are common³⁻⁷. Understanding community-scale effects of antibiotic treatment in biofilms is important, given that antibiotic-tolerant infections are currently among the largest emerging global health threats⁸⁻¹⁵, in part due to the increased tolerance of biofilms to antibiotics¹⁶⁻²⁴.

To investigate the emergent community-level responses of antibiotic exposure on biofilm populations, we subjected mature *V. cholerae* biofilms to antibiotics encompassing the major mechanisms of action (Supplementary Fig. 5.1), including the most commonly used antibiotic classes against cholera infections²⁵. Our recently developed single-cell imaging system for biofilm dynamics²⁶⁻²⁸ enabled us to detect architectural changes of biofilms in response to antibiotic treatment above the minimum inhibitory concentration (MIC), which were particularly striking for translational inhibitors such as tetracycline (Fig. 5.1a-c and Supplementary Fig. 5.1). We observed modifications in cell morphology and biofilm architecture during tetracycline treatment for several parameters, including marked changes in both the cell volume and cell-packing density (Fig. 5.1, Supplementary Fig. 5.2). Without single-cell-level imaging of biofilms, the expansion of biofilm size caused by antibiotic treatment above the MIC (Fig. 5.1) would probably have been misinterpreted as antibiotic-induced biofilm formation (see data from classical crystal violet assays in Supplementary Fig. 5.3 for tetracycline and other antibiotics). To investigate the detailed mechanisms and ecological consequences of antibiotic-induced biofilm architectural changes, unless indicated otherwise, experiments were performed with tetracycline, an antibiotic that is commonly used to treat cholera infections²⁵.

Modifications to the biofilm architecture appeared within the first 6 h of tetracycline exposure, well before the time at which significant cell death became evident (>10 h; Supplementary Fig. 5.4), indicating that other processes were reorganizing the biofilms during inhibition of protein translation. After 6 h of tetracycline treatment, cells within biofilms increased in volume by 2.5-fold on average, and the mean cell density decreased by 29% (Fig. 5.1d). The cell volume increase and the timing of this increase, did not depend on the cellular location within the biofilm (Fig. 5.1e-h), indicating that tetracycline diffuses into all regions of the biofilm quickly, on a shorter time scale than that of the physiological response to translational inhibition.

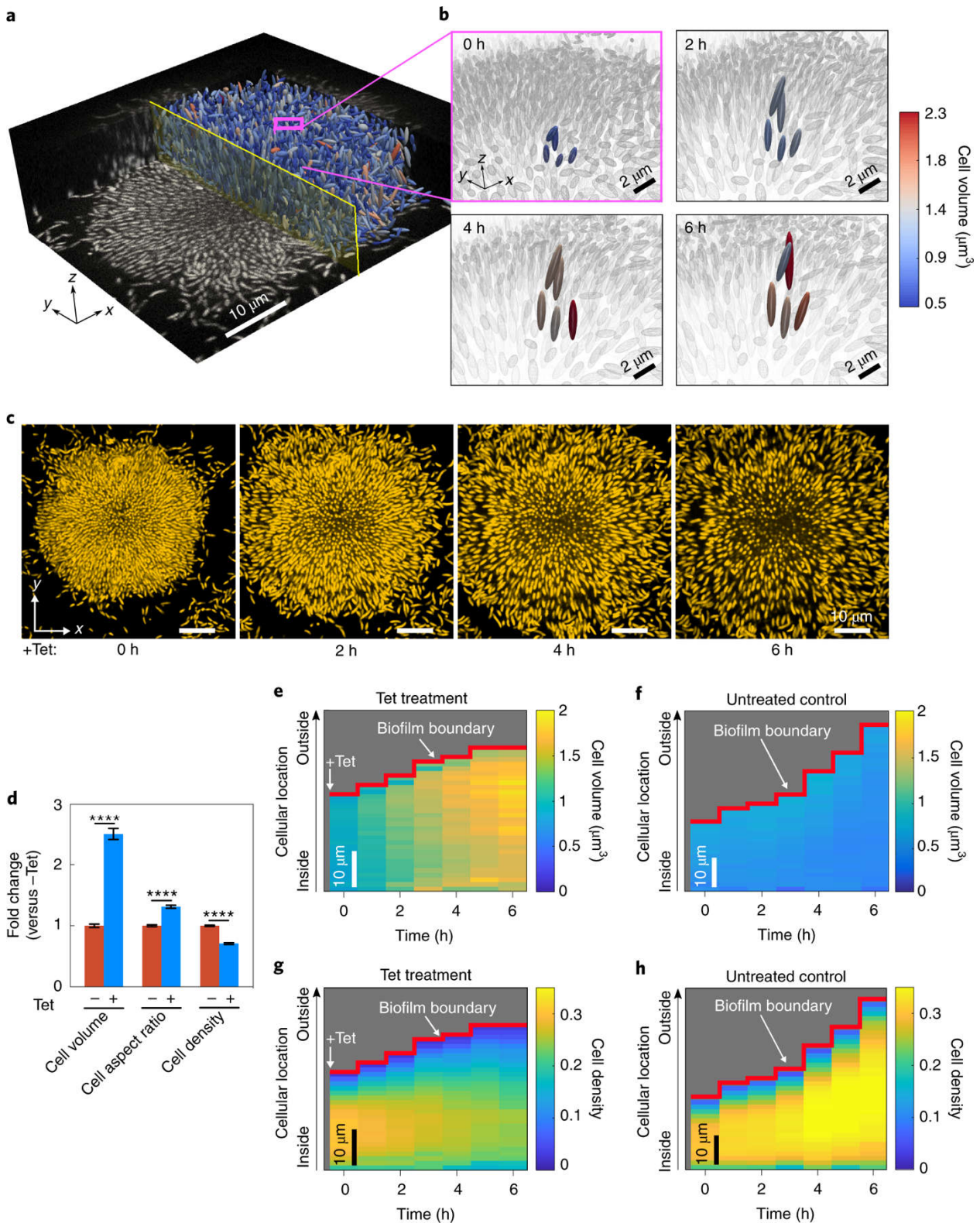


Figure 5.1. Inhibition of protein synthesis triggers strong architectural changes of biofilms. a, Raw microscopy image based on mKO₂ fluorescence of a 24-h-old biofilm and 3D visualization of cells as ellipsoids after segmentation, separated by a central plane with a yellow outline. **b**, The box outlined in pink

in a is enlarged in the four images, showing five cells, which are tracked in 3D during 6 h of tetracycline treatment above the MIC. These five cells are coloured according to their volume and all other cells in the background are coloured grey. Tetracycline treatment results in increased cell volume and decreased cell density (volume fraction). **c**, Snapshots of biofilm architecture dynamics (showing only one confocal xy slice located 2 μm above the coverslip) during a tetracycline (Tet)-treatment time series. Cells are visualized using a constitutively expressed mKOk fluorescent protein. **d**, Fold change of cell volume, cell aspect ratio and cell density (measured as volume fraction) of tetracycline-treated biofilms compared with untreated biofilms grown for the same time without antibiotics. Data are mean \pm s.e.m. ($n = 15$ samples for $-Tet$ and $n = 9$ for $+Tet$; each sample corresponds to a different biofilm). Statistical significance was calculated in relation to control biofilms using a two-sided unpaired t-test ($****P < 0.0001$). **e–h**, Spatiotemporal changes of the average cell volume with tetracycline treatment (**e**) or for untreated control (**f**) and cell density with tetracycline treatment (**g**) or for untreated control (**h**) as a function of time during tetracycline treatment and position inside the biofilm. Each pixel in these heat maps is coloured according to the average cell volume or cell density at a given time and spatial position in the biofilm. Cell volumes and cell density values are averaged over all cells with similar distances from the interface of the biofilm and the growth medium (that is, the biofilm boundary). Heat maps are representative of $n = 5$ different biofilms.

While the observed decrease in cell density is an alteration of the multicellular arrangement within the biofilm, the increase in cell volume is a single-cell-level alteration that could potentially also occur outside the biofilm state following tetracycline exposure. To test whether similar changes in cell shape also occur during tetracycline treatment outside biofilms, we treated single cells attached to glass and planktonic cells grown in liquid culture, and observed that these individual cells also increased in volume (Fig. 5.2a and Supplementary Fig. 5.5a). We next sought to understand the underlying causes of this increase in cell volume.

To test whether tetracycline-treated cells increase in volume passively due to osmotic effects or actively due to a specific response, we first investigated whether the cells remain metabolically active and continue to produce new cell wall components during tetracycline exposure. We followed the incorporation of ^{13}C -labelled glucose into hexose-6-phosphate metabolites (such as glucose-6-phosphate; upper glycolysis, Fig. 5.2b), phosphoenolpyruvate (lower glycolysis, Fig. 5.2c), and the cell wall precursor D-alanyl-D-alanine (Fig. 5.2d). Labelling of both glycolysis metabolites was almost identical with or without tetracycline treatment and their absolute concentrations were higher in tetracycline-treated cells (Fig. 5.2e; for fold-changes of 57 other metabolites, see Supplementary Fig. 5.5b). This indicates that tetracycline-treated cells remain metabolically active and that they catabolize glucose with at least the same rate compared with untreated cells. Cell wall precursors were also continuously produced after tetracycline-treatment, as indicated by the isotope label in D-alanyl-D-alanine (Fig. 5.2d). The cellular energy state remained unchanged between the tetracycline-treated and untreated cells (Fig. 5.2f). Despite their high metabolic activity and production of cell wall, tetracycline-treated cells do not divide, as they cannot synthesize new divisome proteins²⁹.

Chapter V: Breakdown of *Vibrio cholerae* biofilm architecture induced by antibiotics disrupts community barrier function

If there was a causal connection between metabolic activity and cell volume increase, we would expect that the simultaneous inhibition of biosynthetic pathways and protein synthesis would stop the cell volume increase. Indeed, exposing biofilms to the folate-biosynthesis inhibitor trimethoprim abolished the increase in cell volume during tetracycline treatment (Fig. 5.2g). Similarly, cells for which glucose was removed at the same time that tetracycline was added did not increase in volume. Together, these experiments show that continued metabolic activity without cell division is necessary for the observed increase in cell volume.

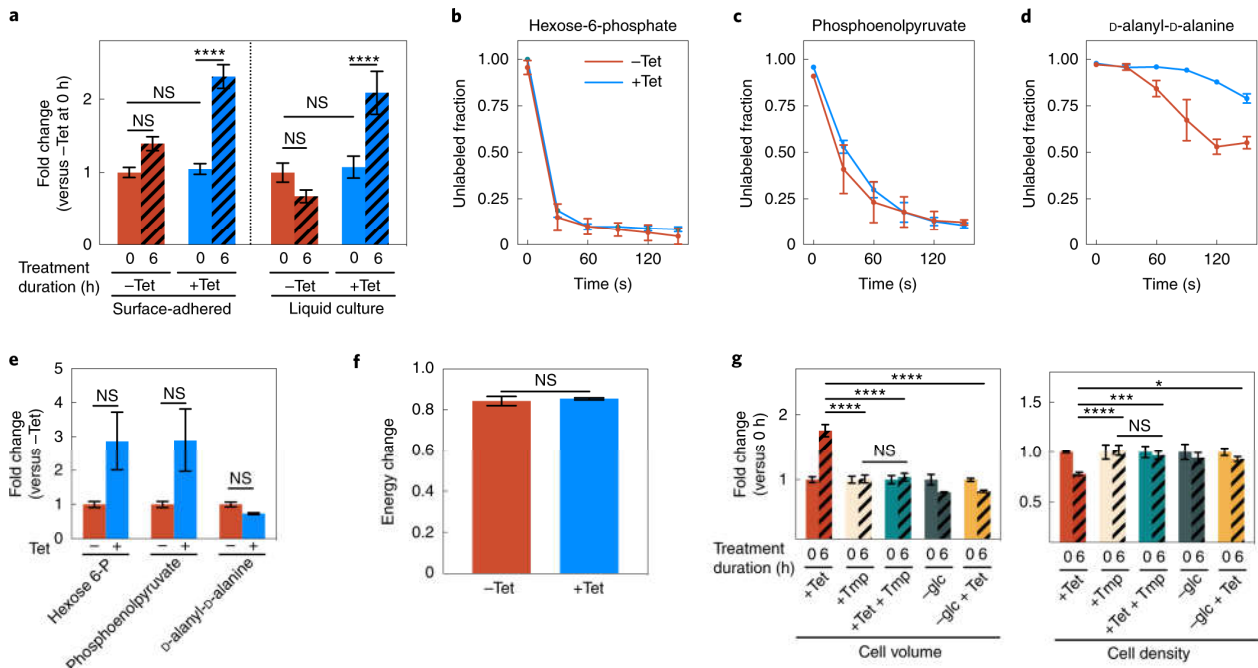


Figure 5.2. Continued metabolic activity of tetracycline-treated cells results during expansion of cell volume. **a**, Fold change of cell volume of surface attached isolated cells grown in a microfluidic device and planktonic cells grown in liquid culture with or without tetracycline treatment, normalized to the untreated cell volume at 0 h. Data are mean \pm s.e.m., $n=3$ independent biological replicates. **b–d**, Tetracycline-treated cells are metabolically active, as shown by unlabelled ratios of hexose-6-phosphate (the first intermediate of glycolysis) (**b**), phosphoenolpyruvate (late glycolysis intermediate) (**c**) and D-alanyl-D-alanine (cell wall precursor) (**d**). Cells treated for 2 h with tetracycline (blue) or untreated control cells (red) were washed with C^{13} -labelled medium for different times, ranging from 0–150 s (mean \pm s.d., $n=3$ independent biological replicates). **e**, Fold change in hexose-6-phosphate, phosphoenolpyruvate and D-alanyl-D-alanine concentration between tetracycline-treated and untreated cells (mean \pm s.e.m., $n=3$ independent biological replicates). **f**, Energy charge, calculated using $([ATP]+0.5[ADP])/([ATP]+[ADP]+[AMP])$, of tetracycline-treated and control cells (mean \pm s.e.m., $n=3$ independent biological replicates). **g**, Fold changes in cell volume and cell density (measured as volume fraction) of biofilms treated with tetracycline, trimethoprim (Tmp) or tetracycline and Tmp, and with glucose removal (–glc) or glucose removal and tetracycline treatment (–glc+Tet). Data are mean \pm s.e.m. Sample sizes (n) are 17 (Tet only), 5 (Tmp only), 6 (Tet + Tmp), 3 (–glc) and 4 (–glc + Tet); each sample corresponds to a different biofilm. For each treatment, the fold change is calculated in relation to the 0 h treatment. In **a** and **g**, statistical significance was calculated using one-way analysis of variance (ANOVA) with Bonferroni’s correction for multiple comparisons. In **e** and **f**, statistical significance was calculated using a two-sided unpaired t-test. Statistically non-significant differences (NS) in **a**: $P=0.067$, 0.99 , 0.24 and 0.78 (left to right); in **e**: $P=0.076$, 0.071 and 0.99 (left to right); in **f**: $P=0.70$; and in **g**: $P=0.99$. * $P<0.05$, *** $P<0.001$ and **** $P<0.0001$.

Of note, biofilms treated with both trimethoprim and tetracycline together also did not display a change in cell packing density (Fig. 5.2g), suggesting that the cell volume increase is necessary for the decrease in cell density in the wild-type *V. cholerae*. Applying tetracycline treatment to biofilms at the same time as removing glucose from the medium yielded results identical to those of trimethoprim treatments (Fig. 5.2g). These results imply that the observed decrease in cell density during tetracycline treatment cannot be caused by a chemical interaction between tetracycline and the biofilm matrix or by an effect of tetracycline on the activity of enzymes that are present at the time of the antibiotic exposure. What then causes the decreased cell density following tetracycline treatment?

The cell packing density in biofilms is probably determined by the local biofilm matrix composition and structure^{11,28,30}. By tracking nanometre-sized beads embedded in the matrix during tetracycline treatment, we observed that the matrix was sheared during the decrease in cell density (Fig. 5.3a), indicating substantial rearrangements of the matrix. To test whether particular matrix components have an effect on the cell density decrease, we investigated deletion mutants of the known *V. cholerae* matrix proteins RbmA, RbmC and Bap1 (ref. ³¹). Only $\Delta rbmA$ biofilms displayed a different phenotype from the wild-type: even though $\Delta rbmA$ cells in mature biofilms showed a similar increase in cell volume with tetracycline treatment, they did not show a strong decrease in cell density (Fig. 5.3b), probably because the untreated biofilms already displayed a low initial cell density. This result suggests that the architectural role of RbmA in wild-type biofilms is connected to the decrease in cell density during tetracycline treatment. RbmA has recently been shown to assume one of two conformational states, open or closed; the open state is associated with binding neighbouring cells together³². The amino acid substitutions D97A or D97K lock RbmA in the open state, whereas R234A locks RbmA in the closed state³². Only biofilms composed of cells with RbmA locked in the open state exhibit a similar biofilm architecture to the wild type, with a decrease in cell density during tetracycline treatment (Fig. 5.3c), indicating that RbmA-dependent cell–cell binding is important for the tetracycline-induced changes in biofilm cell density.

Using immunostaining to visualize RbmA localization, we found that during tetracycline treatment, gaps emerge between cells and the surrounding matrix material (Fig. 5.3d and Supplementary Fig. 5.6), indicating detachment of cells from RbmA. Quantitative immunofluorescence clearly shows that the RbmA levels surrounding each cell decrease rapidly following antibiotic treatment, in contrast to the untreated control (Fig. 5.3e). To further dissect how RbmA is linked to cell density decreases during tetracycline treatment, we used an inducible-RbmA construct in a $\Delta rbmA$ background to vary the amount of RbmA produced during biofilm growth before tetracycline exposure. In the absence of antibiotic treatment, the average cell density increased with increasing RbmA

concentration (Fig. 5.3f and Supplementary Fig. 5.7). Notably, we observed that during tetracycline treatment, the relationship between RbmA concentration and the decrease in cell density has a pronounced minimum (Fig. 5.3g). This suggests that the number of RbmA-mediated cell–cell bonds in the biofilm before tetracycline exposure could be the key to understanding the cause of the change in cell density during tetracycline exposure.

We hypothesized that the detachment of cells from the matrix and each other is due to breakdown of matrix components. However, deletion of known RbmA-processing proteases (HapA, PrtV and IvaP³³) had no effect on cell density (Fig. 5.3i). Nevertheless, RbmA has been shown to bind to the polysaccharide component of the matrix, *Vibrio* polysaccharide (VPS)^{32,33}, presumably acting as a crosslinker for the VPS matrix. This suggests that the RbmA-mediated adhesion between cells can be affected by cleaving VPS. To test this hypothesis, we exposed biofilms that lack the putative VPS-degrading polysaccharide hydrolase RbmB³⁴ to tetracycline. In contrast to biofilms composed of wild-type cells, Δ *rbmB* biofilms barely decreased in cell density during tetracycline treatment (Fig. 5.3i), indicating that the RbmB is necessary for the decreased cell density that is observed in the wild-type. However, wild-type RbmB levels are not sufficient to cause a decrease in cell density without a simultaneous increase in cell volume, as reflected in our trimethoprim and glucose-removal experiments in which the *rbmB* locus was intact (Fig. 5.2g). Overexpression of *rbmB* decreased the cell density—similar to what was observed after tetracycline treatment (Fig. 5.3j)—without requiring a change in cell volume. This shows that when present at high levels, the activity of RbmB is sufficient to alter cell density, but at wild-type RbmB levels, RbmB activity must be accompanied by an increase in cell volume to cause the dissociation of the cells from the matrix, presumably because an increase in cell volume with a simultaneous absence of protein synthesis results in a dilution of the number of cell–RbmA bonds per cell surface area.

Chapter V: Breakdown of *Vibrio cholerae* biofilm architecture induced by antibiotics disrupts community barrier function

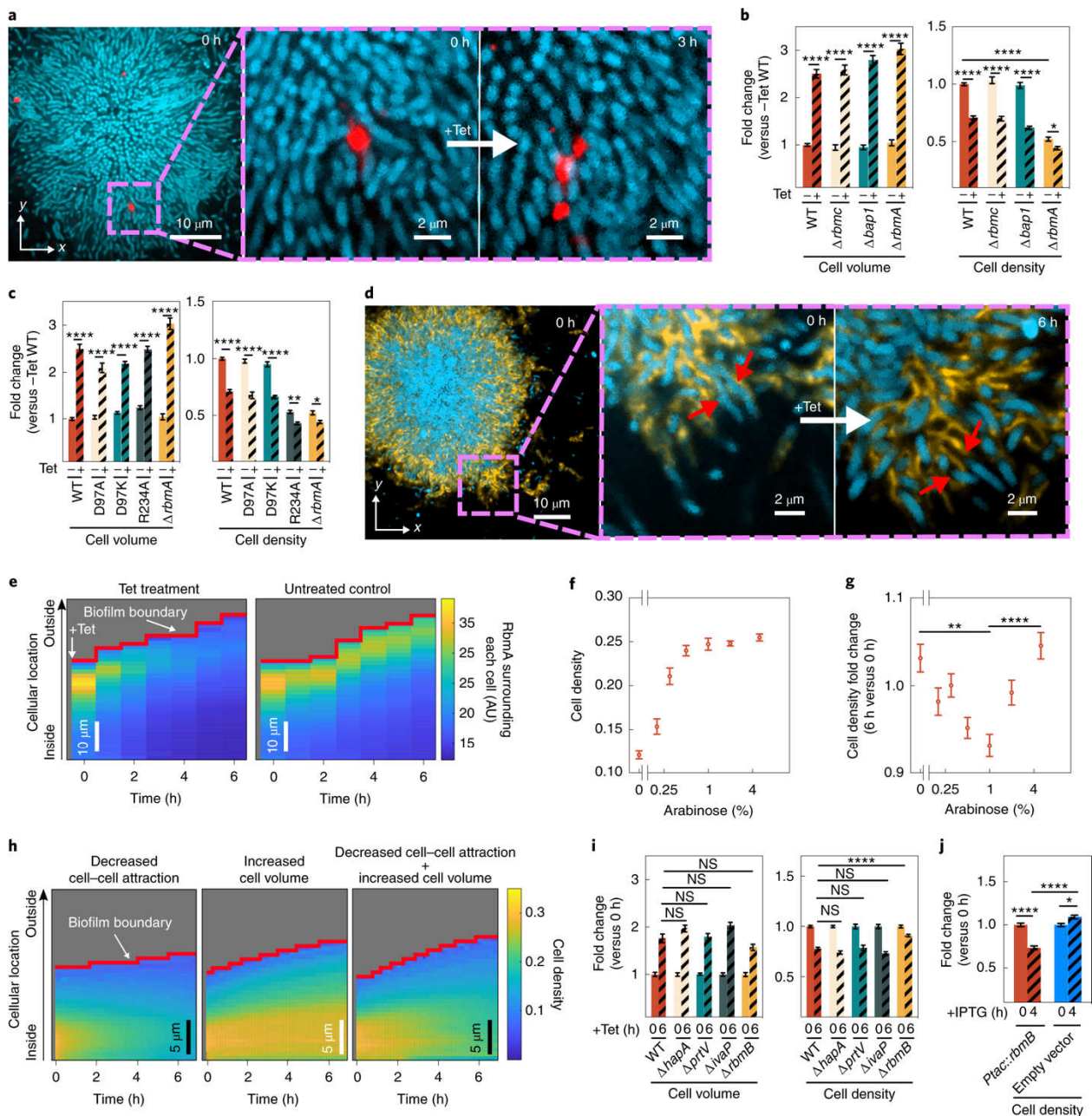


Figure 5.3. Antibiotic-induced architectural breakdown of biofilms. **a**, Matrix movement during antibiotic treatment is visualized by fluorescent beads attached to the matrix. Cells expressing the sfGFP fluorescent protein (cyan) were grown in medium containing fluorescent beads diameter 0.1 μm in diameter (red). Occasionally, beads incorporated into the biofilm matrix. During tetracycline treatment, no new beads entered the biofilm. The magnified inset shows the separation of the red bead cluster during tetracycline treatment, revealing differential movement in the matrix. Images are representative of $n = 3$ different biofilms. **b**, Cell volume and cell density (measured as volume fraction) fold changes of biofilms of matrix-protein deletion mutants in comparison to untreated biofilms. Data are mean \pm s.e.m., $n = 15$ (WT, -Tet), 9 (WT, +Tet), 10 (ΔrbmC , -Tet), 10 (ΔrbmC , +Tet), 15 (Δbap1 , -Tet), 8 (Δbap1 , +Tet) 18 (ΔrbmA , -Tet), 11 (ΔrbmA , +Tet); samples correspond to different biofilms. **c**, Cell volume and cell density fold-changes of RbmA mutants (D97A, D97K and R234A) with different conformations of RbmA structure. Data shown as mean \pm s.e.m.; $n = 15$ (WT, -Tet), 9 (WT, +Tet), 16 (D97A, -Tet), 19 (D97A, +Tet), 19 (D97K, -Tet), 10 (D97K, +Tet), 9 (R234A, -Tet), 10 (R234A, +Tet) 18 (ΔrbmA , -Tet) and 11 (ΔrbmA , +Tet); samples correspond to different biofilms. **d**, During antibiotic exposure, cells (labelled cyan using mTFP1) separate from the matrix

(labelled yellow, using a fluorescent antibody against RbmA–His). The magnified inset shows individual cells detaching from RbmA during tetracycline treatment (indicated by red arrows, which show the same region of the biofilm in both panels). Images are representative of $n = 5$ different biofilms. **e**, Heat maps show the average RbmA–His immunofluorescence surrounding each cell as a function of time and cellular distance from the biofilm boundary for tetracycline-treated (left) and untreated control (right) biofilms. Heat maps are representative of $n = 5$ different biofilms. **f**, Cell density of $\Delta rbmA$ $P_{BAD}:rbmA$ biofilms as a function of arabinose concentration. Data are mean \pm s.e.m., $n = 7$ (0% arabinose), 12 (0.2%), 11 (0.3%), 16 (0.5%), 10 (1%), 18 (2%) and 14 (5%) samples; samples correspond to different biofilms. **g**, Fold change in cell density (comparing 6 h and 0 h of tetracycline treatment) of biofilms grown from the $\Delta rbmA$ $P_{BAD}:rbmA$ strain, as a function of arabinose concentration. Data are mean \pm s.e.m., $n = 5$ (0% arabinose), 12 (0.2%), 11 (0.3%), 16 (0.5%), 10 (1%), 18 (2%) and 14 (5%) samples; samples correspond to different biofilms. **h**, Heat maps of simulated biofilms that were subject to a linear decrease in cell–cell attraction over 7 h (left), a linear increase in cell volume over 6 h (middle) or both effects together (right); $n = 3$ simulation runs. **i**, Fold changes in cell volume and cell density of tetracycline-treated biofilms grown from strains that lack proteases involved in the processing of the matrix protein RbmA ($\Delta hapA$, $\Delta prtV$ and $\Delta ivaP$), or the enzyme RbmB (mean \pm s.e.m., $n = 17$ (WT), 8 ($\Delta hapA$), 16 ($\Delta prtV$), 3 ($\Delta ivaP$) and 15 ($\Delta rbmB$)). **j**, Fold changes in cell density of wild-type biofilms carrying the $P_{tac}:rbmB$ construct on a plasmid or an empty vector with IPTG induction (mean \pm s.e.m., $n = 16$ for $P_{tac}:rbmB$, $n = 11$ for control). In **i**, **j**, each sample corresponds to a different biofilm. Statistical significances were calculated using one-way ANOVA with Bonferroni's correction. Statistically non-significant differences (NS) in **i** correspond to $P = 0.43, 0.99, 0.59, 0.34, 0.99, 0.99$ and 0.99 (left to right, respectively). * $P < 0.05$, ** $P < 0.01$, *** $P < 0.001$ and **** $P < 0.0001$. Images in **a**, **d** were acquired 2 μm above the coverslip. WT, wild type.

For several species, it has been shown that the pressure generated by growth-induced expansion of biovolume within biofilms is counteracted by the adhesion of the matrix, resulting in a net compression³⁵. Microscopically, this is achieved by a balance between attractive and repulsive interactions between cells²⁸. For *V. cholerae*, cell–cell attraction is primarily mediated by RbmA, whereas cell–cell repulsion is mediated by osmotic effects and the secretion of VPS^{28,36}. Should the RbmA-mediated bonds between cells be broken—for example, due to a reduced number of RbmA bonds per cell surface area following the cell volume increase—the balance between attraction and repulsion would be tipped and the cell density would decrease. To test this hypothesis, we used individual-based simulations that use an accurate and calibrated representation of mechanical cell–cell interactions in *V. cholerae* biofilms, enabling us to tune key parameters, including cell volume and cell–cell attraction and repulsion²⁸. Using these simulations, we determined that a reduction in cell–cell attraction causes a decrease in cell density, but this alteration alone was not sufficient to recapitulate the pattern of biofilm volume expansion seen experimentally (Fig. 5.3h, left and Supplementary Fig. 5.8a,c). Similarly, increasing the cell volume without modifying the cell–cell attraction also fails to recapitulate the architectural changes seen in live biofilms (Fig. 5.3h, middle). However, when the cell–cell attraction is decreased and the cell volume is simultaneously increased, our simulations reproduce the architectural changes observed in experimental biofilms treated with antibiotics (Fig. 5.3h, right and Supplementary Fig. 5.8b,c). These results indicate that after the cells

detach from the matrix, the observed changes in the biofilm architecture are primarily due to changes in the mechanical interactions between cells during tetracycline treatment and the accompanying increase in cell volume.

The profound changes in biofilm architecture that result from transient antibiotic exposure could potentially open up niches for external cells to colonize and invade the antibiotic-treated biofilms. Similarly, the dissociation of cells from their matrix during antibiotic exposure may also enable phage entry into the biofilm, which is otherwise prevented by matrix³⁷.

To test these hypotheses, we first exposed tetracycline-treated *V. cholerae* biofilms to planktonic cultures of isogenic cells expressing a different fluorescent protein. Tetracycline-treated biofilms were indeed susceptible to colonization of their interior (Fig. 5.4a and Supplementary Fig. 5.9a,b); when the medium flowing through the growth channels was switched back to antibiotic-free medium, the resident biofilm strain and the colonizing strain proceeded to coexist in the biofilm, with the colonizer increasing in frequency to invade the biofilm population (Fig. 5.4c). In control experiments without antibiotic treatment, biofilms were highly resistant to colonization and population invasion (Fig. 5.4b), consistent with previous investigations³⁸. We also observed that bacterial species which share the natural marine and estuarine habitats with *V. cholerae*, such as *Shewanella putrefaciens*³⁹ and *Pseudomonas aeruginosa*⁴⁰, can also colonize and invade tetracycline-treated *V. cholerae* biofilm populations (Fig. 5.4d–g). Given this susceptibility to population invasion by other bacterial species, we tested whether bacteriophages, which are the primary predator of *V. cholerae* in environmental habitats, could also invade antibiotic-treated biofilms. By exposing *V. cholerae* biofilms to tetracycline and the vibriophage N-4 for 6 h, we observed an accumulation of phages in the outer region of the antibiotic-treated biofilms, in contrast to control biofilms (Fig. 5.4h and Supplementary Fig. 5.9c). In sum, these experiments demonstrate how architectural changes induced by antibiotic treatment can severely affect the ecological succession⁴¹ of *V. cholerae* biofilm communities, and we speculate that architectural changes during antimicrobial treatment could have a key role in invasion susceptibility and succession of microbial communities in general.

Chapter V: Breakdown of *Vibrio cholerae* biofilm architecture induced by antibiotics disrupts community barrier function

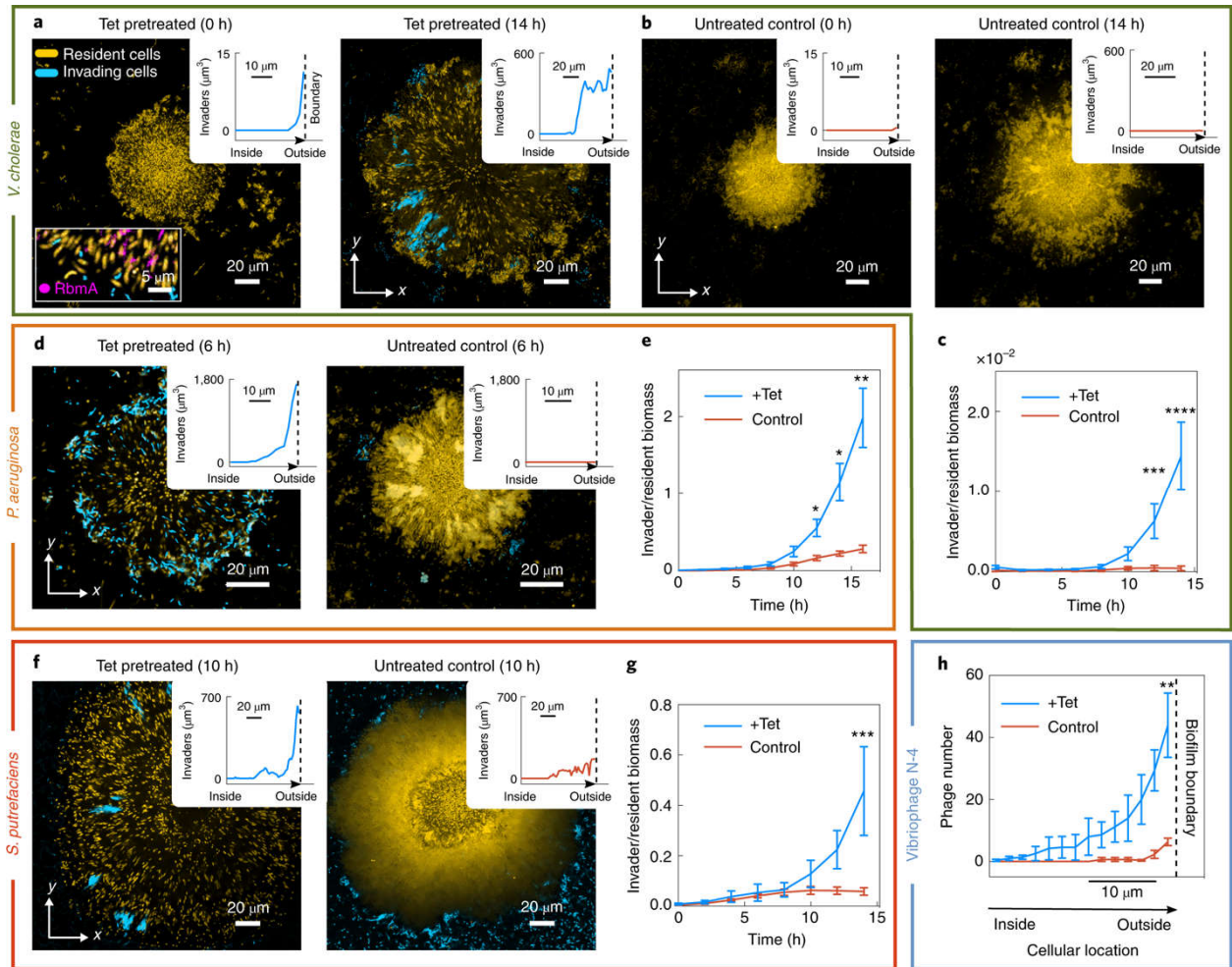


Figure 5.4. Antibiotic-treated biofilms are susceptible to colonization and invasion. **a**, Confocal xy slices of a resident *V. cholerae* wild-type biofilm, expressing mKOκ constitutively (cells shown in yellow). The resident biofilm underwent tetracycline treatment for 6 h, followed by 2 h exposure to invader cells (cyan), which are isogenic except for the fluorescent protein they express (sfGFP instead of mKOκ). Following exposure to planktonic invader cells, the medium was exchanged to fresh, sterile medium and the imaging was started (labelled 0 h here). The inset at 0 h shows a biofilm colonized by invader cells in which RbmA is visualized using immunofluorescence (magenta). Another inset shows the location where planktonic cells have colonized the resident biofilm, measured as a distance from the biofilm boundary. Replicate experiments are shown in Supplementary Fig. 5.9a,b. **b**, Confocal xy slices of a control biofilm (not treated with tetracycline) exposed to *V. cholerae* invader cells for the same duration. Very few cells attach to the glass surface, and none to the resident biofilm, as described in Methods. Images in **a,b** are representative of eight different biofilms. **c**, Quantification of invader biomass divided by resident biomass during invasion of a *V. cholerae* biofilm population; data are mean \pm s.e.m., $n = 8$ for +Tet and $n = 11$ for control conditions. **d**, Confocal xy slice of a tetracycline-treated or control resident *V. cholerae* biofilm invaded by *P. aeruginosa*, following the same protocol as in **a**. Images are representative of 12 different biofilms. **e**, *P. aeruginosa* invader biomass normalized by *V. cholerae* resident biomass; data are mean \pm s.e.m., $n = 12$ for +Tet and $n = 11$ for control. **f**, Confocal xy slice of a tetracycline-treated or control resident *V. cholerae* biofilm invaded by *S. putrefaciens*, following the same protocol as in **a**. Images are representative of eight different biofilms. **g**, *S. putrefaciens* invader biomass normalized by *V. cholerae* resident biomass; mean \pm s.e.m., $n = 12$ for +Tet and $n = 8$ for controls. **h**, Quantification of number of vibriophage N-4 virions as a function of position for tetracycline-treated biofilms and untreated control biofilms after 6 h of phage exposure; data are

Chapter V: Breakdown of *Vibrio cholerae* biofilm architecture induced by antibiotics disrupts community barrier function

mean \pm s.e.m., $n = 5$ for +Tet and $n = 3$ for controls. Images of phage invasion of biofilms are shown in Supplementary Fig. 5.9c. Images shown in **a**, **b**, **d**, **f** were acquired 2 μm above the substrate. Sample sizes (n) correspond to different biofilms. Statistical significances were calculated using two-way ANOVA with Bonferroni's correction. $*P < 0.05$, $**P < 0.01$, $***P < 0.001$ and $****P < 0.0001$.

The ubiquity of biofilm formation in microbial ecology is well-accepted, but we are still in the early stages of understanding how cell-level responses to the local environment translate to the emergent collective responses of biofilm communities. Here we have shown that even transient exposure to translation inhibitors causes changes in cell shape and physiology that yield large-scale alterations of biofilm architecture. The loosening of cell-matrix associations that occurs following antibiotic exposure, in turn, markedly alters community ecology by allowing new cells and phages to invade the community that would otherwise be unable to do so. The unicellular and multicellular processes identified here highlight mechanistic causes underlying ecological succession of microbial communities in response to antimicrobial therapeutics.

Methods

Media and strains. All *V. cholerae* strains used in this study are derivatives of the wild-type *V. cholerae* O1 biovar El Tor strain N16961. *V. cholerae* deletion mutations were created using plasmids derived from the pKAS32 suicide plasmid, harboured in *Escherichia coli* S17-1 λ pir^{27,42}. Plasmids for chromosomal deletions were made by amplification of the 1 kb flanking regions of the corresponding gene. The PCR product was cloned into the suicide plasmid and transformed into *E. coli*. Plasmids were transferred into *V. cholerae* by conjugation. Fluorescent protein expression constructs were introduced into the *lacZ* locus and screening was carried out using a β -galactosidase colony colour conversion assay. For *rbmB* overexpression experiments (Fig. 5.3j), *V. cholerae* strains carrying plasmids were grown with gentamicin (30 $\mu\text{g ml}^{-1}$) throughout all experiments.

All experiments with biofilms or single cells were performed in M9 minimal, medium (M9 minimal salts; M6030, Sigma), supplemented with 2 mM MgSO_4 100 mM CaCl_2 , MEM vitamins, 0.5% glucose and 15 mM triethanolamine (pH 7.1), referred to in the manuscript as ‘M9 medium’ for simplicity, unless stated otherwise. For *S. putrefaciens* invasion assays, biofilms were grown in tryptone broth (10 g l^{-1} tryptone) instead of M9 medium. Overnight cultures were grown in shaking (250 r.p.m.) liquid Luria–Bertani–Miller broth (LB-Miller; 10 g l^{-1} tryptone, 5 g l^{-1} yeast extract and 10 g l^{-1} NaCl) at 37 °C. Detailed lists of all strains, plasmids and DNA oligonucleotides used in this study are provided in Supplementary Tables 5.1–3, respectively.

MIC determination. For MIC determination, the wild-type *V. cholerae* N16961 strain (KDV101) was grown in LB-Miller overnight at 37 °C with shaking at 250 r.p.m. The overnight cultures were then diluted 1:50 in M9 medium (see description of medium above) and grown at 28 °C until exponential phase (absorbance at 600 nm (OD_{600}) of 0.5–0.6). The OD_{600} was then adjusted to 0.5 and the suspension was used to inoculate a 96-well plate (82.1581.001, Sarstedt) containing different antibiotic concentrations. The liquid volume per well was 180 μl and the initial inoculation OD_{600} in each well was 0.05. The 96-well plate was then incubated at 28 °C with shaking in a microtitre plate reader (Spark 10 M, Tecan) for 20 h. MICs were calculated from two independent experiments with two technical replicates per experiment (Supplementary Fig. 5.1c,d and Supplementary Table 5.4).

Flow chamber biofilm experiments. *V. cholerae* biofilms were grown in microfluidic flow chambers made from polydimethylsiloxane bonded to glass coverslips using an oxygen plasma, with four to eight channels on a single coverslip, as previously described²⁶. The microfluidic channels measured 500 μm in width, 100 μm in height and 7 mm in length. Channels were inoculated with overnight cultures of *V. cholerae* strains. Following inoculation, the cells were given 1 h at room temperature (24–26 °C) to

attach to the surface of the channel before fresh M9 medium was flowed through the channel at a flow rate of $50 \mu\text{l min}^{-1}$ for 45 s, to wash away non-attached cells and to completely replace the LB-Miller medium from the channel. The flow rate of fresh M9 medium was then set to $0.05 \mu\text{l min}^{-1}$ for the remainder of the experiment, corresponding to an average flow speed of $17 \mu\text{m s}^{-1}$ in the channel. Flow rates were maintained using a syringe pump (picoPlus, Harvard Apparatus). The flow chamber, M9 medium and syringe pump were maintained at room temperature (24–26 °C) for the duration of all experiments.

Exposure of biofilms to antibiotics. To test the influence of different antibiotics on mature biofilms, biofilms were grown for 24 h in M9 medium before being exposed to one of the following antibiotics: rifampicin ($6 \mu\text{g ml}^{-1}$), ciprofloxacin ($0.5 \mu\text{g ml}^{-1}$), erythromycin ($200 \mu\text{g ml}^{-1}$), kanamycin ($200 \mu\text{g ml}^{-1}$), ampicillin ($400 \mu\text{g ml}^{-1}$), tetracycline ($3 \mu\text{g ml}^{-1}$), chloramphenicol ($10 \mu\text{g ml}^{-1}$), trimethoprim ($10 \mu\text{g ml}^{-1}$) or ceftibuten ($50 \mu\text{g ml}^{-1}$). The concentrations for each antibiotic were at least two times the MIC, which was determined for our strain and media conditions using a microtiter plate reader (Spark 10 M, Tecan), as described in the section on MIC measurements above. For ampicillin and ceftibuten, it was not possible to determine a MIC. Instead, we used concentrations that cause changes in cell morphology due to cell-wall loss. After exposure to an antibiotic for 24 h, the biofilms were stained with $4 \mu\text{M}$ SYTO 9 (S34854, ThermoFisher).

To test for cell death during antibiotic exposure, propidium iodide ($7.5 \mu\text{M}$) was used as a reporter—cells that have a compromised cell envelope are stained red by propidium iodide. During time-series imaging of cell death inside biofilms, a strain carrying a *P_{tac}* promoter fusion to *mTFP1* (KDV392) was used (Supplementary Fig. 5.4).

To investigate biofilm architectural modifications in response to antibiotic treatment in detail, tetracycline was chosen as the main antibiotic for this study, as it is a commonly used treatment against cholera infections²⁵. To avoid investigations of architectural modifications due to cell death, exposure to tetracycline was limited to 6 h in all experiments described in this manuscript, except for those investigating cell death in biofilms as a function of treatment time (Supplementary Fig. 5.4). For the experiments involving a constitutively expressed fluorescent protein for biofilm architecture quantification, we used strains carrying a *P_{tac}* promoter fused to the genes coding for the fluorescent reporters mKusabira orange kappa (mKOκ), a red fluorescent protein (mRuby3), superfolder green fluorescent protein (sfGFP) or bright teal fluorescent protein (mTFP1) at the *lacZ* locus.

Exposure of individual adherent cells to antibiotics. An overnight culture of a wild-type strain carrying the constitutively expressed *Ptac:mKOk* system on the chromosome (strain KDV103) was back-diluted 1:100 in M9 medium and grown under shaking conditions at 250 r.p.m. until $OD_{600} = 0.45\text{--}0.55$. This suspension was then used to inoculate a diffuse monolayer of cells on the glass substratum of microfluidic devices, which were kept at room temperature (24–26 °C). After 30 min, flow was initiated at $0.05\ \mu\text{l min}^{-1}$ using M9 with or without tetracycline. The flow chambers were kept at room temperature throughout the experiment.

Antibiotics treatments in liquid culture and metabolomics. Overnight cultures were back-diluted 1:100 in M9 medium and grown at 25 °C in shaking conditions at 250 r.p.m. until the culture reached $OD_{600} = 0.45\text{--}0.55$. At this point, tetracycline or an equivalent volume of methanol (the stock solvent for tetracycline, as a negative control) was added to the cultures. To measure the cell size as a function of time after tetracycline or clean methanol was added, aliquots of the culture were taken every hour and imaged by microscopy. For metabolome analysis, samples were collected after 2 h for both treatments (tetracycline- and non-tetracycline- exposed cultures).

Metabolome analyses were performed as previously described⁴³, with minor modifications. In brief, for sampling of metabolites by filtration, 1 ml of culture with an OD_{600} of 0.5 was vacuum-filtered on a $0.45\ \mu\text{m}$ pore-size membrane (HVLP02500, Merck Millipore) to remove the spent medium, before cells were exposed to M9 medium containing $U\text{-}^{13}\text{C}$ glucose (99%, Cambridge Isotope Laboratories) for 0, 30, 90, 120 or 150 s. Afterwards, filters were immediately transferred to a mixture of acetonitrile:methanol:water (40:40:20) and stored at $-20\ ^\circ\text{C}$. Metabolite extracts were centrifuged for 15 min at 13,000 r.p.m. at $-9\ ^\circ\text{C}$ to remove cellular debris. The supernatant was used directly for liquid chromatography with tandem mass spectrometry.

RbmA complementation, titration and immunolabelling. To control the amount of RbmA produced by cells, we constructed a $\Delta rbmA$ clean deletion strain into which *rbmA*-His₆ was re-introduced under the control of the tightly regulated, arabinose-inducible P_{BAD} promoter. This construct was inserted by allelic exchange into the *V. cholerae* chromosome at the *lacZ* locus (strain KDV859). The following arabinose concentrations were used to induce RbmA expression in biofilms: 0.2, 0.3, 0.5, 1, 2 and 5%. To stain extracellular RbmA, a strain carrying the *Ptac* promoter fused to *mTFP1* and *rbmA*-His₆ (KDV605) was used. After 4 h of biofilm growth, a His-tag monoclonal antibody conjugated to Alexa Fluor 555 was added at a final concentration of $1\ \mu\text{g ml}^{-1}$ (ThermoFisher, MA1-135-A555) to the inflowing M9 medium. To avoid nonspecific binding, bovine serum albumin ($1\ \text{mg ml}^{-1}$) was added to the medium together with the antibody, as described previously³¹.

Matrix movement assay using fluorescent beads. Biofilms of the sfGFP expressing wild-type strain KDV311 were grown for 24 h in presence of red fluorescent beads of diameter 0.1 μm (F8887, ThermoFisher) in the medium. This led to an incorporation of beads into the extracellular matrix of the biofilms. Subsequently, the medium was exchanged for fresh M9 medium without beads and tetracycline was added. From this point, the biofilms were imaged for 6 h with a time resolution of 1 h.

RbmB controlled overexpression. Biofilms of the mKO κ -expressing wild-type strain carrying either a plasmid-based isopropylthiogalactoside (IPTG)-inducible *rbmB* expression construct (KDV1070) or an empty vector (KDV1078) were grown for 24 h before addition of 1 μM IPTG. Starting from this time point, biofilms were imaged for 4 h with a time resolution of 1 h.

Bacterial biofilm-invasion assay. Biofilms of the mKO κ -expressing wild-type strain KDV103 were grown for 24 h before the inflowing M9 medium was exchanged to one containing tetracycline for 6 h. As a control treatment, M9 medium without tetracycline was added for 6 h. Separately, at the same time, an overnight culture of the sfGFP-expressing wild-type strain KDV311 or an overnight culture of KDP54, a *P. aeruginosa* PAO1 strain expressing sfGFP was diluted 1:200 in M9 and grown at 37 $^{\circ}\text{C}$ under shaking conditions (250 r.p.m.) until exponential phase ($\text{OD}_{600} = 0.4$). After the biofilms were exposed to either tetracycline or control treatment for 6 h, the exponential phase culture of KDV311 or KDP54 was introduced into the flow channel containing the resident KDV103 biofilms at a flow rate of 0.05 $\mu\text{l min}^{-1}$. After the sfGFP-expressing planktonic cells were allowed to colonize and invade the resident biofilms for 2 h, the inflowing medium was exchanged to sterile M9 medium without any cells. Starting from this time point (labelled as '0 h' in Fig. 5.4 and Supplementary Fig. 5.9a,b), biofilms were imaged for 24 h with a time resolution of 2 h.

During experiments in which *V. cholerae* resident biofilms were exposed to planktonic *V. cholerae* cells (Fig. 5.4a,b and Supplementary Fig. 5.9a,b), the planktonic cells rarely attached to the glass surface in either conditions (tetracycline-pretreated or untreated control) during the 2 h initial time window of exposure to the resident biofilms. There was significantly more attachment and colonization to tetracycline-treated biofilms compared with untreated control biofilms at 0 h (Fig. 5.4a,b), and therefore much more biomass accumulation of the invader cells in the tetracycline-treated condition compared with the control. Some of the accumulated invader biomass in the tetracycline-treated condition dispersed and colonized the glass surface surrounding the biofilm, whereas in the control condition there was not enough invader biomass to substantially colonize the glass surface.

For *S. putrefaciens* (CN-32 wild-type strain, KDM77) invasion experiments, the same protocol was used as described above for the *V. cholerae* and *P. aeruginosa* invasion experiments, except for

the following modifications. All *V. cholerae* resident biofilms were grown in tryptone broth. To obtain an exponentially growing culture of *S. putrefaciens*, the frozen stock was streaked on a LB-Miller agar plate, which was incubated at room temperature. From this plate, colonies were picked to inoculate a LB-Miller liquid culture, which was grown under shaking conditions at 28 °C. Using this culture, another flask containing tryptone broth was inoculated with a 1:200 dilution and grown at 28 °C until exponential phase ($OD_{600} = 0.4$). This culture was used as the culture of planktonic invader cells for the invasion assay.

Biofilm phage invasion assay and vibriophage N-4 fluorescent labelling. Bacteriophage were labelled as described previously³⁷. In brief, 100 μ l of purified vibriophage with a concentration of 1×10^{12} plaque-forming units (PFU) per ml were mixed with sodium carbonate (0.1 M final concentration) and then incubated with 0.1 mg Alexa Fluor 488 5-TFP (A30005, ThermoFisher Scientific) for 1 h at room temperature under continuous shaking. The reaction mixture was first dialysed at 4 °C against 500 ml PBS for 3 h and then dialysed overnight at 4 °C against 2 l of PBS. This was done to separate phage from unbound dye. This stock of fluorescently labelled phage was stored at 4 °C.

Biofilms of the mRuby3-expressing *V. cholerae* wild-type strain (KDV657) were grown for 24 h, before the inflowing M9 medium was exchanged to contain tetracycline for 6 h and fluorescently labelled phage (a 1:100 dilution of the fluorescently labelled phage stock). As a control treatment, M9 medium without tetracycline, but containing the same concentration of vibriophage was added for 6 h. Biofilms were imaged for the 6 h of phage exposure with a time resolution of 2 h (Supplementary Fig. 5.9c).

Microscopy and image analysis. Biofilm architecture was imaged and analysed in the biofilm volume between $z = 0 \mu\text{m}$ and $z = 10 \mu\text{m}$ (that is, the part of the biofilm within the 10 μm of the glass substrate) for most experiments, unless indicated otherwise in the figure caption. In control experiments, we determined that this lower part of the biofilm had an identical biofilm architecture to the complete biofilm in terms of cell volume, cell aspect ratio and cell density, both in terms of mean values (Supplementary Fig. 5.10a) and in terms of spatially resolved values at different time points (Supplementary Fig. 5.10b,c). Because of photobleaching and phototoxicity it was not possible to acquire image time series during antibiotic treatment of the whole biofilm at single-cell resolution, so for most experiments only the representative lowest 10 μm of the biofilm were imaged. All imaging was performed using a Yokogawa spinning-disc confocal unit, mounted on a Nikon Ti-E inverted microscope using a $\times 100$ silicone oil objective (numerical aperture (NA) 1.35, Olympus). For confocal imaging, pictures were taken with a z-step size of 0.4 μm .

For biofilm-invasion assays, we used a Nikon ×60 NA 1.4 oil objective on the spinning-disc confocal microscope. For invasion experiments that required three- colour imaging (Fig. 5.4a), we used a point-scanning confocal microscope (LSM 880, Zeiss), equipped with a tuneable emission spectrum selector for each fluorescence channel, and a Zeiss ×60 NA 1.4 oil objective.

Image analysis of biofilms was performed using Matlab (Mathworks), as described previously^{27,28}. After segmentation of all cells in the biofilm images, we calculated for each cell the aspect ratio, the matrix density surrounding each cell (for experiments in which RbmA was labelled fluorescently), the cell density at each cellular location and each cell's distance to the biofilm boundary. The biofilm boundary is defined as the interface between the biofilm and the liquid growth medium. Each of these quantifications is explained in detail below.

To calculate the cellular aspect ratio, an ellipsoid was fitted into each cell and the longest axis of the ellipsoid was used as cell length and the shortest as cell width. The cell aspect ratio is the ratio of cell length and cell width.

To calculate the location of each cell relative to the biofilm boundary, which is the spatial metric used to quantify the cellular location in the biofilms throughout the manuscript, we calculated the shortest distance from each cell to the interface between the biofilm and the liquid growth medium. Qualitatively, this spatial metric for the cellular location in the biofilm corresponds to the shortest distance that nutrients from the growth medium would have to diffuse to reach the cell. We note that *V. cholerae* biofilm communities grow into colonies with roughly hemispherical shape in our conditions^{27,28}. If the colony morphology would be an exact hemisphere, then the distance of each cell to the biofilm boundary would correspond to a path along the radial direction in spherical coordinates, where the origin would be at the centre of mass of the colony projected onto the $z = 0 \mu\text{m}$ plane. Given that *V. cholerae* biofilms differ from exact hemispherical shapes, we opted to use the distance to the biofilm boundary as the spatial metric to quantify cellular location.

To compute the kymograph heat maps for a given parameter (such as the cell volume or cell aspect ratio) at each time point, the parameter value of all cells with the same distance to the biofilm boundary was averaged, resulting in a value that corresponds to the value of a particular pixel in the heat map. This calculation was then performed for all distances to the biofilm boundary and all time points to result in the heat map. We previously used such spatiotemporal heat maps of biofilms to quantify spatiotemporal biofilm development²⁸ and biofilm dispersal²⁷.

To calculate the cell density of biofilms, we used a measurement of volume fraction. We created a sphere of 3 μm radius starting from the centroid of each cell. Then, we calculated how much of the volume of the sphere, excluding the volume of the cell used to create the sphere, was occupied by other cells.

To quantify the RbmA-matrix density surrounding each cell, we measured the fluorescent signal of immunofluorescently labelled RbmA–His₆ that surrounds each cell within a 0.2 μm -thick 3D shell around each cell. The strain with the His-tagged RbmA used for immunostaining phenocopies the wild-type strain before and during antibiotic treatment (Supplementary Fig. 5.6).

To quantify the biofilm-invasion phenotype (Fig. 5.4) we measured the total biomass of the invader cells between $z = 0 \mu\text{m}$ and $z = 10 \mu\text{m}$ (that is, the lowest 10 μm of the biofilm) and divided this value by the total biomass of cells within the lowest 10 μm of the resident biofilm. To analyse images of planktonic cells or single cells that are adherent to a surface (Fig. 5.2a), MicrobeJ was used⁴⁴.

Crystal violet assay. Crystal violet experiments were performed as described previously⁴⁵, with some modifications. In brief, strain KDV103 and strain KDV115 were grown overnight in LB-Miller at 37 °C, shaking at 250 r.p.m. These cultures were then diluted 1:1,000 in M9 and the resulting suspension was used to inoculate a 96-well plate, which was then incubated for biofilm growth at room temperature. At different time points, the biomass was measured using crystal violet methods as described previously⁴⁵

For testing antibiotic exposure of biofilms with the crystal violet assay, biofilms were grown for 14 h in a 96-well plate (82.1581.001, Sarstedt). At this time, tetracycline, trimethoprim, chloramphenicol, kanamycin or erythromycin, were added, reaching a final concentration of 3 $\mu\text{g ml}^{-1}$, 10 $\mu\text{g ml}^{-1}$, 10 $\mu\text{g ml}^{-1}$ 200 $\mu\text{g ml}^{-1}$ or 200 $\mu\text{g ml}^{-1}$, respectively. As a control, the same volume of M9 medium without tetracycline was added to a different well. The treated and untreated wells were then incubated for 6 h. After this incubation period, the biomass was measured using crystal violet. All measurements were performed using a microplate reader (Tecan Spark 10 M). For each measurement, the data were averaged from eight wells (technical replicates) per experiment, and $n = 3$ independent biological replicates.

Biofilm simulations. Biofilm formation was simulated using the agent-based framework described by Hartmann et al.²⁸. Cells are modelled as ellipsoids interacting with the channel wall via a repulsive boundary potential, and with other cells via an interaction potential. This interaction potential accounts for effective cell–cell repulsion due to steric forces and VPS production, and for cell–cell attraction

mediated by adhesion molecules such as RbmA³². For two cells γ and β , we let l_γ and l_β be their lengths and d_γ and d_β their widths in μm ; $\hat{\mathbf{n}}_\gamma$ and $\hat{\mathbf{n}}_\beta$ are their orientation vectors, $r_{\gamma\beta}$ is the distance between their centroids, and $\hat{\mathbf{r}}_{\gamma\beta}$ is the unit vector pointing from the centroid of cell γ to the centroid of cell β . The pairwise interaction potential $U_{\gamma\beta}$ between cell γ and cell β is

$$U_{\gamma\beta} = \epsilon_0 \epsilon_1 \left(\exp(-\rho_{\gamma\beta}^2 / \lambda_r^2) + \frac{v}{1 + \exp((\rho_a - \rho_{\gamma\beta}) / \lambda_a)} \right) \quad (1)$$

where $\rho_{\gamma\beta} = r_{\gamma\beta} / \sigma$ is the shape-normalized cell–cell distance between two cells in μm (ref. ²⁸). The dimensionless range parameter $\sigma(l_\gamma, l_\beta; d_\gamma, d_\beta; \hat{\mathbf{n}}_\gamma, \hat{\mathbf{n}}_\beta; \hat{\mathbf{r}}_{\gamma\beta})$ depends on the cells' ellipsoidal shapes, relative positions and the relative orientations. The overall strength of $U_{\gamma\beta}$ is set by the energy scale ϵ_0 , scaled by the dimensionless geometric factor $\epsilon_1(l_\gamma, l_\beta; d_\gamma, d_\beta; \hat{\mathbf{n}}_\gamma, \hat{\mathbf{n}}_\beta)$ that accounts for the shapes and the relative orientations of the cells²⁸. The range of cell–cell repulsion is set by length parameter λ_r . The relative strength of the cell–cell attraction is set by dimensionless parameter v . The length parameter ρ_a determines the energetically preferred cell–cell distance, and λ_a is the gradient of the attractive barrier. The model parameters ϵ_0 , λ_r and λ_a were obtained by fitting simulated biofilms to experimental biofilms, using the mean square distance of a feature vector as a metric, which incorporated 14 different architectural parameters and their temporal development²⁸. For $\epsilon_0 = 5 \times 10^{-20} \text{ J}$, $\lambda_r = 1.16 \mu\text{m}$, $v = 0.13$, $\lambda_a = 0.11 \mu\text{m}$ and $\rho_a = 2.0 \mu\text{m}$, the simulations yield biofilms with quantitatively and qualitatively similar architectural dynamics as those observed in the experiments for biofilm sizes up to approximately 2,000 cells (for other simulation parameters and detailed comparisons between simulations and experimental biofilms, see Hartmann et al.²⁸).

Using this model, biofilm growth was simulated until the biofilm size reached 1,000 cells. Then, tetracycline-treatment was simulated by stopping cell division and probing three different effects: (1) the cell–cell attraction was linearly decreased to zero over time with varying total duration (0–10 h), following the quantitative relationship between varying RbmA levels and the model parameters, (2) the volume of each ϵ_0 , λ_r , v , ρ_a and λ_a that was established by Hartmann et al.²⁸ cell was increased according to the single cell volume growth rate observed in biofilms after tetracycline-treatment, and (3) the joint effects of loss of cell–cell attraction and increase in cell volume were applied together. In all cases, the cell density of the simulated biofilm was monitored as a function of tetracycline-treatment time and as a function of the shortest distance to the boundary between the biofilm and the growth medium, using the same analysis scripts as for the experimental biofilms.

Statistical analysis. All statistical tests indicated in figure legends were performed using GraphPad Prism v.8.1.1.

Data availability. Raw and analysed data that support the findings of this study are available from the corresponding author upon request.

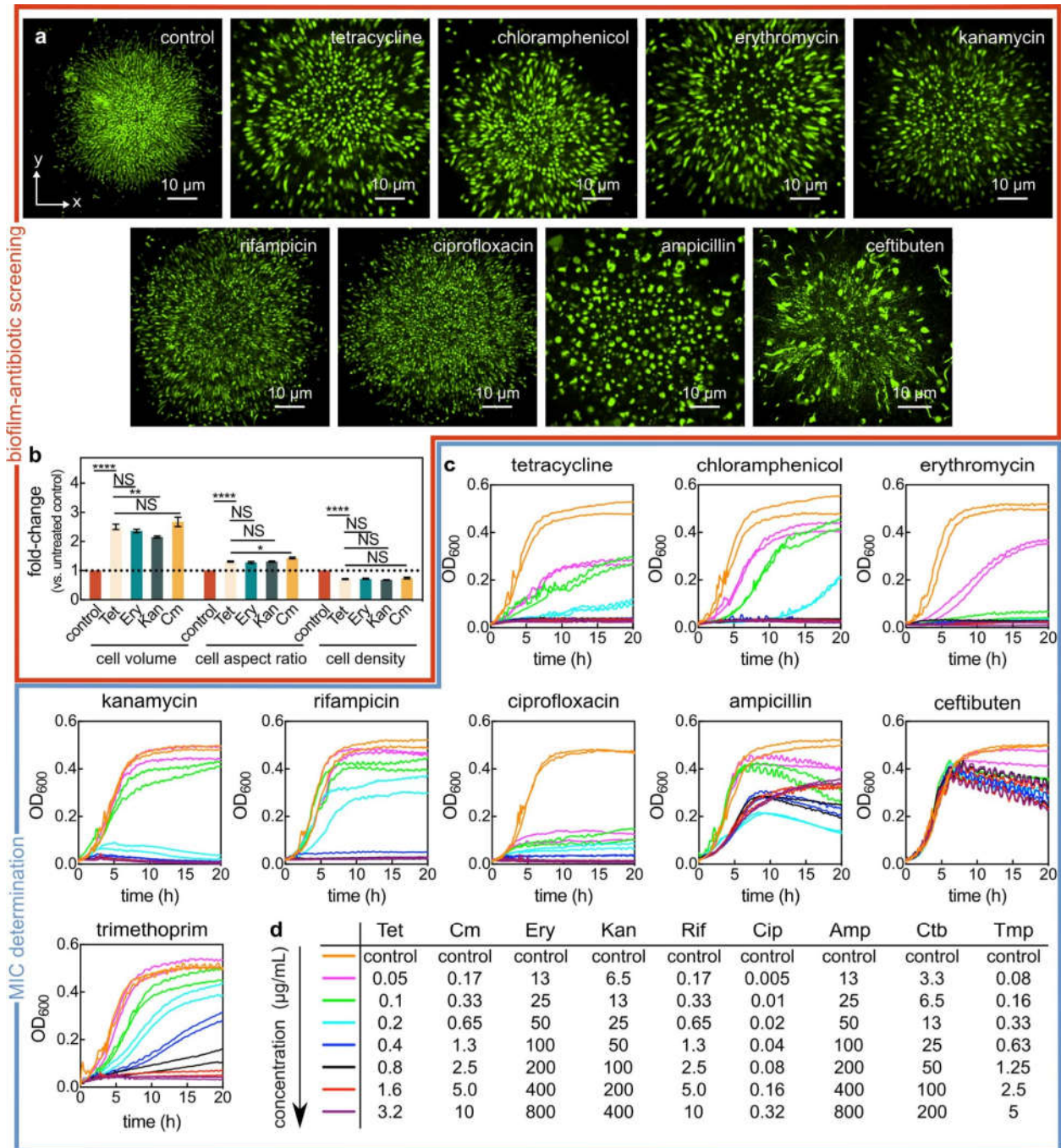
Code availability. Our open-source and user-friendly biofilm image analysis software tool BiofilmQ⁴⁶ is available online (<https://drescherlab.org/data/biofilmQ/>). The raw developer level code used to analyse data is available from the corresponding author upon request.

References

1. D'Costa, V. M. *et al.* Antibiotic resistance is ancient. *Nature* **477**, 457–461 (2011).
2. Baym, M. *et al.* Spatiotemporal microbial evolution on antibiotic landscapes. *Science* **353**, 1147–51 (2016).
3. Hoffman, L. R. *et al.* Aminoglycoside antibiotics induce bacterial biofilm formation. *Nature* **436**, 1171–1175 (2005).
4. Koch, G. *et al.* Evolution of Resistance to a Last-Resort Antibiotic in *Staphylococcus aureus* via Bacterial Competition. *Cell* **158**, 1060–1071 (2014).
5. Jenssen, H., Hamill, P. & Hancock, R. E. W. Peptide Antimicrobial Agents. *Clin. Microbiol. Rev.* **19**, 491–511 (2006).
6. Houry, A. *et al.* Bacterial swimmers that infiltrate and take over the biofilm matrix. *Proc. Natl. Acad. Sci.* **109**, 13088–13093 (2012).
7. Andersson, D. I. & Hughes, D. Microbiological effects of sublethal levels of antibiotics. *Nat. Rev. Microbiol.* **12**, 465–78 (2014).
8. O'Neill, J. ed. Antimicrobial Resistance: Tackling a Crisis for the Health and Wealth of Nations. HM Government (2014).
9. Van Acker, H., Van Dijck, P. & Coenye, T. Molecular mechanisms of antimicrobial tolerance and resistance in bacterial and fungal biofilms. *Trends Microbiol.* **22**, 326–333 (2014).
10. Lebeaux, D., Ghigo, J.-M. & Beloin, C. Biofilm-Related Infections: Bridging the Gap between Clinical Management and Fundamental Aspects of Recalcitrance toward Antibiotics. *Microbiol. Mol. Biol. Rev.* **78**, 510–543 (2014).
11. Koo, H., Allan, R. N., Howlin, R. P., Stoodley, P. & Hall-Stoodley, L. Targeting microbial biofilms: current and prospective therapeutic strategies. *Nat. Rev. Microbiol.* **15**, 740–755 (2017).
12. Meylan, S., Andrews, I. W. & Collins, J. J. Targeting Antibiotic Tolerance, Pathogen by Pathogen. *Cell* **172**, 1228–1238 (2018).
13. Garcia, L. G. *et al.* Antibiotic activity against small-colony variants of *Staphylococcus aureus*: Review of in vitro, animal and clinical data. *J. Antimicrob. Chemother.* **68**, 1455–1464 (2013).
14. Kwan, B. W., Valenta, J. A., Benedik, M. J. & Wood, T. K. Arrested protein synthesis increases persister-like cell formation. *Antimicrob. Agents Chemother.* **57**, 1468–1473 (2013).
15. Grant, S. S. & Hung, D. T. Persistent bacterial infections, antibiotic tolerance, and the oxidative stress response. *Virulence* **4**, 273–283 (2013).
16. Brooun, A., Liu, S. & Lewis, K. A Dose-Response Study of Antibiotic Resistance in *Pseudomonas aeruginosa* Biofilms. *Antimicrob. Agents Chemother.* **44**, 640–646 (2000).
17. Chua, S. L. *et al.* Selective labelling and eradication of antibiotic-tolerant bacterial populations in *Pseudomonas aeruginosa* biofilms. *Nat. Commun.* **7**, 10750 (2016).
18. Gupta, K., Marques, C. N. H., Petrova, O. E. & Sauer, K. Antimicrobial Tolerance of *Pseudomonas aeruginosa* Biofilms Is Activated during an Early Developmental Stage and Requires the Two-Component Hybrid SagS. *J. Bacteriol.* **195**, 4975–4987 (2013).
19. Okshevsky, M. & Meyer, R. L. The role of extracellular DNA in the establishment, maintenance and perpetuation of bacterial biofilms. *Crit. Rev. Microbiol.* **41**, 341–352 (2015).
20. Mah, T.-F. *et al.* A genetic basis for *Pseudomonas aeruginosa* biofilm antibiotic resistance. *Nature* **426**, 306–310 (2003).
21. Nguyen, D. *et al.* Active Starvation Responses Mediate Antibiotic Tolerance in Biofilms and Nutrient-Limited Bacteria. *Science (80-.)*. **334**, 982–986 (2011).
22. Høiby, N., Bjarnsholt, T., Givskov, M., Molin, S. & Ciofu, O. Antibiotic resistance of bacterial biofilms. *Int. J. Antimicrob. Agents* **35**, 322–332 (2010).
23. Tseng, B. S. *et al.* The extracellular matrix protects *Pseudomonas aeruginosa* biofilms by limiting the penetration of tobramycin. *Environ. Microbiol.* **15**, 2865–78 (2013).
24. Dale, J. L., Nilson, J. L., Barnes, A. M. T. & Dunny, G. M. Restructuring of *Enterococcus faecalis* biofilm architecture in response to antibiotic-induced stress. *npj Biofilms Microbiomes* **3**, 15 (2017).
25. Wong, K. C., Brown, A. M., Luscombe, G. M., Wong, S. J. & Mendis, K. Antibiotic use for *Vibrio*

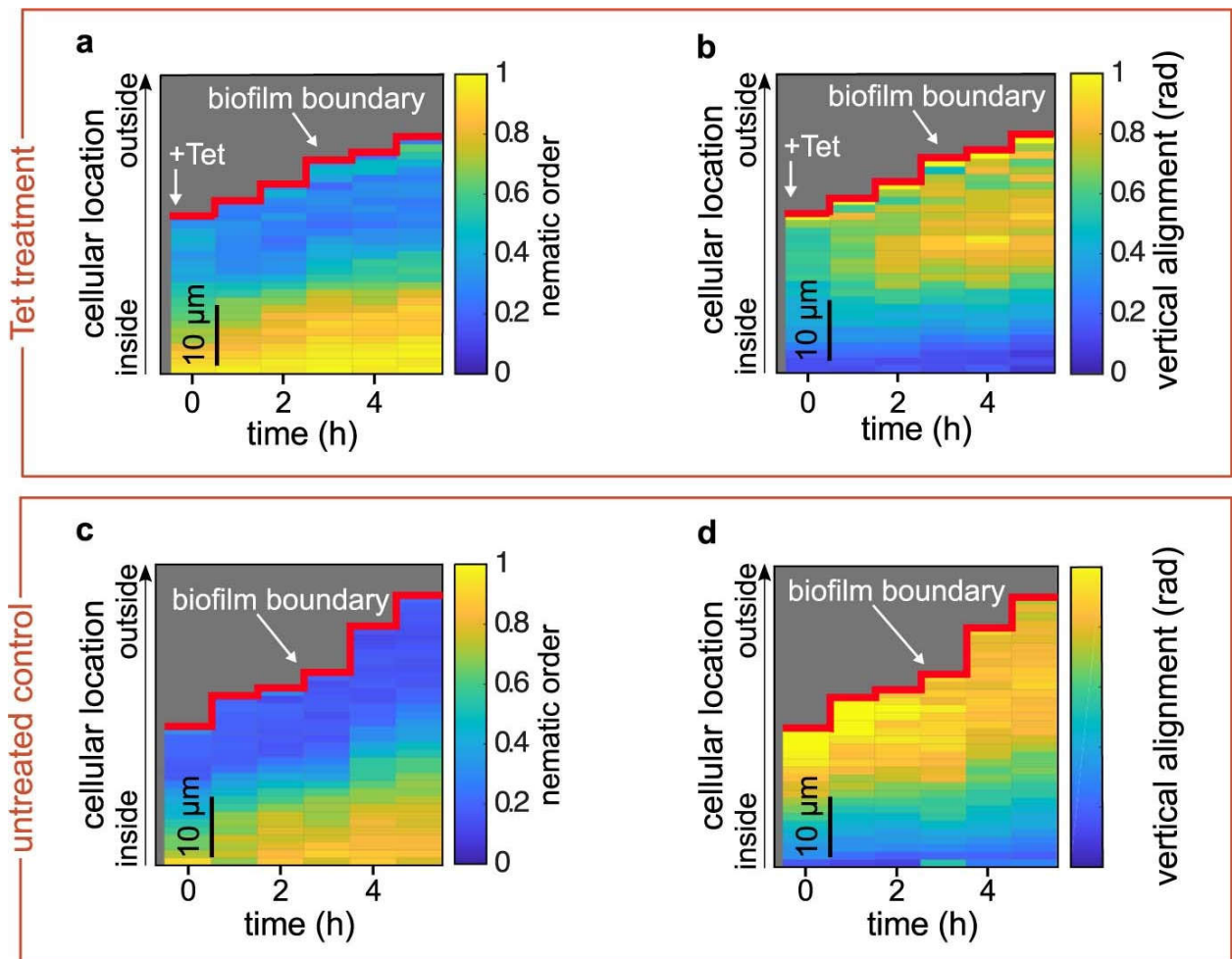
- infections: important insights from surveillance data. *BMC Infect. Dis.* **15**, 226 (2015).
26. Drescher, K. *et al.* Architectural transitions in *Vibrio cholerae* biofilms at single-cell resolution. *Proc. Natl. Acad. Sci.* **113**, E2066–E2072 (2016).
 27. Singh, P. K. *et al.* *Vibrio cholerae* Combines Individual and Collective Sensing to Trigger Biofilm Dispersal. *Curr. Biol.* **27**, 3359–3366.e7 (2017).
 28. Hartmann, R. *et al.* Emergence of three-dimensional order and structure in growing biofilms. *Nat. Phys.* **15**, 251–256 (2019).
 29. Adams, D. W. & Errington, J. Bacterial cell division: Assembly, maintenance and disassembly of the Z ring. *Nat. Rev. Microbiol.* **7**, 642–653 (2009).
 30. Stewart, E. J., Satorius, A. E., Younger, J. G. & Solomon, M. J. Role of Environmental and Antibiotic Stress on *Staphylococcus epidermidis* Biofilm Microstructure. *Langmuir* **29**, 7017–7024 (2013).
 31. Berk, V. *et al.* Molecular architecture and assembly principles of *Vibrio cholerae* biofilms. *Science* **337**, 236–9 (2012).
 32. Fong, J. C. *et al.* Structural dynamics of RbmA governs plasticity of *Vibrio cholerae* biofilms. *Elife* **6**, 1–22 (2017).
 33. Smith, D. R. *et al.* In situ proteolysis of the *Vibrio cholerae* matrix protein RbmA promotes biofilm recruitment. *Proc. Natl. Acad. Sci.* **112**, 10491–10496 (2015).
 34. Fong, J. C. N. & Yildiz, F. H. The *rbmBCDEF* gene cluster modulates development of rugose colony morphology and biofilm formation in *Vibrio cholerae*. *J. Bacteriol.* **189**, 2319–2330 (2007).
 35. Douarche, C., Allain, J.-M. & Raspaud, E. *Bacillus subtilis* Bacteria Generate an Internal Mechanical Force within a Biofilm. *Biophys. J.* **109**, 2195–2202 (2015).
 36. Yan, J., Nadell, C. D., Stone, H. A., Wingreen, N. S. & Bassler, B. L. Extracellular-matrix-mediated osmotic pressure drives *Vibrio cholerae* biofilm expansion and cheater exclusion. *Nat. Commun.* **8**, (2017).
 37. Vidakovic, L., Singh, P. K., Hartmann, R., Nadell, C. D. & Drescher, K. Dynamic biofilm architecture confers individual and collective mechanisms of viral protection. *Nat. Microbiol.* **3**, 26–31 (2018).
 38. Nadell, C. D., Drescher, K., Wingreen, N. S. & Bassler, B. L. Extracellular matrix structure governs invasion resistance in bacterial biofilms. *ISME J.* **9**, 1700–1709 (2015).
 39. Jørgensen, B. R. & Huss, H. H. Growth and activity of *Shewanella putrefaciens* isolated from spoiling fish. *Int. J. Food Microbiol.* **9**, 51–62 (1989).
 40. Kimata, N., Nishino, T., Suzuki, S. & Kogure, K. *Pseudomonas aeruginosa* Isolated from Marine Environments in Tokyo Bay. *Microb. Ecol.* **47**, 41–47 (2004).
 41. Brislawn, C. J. *et al.* Forfeiting the priority effect: turnover defines biofilm community succession. *ISME J.* **13**, 1865–1877 (2019).
 42. Skorupski, K. & Taylor, R. K. Positive selection vectors for allelic exchange. *Gene* **169**, 47–52 (1996).
 43. Guder, J. C., Schramm, T., Sander, T. & Link, H. Time-Optimized Isotope Ratio LC–MS/MS for High-Throughput Quantification of Primary Metabolites. *Anal. Chem.* **89**, 1624–1631 (2017).
 44. Ducret, A., Quardokus, E. M. & Brun, Y. V. MicrobeJ, a tool for high throughput bacterial cell detection and quantitative analysis. *Nat. Microbiol.* **1**, 16077 (2016).
 45. O’Toole, G. A. Microtiter dish biofilm formation assay. *J. Vis. Exp.* 10–11 (2011) doi:10.3791/2437.
 46. Hartmann, R. *et al.* BiofilmQ, a software tool for quantitative image analysis of microbial biofilm communities. *bioRxiv* 735423 (2019) doi:10.1101/735423.

Supplementary information

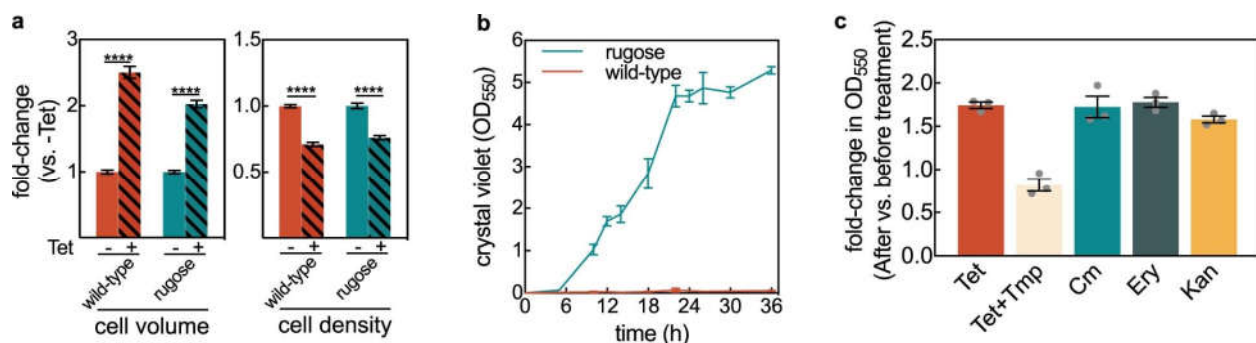


Supplementary Figure. 5.1. Screening biofilm architecture after antibiotic exposure and identifying the minimum inhibitory concentration (MIC). (a) Confocal xy-slices of biofilms exposed to different antibiotics for 24 h and stained with the SYTO 9 nucleic acid dye. The conditions tests were the following: untreated control biofilm, tetracycline (Tet; 3 μg/mL, 8x the MIC), chloramphenicol (Cm; 10 μg/mL, 8x the MIC), erythromycin (Ery; 200 μg/mL, 4x the MIC), kanamycin (Kan; 200 μg/mL, 4x the MIC), rifampicin (Rif; 6 μg/mL, 5x the MIC), ciprofloxacin (Cip; 0.5 μg/mL, 6.3x the MIC), ampicillin (Amp; 400 μg/mL, a concentration at which the cell morphology was significantly modified), and ceftibuten (Ctb; 50 μg/mL, a concentration at which the cell morphology was significantly modified). Images are representative of $n = 3$ independent experiments. (b) Fold-change of cell volume, cell aspect ratio, and cell density (calculated as

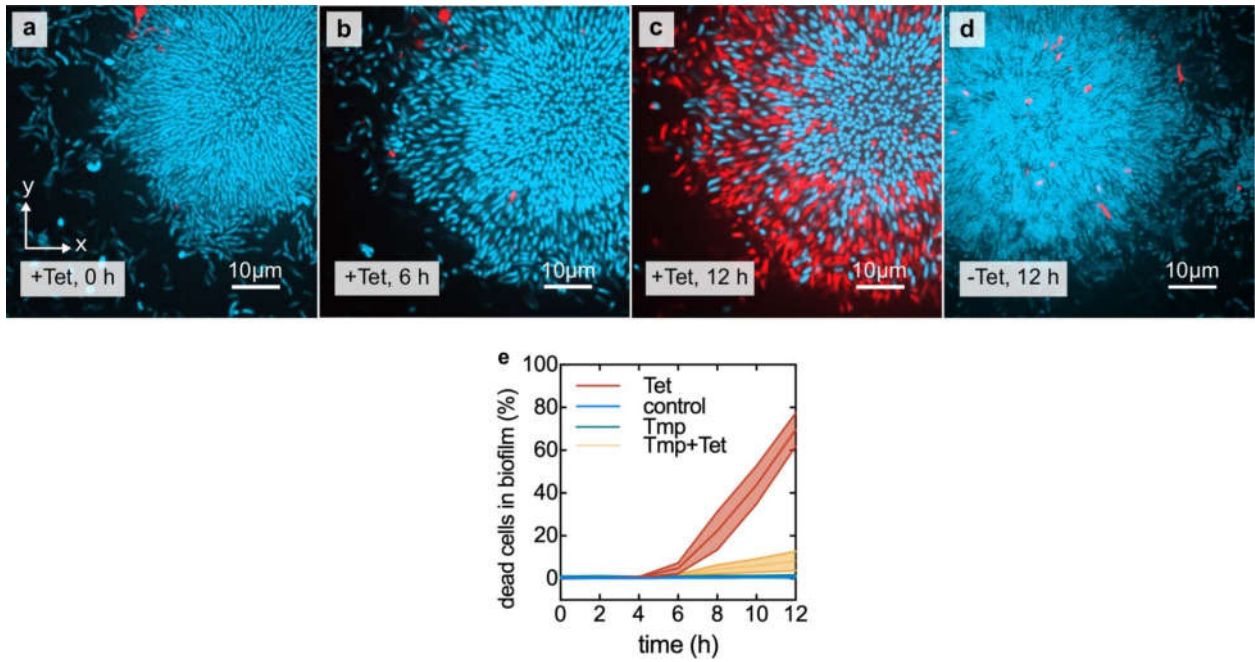
volume fraction) of biofilms treated with different protein synthesis inhibitors for 6 h, relative to untreated biofilms (mean \pm SEM, $n = 15$ samples for control, $n = 9$ for Tet, $n = 7$ for Ery, $n = 14$ for Kan, and $n = 8$ for Cm; samples correspond to different biofilms). Statistical significances were calculated using a one-way ANOVA with Bonferroni's correction. Statistically non-significant differences (NS) correspond to $P = 0.93, 0.51, 0.99, 0.99, 0.99, 0.99, 0.46$ (left to right). *, ** and **** indicate $P < 0.05, P < 0.01$ and $P < 0.0001$ respectively. (c) Batch culture growth curves of wild-type *V. cholerae* N16961 grown in M9 medium supplemented with glucose and with different antibiotic concentrations. Every line corresponds to the average between 2 technical replicates, and each concentration has been tested on 2 separate days (each resulting in one line). For ampicillin and ceftibuten, the MIC determination was not possible from the concentrations tested, due to the lack of cell lysis. (d) List of antibiotic concentrations used in panel c according to their color-coding.



Supplementary Figure 5.2. Nematic order and vertical alignment of cells in biofilms during tetracycline treatment, compared with untreated controls. (a, b) Spatiotemporal changes of the average nematic order (a), or the vertical alignment (b), as a function of time and position inside the biofilm during tetracycline treatment. Each pixel in the heatmap is coloured according to the average nematic order (a) or vertical alignment (b) at a given time and spatial position in the biofilm. (c, d) Spatiotemporal changes of the average nematic order (c), or the vertical alignment (d), for control biofilms that were not treated with tetracycline. In these kymograph heatmaps, the pixel values correspond to averages over all cells with similar distances from the surface of the biofilm at a particular time. Heatmaps are representative of $n = 5$ different biofilms.

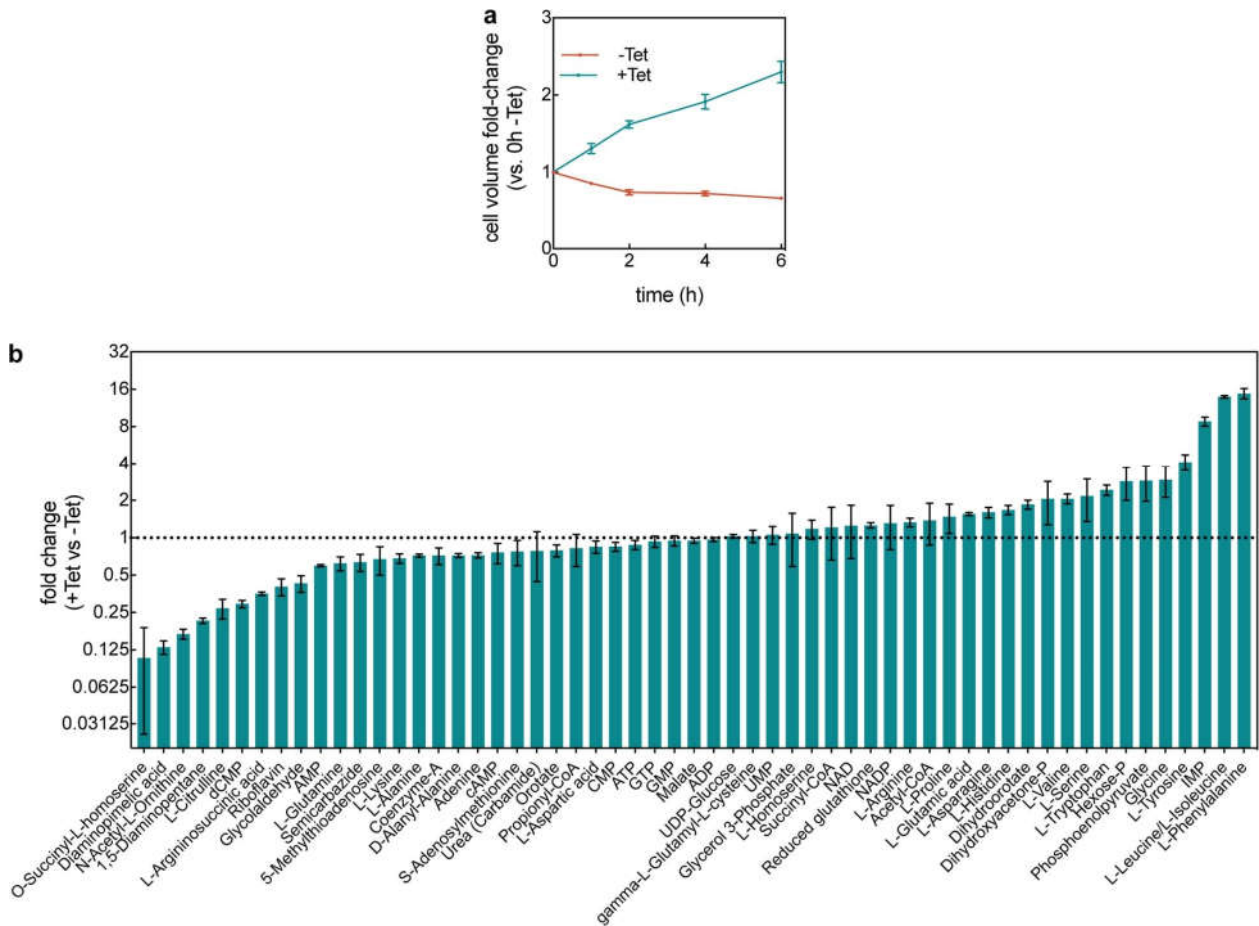


Supplementary Figure. 5.3. Effect of tetracycline treatment on biomass measurements using the crystal violet assay. (a) Fold-changes for the cell volume and cell density of the wild-type (WT) and the *vpvC^{W240R}* rugose strain (which is a biofilm hyper-producer strain¹) for tetracycline-treated biofilms in comparison with untreated biofilms, measured in flow chambers using confocal imaging at the single-cell level. Data are shown as mean \pm SE, $n = 15, 9, 7, 11$, for WT (-Tet), WT (+Tet), rugose (-Tet), and rugose (+Tet), respectively. Each sample corresponds to an independent biofilm. These results show that the rugose strain also displays similar biofilm architecture responses to Tet treatment. Statistical significances were calculated using a one-way ANOVA with Bonferroni's correction. **** indicates $p < 0.0001$. (b) Growth curve of rugose and WT biofilms using the crystal violet assay in 96-well plates; mean \pm SD, $n = 3$ independent biological replicates. These results show that only the rugose strain forms substantial biofilms in static 96-well plates. (c) Fold-change in biofilm biomass measured by crystal violet absorbance of rugose biofilms, which were grown for 14 h in 96-well plates followed by 6 h treatment with tetracycline (Tet; 3 $\mu\text{g}/\text{mL}$, 8x the MIC), trimethoprim (Tmp; 10 $\mu\text{g}/\text{mL}$, 4x the MIC), chloramphenicol (Cm; 10 $\mu\text{g}/\text{mL}$, 8x the MIC), erythromycin (Ery; 200 $\mu\text{g}/\text{mL}$, 4x the MIC), or kanamycin (Kan; 200 $\mu\text{g}/\text{mL}$, 4x the MIC); mean \pm SE, $n = 3$ independent biological replicates. For all experiments, each biological replicate is the average of 8 technical replicates from different wells on the same microtiter plate. The translational inhibitors Tet, Cm, Ery, and Kan show the same qualitative behaviour: an increase in crystal violet biofilm signal after 6 h of antibiotic exposure. Only the Tet+Tmp treatment does not show the increase in crystal violet signal, consistent with Fig. 5.2g of the main text.

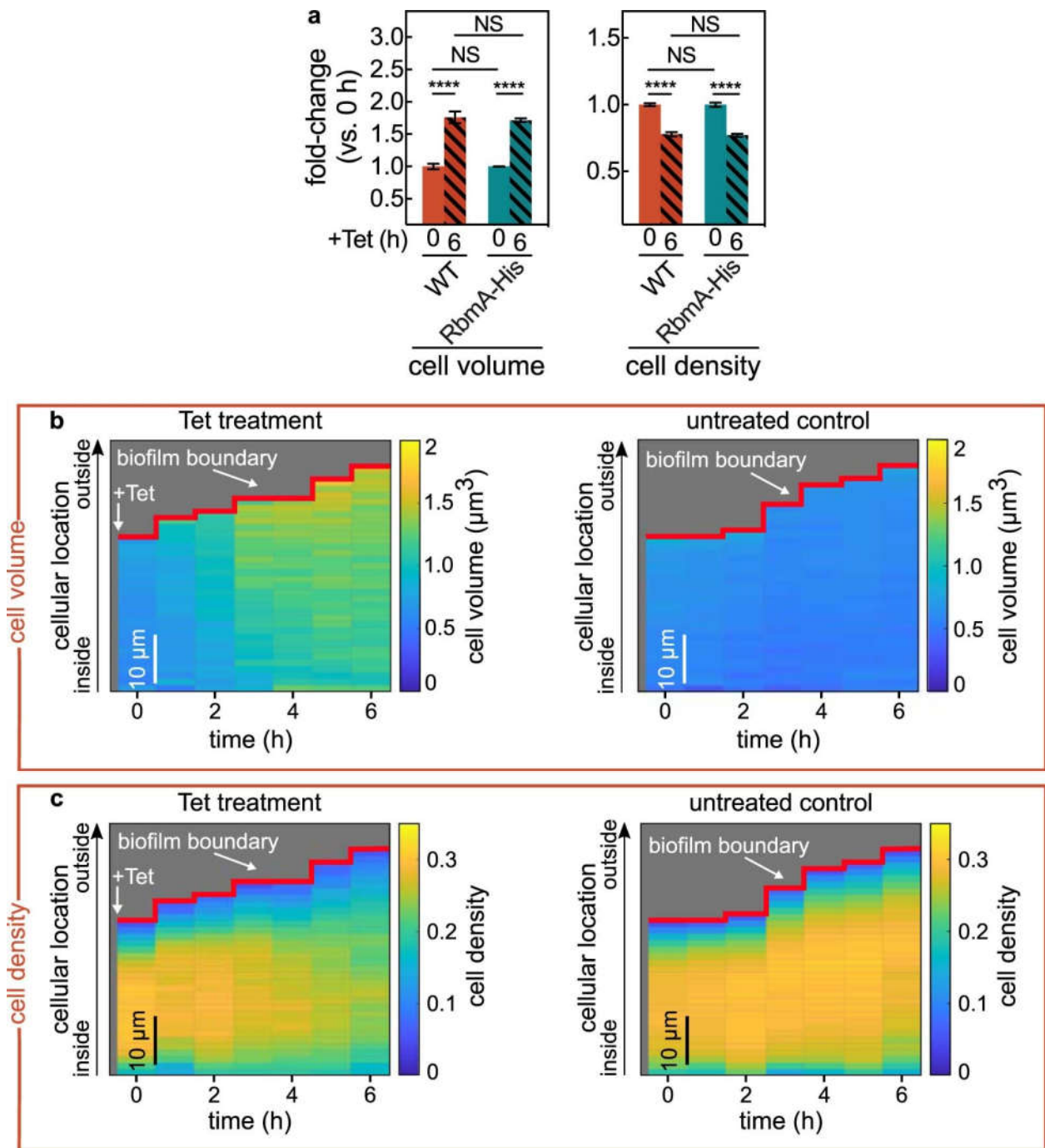


Supplementary Figure. 5.4. Increase in cell volume and decrease in cell density precede cell death. (a) Confocal *xy*-slices of a biofilm constitutively expressing mTFP1 (shown in cyan), grown in the presence of propidium iodide. Alive cells are only visible in the cyan fluorescent channel, whereas dead cells are also visible in the red fluorescent channel. (b) Same biofilm as in panel a, now imaged after 6 h of tetracycline (Tet) treatment. (c) Same biofilm as in panel a, after 12 h of Tet treatment. (d) Untreated control biofilm. (e) Percentage of dead cells in the biofilm as a function of treatment time. Centre lines correspond to mean and width of the shaded areas around each line correspond to standard errors, $n = 13$ samples for Tet, $n = 9$ for control, $n = 4$ for Tmp, $n = 4$ for Tmp+Tet. Each sample corresponds to a different biofilm.

Chapter V: Breakdown of *Vibrio cholerae* biofilm architecture induced by antibiotics disrupts community barrier function

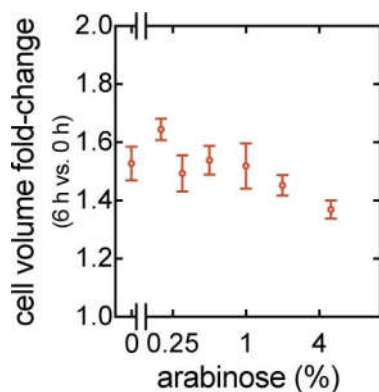


Supplementary Figure. 5.5. Changes in cell volume and metabolite levels of planktonic cells during exposure to tetracycline. (a) Cell volume fold-change (comparing each time point to the untreated (-Tet) sample at 0 h (mean \pm SEM, $n = 5$ independent biological replicates). (b) Fold-changes in 57 metabolites after 2 h of Tet treatment in comparison with untreated cells (mean \pm SEM, $n = 3$ independent biological replicates).

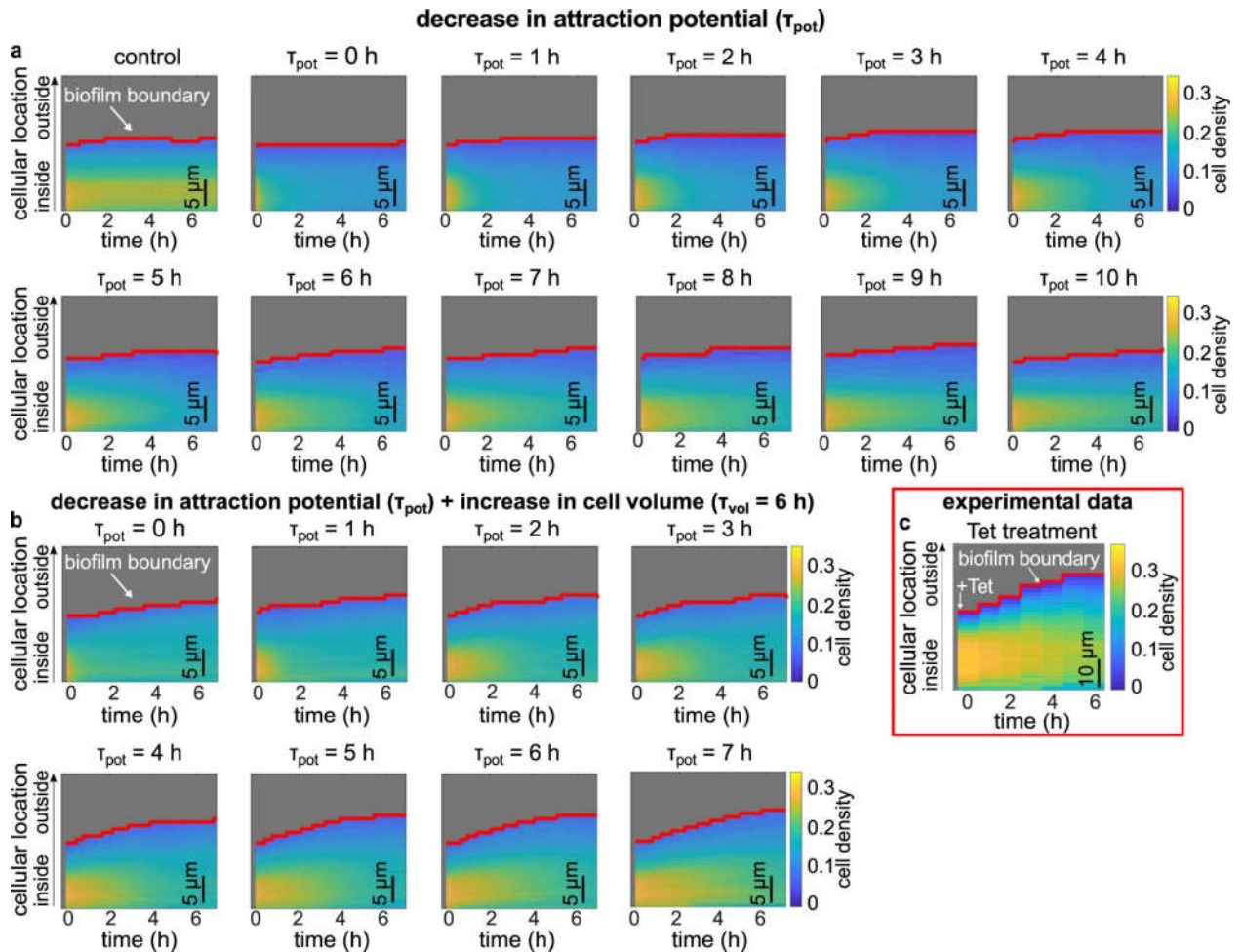


Supplementary Figure. 5.6. The RbmA-His strain phenocopies the wild-type strain. (a) Fold-change of cell volume and cell density (measured as volume fraction) of wild-type biofilms and biofilms formed by a strain producing His-tagged RbmA (RbmA-His) treated with tetracycline, relative to the biofilms before the treatment. Values are displayed as mean \pm SEM ($n = 17$ different biofilms). Statistical significances were calculated using a one-way ANOVA with Bonferroni's correction for multiple comparisons. Statistically non-significant differences are labelled NS, which both correspond to $p = 0.99$. **** indicates $p < 0.0001$. (b, c) RbmA-His biofilms, shown here, display the same spatiotemporal changes in biofilm architecture as the WT biofilms, for which the corresponding kymograph heatmaps are shown in Fig. 5.1e–h. Heatmaps show the changes of the average cell volume (b) and cell density (c) as a function of time and spatial location during tetracycline treatment inside the RbmA-His biofilms. Panels on the left correspond to Tet treatment and panels on the right correspond to untreated control conditions. Each pixel in these kymograph heatmaps is

coloured according to the average cell volume or cell density at a given time and spatial position in the biofilm. Cell volumes and cell density volume fraction values are averaged over all cells with similar distances from the surface of the biofilm. The RbmA-His strain was grown and imaged using antibodies as described in the methods section. Heatmaps are representative of $n = 5$ different biofilms.

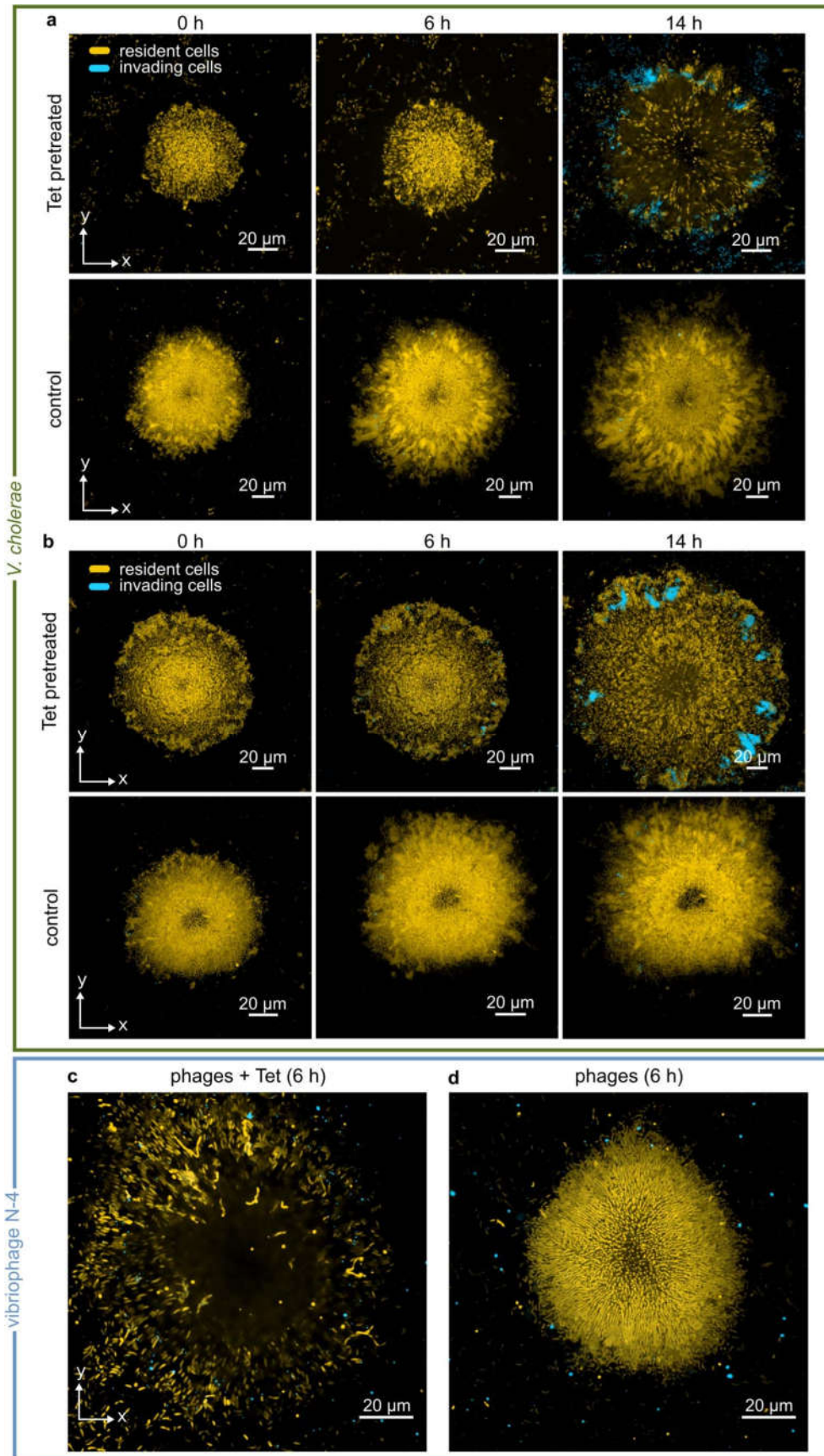


Supplementary Figure. 5.7. Antibiotic-induced cell volume increase is independent of RbmA concentration. Cell volume fold-change (comparing 6 h and 0 h of Tet treatment) in biofilms of a $\Delta rbmA$ strain carrying the $P_{BAD}:rbmA$ construct, measured as a function of arabinose concentration (mean \pm SEM, $n = 7, 12, 13, 17, 10, 18, 14$ samples for arabinose concentrations of 0%, 0.2%, 0.3%, 0.5%, 1%, 2%, and 5% respectively). Each sample corresponds to a different biofilm.



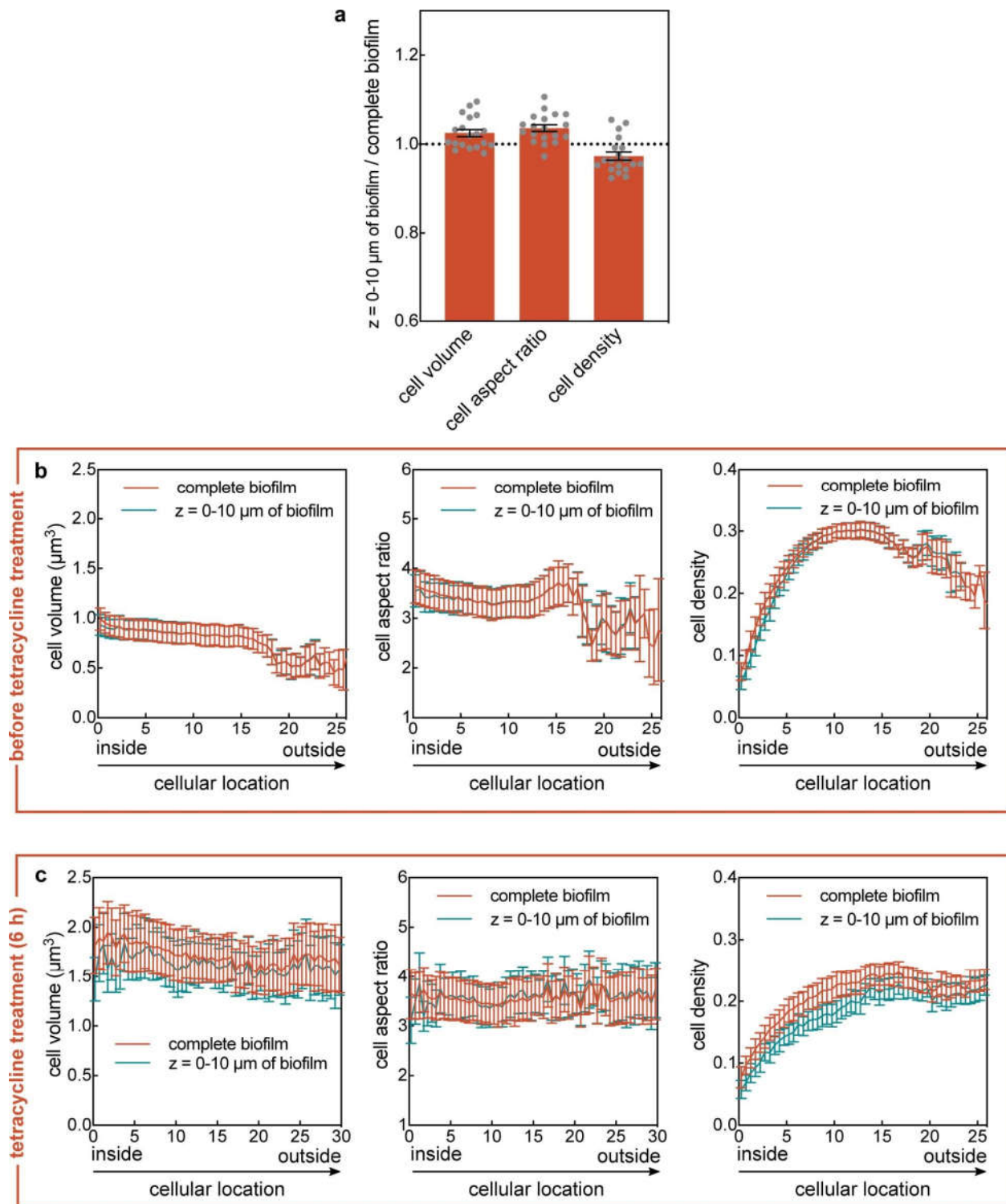
Supplementary Figure 5.8. Simulated biofilms were subjected to a decrease in cell-cell attraction and an increase in cell volume, revealing the contribution of each effect to the antibiotic-induced biofilm architecture changes. Biofilm growth was simulated as described in the methods section until the biofilm size reached 1,000 cells, corresponding to the 0 h time point in the heatmaps in this figure. For these 1,000-cell biofilms, tetracycline treatment was simulated by decreasing the attraction potential, or by increasing the cell volume, or by both effects together. **(a)** Kymograph heatmaps of simulated 1,000-cells biofilms subject to a linear decrease in cell-cell attraction over the course of different times τ_{pot} . The value of τ_{pot} corresponds to the time for the cell-cell attraction potential to decrease to zero, starting from the value used to simulate biofilm growth. If the attraction potential is set to zero immediately (corresponding to $\tau_{pot} = 0$), the resulting biofilm dynamics do not closely resemble the experiments, indicating that the cell-cell attraction decreases over an extended period of time. The control kymograph heatmap corresponds to biofilms where neither the attraction potential nor the cell volume were changed. Each heatmap is the average of $n = 3$ simulations. **(b)** Heatmaps of simulated 1,000-cells biofilms that were subjected to a decrease in cell-cell attraction over different times (τ_{pot}) and simultaneously subjected to a linear increase in cell volume over 6 h ($\tau_{vol} = 6$ h). Each heatmap is the average of $n = 3$ simulations. In Fig. 5.3h of the main text, a kymograph heatmap is shown for simulations in which only the cell volume is linearly increased with a time scale $\tau_{vol} = 6$ h, according to the experimentally determined single-cell volume growth rate during Tet- treatment. **(c)** Experimental changes of the average cell density as a function of space and time during tetracycline treatment inside the biofilm as shown in Fig. 5.1g, reproduced here for convenience. Heatmap in panel c is a representative of $n = 5$ different biofilms.

Chapter V: Breakdown of *Vibrio cholerae* biofilm architecture induced by antibiotics disrupts community barrier function



Supplementary Figure. 5.9. Tetracycline-treated *V. cholerae* biofilms are susceptible to colonization and population invasion by an isogenic strain and by bacteriophages. (a-b) Each of the two panels shows an independent replica experiment of a tetracycline-treated *V. cholerae* biofilm colonized by an isogenic strain, which is expressing a different fluorescent protein. Resident biofilms constitutively express mKOκ (cells shown in yellow), invaders constitutively express sfGFP (cells shown in cyan). Images correspond to confocal *xy*-slices, acquired 2 μm above the substrate. The resident biofilm underwent tetracycline (Tet) treatment for 6 h or control treatment (medium without Tet), followed by 2 h exposure to invader cells. Following exposure to invader cells, the medium was exchanged to fresh, sterile medium and the imaging was started (labelled as the 0 h time point here). A third independent replica experiment is shown in Fig. 5.4a,b of the main text. **(c)** Confocal *xy*-slice of a resident *V. cholerae* WT biofilm, expressing mKOκ constitutively (cells shown in yellow), imaged directly above the glass substrate. The resident biofilm underwent exposure to tetracycline (Tet) and fluorescently labelled vibriophage N-4 virions (visible as cyan spots) for 6 h. During 6 h of Tet-treatment cell death is negligible, as shown in Supplementary Fig. 5.4. **(d)** Confocal *xy*- slice of control biofilm (not treated with tetracycline) exposed to vibriophage N-4 virions for 6 h. Images are representative of *n* = 5 different biofilms.

Chapter V: Breakdown of *Vibrio cholerae* biofilm architecture induced by antibiotics disrupts community barrier function



Supplementary Figure. 5.10. Biofilm architecture in the lower part of the biofilm is representative of the whole biofilm. (a) Comparison between the cell volume, cell aspect ratio, and cell density (measured as volume fraction) between the lower part of the biofilm and the whole biofilm. The ratio of these biofilm architecture parameters was calculated using the mean value of these parameters in the part of the biofilm that is bounded by the $z = 0 \mu\text{m}$ and $z = 10 \mu\text{m}$ planes, and the mean value of these parameters in the whole biofilm (mean \pm SEM, $n = 19$ different biofilms). (b, c) Cell volume, cellular aspect ratio, and cell density before tetracycline treatment (panel b) or after 6 hours of tetracycline treatment (panel c) as measured for

Chapter V: Breakdown of *Vibrio cholerae* biofilm architecture induced by antibiotics disrupts community barrier function

complete biofilm volumes, or for the cells located in the biofilm volume bounded by the $z = 0 \mu\text{m}$ and $z = 10 \mu\text{m}$ planes (mean \pm SD, $n = 8$ samples in panel **b** and $n = 5$ samples in panel **c**; each sample corresponds to a different biofilm). The cellular location was measured as the shortest distance of each cell to the interface between the biofilm and the liquid growth medium. This interface is termed “biofilm boundary” in this manuscript. For the experiments in this figure, biofilms were stained with the nucleic acid dye SYTO 9 prior to imaging. The cell volume, aspect ratio, and cell density were nearly identical between the whole biofilm and the bottom-most $10 \mu\text{m}$ of the biofilms.

Chapter V: Breakdown of *Vibrio cholerae* biofilm architecture induced by antibiotics disrupts community barrier function

Supplementary Table 5.1. Bacterial strains and bacteriophages used in this study.

Strains	Genotype/ Relevant features	Reference
<i>E. coli</i>		
S17-1 λ pir	Wild type	de Lorenzo & Timmis ²
<i>V. cholerae</i>		
KDV101	Wild type N16961 (O1 El Tor, Strep ^R)	Meibom <i>et al.</i> ³
KDV103	N16961 <i>lacZ::P_{tac}:mKOk</i>	Drescher <i>et al.</i> ⁴
KDV115	N16961 <i>vpvC^{W240R}, lacZ::P_{tac}:mKOk</i>	Drescher <i>et al.</i> ⁴
KDV311	N16961 <i>lacZ::P_{tac}:sfGFP:sfGFP</i>	This study
KDV383	N16961 <i>lacZ::P_{tac}:mKOk, ΔrbmA</i>	This study
KDV385	N16961 <i>lacZ::P_{tac}:mKOk, ΔrbmC</i>	This study
KDV387	N16961 <i>lacZ::P_{tac}:mKOk, Δbap1</i>	This study
KDV392	N16961 <i>lacZ::P_{tac}:mTFP1</i>	Drescher <i>et al.</i> ⁵
KDV605	N16961 <i>lacZ::P_{tac}:mTFP1, rbmA:His(6x)</i>	This study
KDV657	N16961 <i>lacZ::P_{tac}:mRuby3</i>	This study
KDV677	N16961 <i>lacZ::P_{tac}:mKOk, rbmA^{D97A}</i>	This study
KDV679	N16961 <i>lacZ::P_{tac}:mKOk, rbmA^{D97K}</i>	This study
KDV681	N16961 <i>lacZ::P_{tac}:mKOk, rbmA^{R234A}</i>	This study
KDV859	N16961 <i>lacZ::P_{tac}:mKOk, P_{BAD}:rbmA:His(6x), ΔrbmA</i>	This study
KDV619	N16961 <i>lacZ::P_{tac}:mKOk, ΔhapA</i>	This study
KDV621	N16961 <i>lacZ::P_{tac}:mKOk, ΔivaP</i>	This study
KDV1020	N16961 <i>lacZ::P_{tac}:mKOk, ΔprtV</i>	This study
KDV1064	N16961 <i>lacZ::P_{tac}:mKOk, ΔrbmB</i>	This study
KDV1070	N16961 <i>lacZ::P_{tac}:mKOk, pNUT996</i>	This study
KDV1078	N16961 <i>lacZ::P_{tac}:mKOk, pNUT1246</i>	This study
<i>P. aeruginosa</i>		
KDP54	PAO1 Wild type, <i>ctx::sfGFP</i>	Drescher lab stock
<i>S. putrefaciens</i>		
KDM77	CN-32 Wild type, Transposon inserted in chromosome, carrying Cm ^R , and <i>Tn7:eGFP</i>	This study

Chapter V: Breakdown of *Vibrio cholerae* biofilm architecture induced by antibiotics disrupts community barrier function

Bacteriophage		
Vibriophage N-4	Wild type vibriophage N-4	ATCC 51352-B1

Abbreviations: Strep = streptomycin. Cm = chloramphenicol. Superscript "R" = resistance. ":" = fusion. "::" = insertion.

Chapter V: Breakdown of *Vibrio cholerae* biofilm architecture induced by antibiotics disrupts community barrier function

Supplementary Table 5.2. Plasmids used in this study.

Plasmid	Origin, marker	Comments	Template(s), primers	Source
pNUT129	pR6K, Amp ^R	pKAS32 with <i>lacZ::P_{tac}:mKO::lacZ</i>		Drescher <i>et al.</i> ⁴
pNUT144	pR6K, Amp ^R , Kan ^R	pKAS32 backbone with Kan ^R		Drescher <i>et al.</i> ⁴
pNUT276	pR6K, Amp ^R , Kan ^R	pKAS32 with <i>lacZ</i> flanking regions		Drescher Lab strain
pNUT336	pR6K, Amp ^R	pKAS32 Δ <i>rbmA</i>		Nadell <i>et al.</i> ⁶
pNUT337	pR6K, Amp ^R	pKAS32 Δ <i>rbmC</i>		Nadell <i>et al.</i> ⁶
pNUT338	pR6K, Amp ^R	pKAS32 Δ <i>bap1</i>		Nadell <i>et al.</i> ⁶
pNUT462	pR6K, Amp ^R	<i>rbmA</i> :FLAG(3x)		Nadell <i>et al.</i> ⁶
pNUT480	pR6K, Amp ^R , Kan ^R	pKAS32 <i>lacZ::P_{tac}:sfGFP:sfGFP</i>		Singh <i>et al.</i> ⁷
pNUT909	pR6K, Amp ^R , Kan ^R	pKAS32 Δ <i>hapA</i>	pNUT144, KDO1094, KDO1095, KDO1096, KDO1097	This study
pNUT910	pR6K, Amp ^R , Kan ^R	pKAS32 Δ <i>ivaP</i>	pNUT144, KDO1088, KDO1089, KDO1090, KDO1091	This study
pNUT918	pR6K, Amp ^R	pKAS32 <i>rbmA</i> :His(6x)	pNUT462, KDO1128, KDO1129	This study
pNUT963	pR6K, Amp ^R , Kan ^R	pKAS32 Δ <i>rbmB</i>	pNUT144, KDO1149, KDO1150, KDO1151, KDO1152	This study
pNUT996	pSC101, Gent ^R	<i>P_{tac}:rbmB</i> , Gent ^R , <i>lacIQ</i>	pNUT1076, gDNA from <i>V. cholerae</i> N1696, KDO1120, KDO1247, KDO1245, KDO1246	This study
pNUT1076	pSC101, Gent ^R	Backbone plasmid with <i>lacIQ</i> and <i>P_{tac}</i>		Singh <i>et al.</i> ⁷
pNUT1077	pR6K, Amp ^R , Kan ^R	pKAS32 <i>rbmA</i> ^{D97A} . Codon usage for amino acid substitution: GCC.	<i>V. cholerae</i> gDNA from FY_VC_10039 (Fong <i>et al.</i> ⁸), pNUT144, KDO1334, KDO1335	This study
pNUT1079	pR6K, Amp ^R , Kan ^R	pKAS32 <i>rbmA</i> ^{D97K} . Codon usage for amino acid substitution: AAA.	<i>V. cholerae</i> gDNA from FY_VC_10039 (Fong <i>et al.</i> ⁸), pNUT144, KDO1334, KDO1335	This study

Chapter V: Breakdown of *Vibrio cholerae* biofilm architecture induced by antibiotics disrupts community barrier function

pNUT1081	pR6K, Amp ^R , Kan ^R	pKAS32 <i>rbmA</i> ^{R234A} . Codon usage for amino acid substitution: GCT.	<i>V. cholerae</i> gDNA from FY_VC_10039 (Fong <i>et al.</i> ⁸), pNUT144, KDO1334, KDO1335	This study
pNUT1358	pR6K, Amp ^R , Kan ^R	pKAS32 Δ <i>ivaP</i>	pNUT144, KDO1106, KDO1107, KDO1108, KDO1109	This study
pNUT1246	pSC101, Gent ^R	Control vector, Gent ^R , pSC101 ori, <i>lacIQ</i>	pNUT1076, KDO27, KDO1358	This study
pNUT1268	pSC101, Gent ^R	$P_{BAD}::rbmA$		Hartmann <i>et al.</i> ⁹
pNUT1281	pR6K, Amp ^R , Kan ^R	pKAS32 with <i>lacZ</i> :: $P_{tac}::mKO::lacZ$	pNUT129, pNUT276, KDO1526, KDO1527, KDO1528, KDO1529	This study
pNUT1313	pR6K, Amp ^R , Kan ^R	<i>lacZ</i> :: $P_{tac}::mKOk$, $P_{BAD}::rbmA::His(6x)$	pNUT1281, pNUT1268, KDO1429, KDO1546, KDO1342, KDO1562, KDO1561, KDO1547	This study

Abbreviations: Amp = ampicillin, Gent = gentamicin, Kan = kanamycin, gDNA = genomic DNA. Superscript "R" = resistance. ":" = fusion. "::" = insertion.

Supplementary Table 5.3. DNA oligonucleotides used in this study.

Name	Sequence	Description
KDO27	5'-GAAGGCGAAGCGGCAT-3'	pNUT1246 construction
KDO1088	5'-TTTTCTAGACTTTTGCTTTGCACCAACCGCTTG-3'	pNUT910 construction
KDO1089	5'-GACATTGTAAACTCCCTTGGATGAAAAGAAGTTATTCATGAAAAC-3'	pNUT910 construction
KDO1090	5'-CTTTTCATCCAAGGGAGTTTAACAATGTCAGTTTGGTGGCTCG-3'	pNUT910 construction
KDO1091	5'-TTTGC GGCCGCGTTTGACCGCAGCAACTGCTG-3'	pNUT910 construction
KDO1094	5'-TTTTCTAGAGTGTTAAACTCAAAGTGAGTTGGCAG-3'	pNUT909 construction
KDO1095	5'-CAAGCGTAACTCAGAGGACGTTGTATCATTTCATTCTC-3'	pNUT909 construction
KDO1096	5'-CAACGTCCTCTGAGTTACGCTTGACTAACTCCTTG-3'	pNUT909 construction
KDO1097	5'-TTTGC GGCCGCCACGCTGAGTCACAACGAGATC-3'	pNUT909 construction
KDO1106	5'-TTTTCTAGACCAGCGACACATAACCACGTCC-3'	pNUT1358 construction
KDO1107	5'-GAATTACAGTTTGACTTTGAAGCTAATAGCGTTTTTTTGATCGTTTTTCAT-3'	pNUT1358 construction
KDO1108	5'-CGCTATTAGCTTCAAAGTCAAAGTGAATTCTCCTTCTCC-3'	pNUT1358 construction
KDO1109	5'-TTTGC GGCCGCGCTGGATTGTAGGAGCTTGCCATG-3'	pNUT1358 construction
KDO1120	5'-TTTGC GGCCGCCAGAGGCCTGCTAGCGGATC-3'	pNUT996 construction
KDO1128	5'-CATCATCACCATCACCATTAAATTTACCTAGTCACTTAGTCGTATGT-3'	pNUT918 construction
KDO1129	5'-GCCGCTACCACCGCTGCCTTTTTTACCCTGTCATTGACTGTT-3'	pNUT918 construction
KDO1149	5'-GGGGTCTAGAGCACGCATTTGCTCGTTCTGG-3'	pNUT963 construction
KDO1150	5'-GCTGTATATAATAATGGTCGCGCCACCCTCTTATTGAATTGATTTAAG-3'	pNUT963 construction

Chapter V: Breakdown of *Vibrio cholerae* biofilm architecture induced by antibiotics disrupts community barrier function

KDO1151	5'-GGGTGGCGCGACCATTATTATATACAGCACTTTATTAAG-3'	pNUT963 construction
KDO1152	5'-TTTGCGGCCGCTCTAGTCAGCTAGGGATCCGTAATG-3'	pNUT963 construction
KDO1245	5'-GGAGGTCTAAAGTGCTGTTATACTTAAATCAATTCAATAAAGAGG-3'	pNUT996 construction
KDO1246	5'-TTTGCGGCCGCCCTATCAATCCAAGTCATTAGCTATATATC-3'	pNUT996 construction
KDO1247	5'-GTATAACAGCACTTTAGACCTCCTTAGCTCCTGAATTCC-3'	pNUT996 construction
KDO1334	5'-TTGCGGCCGCCACAGGCGTGGATGTACCTTTCA-3'	pNUT1077, pNUT1079 and pNUT1081 construction
KDO1335	5'-GTGCTAGCTGGCAGCACTAAAGGTACCTTAGTG-3'	pNUT1077, pNUT1079 and pNUT1081 construction
KDO1342	5'-CCGACATCATAACGGTTCTGGCA-3'	pNUT1313 construction
KDO1358	5'-ATTTACCTAGTCACTTAGTCGTATGTAT-3'	pNUT1246 construction
KDO1429	5'-GCCACCTGACGTCTAAGAAACCATTATTATCATG-3'	pNUT1313 construction
KDO1526	5'-AGTAGTCTTGAATTGGCATTGTGATTGC-3'	pNUT1281 construction
KDO1527	5'-GCAATCACAATGCCAATTCAAGACTACT-3'	pNUT1281 construction
KDO1528	5'-GCGCTTAATTAAGTGCAGAGGCCTGCTAGACG-3'	pNUT1281 construction
KDO1529	5'-TGTCGGTACCCGACATCATAACGGTTCTGGCAAATATT-3'	pNUT1281 construction
KDO1546	5'-TTAAGCGCTGTCCATGGGGATTCACTCTTTGCCG-3'	pNUT1313 construction
KDO1547	5'-GAGTGAATCCCATGGACAGCGCTTAATTAAGTGCAGAGGC-3'	pNUT1313 construction
KDO1561	5'-CTCAGCGATCTGTCTATTTTCGTTTCATCCAT-3'	pNUT1313 construction
KDO1562	5'-ATGGATGAACGAAATAGACAGATCGCTGAG-3'	pNUT1313 construction

Supplementary Table 5.4. Minimum inhibitory concentration (MIC), based on growth curves shown in Supplementary Fig. 5.1c.

Antibiotic	MIC ($\mu\text{g}/\text{mL}$)
ciprofloxacin	0.08
chloramphenicol	1.3
erythromycin	50
kanamycin	50
rifampicin	1.3
tetracycline	0.4
trimethoprim	2.5

References for supplementary information

1. Beyhan, S. & Yildiz, F. H. Smooth to rugose phase variation in *Vibrio cholerae* can be mediated by a single nucleotide change that targets c-di-GMP signalling pathway. *Mol. Microbiol.* **63**, 995–1007 (2007).
2. de Lorenzo, V. & Timmis, K. N. Analysis and construction of stable phenotypes in gram-negative bacteria with Tn5- and Tn10-derived minitransposons. *Methods Enzymol.* **235**, 386–405 (1994).
3. Meibom, K. L. *et al.* The *Vibrio cholerae* chitin utilization program. *Proc. Natl. Acad. Sci.* **101**, 2524–2529 (2004).
4. Drescher, K., Nadell, C. D., Stone, H. A., Wingreen, N. S. & Bassler, B. L. Solutions to the Public Goods Dilemma in Bacterial Biofilms. *Curr. Biol.* **24**, 50–55 (2014).
5. Drescher, K. *et al.* Architectural transitions in *Vibrio cholerae* biofilms at single-cell resolution. *Proc. Natl. Acad. Sci.* **113**, E2066–E2072 (2016).
6. Nadell, C. D., Drescher, K., Wingreen, N. S. & Bassler, B. L. Extracellular matrix structure governs invasion resistance in bacterial biofilms. *ISME J.* **9**, 1700–1709 (2015).
7. Singh, P. K. *et al.* *Vibrio cholerae* Combines Individual and Collective Sensing to Trigger Biofilm Dispersal. *Curr. Biol.* **27**, 3359–3366.e7 (2017).
8. Fong, J. C. *et al.* Structural dynamics of RbmA governs plasticity of *Vibrio cholerae* biofilms. *Elife* **6**, 1–22 (2017).
9. Hartmann, R. *et al.* Emergence of three-dimensional order and structure in growing biofilms. *Nat. Phys.* **15**, 251–256 (2019).

Chapter VI: Discussion

Biofilms are structured communities in which bacteria are densely packed, enabling a high-level of unique interactions between cells¹⁻³. These interactions are important for the initial steps of biofilm formation and are determining factors for the subsequent development of biofilm architecture, local environments, growth dynamics, metabolism and stress response³⁻⁶. These interactions can be mechanical, chemical or biochemical and take place at various time-points during biofilm development. Although they are all acknowledged as relevant, it remains unknown which interactions determine each stage of biofilm growth and architecture. One of the reasons for this knowledge gap is the lack of interdisciplinary collaborations in biofilm research. Such a multi-faceted research approach allows for the biological aspects of biofilm formation to be inferred from the study of physicochemical interactions, or vice-versa. Further challenges include technical limitations to image with high spatial and temporal resolution and the difficulty to determine which interactions are sufficient to predict a desired feature. This dissertation contributes to the understanding of biofilm formation, metabolism and stress response, using multidisciplinary approaches. Studying different features of biofilm formation unveiled distinct salient inter-cellular interactions, which when combined, provided a better understanding of the heterogeneity and compound nature of bacterial biofilms. It is to be emphasized that only by applying an interdisciplinary perspective and integrating techniques from several fields of research, was it possible to understand the whole process of biofilm formation, from single cell responses to the multicellular global phenotypes.

An example of a research area that requires interdisciplinary examination is biofilm development. When a biofilm-founder cell attaches to a substrate, it divides and the number of bacteria within this incipient biofilm starts to increase. During this process, bacteria interact with each other mechanically and biochemically, either directly or indirectly^{1,6}. As shown in chapter 2, mechanical interactions are the most important driver during growth until biofilms become large enough to display phenotypical and chemical heterogeneity. Mechanical interactions are determined by attractive and repulsive forces among and between the cells and matrix components. In conjunction with cellular growth dynamics, they create the basis of biofilm architecture and establish the location of cells within a biofilm. Solely by analyzing mechanical interactions and cellular growth, we were able to predict several features, such as overall architecture, cellular density, alignments, nematic order and response to shear stress.

As demonstrated in chapter 2, studying the physical parameters of a biofilm could lead to the interference of emergent biological properties, such as architectural order or cell-cell interactions. For this, a model was designed that could accurately predict *V. cholerae* biofilm architecture. However, several assumptions were necessary in order to simplify the model and to recapitulate the experimental system. It was defined for *V. cholerae* biofilms grown in a microfluidic device with a non-

nutritious attachment substrate, with a rod-shape and an aspect ratio of approximately four. The only interaction modified experimentally was the cell-cell attraction by tuning the levels of the matrix protein RbmA. Furthermore, the model assumed a homogenous environment, gene expression and cellular growth. This raises the question of what would happen if these assumptions were to be relaxed? The cellular architecture and ordering of a biofilm rely heavily on the aspect ratio of the cells within it. In particular, straight cells with a small aspect ratio are expected to verticalize more easily than longer cells³. To expand the understanding of biofilm growth dynamics to different bacterial species, new models and interaction dynamics need to be developed and tested to account for variations in aspect ratio and its impact on biofilm architecture. Moreover, the model needs to be expanded to include other bacterial species with different matrix compositions. Could parameters related to biofilm architecture of different species be predicted based on cell aspect ratio and cell-cell interactions? In an ongoing unpublished study, we have found that for different bacterial species, including *Salmonella enterica*, *Pseudomonas aeruginosa*, *Vibrio cholerae* and *Escherichia coli*, many parameters of biofilm architecture can be predicted based on the cell aspect ratio and cell-cell attraction interactions (data not shown). This would allow to include other bacterial species with different matrix composition into the model, and predict their biofilm architecture by using their aspect ratio and cell-cell interactions. The presence or absence of a substrate for attachment is important for biofilm growth dynamics⁷. To include other biofilm types that are not attached to a substrate, such as pellicles biofilms, the model needs to be adapted to include the effect of the substrate into the verticalization of cells. Incorporating different bacterial species and biofilm types into a model that considers the effects of surface attachment, aspect ratio and cell-cell interaction would allow the development a biofilm theory that could account for various growth dynamics during biofilm development.

Models that predict physical interactions during biofilm formation generally hold true in small biofilms that consist of cells exposed to a homogeneous environment. When biofilms reach a critical size, mechanical interactions are not sufficient to explain biofilm growth dynamics and architecture. At this point, biological and chemical interactions become important due to the presence of solute heterogeneities created by nutrient consumption, waste product secretion, and decreased diffusion of molecules in the biofilm^{2,6}. Phenotypes that cannot be predicted solely on the basis of mechanical interactions include metabolic cross-feeding, persister formation, and responses to stress.

To understand the development of metabolic interactions within biofilms, it is important to consider the physical properties of the cells and extracellular matrix, but even more necessary is to take into account the metabolic state of the bacteria and chemical characteristics of their microenvironment. Similar to what is observed in eukaryotic tissues⁸, it is likely that the presence of

multiple solute gradients and secreted molecules creates a continuum of transcriptional states in biofilms. Each of those states possesses the potential to alter metabolism, and therefore could possibly be responsible for creating cross-feeding interactions. Bacterial macrocolonies, such as those formed by *E. coli*, harbor these aforementioned conditions that have the large potential to give rise to cross-feeding⁹. However, only one metabolic cross-feeding had been described for *E. coli* colonies before this dissertation: the acetate cross-feeding between the anaerobic and aerobic regions of *E. coli* colonies first suggested by Cole *et al.*¹⁰. Considering the high number of physical and chemical parameters that favor the emergence of cellular metabolic heterogeneity, it is surprising that so few have been discovered. One reason for this is that cross-feeding interactions usually lack biological indicators that are either highly specific or visible at a macroscopic scale⁹.

In chapter 3, we overcame some of these problems by applying metabolomics and spatial transcriptomics to find new metabolic cross-feeding in an unbiased approach. During the formation of *E. coli* colonies, an oxygen gradient caused by bacterial metabolism drives the formation of two subpopulations. As oxygen modulates the fluorescence of proteins derived of GFP, these subpopulations had different levels of fluorescence. This naturally developed divergence in fluorescence levels enabled us to obtain sorted bacterial cells from the two sub-populations and analyse their transcriptome. Using a combination of metabolomics and spatial transcriptomics, we showed that *E. coli* colony biofilms cross-feed alanine between parts of anaerobic and aerobic subpopulations. Our proposed model suggests that cells performing anaerobic metabolism at the bottom of the colony secrete alanine into the colony extracellular space. Alanine can then be taken up by cells in the aerobic region lacking other nutrients. This cross-feeding of alanine is mediated by the alanine exporter AlaE, which is the first amino acid exporter to be linked to metabolic cross-feeding in an isogenic system. This is of particular relevance because the benefit of expressing amino acid exporters has remained largely debated and unclear, with most research conducted for biotechnology applications of amino acid hyperproducer strains¹¹. This amino acid cross-feeding has important consequences for bacterial viability and growth, which suggests that new methods that could impair this type of interactions could be used to develop new methods to combat biofilms.

To discover new metabolic interactions within a system such as *E. coli* biofilms, new methods with increased spatial resolution need to be developed in order to determine, isolate and characterize subpopulations created by chemical gradients. The most common approach to isolate a sub-population is by using fluorescence-activated cell sorting (FACS), which allows the separation of cells by fluorescence. The main limitation to apply FACS to biofilm-dwelling cells is the lack of reporters that can be used throughout the whole biofilm community regardless of the local microenvironment. The reason for this is two-fold; 1) The majority of optimized and bright fluorescent proteins, including

photoactivable proteins, are derived from GFP. These proteins need molecular oxygen to be fluorescent, limiting their application to the aerobic biofilm regions¹². This can be improved using fluorescent dyes, such as maleimide-conjugated dyes, wherein fluorescence is independent of molecular oxygen¹³. II) Technical complications include light scattering and the lack of penetration depth of lasers used for fluorophore excitation. When using standard confocal laser scanning microscopy systems, a large amount of light is required to illuminate deep biofilm layers. However, these technical limitations can be partly circumvented by using microscope systems that apply two-photon excitation. These systems use two photons with long wavelengths to excite a fluorophore instead of one photon of a shorter wavelength and hence increase its penetration depth¹⁴.

Another biofilm feature that cannot be predicted solely on the basis of mechanical interactions is the presence of low abundant populations of cells, such as slow-growing cells, that arise due to local chemical heterogeneity or stochastic genetic expression¹⁵. These subpopulations are highly tolerant to antibiotics and detailed understanding of their frequency and location within biofilms is key in context of developing new methods to combat biofilms. Yet, similar to what occurs with cross-feeding populations, the study of slow-growing cells is limited by the lack of reliable reporters. In chapter 4 we developed a method that allows isolation and study of slow-growing cells in an *E. coli* library using the protein TIMER as a growth-dependent fluorescent reporter. This reporter requires molecular oxygen; therefore, this method can be applied to planktonic cultures and aerobic biofilm communities to isolate slow growing cells. This would allow unprecedented studies of highly antibiotic-tolerant cells in biofilms, termed persisters, in particular answering key questions in the field as what is the localization, frequency and regulation of persister cells within biofilms¹⁶. To expand this study to anaerobic regions of a biofilm new fluorescent proteins or fluorescent dyes that do not rely on oxygen-mediated maturation to emit fluorescence need to be developed.

The integration of mechanical, metabolic and biochemical interactions is also required to understand and predict biofilm stress response. Research on biofilm stress response has been pivotal to understand the ecology of bacterial communities and to develop new ways to combat biofilms in clinical and industrial systems^{17,18}. In chapter 5, we showed that the biofilm response to antibiotics relies on mechanical and biological interactions, and occurs at the single-cell level and at the multicellular level. We found that when *V. cholerae* biofilms are exposed to translational inhibitors, there is an increase of the cell volume and a decrease of the biofilm cell density. The increased cell volume observed occurred independently of the biofilm lifestyle and therefore is a single-cell response. The main driver of this phenotype was an altered cellular metabolism caused by protein synthesis inhibition. Furthermore, it was an active response driven by continued enzymatic activity, and it was absent when the sole carbon source, i.e., glucose, was removed. The decreased cell density observed

upon antibiotic exposure corresponded to a multicellular response driven by mechanical and biochemical interactions. In particular, the antibiotic-induced cell volume increase, combined with the polysaccharide lyase activity of the protein RbmB, detached the cells from the biofilm matrix. This detachment allowed for a mechanical expansion of the biofilm and a separation of the cells driven by a release of tension. The decreased cell density can only occur at the community level, and required the combination the single cell responses and the mechanical properties of the matrix.

Responses at the multicellular level can provide benefits to the community that are not the additive result of individual responses. The antibiotic-induced decrease of cell density of biofilms and cell-matrix detachment had important consequences for biofilm ecology and community succession. Antibiotic-treated biofilms could be invaded by other bacterial species and bacteriophages creating multi-species communities or promoting predation, that was otherwise not possible. One hypothesis is that biofilms could benefit from this response by migration and incorporation of antibiotic resistant cells. These cells could then either degrade the antibiotic and decrease its local concentration or by horizontal gene transfer events enable the dissemination of antibiotic resistance^{19,20}.

The capability to distinguish between single-cell and multicellular responses is required to understand the causes and consequences of the responses at a biofilm level. As mentioned previously, this calls for techniques with spatial and temporal resolution that is high enough to characterize and analyze individual cells within a biofilm. Without sufficient temporal and spatial resolution, the results obtained are of little value and might even be misinterpreted. For instance, applying widely-used techniques without single cells analysis, such as crystal violet, the increased cell volume and cell-cell spacing observed in chapter 5 could have been interpreted as an increase in biofilm volume. This would have led to an erroneous conclusion that antibiotic stress induces biofilm formation. To avoid these problems, future research should aim to elucidate how biofilms respond to other stresses and distinguish between single-cell and multicellular responses. In particular, responses to additional antibiotics, predation, environmental changes and starvation should be studied in this manner. This would allow to discover new mechanisms of response, the advantages and disadvantages of a biofilm lifestyle in contrast to planktonic growth, and new interactions between cells and matrix components.

In conclusion, this dissertation shows that biofilm architecture during the first stages of biofilm growth is mostly driven by mechanical interactions amongst actively growing bacteria. Afterwards, when biofilms become large enough, different biofilm regions become metabolically differentiated due to chemical heterogeneity. This heterogeneity in turn creates metabolic cross-feeding interactions that are essential for overall biofilm fitness and survival. Finally, the integration of mechanical, metabolic and biochemical responses enabled the discovery of novel biofilm responses to antibiotics, and its

ecological consequences from a single-cell and multicellular point of view. The sum of these new discoveries could facilitate the development of the much-needed methods and strategies to combat biofilms using mechanical, chemical or biological agents in clinical and industrial settings.

On the future of biofilm research

The work discussed in this dissertation was mainly driven by the need to answer open questions in biofilms research. For this, we applied cutting-edge techniques and advanced equipment. The development of new microscopy techniques with increased temporal and spatial resolution combined with novel pieces of software with improved segmentation capabilities would allow the discovery of further exciting discoveries within bacterial communities. Strikingly, this is even true when applied to old questions that have been of fundamental interest in the biofilm research field for many decades, such as antibiotic response and biofilm growth, exemplified by chapters 2, 3 and 5,

Using new techniques, research on biofilms can be made transferable so as to understand their behaviour in niches that are more comparable to natural environments. Until now, most of the research on biofilms has been performed on communities composed of one or few bacterial species. This is in stark contrast to what is observed in natural systems where up to thousands of bacterial species can coexist^{21,22}. Therefore, future biofilm research will likely focus on more complex communities. This is currently strongly driven by the discovery that highly diverse communities play essential roles²³. Famous examples are the roles of the human gut microbiome on human health and the rhizosphere microbiome in plant development^{21,24}. To study this type of bacterial communities, it is necessary to implement and upgrade the current tools. There are several reasons of why this is unaccomplished so far. Replicating the natural conditions that allow a robust and reproducible establishment of large bacterial communities has remained an extremely difficult task particularly because the vast majority of bacterial species cannot yet be cultivated in laboratory systems²⁵. One possible way to circumvent this problem would be to study these biofilm communities *in situ*. Nevertheless, there are hitherto no techniques that allow to visualize diverse communities with high temporal resolution, while keeping the spatial structures of the community. Current state-of-the-art tools as imaging mass spectrometry and fluorescence in situ hybridization (FISH) are usually destructive or require a fixed sample^{26,27}. Moreover, the most common confocal microscopes that permit to image different fluorescent proteins simultaneously have an upper limit of 3-4 emission spectra with minimal crosstalk. Furthermore, these fluorescent proteins often rely on oxygen to emit fluorescence, making their use for direct imaging of anaerobic samples such as the gut microbiome impossible. Moreover, the use of fluorescent proteins

has only been optimized for few bacterial species that can be grown in the laboratory and its use for unculturable microorganism remains extremely challenging.

Nevertheless, in the last years promising new technologies have been developed. They include the recent imaging techniques such as light-sheet microscopy and two-photon microscopy with decreased photobleaching and increased penetration depth, respectively^{14,28}, the development of neural networks for the analysis of complex samples^{29,30}, and the improvement of single-cell bacterial RNAseq^{31,32}. The utilization of these techniques on biofilm research promise great advances that will helps us to study multi-species biofilms in natural, clinical, and industrial settings.

References

1. Teschler, J. K. *et al.* Living in the matrix: assembly and control of *Vibrio cholerae* biofilms. *Nat. Rev. Microbiol.* **13**, 255–268 (2015).
2. Stewart, P. S. & Franklin, M. J. Physiological heterogeneity in biofilms. *Nat. Rev. Microbiol.* **6**, 199–210 (2008).
3. Beroz, F. *et al.* Verticalization of bacterial biofilms. *Nat. Phys.* **14**, 954–960 (2018).
4. Díaz-Pascual, F. *et al.* Breakdown of *Vibrio cholerae* biofilm architecture induced by antibiotics disrupts community barrier function. *Nat. Microbiol.* **4**, 2136–2145 (2019).
5. Singh, P. K. *et al.* *Vibrio cholerae* Combines Individual and Collective Sensing to Trigger Biofilm Dispersal. *Curr. Biol.* **27**, 3359–3366.e7 (2017).
6. Hartmann, R. *et al.* Emergence of three-dimensional order and structure in growing biofilms. *Nat. Phys.* **15**, 251–256 (2019).
7. Qin, B. *et al.* Cell position fates and collective fountain flow in bacterial biofilms revealed by light-sheet microscopy. *Science (80-.)*. **369**, 71–77 (2020).
8. Adler, M., Korem Kohanim, Y., Tendler, A., Mayo, A. & Alon, U. Continuum of Gene-Expression Profiles Provides Spatial Division of Labor within a Differentiated Cell Type. *Cell Syst.* **8**, 43–52.e5 (2019).
9. San Roman, M. & Wagner, A. An enormous potential for niche construction through bacterial cross-feeding in a homogeneous environment. *PLOS Comput. Biol.* **14**, e1006340 (2018).
10. Cole, J. A., Kohler, L., Hedhli, J. & Luthey-Schulten, Z. Spatially-resolved metabolic cooperativity within dense bacterial colonies. *BMC Syst. Biol.* **9**, 15 (2015).
11. Katsube, S., Ando, T. & Yoneyama, H. L-Alanine Exporter, AlaE, of *Escherichia coli* Functions as a Safety Valve to Enhance Survival under Feast Conditions. *Int. J. Mol. Sci.* **20**, 4942 (2019).
12. Drepper, T. *et al.* Reporter proteins for in vivo fluorescence without oxygen. *Nat. Biotechnol.* **25**, 443–5 (2007).
13. Ellison, C. K., Dalia, T. N., Dalia, A. B. & Brun, Y. V. Real-time microscopy and physical perturbation of bacterial pili using maleimide-conjugated molecules. *Nat. Protoc.* **14**, 1803–1819 (2019).
14. Neu, T. R., Walczysko, P. & Lawrence, J. R. Two-Photon Imaging for Studying the Microbial Ecology of Biofilm Systems. *Microbes Environ.* **19**, 1–6 (2004).
15. Bakkeren, E., Diard, M. & Hardt, W.-D. Evolutionary causes and consequences of bacterial antibiotic persistence. *Nat. Rev. Microbiol.* **18**, 479–490 (2020).
16. Yan, J. & Bassler, B. L. Surviving as a Community: Antibiotic Tolerance and Persistence in Bacterial Biofilms. *Cell Host Microbe* **26**, 15–21 (2019).
17. Stewart, P. S. *et al.* Contribution of Stress Responses to Antibiotic Tolerance in *Pseudomonas aeruginosa* Biofilms. *Antimicrob. Agents Chemother.* **59**, 3838–3847 (2015).
18. Boudarel, H., Mathias, J.-D., Blaysat, B. & Grédiac, M. Towards standardized mechanical characterization of microbial biofilms: analysis and critical review. *npj Biofilms Microbiomes* **4**, 17 (2018).
19. Abe, K., Nomura, N. & Suzuki, S. Biofilms: hot spots of horizontal gene transfer (HGT) in aquatic environments, with a focus on a new HGT mechanism. *FEMS Microbiol. Ecol.* **96**, 1–12 (2020).
20. Madsen, J. S., Burmølle, M., Hansen, L. H. & Sørensen, S. J. The interconnection between biofilm formation and horizontal gene transfer. *FEMS Immunol. Med. Microbiol.* **65**, 183–195 (2012).
21. Berendsen, R. L., Pieterse, C. M. J. & Bakker, P. A. H. M. The rhizosphere microbiome and plant health. *Trends Plant Sci.* **17**, 478–86 (2012).
22. Almeida, A. *et al.* A new genomic blueprint of the human gut microbiota. *Nature* **568**, 499–504 (2019).
23. Burmølle, M., Ren, D., Bjarnsholt, T. & Sørensen, S. J. Interactions in multispecies biofilms: do they actually matter? *Trends Microbiol.* **22**, 84–91 (2014).
24. de Vos, W. M. & de Vos, E. A. Role of the intestinal microbiome in health and disease: from correlation to causation. *Nutr. Rev.* **70**, S45–S56 (2012).
25. Nayfach, S., Shi, Z. J., Seshadri, R., Pollard, K. S. & Kyrpides, N. C. New insights from uncultivated genomes of the global human gut microbiome. *Nature* **568**, 505–510 (2019).
26. Tropini, C., Earle, K. A., Huang, K. C. & Sonnenburg, J. L. The Gut Microbiome: Connecting Spatial Organization to Function. *Cell Host Microbe* **21**, 433–442 (2017).
27. Zhang, J. *et al.* Cryo-OrbiSIMS for 3D Molecular Imaging of a Bacterial Biofilm in Its Native State. *Anal. Chem.* **92**, 9008–9015 (2020).
28. Power, R. M. & Huisken, J. Adaptable, illumination patterning light sheet microscopy. *Sci. Rep.* **8**, 9615 (2018).

29. Falk, T. *et al.* U-Net: deep learning for cell counting, detection, and morphometry. *Nat. Methods* **16**, 67–70 (2019).
30. Van Valen, D. A. *et al.* Deep Learning Automates the Quantitative Analysis of Individual Cells in Live-Cell Imaging Experiments. *PLoS Comput. Biol.* **12**, e1005177 (2016).
31. Blattman, S. B., Jiang, W., Oikonomou, P. & Tavazoie, S. Prokaryotic single-cell RNA sequencing by in situ combinatorial indexing. *Nat. Microbiol.* (2020) doi:10.1038/s41564-020-0729-6.
32. Imdahl, F., Vafadarnejad, E., Homberger, C., Saliba, A. & Vogel, J. Single-cell RNA-sequencing reports growth-condition-specific global transcriptomes of individual bacteria. *Nat. Microbiol.* (2020) doi:10.1038/s41564-020-0774-1.